Estimation Curve Numbers using GIS and Hec-GeoHMS Model

Hayat Kareem Shukur
Instructor
Engineering Collage – Al-Mustansiryah University
Corresponding Author E-mail: hayat.azawi@okstate.edu

ABSTRACT

Recently, the development and application of the hydrological models based on Geographical Information System (GIS) has increased around the world. One of the most important applications of GIS is mapping the Curve Number (CN) of a catchment. In this research, three softwares, such as an ArcView GIS 9.3 with ArcInfo, Arc Hydro Tool and Geospatial Hydrologic Modeling Extension (Hec-GeoHMS) model for ArcView GIS 9.3, were used to calculate CN of (19210 ha) Salt Creek watershed (SC) which is located in Osage County, Oklahoma, USA. Multi layers were combined and examined using the Environmental Systems Research Institute (ESRI) ArcMap 2009. These layers are soil layer (Soil Survey Geographic SSURGO), 30 m x 30 m resolution of Digital Elevation Model (DEM), land use layer (LU), "Look–Up tables" and other layers resulted from running the software.

Curve Number which expresses a catchment's response to a storm event has been estimated in this study to each land parcel based on LU layer and soil layer within each parcel. The results showed that a CN of 100 (dark Blue) means surface water. The high curve numbers (100 -81) (Blue and light Blue) corresponding to urbanized areas means high runoff and low infiltration; whereas low curve numbers (77- 58) (Brown and light Brown) corresponding to the forested area means low runoff and high infiltration. Four classes of land cover have been identified; these are surface water, medium residential, forest and agriculture.

Keywords:GIS, land use, curve number (CN), watershed planning.

تقدير ارقام المنحني CN بأستخدام نظم المعلومات الجغرافية GIS و HEC-GeoHMS

حياة كريم شكر
مدرس
كلية الهندسة - الجامعة المستنصرية

الخلاصة

في الآونة الاخيرة ازداد تطوير وتطبيق النماذج الهيدرولوجية على أساس نظم المعلومات الجغرافية (GIS) في جميع أنحاء العالم. واحد من اهم التطبيقات هو حساب (قيم ارقام المنحني Curve Numbers) . في هذا البحث ، تم استخدام ثلاث برامج مع بعضها لغرض حساب قيم ارقام المنحني لمستجمع مياه الجدول المالح البالغ مساحته 19210 هكتار ، ولاية اوكلاهوما والواقع في امريكا. وبتراكب عدة طبقات كطبقة التربة (مسح التربة الجغرافي SSURGO) وطبقة نظم ملف موديل الارتفاع الرقمي DEM وطبقة ملف الغطاء الأرضي (LU) مع دمج جدول Look-Up وطبقات اخرى ناتجة من عمل البرامج المستخدمة.
في هذه الدراسة، تم حساب قيم ارقام المنحني التي تعبر عن مدى استجابة المستجمع المائي الى عاصفة مطرية . اظهرت النتائج ان رقم المنحني المتمثل باللون الأزرق الغامق والمساوي الى 100 يعني مياه سطحية . ان الأرقام العالية بين (100-81) والمتمثلة

بالمناطق العمرانية (اللون الأزرق والازرق الفاتح) تعني ان الاستجابة لامتصاص الماء قليل جداً في هذه المناطق، بينما الأرقام الواطئة بين (77-58) والمتمثلة بمناطق الغابات والمناطق الزراعية (اللون البني والبني الفاتح)، تعني ان الاستجابة لامتصاص الماء كبيرة .لقد تم تصنيف أربعة انواع من الغطاء الأرضي لمنطقة الدراسة: مناطق مائية، مناطق سكنية متوسطة، مناطق غابات، ومناطق زراعية.

الكلمات الرئيسية : نظم المعلومات الجغرافية، ملف الغطاء الأرضي، الرقم المنحني، التخطيط العمراني.

1. INTRODUCTION

A curve number (CN), an index developed by the Soil Conservation Service (SCS) now called the Natural Resource Conservation Service (NRCS), is used to estimate the amount of rainfall that infiltrates into the soil and the amount of surface runoff **Chin, 2000 ; Durrans, 2003**. It is first developed for agricultural watersheds, and then it was consequently used in urban areas. This method should be used only with 24- hour rainfall duration. It is not time dependent; thus, it neglects differences resulting from varying rainfall durations and intensities **Durrans, 2003; USDA, 1986**. Modeling is increasingly used to determine Curve number. ArcView 9.3 has been developed by the Environmental Systems Research Institute (ESRI) for analyzing, modeling, manipulating, querying, and visualizing data from many different sources, **Wang and Cui, 2004**. Various types of watershed models, such as SWMM **James, et al. 2010** and SWAT **Arnold et al. 1996,** TR-55, Tr-20, HIC-!, WMS, and HIC-HMS use this method to determine runoff **Shadeed and Almasri, 2010**. Sediment and pesticide are then calculated based on the runoff. An area weighted average curve number is often used to calculate the runoff for the entire watershed by helping GIS. Implementing GIS techniques for producing spatially varied curve number can reduce the time from days, if not weeks, to hours. In addition, GIS can be used for future analysis to predict watershed response associated with change in urbanization Zhan &Huang 2004. Because curve number is a function of the soil and land use of a drainage basin, estimation of a curve number requires mapping of the soil and land use within the drainage basin boundaries, and specification of unique soil types and unique land use categories. The manual calculation of curve numbers for large areas or many drainage basins can be cumbersome and time-consuming; therefore, a Geographic Information System (GIS) is an appropriate tool to use for such an application.

Most researchers seem to agree that using GIS for estimating CN is effective and is an efficient use of time. **Gumbo, et al., 2002** described a method of assessing the effectiveness of storm drainage by combining a digital elevation model (DEM) with a rainfall-runoff model based on the Soil Conservation Service South African manual (SCS-SA). The land use, watershed and soil map of the University of Zimbabwe's (UZ) main campus was merged in Arc View and initial Curve Numbers (CN) were assigned. A composite curve number (CNc) was determined for a watershed with sub-area of different soil types and land cover by weighting the CN's for different subareas in proportion to the land area associated with each area. A combination of a DEM and rainfall-runoff model with in GIS platform proves to be useful in estimating runoff on urbanized watersheds. **Nayak, et al. 2012** calculated the curve number of Uri river watershed in Lower Narmada basin in Central India. Satellite images for two different periods (2001 and 2007) have been interpreted in ILWIS GIS platform for preparation of land use/land cover maps. The weighted average curve numbers (CN) for both years was calculated and the surface runoff volume was computed by using the SCS curve Number method. The results of runoff volume were compared with the observed volume calculated from recorded hydrograph for the selected rainfall events. The results showed

that the percent increase in runoff volume in 2007 was 20-40 % compare to those in 2001for the similar rainfall events. The major advantage of employing GIS and rainfall-runoff modeling in storm drainage design is that more accurate sizing and orientation can be achieved. Furthermore the calculation can be done much faster and predictive modeling can be performed **Schulze et al., 1992**; **Gumbo, et al., 2002**.

Milhalik, et al., 2008 estimated storm water runoff and peak runoff rates by using GIS. In this study, two runoff modeling methods have been applied, the rational method and SCS_CN method. Rainfall intensities from five storms were used in the models together with the runoff coefficients and curve numbers (CN) for many lands, and then the results from the two methods were compared. The results showed that the values of peak rate estimated by SCS_CN method were more accurate than those in the Rational Method. **Zhan &Huang 2004** used the ArcCN Runoff tool, an extension of ESRI ARCGIS software, to determine curve numbers and calculate runoff for a storm event within a watershed. **Merwede, 2009** used HEC-GeoHMS to create an SCS curve number grid for Cedar Creek in northeast Indiana. Soil and land use/ land cover data were downloaded from the U.S. geological Survey (USGS) 2001 national Land Cover Dataset (USGS 2007**)** and clipped to the Cedar Creek study watershed by using GIS tools. This model saves time and effort when it was used to calculate curve number for each land use. Because of these recent advancements, the objective of this research was to apply GIS software to determine Curve Number for SC watershed as a first step for larger project to study many hydrologic models such as rainfall-runoff model to calculate runoff volume and peak discharge.

2. STUDY AREA DESCRIPTION

The watershed in Salt Creek Study Area is located in Northern Oklahoma as shown in **Fig. 1.** The drainage area for water bodies included in this study is located in Osage County. A Hec-GeoHMS model had been used to assign curve numbers (CN), which is a function of land use, soil type, and soil moisture, to Salt Creek Watershed. The model is linked to a geographic information system (GIS) for convenient generation and management of model input and output data. A CN of 100 represents a perfectly impermeable watershed. A CN of zero, on the contrary, represents a watershed abstracting all the rainfall with no runoff.

3. PROCCESSING DATA

In this study, spatial data layers (Digital Elevation Models (DEM), soil, and land use/ land cover were collected from the local USDA, NRCS United State Department of Agriculture natural resources data **USDA, 2012**. These data are usually available on the Internet. Once the data has been gathered and the software programs (ArcView GIS 9.3 with ArcInfo, Arc Hydro Tool and Hec-GeoHMS) were downloaded, then the next step is to clip these data for the study area.

The following procedure of how to incorporate GIS with soil data, land use / land cover data, and DEM to estimate CN is presented for Salt Creek watershed. Sc_dem, the raw 30 DEM for SC, Sc_lc, the land cover grid, and Sc_soil, the geodatabase with SSURGO spatial and tabular data, were all clipped using a polygon feature from the overlay layer (watershed boundary layer) as

shown in **Fig.2** (a) & (b). All datasets were projected to the same coordinate system (NAD_1983_UMT_16).

The numbers in land use shown in **Fig. 3a** represent the land use class defined according to the USGS land cover institute (LCI). However, after reclassifying, the numbers which represent the land use are shown in **Fig. 3b**. The classification system used for NLCD is modified from the Anderson land-use and land-cover classification system. Many of Anderson classes especially the level III classes are best derived using aerial photography.

In the attribute table of Sc_lu, the dominant land used throughout all of the study area is grassland. The second most prevalent land use is the combination of Pasture/hey and grassland/herbaceous, and the third is the developed land and then water. Sc_lc was reclassified using **Table 1** to represent these four major classes. Sc_lc was reduced from 11 to 4 as shown in **Fig. 3a** and **3b**.

4. PREPARING SOIL DATA FOR CN GRID

To prepare soil data for CN, the author first created an empty field named Soil Code for storing soil groups because the attribute table for Sc-soil_clip has no field for storing these data. A table called "comp" in soil data, which contains the attribute hydrogroup and soil data, is linked to the map document. The polygon features in Sc_soil_clip are related to component table through mukey field **Merwade, 2009**. Usually soil surveys list soil type (e.g., Norge silt clay) by name, however, the information needed to determine a curve number is the hydrologic soil group, which indicates the amount of infiltration that occurs in each type of soil. There are four hydrologic soil groups: A, B, C and D. The definition of each is given in **Table 2.**

Four fields named PctA, PctB, PctC, and PctD were created. For Salt Creek area, only one soil group assigned to each polygon so a polygon with soil group "A" will have PctA = 100, PctB = 0, PctC = 0, and PctD = 0. Similarly for a polygon with soil group D, only PctD = 100, and the other three Pcts are zero. The attribute table below was obtained. After the calculations were done, the Soil Code will be populated with letters A, B, C, D as shown in **Fig. 4.**

5. MERGING OF SOIL AND LANDUSE DATA

By using the Union tool in ArcToolbox, Soil and land use data were merged and CNLook-Up table was created using Arc Catalogue as shown in **Fig.**

6. CREATING CN Grid

After combining land use and hydrologic soil group maps using GIS, a CN grid was created using Hec-geoHMS. Hec-geoHMS uses the merged feature class (lc_soil_union) and the lookup table (CNLookUp) to create the curve number grid. The author created a field named "LandUse" in the lc_soil_union that will have land use category information to link it to "CNLookUp". Hec-geoHMS look for this information in Landuse field while it is stored in GRIDCODE field. The author added field named landUse and equated it to GRIDCODE as shown in **Fig.6**. By clicking on Utility → Creat parameter Grids, the author chose the lookup parameter as Curve Number, and

lc_soil_Union for Curve number Polygon and left the default CNGrid name for the curve Number Grid. In a minute A CNGrid will be add to the map document as shown in **Fig.7**.

7. RESULTS AND ANALYSIS

Geographic Information System (GIS) in combination with HegGeoHMS model provide ideal tools for calculating curve numbers. Curve Numbers were successfully and easily calculated. The power of combining soil layers and land use layers which is the input of the curve number method facilitates the computations and gives an accurate CN. CN estimation without the use of GIS can be time-consuming and labor intensive. The results are summarized below:

1. GIS and Hec-GeoHMS are capable of building up most of the input data required to calculate CN. The procedure of calculating CNs, which can be applied to any watershed in Iraq such as Baghdad city, Arbil city, etc.), is depending on the availability of GIS data. The step by step method for calculating CN for any watershed is presented in **Merwade, 2009.**

2. Four hydrologic soil groups were found in the case study, soil groups A, B, C, and D. and four classes of land cover have been identified; these are surface water, medium residential, forest and agriculture. This information is very useful for Rainfall-Runoff Modeling to estimate peak discharge.

3. A CN of 100 is surface water with zero infiltration. High CNs (100-81) corresponded to the urbanized areas of the watershed (Blue and light Blue), which has the potential to generate the greatest amount of runoff in a storm event.

4. Low curve numbers (77-58) (Brown and light Brown) corresponded to the forested and agricultural areas of the watershed, which generates little runoff and high infiltration rate as shown in **Table 2**.

5. This analysis can be extended further to estimate the effect of change in land use on direct runoff and to find how curve numbers vary with season and with rainfall amount. In addition, CNs can be used with Long-Term Hydrologic Impact Assessment (L-THIA) to calculate annual runoff and nonpoint source pollution at the watershed.

8. REFERENCES

- Arnold, J.G., Williams, J.R., Srinivasan, R., King, K.W., 1996.SWAT: *Soil and Water Assessment Tool.* USDA-ARS, Grass-Land, Soil and Water Research Laboratory, Temple, TX.
- Chin, D. A., 2000. *Water Resources Engineering*. Upper Saddle River, New Jersey: Pearson Prentice Hall.
- Durrans, H., 2003, *Stormwater Conveyance Modeling and Design*. Haestad Press, Waterbury, CT. Environmental protection agency 841-B-09-001. Washington, DC.
- Gumbo, B., Munyamba, N., Sithole, G., and Savenije, H., H., G., 2002, *Coupling of Digital Elevation Model and Rainfall-Runoff Model in Storm Drainage Design*, Physics and chemistry, 24:755-764.

- James, W. R. C., Rossman, L. E., & James, W. 2010, *User's Guide to SWMM5:* Computational Hydraulic International (CHI), 12th edition. USA.
- Merwade, V., 2009, *Creating SCS Curve Number Grid Using HEC-GeoHMS*. Retrieved from http://web.ics.purdue.edu/~vmerwade/tutorial.html.
- Mihalik, N.E., Levine, S.N., and Amatya, M.D., 2008, *Rainfall-Runoff Modelling of the Chapelbranch Creek Watershed Using GIS-Based Rational and SCS-SC Methods*. ASABE: 083971: St.Joscph, Mich.
- Nayak, T. Verma, K. M.and Hema, B. S., 2012, *SCS Curve Number Method in Narmada Basin*. Journal of international of Geomatics and Geosciences. 3,1:219-228.
- Schulze, R. E., Schmidt, E. J., and Smithers, J. C., 1992, *SCS-SA User Manual PC Based SCS Design Flood Estimates for Small Catchment in Southern Africa Pietermaritzburg*: Department of Agricultural Engineering, University of Natal.
- Shadeed, S., and Almasri, M., 2010, Application of GIS-based SCS-CN method in West Bank Catchments, Palestine. Journal of Water Science and Engineering, 3,1:1-17

- United State Department of Agricultural (USDA) 1986. *Urban Hydrology for Small Watersheds* (TR-55). Second Edition. Natural Resources Conservation Service.

- United States Department of Agriculture (USDA), 2012, *Geospatial Data Gateway*. Retrieved from <datagateway.nrcs.usda.gov>.

- United States Geological Survey (USGS), 2013, *Land Cover Institute (LCI). NLCD land Cover Class Definitions*. Retrieved from < http://landcover.usgs.gov>.

- Wang, X., and P. Cui, 2004, *Linkage of ArcView Gis with RZWOM.* Journal of Spatial Hydrology, 4, 2:1-16.
- Zhan, X. Y., and Huang, M. L., 2004. *ArcCn-Runoff: An ArcGIS Tool for Generating Curve Number and Runoff Maps*, Journal of Environmental Modeling and software, 19: 875-879.

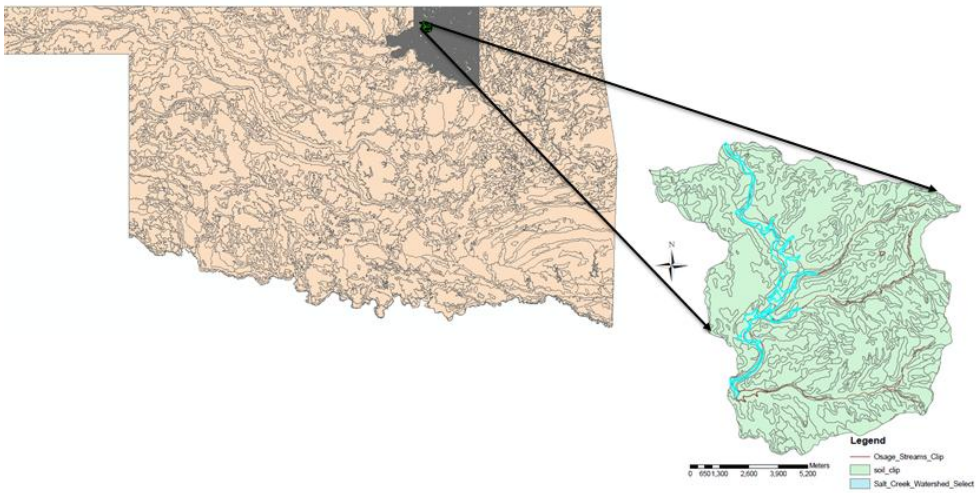

Figure 1. Location of the case study showing Osage River and streams.

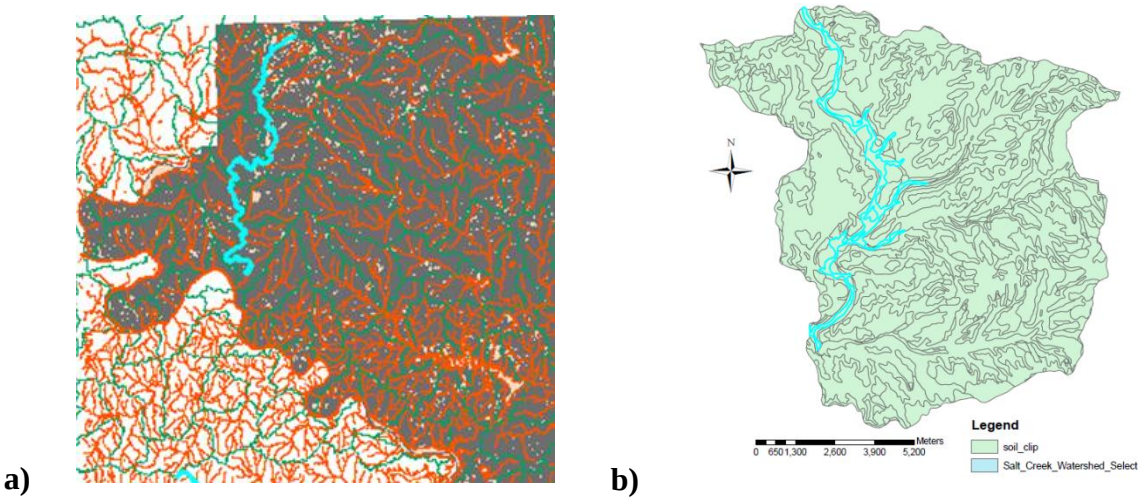

Figure 2. a) Soil data for Osage county before clipping. **b)** Soil clip map by watershed

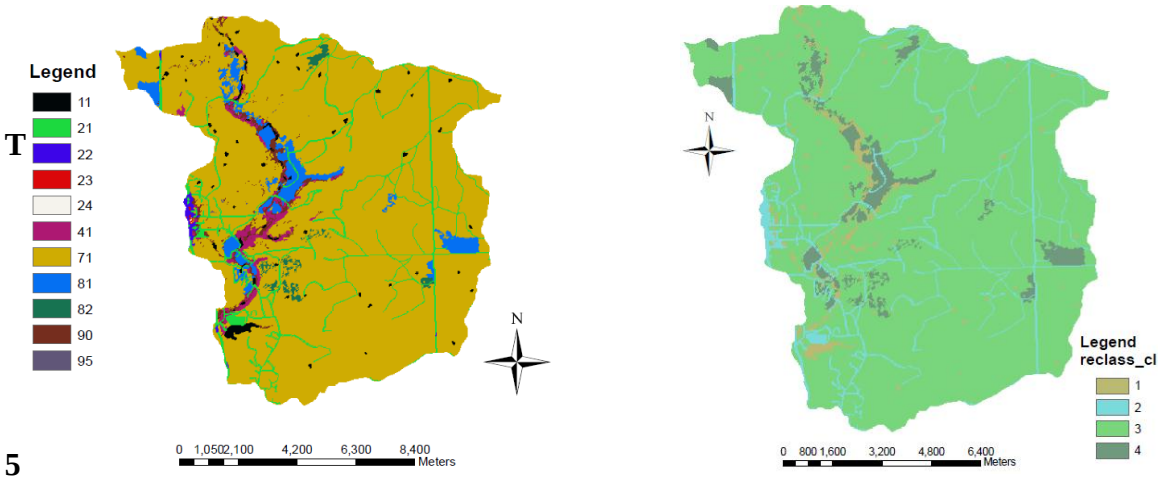

Figure 3. Prepared land use data for CN grid **a)** Land use class defined according to USGS land cover institute **b)** Land use class after reclassification which was reduced from 11 to 4 classes.

Attributes of SC_SOIL

FID	Shape *	AREASYMBOL	SPATIALVER	MUSYM	MUKEY	SoilCode	PctA	PctB	PctC	PctD
0	Polygon	OK113	2	67	623462	B	0	100	0	0
1	Polygon	OK113	2	62	623457	D	0	0	0	100
2	Polygon	OK113	2	54	623449	D	0	0	0	100
3	Polygon	OK113	2	62	623457	D	0	0	0	100
4	Polygon	OK113	2	54	623449	D	0	0	0	100
5	Polygon	OK113	2	61	623456	D	0	0	0	100
6	Polygon	OK113	2	68	623463	C	0	0	100	0
7	Polygon	OK113	2	54	623449	D	0	0	0	100
8	Polygon	OK113	2	49	623444	D	0	0	0	100
9	Polygon	OK113	2	69	623464	C	0	0	100	0
10	Polygon	OK113	2	70	623465	C	0	0	100	0

Record: 1 Show: All Selected Records (0 out of 380 Selected) Options

Figure 4. Attribute table of Sc_soil. SoilCode field populated with letters A, B, C, D.

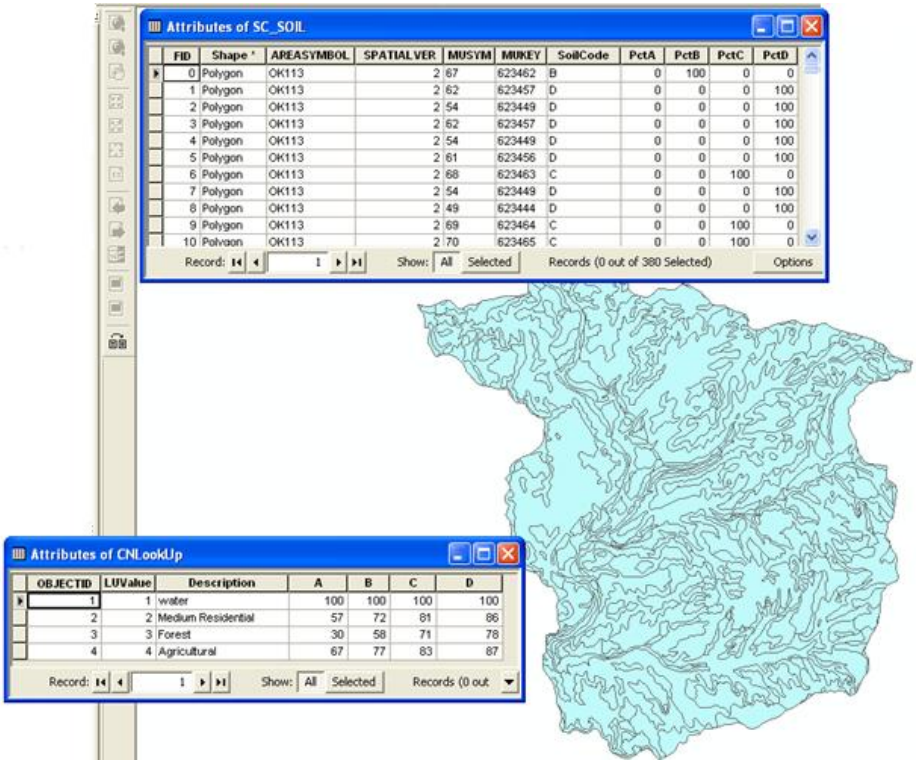

Figure 5. Creating CNLook-Up table for SC watershed

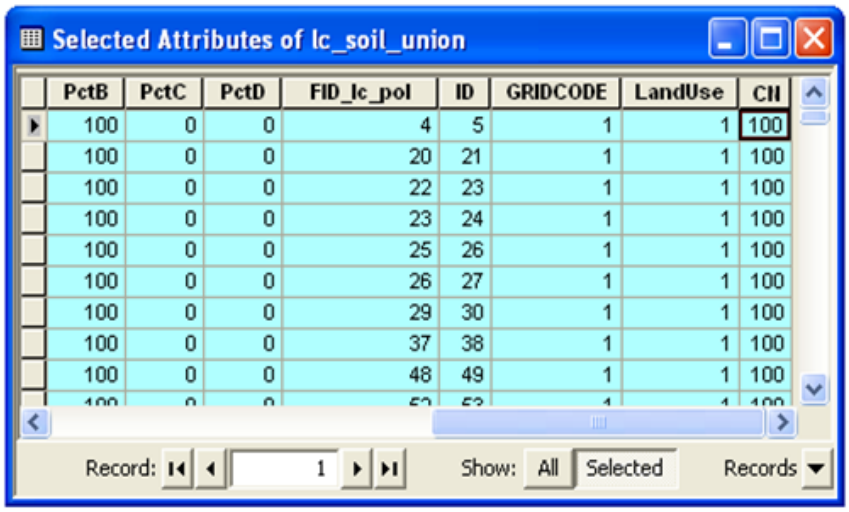

Selected Attributes of lc_soil_union

PctB	PctC	PctD	FID_lc_pol	ID	GRIDCODE	LandUse	CN
100	0	0	4	5	1	1	100
100	0	0	20	21	1	1	100
100	0	0	22	23	1	1	100
100	0	0	23	24	1	1	100
100	0	0	25	26	1	1	100
100	0	0	26	27	1	1	100
100	0	0	29	30	1	1	100
100	0	0	37	38	1	1	100
100	0	0	48	49	1	1	100

Record: 1 Show: All Selected Records

Figure 6. Creating LandUse" in the lc_soil_union attribute table

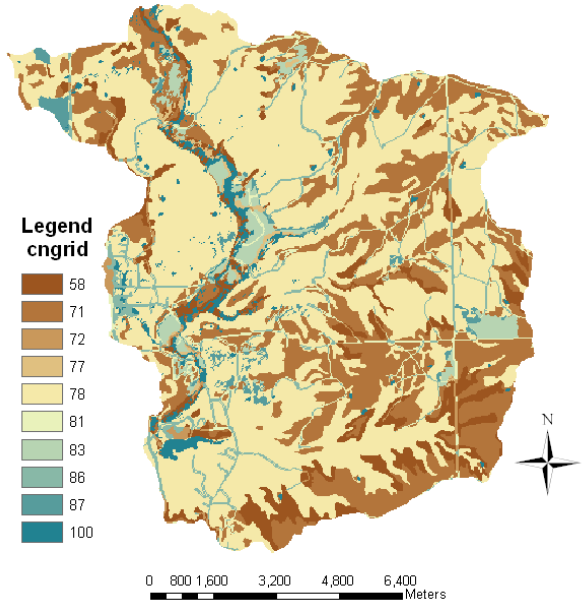

Figure 7. Curve Number (cngrid) calculations for the case study. The highest CN=100 &the lowest CN =58.

Table1. Original NLCD classification and reclassification **USGS, 2013**.

Original NLCD classification		**Revised classification (re-classification)**	
Number	*Description*	*Number*	*Description*
11	Open water	1	Water
90	Woody wetlands		
95	Emergent herbaceous wetlands		
21	Developed, open space	2	Medium Residential
22	Developed, low intensity		
23	Developed, medium intensity		
24	Developed, high intensity		
41	Deciduous forest	3	Forest
42	Evergreen forest		
43	Mixed forest		
31	Barren land	4	Agricultural
52	Shrub/scub		
71	Grassland/herbaceous		
81	Pasture/hay		
82	Cultivated crops		

Table 2. Description of NRCS Soil Groups **James, et al., 2010.**

Group	Description	Saturated Hydraulic Conductivity (in/hr)
A	High infiltration rates, well to excessively drained sands or gravels	≥ 0.45
B	Moderate infiltration rates , Shallow loess, sandy loam	0.30-0.15
C	Slow infiltration rates, clay loams, shallow sandy loam	0.15-0.05
D	Very slow infiltration rates, consisting chiefly of clay soil	0.05-0.00

Evaluation of Urban Planning Projects Criteria Using Fuzzy AHP Technique

Dr. Walid Mustafa Kamas
Professor
Department of Cities Planning Engineering
Technical College
Technical University of Sulaymaniyah
Email:proff_walid @yahoo.com

Dr. Hafeth I. Naji
Assist. Professor
Department of Civil Engineering
College of Engineering
University of Diyala
Emai:hafizibrahem1973 @gmail.com

Aya A. Hasan
M.Sc.Student
Department of Civil Engineering
College of Engineering
University of Diyala
Email:aya_ali393930@yahoo.com

ABSTRACT

In this research, Fuzzy Analytic Hierarchy Process technique is applied (Fuzzy AHP) which is one of multi-criteria decision making techniques to evaluate the criteria for urban planning projects, the project of developing master plan of Al-Muqdadiyah city to 2035 has been chosen as a case study. The researcher prepared a list of criteria in addition to the authorized departments criteria and previous researches in order to choose optimized master plan according to these criteria. This research aims at employing the foundations of (Fuzzy AHP) technique in evaluating urban planning criteria precisely and flexible. The results of the data analysis to the individuals of the sample who are specialists, in this aspect. The land use criteria are more important than the rest of the criteria in these projects, where it received the relative importance with percentile (42.1 %).

Key words: Fuzzy AHP , urban planning , master plan criteria.

تقييم معايير مشاريع التخطيط الحضري باستخدام تقنية Fuzzy AHP

د. وليد مصطفى خماس
استاذ
قسم هندسة تخطيط المدن
كلية التقنية/ الجامعة التقنية سليمانية

د. حافظ ابراهيم ناجي
استاذ مساعد
قسم الهندسة المدنية
كلية الهندسة/جامعة ديالى

اية علي حسن
طالبة ماجستير
قسم الهندسة المدنية
كلية الهندسة/ جامعة ديالى

الخلاصة

في هذا البحث تم تطبيق تقنية التحليل الهرمي الضبابي (Fuzzy AHP) وهي احدى تقنيات اتخاذ القرار المتعدد المعايير لتقييم المعايير الخاصة بمشاريع التخطيط الحضري وقد اختير مشروع تطوير التصميم الاساس لمدينة المقدادية للعام 2035كحالة دراسية. قام الباحث بأعداد قائمة من المعايير بالإضافة الى معايير الدوائر المختصة والبحوث السابقة لكي يتم اختيار المخطط الاساس الامثل وفق هذه المعايير. يهدف هذا البحث الى توظيف اسس تقنية (Fuzzy AHP) في تقييم معايير التخطيط الحضري بشكل دقيق ومرن .وتشير نتائج تحليل البيانات لأفراد العينة من ذوي الاختصاص في هذا المجال ان معايير استعمالات الارض هي اكثر اهمية من بقية المعايير في هذه المشاريع حيث حصل على اهمية (42.1%).

الكلمات الدالة: عملية التحليل الهرمي الضبابي ، التخطيط الحضري ، معايير المخطط الاساس.

1. INTRODUCTION

Urban planning is the science of large combines of many variables natural, social and engineering work to guide the city's growth and to address their problems, and provides them with their requirements for urban balanced life, and that the most important quest is to minimize the environmental problems caused by human-induced air pollution and haphazard construction and other, **Mahmoud, 2012**. Whereas **Pleho,** and **Avdgic, 2008** have defined urban planning as to predict possible number of people in space and fulfill people needs for living, working and other activities, with providing needs for infrastructure (water, energy, traffic, etc.). The urban planning is to be balanced with and meets the requirements of the current generation for resources and energies without exposure to, or consuming the share of future generations; the urban planning must be sustainable, **Abdallah, 2015**.

The importance of urban planning is contributing to a sustainable pattern of development. Despite the emergence of urban regeneration and sustainable development as parallel strands of urban policy, there has been little co-ordination between them and an imbalance in action, with greater emphasis given to achieving urban regeneration especially economic regeneration, than to sustainability. It can be argued that all urban regeneration contributes to sustainable development through the recycling of derelict land and buildings, reducing demand for peripheral development and facilitating the development of more compact cities, **Couch**, and **Dennemann ,2000**.

2- MASTER PLAN CRITERIA

The modern urban planning process includes multi-criteria analysis models. Numerous criteria are typically considered during decision making, **Kurtener**, and **Badenko, 2000**.
The standards mean provide a certain share of each individual, when standards applied properly it means everyone gets his share. Application planning standards accurately in all fields is to ensure proper implementation of the plans and achieve efficient performance. The criteria can be summarized as follows:

2-1 Economic Criteria

The existence of investments resulting in a number of jobs, it means raising taxes. This in turn will lead to an increase in spending, consumption and improving services is in one hand, while on the other hand, the presence of investment will lead to the presence of suitable work atmosphere. All this shows that the subject of the most important topics in the continuing evolution of urban life to any area it is known that good government is behind the investment, **Phillips**, and **Chistine, 2003**, as shown in **Table 1**.

2-2 Environmental Criteria

Environmental considerations into urban planning and administration gives noteworthy advantages in each place of urban life, crosswise over issues, for example, health, security and economic development. The initial stage in urban environment quality assessment is to recognize important environmental segments (air, water, chaos, waste substances, green zone) and after

that to set up significant assessment criteria by utilizing these components or segments, **Pleho**, and **Avdagic, 2008**. As shown in **Table 1**.

2-3 Social Criteria

It highlights the importance of citizen participation. It is not visible aspect in the planning process, but with visible results and that is considered as one of the important aspects for the planner because of a contactless directly to humans, **Silberstein et al., 2000**. **Jaafar ,2007** mentions that social criteria represents the social nature of society and the nature of the composition and unity of the neighborhood and the social values and symbols in that city. This is shown in **Table 1**.

2-4 Land use Criteria

There are multiple local standards to regulate land used within the master plans, including Iraqi cadres proposals that have been approved by the Urban Planning who is responsible for the master plans that addressed the urban organization of residential areas and land use, including global standards allocated to determine land use to be a benchmark in the preparation of the design basis, **Abdul Wahid, 2010**. The decision-making process for urban area used portion has dependably been entangled, **Arefiev et al., 2015**. When objectives are spatial, information are required on the geological areas, spatial formulations of objectives and data on the spatial pattern of criterion values, **Stewart**, and **Janssen, 2014**.

Haque, and **Asami, 2014** clarify that land-use planning might be characterized as the procedure of assigning diverse exercises or uses, (for example, neighborhoods, manufacturing industries, recreational activities) to particular units of range inside a region.

2-5 Technical Criteria

At the beginning of this century, many countries for many reasons, mostly Arab countries adopt a standard 100 square meter for each individual, and on the basis of it , the future needs for urban expansion is accounted, per capita be according to that square meter and it is distributed according to the services that enjoy it. In light of the trend towards vertical construction, the minimum ratio to less than that and perhaps up to less than 50 square meter, thus the decline is limited in the residential share of first place, this is driven by the educational, health and entertainment and cars parking. So, it should reconsider with one per capita in sharing of the land and city thus the ratio is vary according to directions and the policy of every state, some of them directed to the vertical construction and the other toward the horizontal, where the need is increasing for greater expansion in the horizontal space and up per capita to more than 80 square meter, **Al-Diliamy, 2014**.

3. THE MAJOR CONSIDERATIONS INFLUENCING MASTER PLAN PREPARATION

Main concerns which may affect preparing master plan are as follows, **Al-Diliamy, 2014**:

1. Natural condition on topography and prevailing climatic characteristics, because it affect the engineering projects in construction roads, which need a large area of land,

and the planning and design must be in harmony with the natural, topography and climate realities.

2. The social reality and the nature of the social situation in terms of customs, traditions and culture, as well as it must stay away from imported designs and plans that do not fit in often with social and environmental reality and the specificity of the Arab and Islamic societies.
3. Achieving urban construction in harmony with the present and future construction, which is lacking in many Arab cities as well as the preservation of cultural heritage.
4. Achieving homogeneity in the distribution of the urban land uses, which has approved standards at the local and global levels, also take into account the future expansion of the city, in many cities are given, land use planning in specific spot which may not be appropriate at the time, but it turns into an obstacle to the expansion of the city and its evolution in the future **Jaafar, 2007**.
5. Achieving the requirements of the basic human beings and that means achieving the basic needs of a convenient housing, providing job opportunities for the residents of the city, providing recreational and cultural activities, road network and transportation planning that serves all residents and facilitate their transition, community planning of services (schools, health, etc.), infrastructure (water, electricity, sewage and solid waste) in accordance with approved standards in tourism.
6. Sewerage network and rain water planning according to rigorous studies to take into account the future expansion, damaging interfaces and the risks that ensue, through the study of treatment plants, take advantage of the solid and water caused by waste, and avoid directing them to the rivers before they are treated properly, as it is resulted environmental and humans risks **Al-Diliamy, 2002**.
7. Locating suitable solid waste landfill sites within residential neighborhoods and other areas in the city. It must allocate specific places approved in plans and basic designs , also waste collection ought to be outside of the city sites, not leave it in the form of piles of scattered but buried in deep pits, that such those wastes in the landfill areas used in China for the production of electrical power **Al-Diliamy, 2002**.

3. FUZZY AHP TECHNIQUE STEPS

The Fuzzy Analytic Hierarchy process technique (Fuzzy AHP) is to develop AHP technique was developed by **Thomas L. Saaty in 1980**. Hierarchical structure for FAHP, is shown in **Figure.1**

The steps are as follows, **Kahramana et al. , 2004**:

Decision Maker compares the criteria via linguistic terms shown in **Table.2** and **Table1.3**.

Where gi is the goal set (i= 1,2,3,4,……,n) and M_{gi}^{j} (j=1,2,3,4,……,m), all are Triangular Fuzzy number , as shown in **Figure.2** .

1. The value of fuzzy synthetic extent with respect to the ith object is defined as:

$$S_i = \sum_{j=1}^{m} M_{g_i}^{j} \otimes \left[\sum_{i=1}^{n}\sum_{j=1}^{m} M_{g_i}^{j}\right]^{-1} \quad (1)$$

To obtain $\sum_{j=1}^{m} M_{g_i}^{j}$, form Eq.(3):

$$\sum_{j=1}^{m} M_{g_i}^{j} = \left(\sum_{j=1}^{m} l_j , \sum_{j=1}^{m} m_j , \sum_{j=1}^{m} u_j\right) \quad (2)$$

and to obtain $\left[\sum_{i=1}^{n}\sum_{j=1}^{m} M_{g_i}^{j}\right]^{-1}$, where M_{gi}^{j} (j=1 ,2,3,4,…..,m) such that:

$$\sum_{i=1}^{n}\sum_{j=1}^{m} M_{g_i}^{j} = \left(\sum_{i=1}^{n} l_i , \sum_{i=1}^{n} m_i , \sum_{i=1}^{n} u_i\right) \quad (3)$$

and then compute the inverse of the vector in Eq. (3) such that

$$\left[\sum_{i=1}^{n}\sum_{j=1}^{m} M_{g_i}^{j}\right]^{-1} = \left(\frac{1}{\sum_{i-1}^{n} u_i}, \frac{1}{\sum_{i-1}^{n} m_i}, \frac{1}{\sum_{i-1}^{n} l_i}\right) \quad (4)$$

2. $M_1 = (l_1,m_1,u_1)$ and $M_2=(l_2,m_2,u_2)$ are two TFNS, the degree of possibility of $M_2=(l_2,m_2,u_2) \geq M_1 = (l_1,m_1,u_1)$ and can be equivalently expressed as follows:

$$V(M2 \geq M1) = \begin{cases} 1 , & if\ m_2 \geq m_1. \\ 0 , & if\ l_1 \geq u_1 \\ \frac{l_1 - u_2}{(m_2 - u_2) - (m_1 - l_1)} & , otherwise \end{cases} \quad (5)$$

where d is the ordinate of the highest intersection point D between M_1 and M_2.To compare M_1 and M_2; both the values of $V(M_1 \geq M_2)$ and $V(M_2 \geq M_1)$ are needed.

3. The degree possibility for a convex fuzzy number to be greater than k convex fuzzy numbers Mi (I=1, 2, 3, 4,….., K) can be defined by:

$V(M \geq M_1 ,M_2,M_3,M_4,\ldots..,M_K)= V[(M \geq M_1)$ and $(M \geq M_2)$ and ….. and $(M \geq M_K)] = \min V(M \geq M_i)$, i= 1,2,3,4,…..,k. (6)

Assume that $d'(C_i) = \min V(S_i \geq S_k)$ for k= 1,2,3,4,…..,n. $k \neq 1$,then the weight vector is given by :

$$W' = [\, d'(C_1) , d'(C_2) , d'(C_3) , d'(C_4),\ldots..,d'(C_5)]^T \quad (7)$$

4. Via normalization, the normalized weight vectors is given :

$$W = [d(C_1) , d(C_2) , d(C_3) , d(C_4),\ldots..,d(C_n)] \quad (8)$$

4. RESULTS

Through the received data from questionnaire related to the assessment of criteria by experts and relying on applying (FAHP) technique, forming of pair-wise comparison matrix of criteria which is shown in Table 3 is done. Also, it is based on comparison values that are illustrated in Table 2, after making the required calculations to extract the relative importance of each criterion of the main criteria used as shown in Table 5. It is shown that the relative importance of land used criteria has a larger relative importance (42.1%) compared with the other criteria which obtained the following relative importance: economic (18.3%), environmental (17.2%), social (14.1%) and technical (8.3%). Through these criteria, master plans can be evaluated and chosen the optimal ones, because land uses criteria is considered as the most important part of the project. When there is any defect it will influence the rest of the project criteria where land use criteria mainly affect the possibility of implementing the master plan, the land use has touched an impact of land use the progress of works special master plan projects of cities, their impact large and clear and on the possibility of completing the project according to the required specifications and requirements.

5. CONCLUSIONS

That formation of the city depends on the criteria used in the selection of the optimized master plan because the importance of criteria and indicators selection enhances the linking of optimized master plan by economic efficiency, production efficiencies, structural balance of land use and distribution of infrastructure services are reducing the operational costs and increase economic benefits by encouraging investment and environmental benefits such as an example the issue of transport within cities to gain access to public services (health, education,.., etc.), it must promote effectively and good transport networks environmentally and easy to use and the least effective and sound banging. Reduce costs for random housing that weigh on the shoulders of the state within high costs for its exceeding the infrastructure to other areas services, therefore, the choice of the optimized master plan in accordance with the required criteria in this study, the optimum distribution of services and housing projects are achieved, leading to reduce the problems of cities.

REFERENCES

- Al-Diliamy, K. H., 2002, *Urban Planning Concepts and Foundations*, Edition 1, House of Culture Publishing, Amman, Jordan.

- Abdul Wahid, H. A. , 2010 ,*Studying Effect of Land Uses on The Design of Roads Network in preparing The City Master Plan Case Study / Master Plan of Karbala City* , A thesis of the Master Degree , the High Institute of Urban and Regional Planning, University of Baghdad.

- Ayhan, M.B. (2013).*A fuzzy AHP Approach for Supplier Selection Problem: A case Study in a Gearmotor Company*. International Journal of Managing Value and Supply Chains(IJMVSC),Vol.4(3), pp. 11-23.

- Al-Diliamy,K. H., 2014, *Application of the Standards of Urban Planning in the Planning of Neighborhood* , Anbar University – Iraq, Geo Science Publications.

- Abdallah, M., 2015, *Integrated Structure for the Development of Sustainable Urban Planning in Iraqi Cities*, Ph.D thesis, Baghdad University, Iraq.

- Arefiev,N. ,Terleev,V. and Badenko ,V.,2015, *GIS- based Fuzzy Method for Urban* Planning , Procedia Engineering, Vol. 117 , PP.39-44.

- Couch, C., and Dennemann, A. ,2000, *Urban regeneration and sustainable development in Britain; The example of the Liverpool Ropewalks Partnership*. Journal of Cities, Vol. 17 (2), PP.137-147.

- Haque, A. , and Asami, Y. ,2014, *Optimizing Urban Land use Allocation for Planners and Real Estate Developers*, Computers, Environment and Urban Systems. Vol. 46 , PP.57–69.

- Jaafar, F. H., 2007, *The Urban Land Use Planning Policies*, PhD thesis submitted to the Higher Institute of Urban Planning and Regional / Baghdad University.

- Kurtener, D., and Badenko, V., 2000, *A GIS methodological framework based on fuzzy sets theory for land use management*, Journal of the Brazilian Computer Society, Vol.6(3) , PP.26-32.

- Kahramana , C., Cebeci, U., and Ruan , D. ,2004, *Multi-Attribute Comparison of Catering Service Companies Using Fuzzy AHP : The case of Turkey* ,International Journal of Production Economics, Vol.87, PP.171-184.

- Mahmoud, H.M. ,2012, *Urban planning and its Relationship to Urban Communities to the Iraqi City Urban Environment by Making it Balanced* , Proceedings of the Conference Faculty of Urban Planning,University of Kufa.

- Phillips, C. , 2003,*Sustainable Place: A Place of Sustainable Development* , Wiley Academy , Published in Great Britain , PP.44.

- Pleho, J., and Avdagic,Z., 2008, *Fuzzy Model in Urban Planning*, 9th WSEAS International Conference on Fuzzy Systems (FS'08).Sofia, Bulgaria, PP.156-160.

- Saaty ,T.L., 1980, *The Analytic Hierarchy Process*, New York: McGraw-Hill.

- Silberstein, J., and Maser , C.,2000, *Land Use Planning for Sustainable Development* , Sustainable Community Development Series , Lewis Publishers , USA ,PP.106.

- Stewart, T.J. , and Janssen, R.,2014 , *A multi Objective GIS-Based Land Use Planning Algorithm*, Computers, Environment and Urban Systems. Vol. 46, PP. 25-34.

Table 1. The main criteria and sub-criteria.

Main Criteria	Sub-Criteria		Description
1) Economic	Financial		1- Directing investment in the city. 2-Consider construction cost for new infrastructures and updates to existing system. 3-Highlight major projects that significantly contribute to the capital cost. 4-Finacncial support availability of financial resources and support from local lending institutions are important to remove economic Constraints since most projects tend to expensive.
	Infrastructure		1- Availability of infrastructure for water, sewage, gas and electricity have an impact on overall investment required for the future projects. 2- Distance between transportation networks are important factors for industrial and commercial land uses (Effect on transportation costs of materials and transportation costs for products). 3- Highlight on level of ability to balance infrastructure costs with level of urban growth.
	Site conditions	Physical conditions	Physical conditions like geological risks, it will impact on the cost and feasibility of redevelopment.
	Site conditions	Environmental conditions	The type, severity and extent of the contamination must be evaluated to assess costs and time for remediation.

	Land value	Land prices in the city.
	Costs	1- Capital costs 2- Operation and maintenance costs 3-Other contingencies
	Economic revenue	
	Ability to interact with another sector economy	1- Projects which interact with more than one sector of the economy and creating greater opportunities for diverse sectors of the economy. 2- Evaluating how much the project would contribute to creating employment and an increase in income for the community productive sector.
2)Environmental	Noise pollution	The source of most noise worldwide is mainly caused by machines and transportation systems, motor vehicles, aircraft, and trains. . Poor urban planning may give rise to noise pollution because construction industrial buildings in residential regions can result in noise pollution in the residential regions.
	Water pollution	The contamination of water (Pollutants such as Materials' chemical, physical, radioactive …etc.).
	Wastewater network	The Stations for wastewater must constitute in a way a correct and not harmful to the environment.
	Soil pollution	Contaminated soil is one of the most prominent environmental problems and the most complex. Soil contaminants may be a waste (industrial, radioactive... etc.).
	Impact of carbon dioxide emissions	

	Local air quality	
	Aquatic impacts	Potential effects on water resources and not to overtaking on water natural that affect the environment.
	Environmental legislation	Global and local laws are restrictions.
	Protect the natural environment	Such as green space and Forests… etc.
3) Social	Services	1- Housing, transportation, schools, Medical, police, Firefighter...etc. 2- Projects that offer flexibility of servicing the city growth. 3- Utilization of existing infrastructure. 4- Ability to executing requirement and service level.
	Quality and cost of living	
	Job opportunities	Redevelopment can create new jobs and increase incomes.
	Population	Population size, Household size, Population density and Distribution of population.
	Aesthetic	Improving aesthetic by the redevelopment can provide significant benefit to areas with pleasant surroundings, redevelopment results giving better quality and appearance.
4) Land uses		1- Land uses Planning policies. 2- Coordination with existing and land uses. 3- Potential land requirements.
	Dealing with the regional dimension	
	Dealing with the concept of investment	
	Dealing with the problem of land occupancy	
	Dealing with public places	

	Types of land use	Residential use	Depending on the regional planning organization for the year 1977 , criteria of public housing for the year 1982 and The urban planning and design criteria / The Ministry of Housing and Construction and Municipalities and Public Works in 2008
		Commercial use	
		Administrative use	
		Industrial use	
		Recreational use	
		Cultural use	
		Sports use	
		Health use	
		Educational use	
		Agricultural use	
5)Technical	The size of planned and existing infrastructure		Describe the difficulty of construction in limited areas and with possibility limited access.
`	Servicing integrations structural		Potential impact related to opportunity for integrated planning, construction, design, with other servicing such as road improvement and bridge construction, establishing rail and airport... etc.
	Construction density		1- Structural density: is the relationship of the total area of origin to the site area. 2- Coverage (%), the ratio of building to the site area.
	Construction patterns		Construction vertical and horizontal construction
	Height for building		

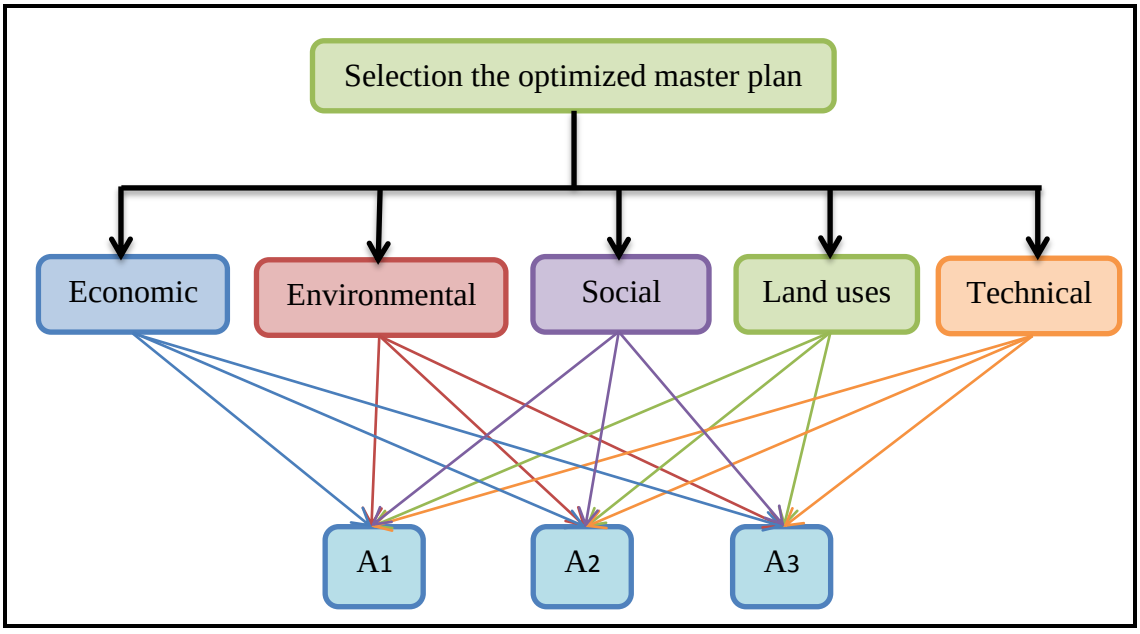

Figure 1. The hierarchical structure for FAHP.

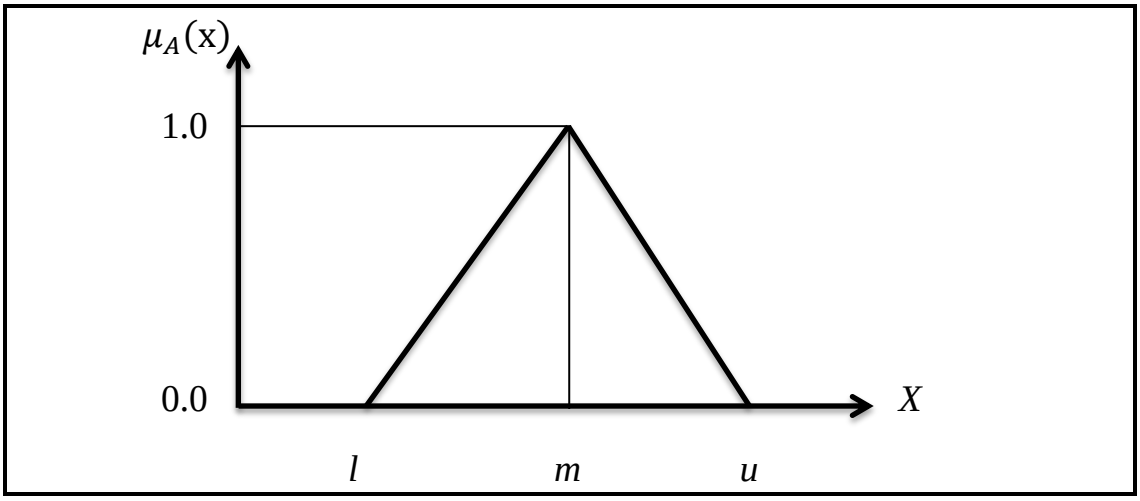

Figure 2. A triangular fuzzy number.

Table 2. Linguistic terms and the corresponding triangular fuzzy numbers, **Ayhan , 2013**.

Linguistic variable	Fuzzy number	Explanation
Equally important	(1 , 1 , 1)	The criterion i is equally important when compared to criterion j.
Weakly important	(2 , 3 , 4)	The criterion i is Weakly important when compared to criterion j.
Fairly important	(4 , 5 , 6)	The criterion i is Fairly important when compared to criterion j.
Strongly important	(6 , 7 , 8)	The criterion i is Strongly important when compared to criterion j.
Absolutely important	(9 , 9 , 9)	The criterion i is Absolutely important when compared to criterion j.
Intermediate values between the two adjacent judgments	(1, 2 ,3) (3, 4 ,5) (5 , 6 ,7) (7, 8 ,9)	When compromise is needed.
Reciprocals number	The reciprocals, such as 1/3, 1/5, 1/7, 1/9, etc.,	

Table 3. Aggregate fuzzy numbers decision making matrix.

Criteria	C1	C2	C3	C4	C5
C1	(1,1,1)	(2.01, 2.77, 3.54)	(1.69,2.09 , 2.53)	(0.34, 0.46, 0.64)	(1.02,1.44 ,1.91)
C2	(0.29, 0.36, 0.49)	(1,1,1)	(5 ,5.97 ,6.95 ,6.95)	(0.26 ,0.34 , 0.47)	(0.19, 0.26, 0.32)
C3	(0.39 , 0.48, 0.59)	(0.14, 0.17, 0.2)	(1,1,1)	(0.26, 0.34, 0.47)	(4.31 ,5.34 , 6.44)
C4	(1.59,2.17 , 2.94)	(2.13 , 2.94, 3.84)	(2.13,2.94 , 3.85)	(1,1,1)	(3.02,3.93 ,4.89)
C5	(0.52 ,0.69 ,0.98)	(3.13, 3.84, 5.26)	(0.16,0.19 , 0.23)	(0.21, 0.25 , 0.33)	(1,1,1)

Table 4. The relative importance of main criteria

Main criteria	Relative importance	%
Economic criteria	0.183	18.3
Environmental criteria	0.172	17.2
Social criteria	0.141	14.2
Land use criteria	0.421	42.1
Technical criteria	0.083	8.3

Influence of Internal Sulfate Attack on Some Properties of Self Compacted Concrete

Hadeel Khalid Awad Al-Obaidy
Assistant Lecturer
Engineering College-Baghdad University
E-mail:Hadeel_k_awad@yahoo.com

ABSTRACT

Self-compacted concrete (SCC) is a highly flowable concrete, with no segregation which can be spread into place by filling the structures framework and permeate the reinforcement without any compaction or mechanical consolidation **ACI 237R-14**. One of the most important problems faced by concrete industry in Iraq and Gulf Arab land is deterioration due to internal sulfate attack (ISA) that causes damage of concrete and consequently reduces its compressive strength, increases expansion and may lead to its cracking and destruction.

The experimental program was focused to study two ordinary Portland cements with different chemical composition with (5, 10 and 15) % percentage of high reactivity metakaoline (HRM) as a cement replacement and with W/Cm ratio 0.35. The SCC mixes with AL Shemalia OPC cement that produced in Saudi Arabia (C_3A=7.02%) shows higher resistance to ISA than mixes with Tasluja OPC cement that is produced in Iraq (C_3A=4.13%). The results indicate that the SCC mixes containing 15% HRM shows higher opposition to ISA. A good correlation was obtained between concrete splitting tensile strength and compressive strength from the results of this study.

Keywords: self compacted concrete (SCC), high reactive metakaoline (HRM)

تأثير مهاجمة الاملاح الداخلية على بعض خواص الخرسانة ذاتية الرص

هديل خالد عواد العبيدي
مدرس مساعد
كلية الهندسة – جامعة بغداد

الخلاصة

تعرف الخرسانة ذاتية الرص بأنها خرسانة ذات أنسيابية عالية بدون حصول أنعزال والتي بالامكان أنتشارها ، و ملئ القالب و تغليف حديد التسليح بدون أي رص ميكانيكي حسب متطلبات الجمعية الامريكية 237R للعام 2014. تعد مهاجمة الاملاح الداخلية من أهم المشاكل التي تواجه صناعة الخرسانة في العراق واراضي الخليج العربي والتي تؤدي الى التدهور الذي يسبب تضرر الخرسانة ويؤدي بالنتيجة الى تقليل مقاومة الانضغاط ، وزيادة التمدد والذي قد يؤدي الى تشققها و دمارها.

البرنامج العملي لهذه الدراسة يبحث تأثير التركيب الكيميائي المختلف لإثنين من السمنت البورتلاندي الاعتيادي ،أضافة نسب من الميتاكاؤلين العالي الفعالية كأستبدال من وزن السمنت (5، 10 و 15)% ونسبة وزن ماء الى سمنت 0,35 .الخلطات الخرسانية ذاتية الرص المستخدم فيها السمنت الاعتيادي الشمالية المصنوع في المملكة العربية السعودية (C_3A=7.02%) أظهرت مقاومة اعلى لمهاجمة الاملاح الداخلية مقارنة بالسمنت الاعتيادي طاسلوجة المصنوع في العراق (C_3A=4.13%). النتائج تشير الى أن الخلطات الخرسانية ذاتية الرص الحاوية على 15% من الميتاكاؤلين العالي الفعالية اظهرت مقاومة اعلى لمهاجمة الاملاح الداخلية. وهناك علاقة بين نتائج مقاومة الانضغاط للخرسانة ومقاومة شد الانفلاق اوجدت من نتائج هذه الدراسة.

الكلمات الرئيسية: خرسانة ذاتية الرص، الميتاكاؤلين العالي الفعالية .

1. INTRODUCTION

Self compacted concrete (SCC) was first developed in Japan 1988 as a mean to create uniformity in the quality of concrete. The SCC differs from conventional concrete in main characteristic features, namely, appropriate flowability, no segregation and no blocking tendency. Durability was the main concern and the purpose to develop a concrete mix that would reduce or eliminate the effect of internal sulfate attack. An excess amount of gypsum in concrete from either, cement or aggregates is of great importance. This is because of their adverse effect on the structure developed of cement paste. Excess percentages of sulfate may impair the physical and mechanical properties of the hardened concrete at subsequent ages. The ettringite formation when occurs homogeneously and immediately (within hours or days) in a mixture or in a deformable concrete – early ettringite formation (EEF) - the related expansion does not cause any significant localized disruptive action. This happens when ground gypsum reacts with anhydrous calcium aluminates within some hours (set regulation) or when a calcium aluminates sulfate (C_4A_3S) hydrates within few days producing a relatively small, homogeneous, harmless and rather useful stress (expansive cements for shrinkage compensating concretes). On the other hand, when ettringite forms heterogeneously and later (after months or years) - delayed ettringite formation (DEF) - the localized related expansion in a rigid hardened concrete produces cracking, spilling, and strength loss, **Collepardi, 2005.**

Husaian, 2008 has studied the influence of high reactivity metakaoline (HRM) as a partial replacement by weight of cement on the properties of SCC in fresh and hardened state. Many different mixes of SCC have been studied, in which concrete mixes contain 500kg/m^3 cement and water/cement ratios ranging between 0.35 - 0.58. Result indicated that the workability of all studied mixes is very good. The inclusion of 10% HRM as a partial replacement by weight of cement decreases the flowability and increases the viscosity of fresh concrete and this leads to use high superplastizer dosage. The addition of HRM as replacement for the weight of cement increases the value of compressive strength and splitting tensile strength by 5 - 22 %, 3 - 25 % respectively as compared with reference mixes without any addition of HRM.

Ahmed, 2010 concluded in her study that the compressive strength was increased to (29, 45 and 69)% for the SCC concrete mixes with replacement of cement by HRM (5, 10 and 15)% by weight of cement at 90-days for the different mixes with 500 Kg/m^3 of cement and 170 Kg/m^3 water. **Salih, and Salman, 2011** results showed that SCC mixes containing metakaoline required higher superplastizer content to 9% by weight of cement compared with 8% by weight of cement for mixes without pozzolanic materials to maintain the self compatibility of mixes. And they saw that a significant improvement was observed in the mechanical properties of mixes including compressive and splitting tensile strength, modulus of rupture, static modulus of elasticity, and impact resistance. The improvement percentages at 28 days were (8.43%, 7.6%, 6.08%, 4.03%, and 30.30%) respectively for SCC with high reactive metakaoline mixes.

The resistance of high performance concrete to internal sulfate attack after adding natural gypsum to sand as a partial replacement by weight was studied by **AL-Robayi, 2005**. The sulfate contents (0.5, 1.5, 2.0, and 2.5 %) in fine aggregate were studied. He concluded that there was a reduction in strength at early ages (less than 28 days) for normal and high performance concrete. This reduction was related to the increase of sulfur trioxide content (SO_3) in sand. At later ages (more than 28 days) in High Performance Concrete, the reduction in

strength decreased while in normal concrete it increased continuously. The low permeability and pozzolanic action of HRM could be the cause of strength improvement. **Alwash, 2013** studied the effect of using local fillers (pigment and metakaolin) on self compacting concrete, $SO_{3\%}$ content in sand were investigated by using five levels, these levels were [0.24% , 0.5% , 1% , 2% , and 3%], which yielded [3.05% , 3.47% , 4.28 % , 5.9% , and 7.52%] total SO_3 content by weight of cement respectively for SCC mixes with pigment powder filler and [3.08%, 3.5% ,4.31% , 5.94% , and 7.56%] for self compacted concrete mixes with metakaolin powder. There is an optimum gypsum content (SO_3=1.0%) by wt. of sand which gives the highest results in compressive strength, flexural strength and ultrasonic pulse velocity of self compacted concrete. The mechanical properties will be decreased as gypsum content increases beyond this limit.

2. MATERIAL CHARACTERISTICS

2.1 Cement

Two ordinary Portland cements conforming the **IQS NO.5/1984** are used. Tasluja OPC cement that is produced in Iraq and AL Shemalia OPC cement that is produced in Saudi Arabia. The chemical analysis of the two cements used is listed in **Table 1,** while **Table 2** consist of the physical properties for the same cements.

2. 2 Fine aggregate

The natural fine aggregate used in this study is from Al-Ukhaider district. The grading of sand is within the Iraqi specification **IQS NO.45/1984** and affirms to zone two. **Table 3** shows the sieve analysis of fine aggregate used and **Table 4** shows the physical properties and sulfate content of fine aggregate used.

2.3 Natural gypsum

The natural gypsum was brought from the State Company of Geological Survey and Mining. It was crushed and grinded by hammer and passed through the same sieve set of fine aggregate used in the mix of internal sulfate attack to get the same gradation and to avoid the affect of large surface area of particles, the gypsum was used as a partial replacement by weight of sand with limited percentage. To control the content of SO_3, the quantity of natural gypsum add to the sand is according to Eq.(1).

$$W= [(R- M\%) \times S]/N \quad (1)$$

where:

W is the weight of natural gypsum ground needed to be added to sand (kg).

R is the percentage SO_3 required in sand %.

M is the actual SO_3 in sand (0.1 %).

S is the weight of sand in the mix (kg).

N is the percentage SO_3in the used gypsum.

The chemical composition of the gypsum used is listed in **Table 5.**

2.4 Coarse aggregate

A crushed natural coarse aggregate with maximum size of 14mm was used. It was brought from Al-Niba`ee region. The grading of the aggregate used is within the Iraqi specification **IQS NO.45/1984.** The coarse aggregate sieve analysis is shown in **Table 6,** while **Table 7 s**hows the physical properties and sulfate content for the same aggregate used.

2.5 Mixing water

The water used in this study was potable water for both casting and curing of concrete specimens.

2.6 High reactive metakaoline (HRM)

HRM is a reactive aluminosilicate pozzolan produced by clinking China clay at temperatures between 700 – 900°C. In this work, the locally available China clay was burned using the burning kiln at 700°C for one hour then left to cool down**, Raya, 2003** and **Justice, 2005.** The chemical composition of HRM in powder form is shown in **Table 8**, satisfying the **ASTM C 618 –08.** At 28-days the accelerated pozzolanic strength activity index with Portland cement was 105% (min 75%). The specific gravity and the fineness were 2.62 and 19000 cm^2/g respectively.

2.7 Chemical admixture

A high performance concrete superplasticizer (Sika ViscoCrete -5930) is a third generation for concrete and mortar as chemical admixture was used in this research. It meets the requirements for superplasticizer according to **ASTM C494-05.T**ypes G and F. **Table 9** shows the typical properties of the superplasticizer used.

3. PREPARATION OF CONCRETE SAMPLES

3.1 Mix Proportion

The method of mix design for the self compacted concrete used in the study is accordance to **EFNARC, 2002.** The materials contents are revised after gaining acceptable self-compatibility by assessing fresh concrete tests. Water to cementituse is 0.35 used for all mixes in this study and the optimum dosage of superplasticizer (Sika ViscoCrete -5930) (1.2 liter for each 100 kg of cement) is prevailed from several trail mixes, by fixing the W/Cm ratios, and increasing the dosage of the admixture gradually to ensure the self-compatibility. The mix proportion is presented in **Table 10.**

3.2 Mixing, Casting and Curing of Concrete

The mixing process was done by manually operated mixer according to ASTM C192, 2006. Cast iron cube moulds, with dimensions of (150x150x150) mm and (150x300) mm cylindrical moulds are provided, cleaned and oiled before adding water to the mix. Nylon bag were used to cover the moulds, after 24hr the moulds were opened and the concrete were placed in water curing tanks until the time of test (7, 28, 90 and 180-day).

4. TEST PERFFORMED

4.1 Fresh concrete tests

4.1.1 Slump flow test and T50cm test

The horizontal free flow of self-compacting concrete is assessed by the slump flow test. This test is widely used; it gives an evaluation of resistance to segregation and an indication of filling ability. The benefit of T50cm test is to measure the viscosity of SCC by measuring the speed of flow, **EFNARK, 2002**.as shown in **Fig. 1**.

4.1.2 V-funnel test and V-funnel test at $T_{5minutes}$

This test is to estimate the filling ability and viscosity of the self-compacting concrete. High flow time can also be associated with low deformability due to a high paste viscosity, and with high inter-particle friction**, EFNARK, 2002**, as shown in **Fig. 2**.

4.1.3 L-Box test

The flow of self-compacted concrete is assessed to this test, and furthermore it gives a conception to reinforcement blocking. This test is largely used. It estimates passing and filling ability of SCC, **EFNARK, 2002**. As shown in **Fig. 3**.

4.2 Hardened concrete tests

4.2.1 Compressive strength test

The compressive strength test in this study was done according to the **BS 1881: Part 116: 1983**. The concrete cubes of (150x150x150) mm were tested at ages of (7, 28, 90, 180-day). The load at failure was registered and the compressive strength was calculated by taking the average of 3- cubes for each test age.

4.2.2 Splitting tensile strength

The splitting tensile strength test was carried out in accordance with the **ASTM C496-/C496M-11**. (150×300) mm cylindrical concrete specimens were used. This test was done at ages of (7, 28, 60, 90 and 180) days.

4.2.3 Ultrasonic pulse velocity (UPV)

According to the **ASTM C597–02.**The ultrasonic pulse velocity test was done using portable equipment called PUNDIT. The equipment was used with direct transmission method by placing the transducer on opposite face of the concrete cubes (150x150x150) mm.

5. RESULTS AND DISCUSSION

5.1 Fresh Concrete

The increased of total effective SO_3% content in all cases, resulted in a considerable decrease in the slump flow of the concrete presented in **Table 11.** For Iraqi and Saudi Arabia cements, slump flow values ranged between (776 - 800) mm and the T50 cm of slump flow values ranged between (2.2 - 4.51) sec. For the V–funnel test the time of the concrete to pass through ranges between (6.1-10.3) sec and L-box results ranged between (0.81-0.95).

5.2 Hardened Concrete

The results of compressive strength test for all concrete mixes used in this study are shown in **Table 12.** The results declared that all concrete mixes including (reference mix) shows a consecutive increase in compressive strength with the progress of age. This increase in

compressive strength is submitted in **Fig. 4** and **Fig. 6** for all concrete mixes using Iraqi cement. The results showed that HRM when used improves the compressive strength of concrete and increases the resistance to ISA. This behavior is due to the consumption of $Ca(OH)_2$, which gives a micro filling action due to the higher pozzolanic reaction. The addition of 15% of HRM as a cement replacement increases the compressive strength for all mixes with age relative to their reference. The percentage increase of compressive strength at 28 days are (14.35%) and (20.6%) for total SO_3% by wt. of sand (1.5) for Tasluja OPC and AL Shemalia OPC cements respectively. This behavior is due to reaction of HRM (silica –based product) with $Ca(OH)_2$ during the hydration of C_3S and C_2S of cement produces CSH gel contributes the densification of concrete matrix, pore-size and grain-size refinement processes **Justice, 2005**. The reduction of compressive strength increases with increase in total SO_3% content as it is presented in the results for both types of cement. This behavior is due to the formation of DEF which is a type of internal sulfate attack that occurs when the constituents of concrete provide an initial source of sulfate, **Pavoine, et al., 2012.** That affects cementitious materials which possibly causes cracking and swelling of concrete**, Collepardi, 2003.**

The concrete mixes using AL Semalia cements produced in Saudi Arabia with higher C_3A content (C_3A =7.02%) show higher resistance to ISA than Tasluja cement produced in Iraq (C_3A =4.13%) and that is confirmed with the literatures.

Table 12 also shows the results of splitting tensile strength for all mixes. The splitting tensile strength of concrete mixes contained HRM increases with the progress of curing age and it increases with increase the HRM a cement replacement to 15% as presented in **Fig. 5** and **Fig. 7** for all concrete mixes using Iraqi cement. These results are due to the reduction in the micro cracking and by strengthening the transition zone because of the pozzolanic reaction**, Naji, 2012.** The increase in splitting tensile strength for reference mix is continued for all ages due to the continuity of hydration process, other concrete specimens the splitting tensile strength is reduced with the increase of total SO_3% content due to the effect of ISA as the formation of DEF. **Fig. 9** shows the relationship between compressive strength and splitting tensile strength at different ages with R^2 equal to 0.952.

Table 13 shows the Ultrasonic pulse velocity (UPV) results for reference mixes and concrete mixes with HRM as a cement replacement with different percentages of sulfate content and this is submitted in **Fig. 8.** The results demonstrate that the pulse velocity for reference mix is increased with the age. The other mixes with the increased total SO_3% content, the pulse velocity is less increased than reference mix with the age and that increase continued till 90-day then the pulse velocity starts to decrease. That is compatible with the results of compressive strength test. The relation between the compressive strength with ultrasonic pulse velocity for different concrete mixes demonstrated in **Fig. 10**. The results indicate that the compressive and pulse velocity are related to each other with R^2 equal to 0.9309.

When using SO_3% by wt. of sand more than 1.5% there is reduction in compressive strength, splitting tensile strength and ultrasonic pulse velocity in later ages (180 days) than (90 days) curing age compared with other mixes containing less than 1.5% of SO_3% by wt. of sand.

6. CONCLOSIONS

1. A good workability properties of fresh concrete was detected for all SCC mixes containing Sika ViscoCrete -5930 and HRM , the results shows that the slump flow test ranges between

(767- 800) mm and T50 cm results range between (2.2-4.51) sec. The V–funnel time results ranges between (6.1-10.3) sec and L-box results ranges (0.81-0.95).
2. The results show that mixes containing HRM as cement replacement materials improves the compressive strength of concrete and increases the resistance to ISA.
3. The concrete mixes using AL Shemalia OPC cement that produced in Saudi Arabia (C_3A =7.02%) cements show higher resistance to ISA than Tasluja OPC cement that produced in Iraq (C_3A =4.13%).
4. The compressive strength and splitting tensile strength of concrete mixes contained HRM increases with the progress of curing age for mixes containing less than 1.5% of SO_3 by wt. of sand. By increasing the SO_3 % beyond this limit all the mechanical properties will be declined spicily at later ages.

REFRENCES

- ACI 237R-14, *Self-Consolidation Concrete*, Emerging Technology Series, Reported by ACI Committee 237.

- Ahmad, H. I., 2010**,** *Effect of Different Types of Admixture on the Properties Self Compacting Concrete (SCC)*, M.SC. Thesis, Baghdad University.

- Al - Kadimi, T. K., and Abood , F., 1983, *Effect of gypsum present in sand on the properties of concrete*, BRC Journal , vol. Nov., PP. 17-41 .

- Al-Robayi, A. H., 2005, *Resistance of High Performance Concrete to External and Internal Sulfate Attack*, M.SC. Thesis, University of Technology.

- Alwash, J. J., 2013, *Resistance of Self Compacting Concrete to Internal Sulphates Attack*, Journal of Babylon University/Engineering Sciences, Vol.(21), No.(3), PP. 839-851.

- ASTM C494/C494M – 05, *Standard specification for chemical admixtures for concrete*, American Society for Testing and Materials.

- ASTM C496-/C496M-11, *Standard Test Method for Splitting Tensile Strength for Cylindrical Concrete Specimens*, American Society for Testing and Materials, Volume 4.02 .

- ASTM C597/C597-02, *Standard tests method for pulse velocity through concrete*, American Society for Testing and Materials.

- ASTM C618-08, *Standard Specification for Coal Fly Ash and Raw or Calcined Natural Pozzolan for Use in Concrete*, American Society for Testing and Materials.

- BS 1881: Part 116: 1983, *Methods for determination of compressive strength of concrete cubes*, British Standard Institution.

- Collepardi, M., 2003, *A state of the art review on delayed ettringite attack on concrete*, Cement and Concrete Composites Journal, Vo.25, PP.7-401.

- Collepardi, M., 2005, *Sulphate Attack and Alkali-Silica Expansion*, International Symposium on Concrete Technology for Sustainable, Development with Emphasis on Infrastructure, Hyderabad, India, pp. 55-67.

- EFNARC, 2002, *Specification and Guidelines for Self-Compacting Concrete*, pp.32, www.efranice.org

- Hussain, Z. M. A., 2008, *The Effect of Grading of Aggregate on the Properties of Self-Compacting Concrete*, .SC. Thesis, AL-Mustansiriya University.

- IQS NO.1703/1992, *Iraq standard specification for Water used in concrete,*.

- IQS NO.45/1984, *Iraq standard specification for Aggregate from natural sources for concrete and building construction,*.

- IQS NO.5/1984, *Iraq standard specification for Portland cements,*.

- Justice, J. M., 2005, *Evaluation of Metakaolines for Use as Supplementary Cementitious Materials*, M.Sc. Georgia Institute of Technology, pp. 134.

- Naji, Z. H., 2012, *Some properties of nano metakaolin concrete*, M.Sc. Thesis, Building Materials Engineering, University of Technology.

- Pavoine, A., Brunetaud, X., and Divet, L., 2012, *The impact of cement parameters on Delayed Ettringite Formation*, Cement and Concrete Composites Journal, Vo.34, PP.521-528.

- Raya, Y., 2003, *Durability of High Performance Concrete Incorporating High Reactivity Metakaolin and Rice Husk Ash*, MSc. Thesis, Department Of Building and Construction Engineering, University of Technology.

- Salih, S. A., and Salman, G. A., 2011, *The Effect of Addition of Carbon Fibers on Some Properties of Self Compacting Concrete***,** Engineering and technology Journal,Vol (29).

NOMENCLATURE

ACI	American Concrete Institute
ASTM	American Society for Testing and Materials
BS	British standard
DEF	delayed ettringite formation
EEF	early ettringite formation
HRM	high reactive metakaoline
IQS	Iraq standard specification
ISA	internal sulfate attack
SCC	self compacted concrete

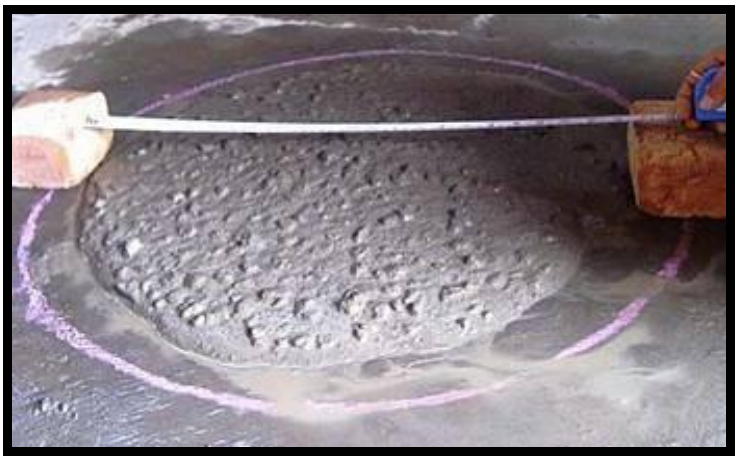

Figure 1. Slump flow test.

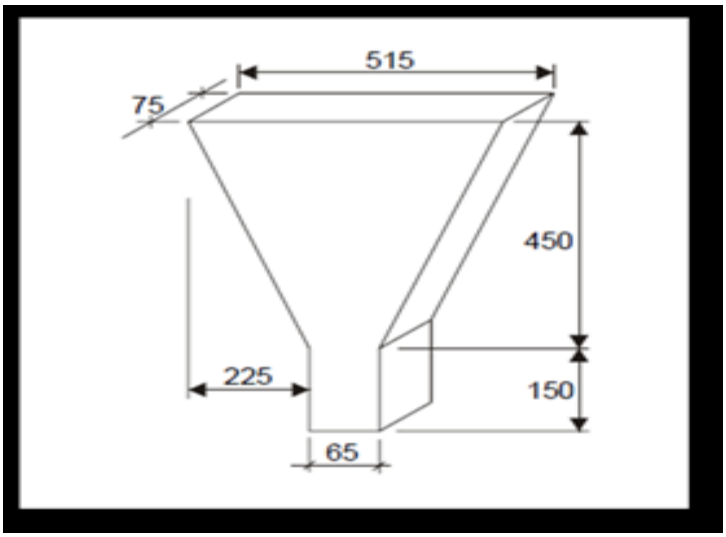

Figure 2. V-Funnel test.

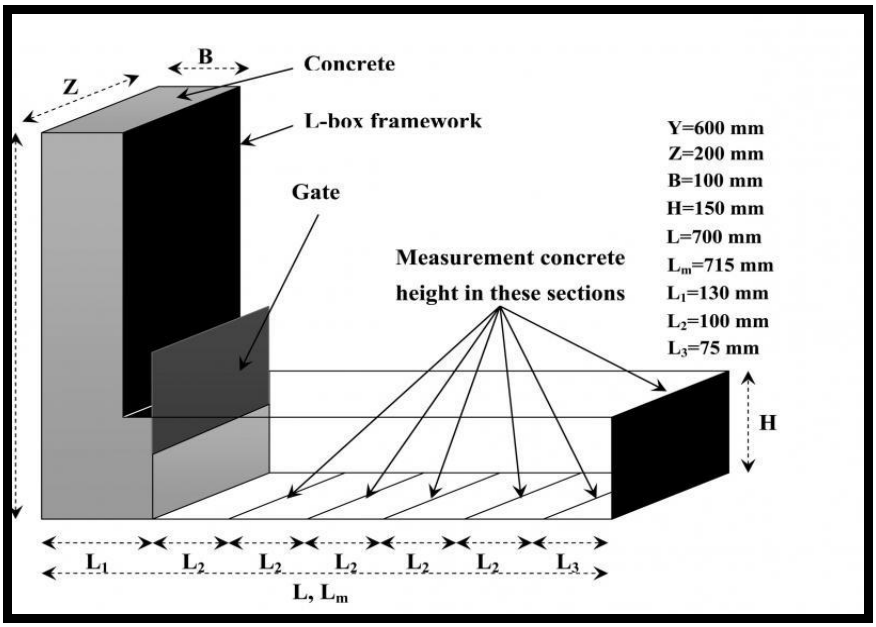

Figure 3. L-Box Test.

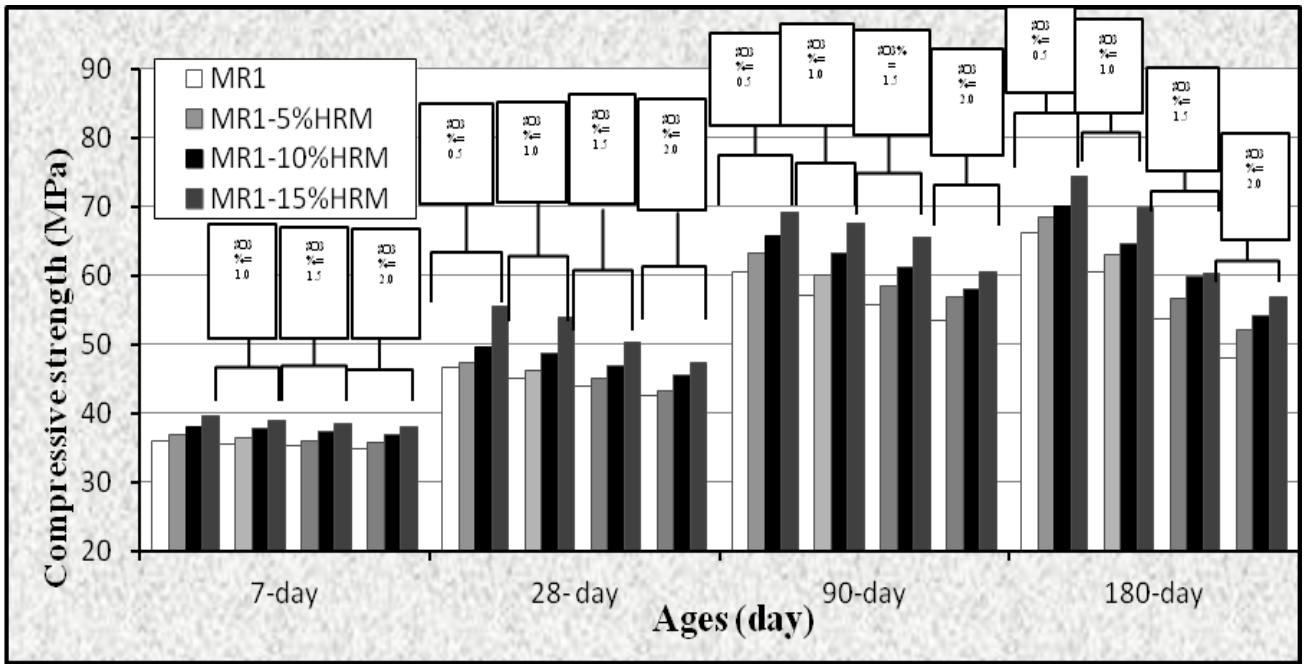

Figure 4. Compressive strength verses ages for different SO_3% content of SCC mixes using Iraqi Cement.

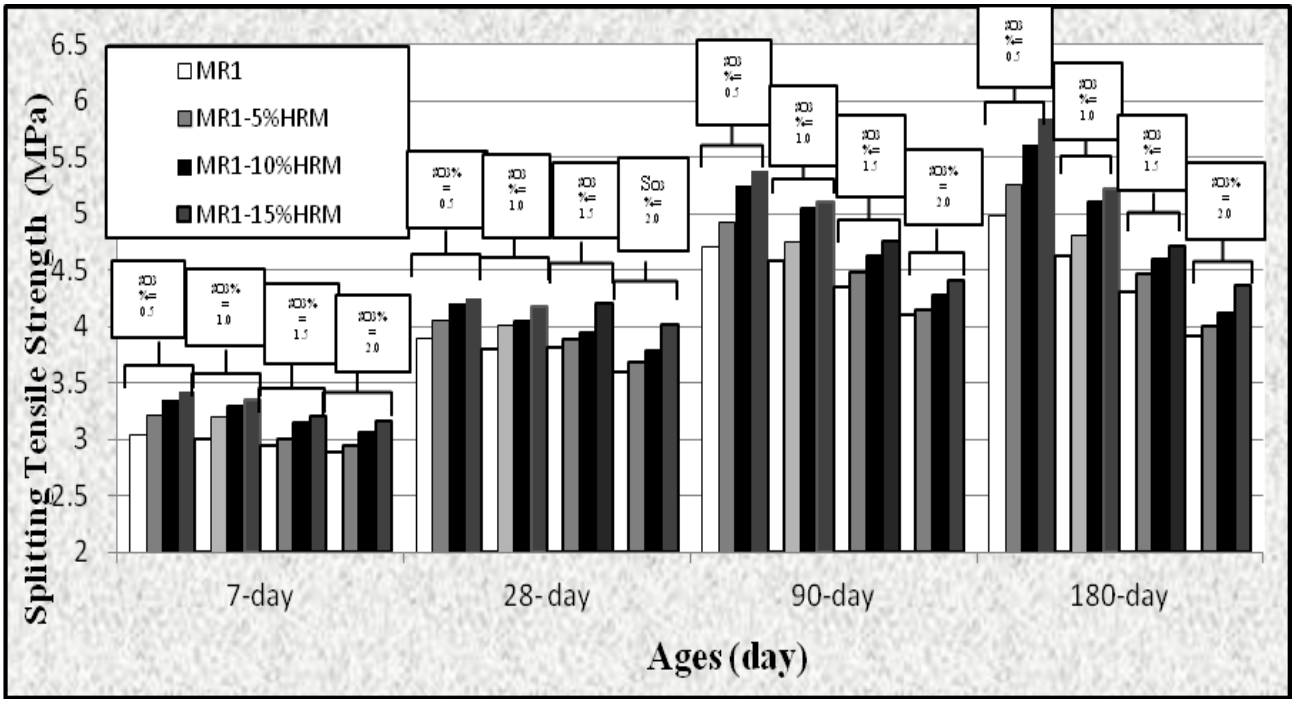

Figure 5. Splitting tensile strength verses ages for different SO_3% content of SCC mixes using Iraqi Cement.

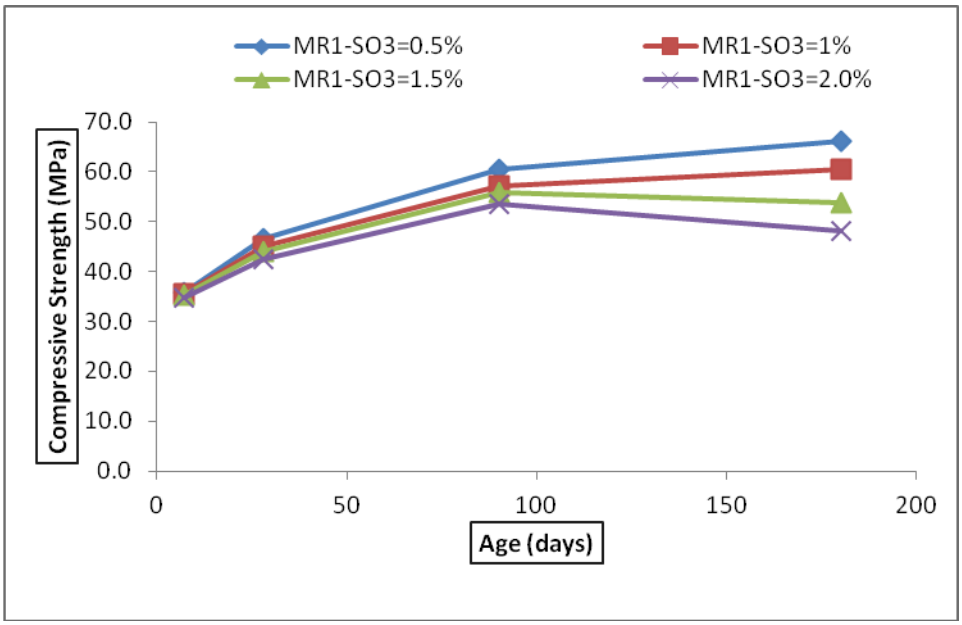

Figure 6. Relationship between compressive strength and Age for Different SO_3% content of SCC mixes using Iraqi Cement.

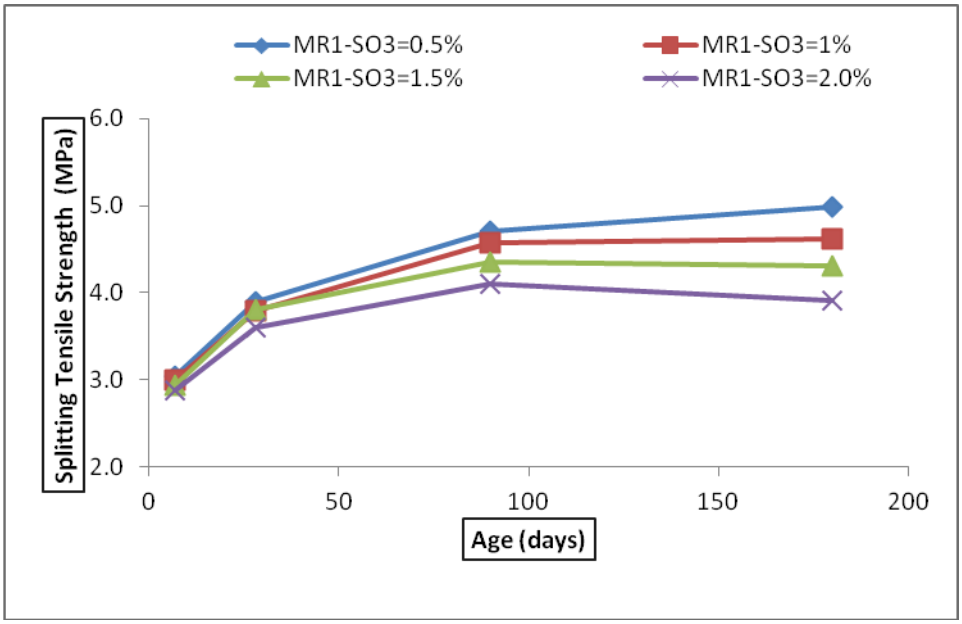

Figure 7. Relationship between Splitting tensile strength and Age for Different SO_3% content of SCC mixes using Iraqi Cement.

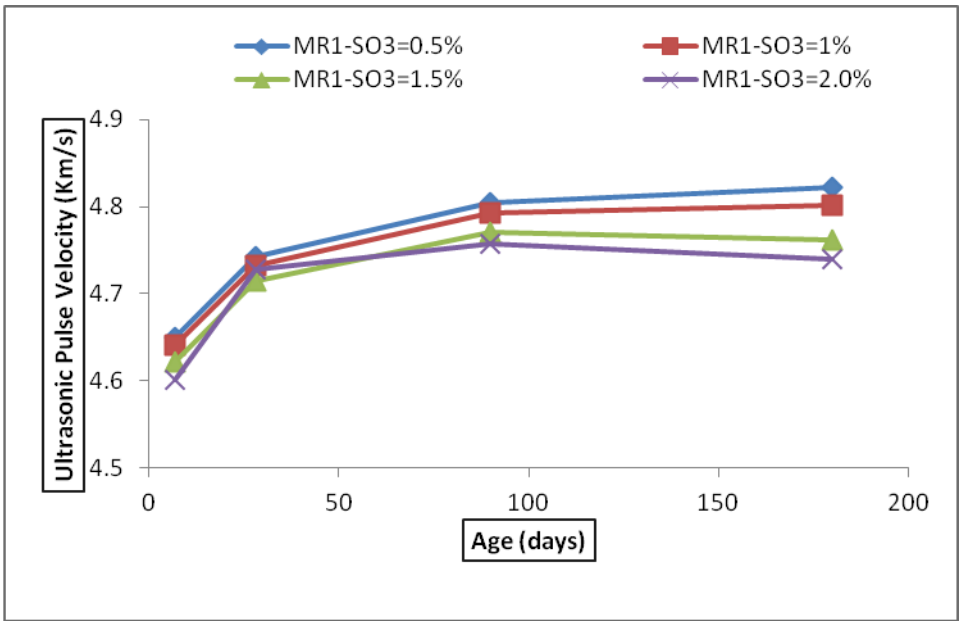

Figure 8. Relationship between Ultrasonic Pulse Velocity and Age for Different SO_3% content of SCC mixes using Iraqi Cement.

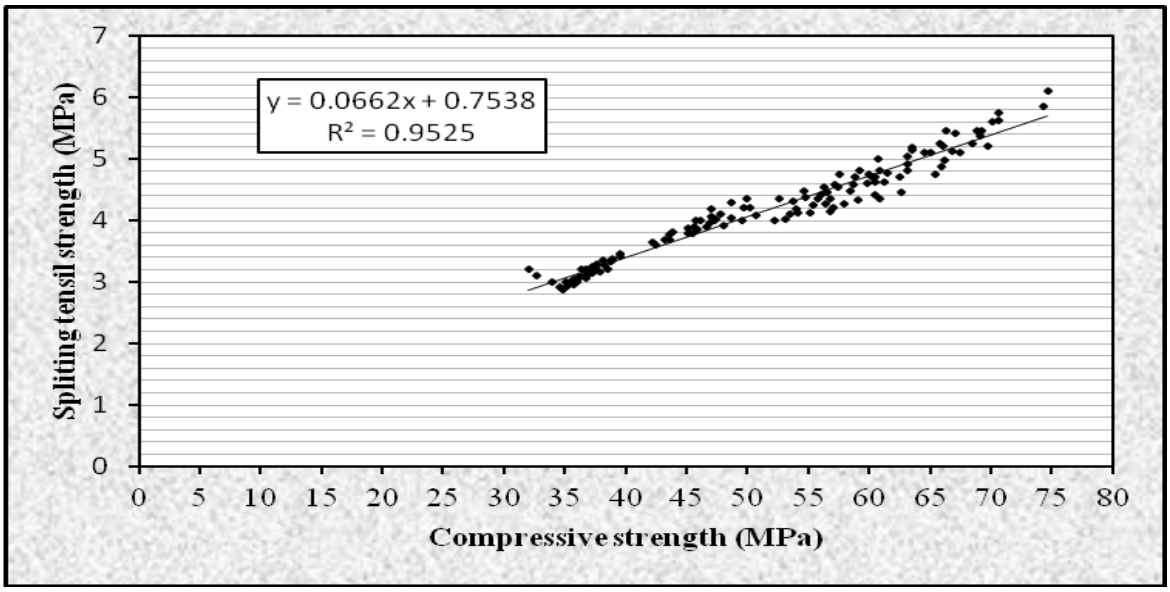

Figure 9. Relationship between compressive strength and splitting tensile strength.

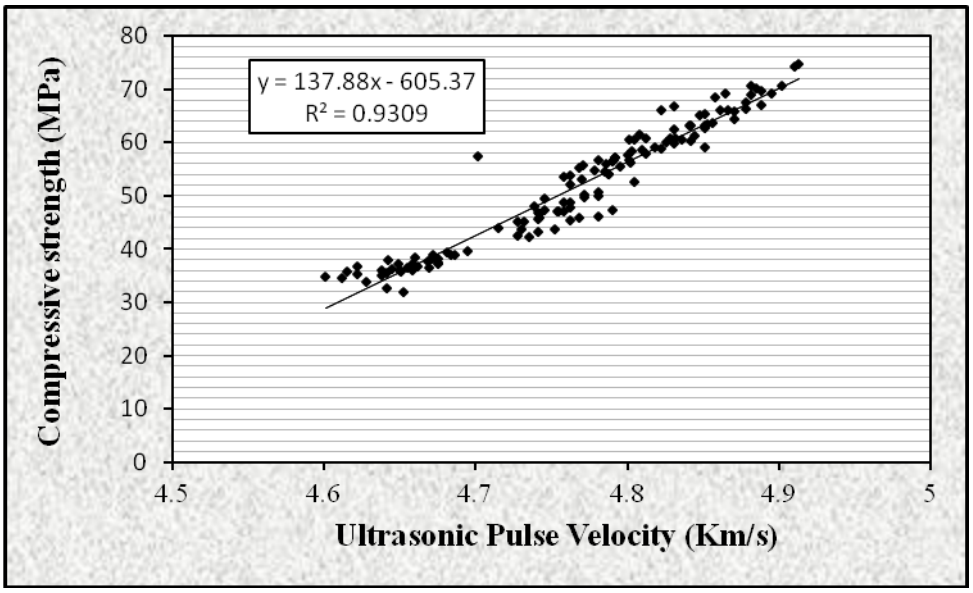

Figure 10. Relationship between compressive strength and ultrasonic pulse velocity.

Table 1. Chemical composition of cement used.

Oxide Content %	Tasluja OPC cement (Iraqi)	AL Shemalia OPC cement (Sudi Arabia)	Limits of Iraqi specification IQS NO.5/1984
SiO_2	20.6	20.4	-
Al_2O_3	4.49	5.1	-
Fe_2O_3	4.59	3.84	-
CaO	60.23	60.34	-
SO_3	2.1	2.68	≤ 2.8 %
MgO	2.97	4.58	≤ 5 %
L.O.I	2.11	2.35	≤ 4 %
I.R	1.2	0.62	≤ 1.5 %
L.S.F	0.97	0.89	0.66-1.02
Compound Composition (Bogue` s Equation)			
C_3S	51.85	43.20	-
C_2S	19.89	25.95	-
C_3A	4.13	7.02	-
C_4AF	13.96	11.68	-

- Chemical tests were conducted by Central Organization for Standardization and Quality Control, Ministry of Planning

Table 2. Physical properties of cements used.

Properties	Tasluja OPC Cement (Iraqi)	AL Shemalia OPC Cement (Sudi Arabia)
Specific surface (Air permeability test),m^2/kg	350	365
Autoclave expansion,%	0.04	0.04
Setting time (vicate apparatus), a. Initial - hr:min b. Final - hr:min	 1:30 4:40	 1:25 4:30
Compressive strength MPa(N/mm^2): 3-days 7-days	 17.5 26.5	 16.8 27.2

- Physical tests were conducted by the Central Organization for Standardization and Quality Control, Ministry of Planning.

Table 3. Sieves analysis of fine aggregate.

Sieve Size	% Passing by Weight	Limits of IQS NO.45/1984 (Zone 2)
10mm	100	100
4.75mm	95.1	90-100
2.36mm	80.5	75-100
1.18mm	72.8	55-90
600µm	45.5	35-59
300µm	24.5	8-30
150µm	4.8	0-10

Table 4. Physical properties and sulfate content of fine aggregate used in experimental work.

Properties	Results	IQS NO.45/1984
Fineness modulus	2.76	
Specific gravity	2.58	
Absorption ,%	1.2	
Moisture content,%	0.4	
Material passing sieve size 75µm%	2.5	Max. 5% for natural fine aggregate
Sulfate content (SO_3), %	0.1	Max. 0.5%

-Tests are carried out in the Material Laboratory of the Engineering College -Baghdad University

Table 5. The chemical properties of Gypsum.

Compound Composition	Percent %
SiO_2	8.34
R_2O_3	2.25
CaO	32.02
MgO	0.95
SO_3	42.1
I.R	6.99

Table 6. Sieves analysis of coarse aggregate with 14mm maximum size.

Sieve size	% Passing by Weight	Limits of IQS NO.45/1984
20mm	100	100
14mm	95	90-100
10mm	75	50-85
5mm	4	0-10

Table 7. Physical properties and sulfate content of coarse aggregate.

Properties	Results	IQS NO.45/1984
Specific gravity (SSD)	2.65	--
Absorption ,%	0.3	--
Moisture content ,%	0.2	--
Passing sieve size 75µm,%	1.5	Max. 3%
Sulfate content (SO_3),%	0.03	Max. 0.1%

-Tests are carried out in the Material Laboratory of the College of Engineering-Baghdad University

Table 8. Chemical analysis of HRM

Oxides %	Content (%)	Mineral Admixture Class N ASTM C 618 –03
SiO_2	57.46	-
Fe_2O_3	1.52	-
Al_2O_3	36.82	-
CaO	0.9	-
SO_3	< 0.07	Max. 4.0%
L.O.I	1.3	Max. 10%
Moisture content	0.82	Max. 3.0%
$SiO_2 + AL_2O_3 + Fe_2O_3$ min %	95.8	Min. 70%

-The chemical analysis done by Geological Survey and Mining

Table 9. Typical properties of superplasticizer (Sika ViscoCrete -5930)

Form	Viscous liquid
Basis	Aqueous solution of modified polycarboxlate
Appearance	Turbid liquid
Relative density	1.08 kg/1t.±0.005

Table 10. The mix proportions used in preparing the test specimens

Index	Cement type	Cement (kg/m^3)	HRM (kg/m^3)	Fine aggregate (kg/m^3)	Coarse aggregate (kg/m^3)
Ref. -MR1	Iraqi	560	0	728	784
MR1-5%HRM		532	28	728	784
MR1-10%HRM		504	56	728	784
MR1-15%HRM		476	84	728	784
Ref.-MR2	Saudi Arabia	560	0	728	784
MR2-5%HRM		532	28	728	784
MR2-10%HRM		504	56	728	784
MR2-15%HRM		476	84	728	784

Table 11. Fresh concrete test results (slump flow, T 50cm slump flow, V-funnel and L-box)

Mixes No.	Cement type	SO_3 (%) by wt. of sand	Tests			
			Slump flow (mm)	T 50cm slump flow (sec)	V-funnel (sec)	L-box (h_2/h_1)
			650-800*	2-5*	6-12*	0.8-1.0*
Ref. -MR1	Iraqi	0.5	800	2.2	6.1	0.95
MR1-5%HRM			798	2.25	6.15	0.93
MR1-10%HRM			795	2.3	6.31	0.91
MR1-15%HRM			792	2.4	6.45	0.9
Ref.-MR2	Saudi Arabia		801	2.3	6.11	0.94
MR2-5%HRM			798	2.35	6.17	0.94
MR2-10%HRM			796	2.4	6.33	0.92
MR2-15%HRM			791	2.45	6.51	0.9
Ref. -MR1	Iraqi	1.0	794	2.5	7.01	0.88
MR1-5%HRM			791	2.56	7.11	0.87
MR1-10%HRM			788	3.1	7.27	0.85
MR1-15%HRM			785	3.15	7.34	0.85
Ref.-MR2	Saudi Arabia	1.0	795	3.30	7.42	0.89
MR2-5%HRM			791	2.51	7.08	0.88
MR2-10%HRM			789	2.58	7.15	0.86
MR2-15%HRM			784	3.45	7.30	0.85
Ref. -MR1	Iraqi	1.5	785	3.0	8.30	0.86
MR1-5%HRM			781	3.15	8.51	0.85

MR1-10%HRM			778	3.35	8.58	0.85
MR1-15%HRM			774	3.55	9.06	0.83
Ref.-MR2	Saudi Arabia		786	3.08	8.25	0.83
MR2-5%HRM			783	3.21	8.38	0.87
MR2-10%HRM			780	3.41	8.55	0.86
MR2-15%HRM			775	3.55	9.0	0.85
Ref. -MR1	Iraqi	2.0	778	4.01	9.50	0.85
MR1-5%HRM			775	4.11	9.58	0.84
MR1-10%HRM			770	4.35	10.15	0.83
MR1-15%HRM			767	4.48	10.25	0.80
Ref.-MR2	Saudi Arabia		780	4.08	9.45	0.86
MR2-5%HRM			776	4.16	9.59	0.84
MR2-10%HRM			772	4.36	10.11	0.82
MR2-15%HRM			776	4.51	10.30	0.81

*Permissible limits according to, **EFNARK, 2002.** guidelines

Table 12. Compressive strength and splitting tensile strength results for all SCC mixes.

Mixes No.	Cement Type	SO_3 (%)*	Compressive Strength (MPa)				Splitting Tensile Strength (MPa)			
			7-day	28-day	90- day	180-day	7-day	28-day	90- day	180-day
Ref. -MR1	IQ	0.5	35.9	46.6	60.5	66.2	3.04	3.9	4.71	4.98
MR1-5%HRM			36.8	47.2	63.2	68.5	3.21	4.05	4.92	5.25
MR1-10%HRM			38.1	49.7	65.8	70.1	3.35	4.21	5.25	5.61
MR1-15%HRM			39.5	55.4	69.1	74.3	3.42	4.25	5.38	5.85
Ref.-MR2	SA		36.1	47.3	60.9	66.9	3.06	4	4.81	5.12
MR2-5%HRM			37.2	47.8	63.5	69.2	3.25	4.11	5.15	5.46
MR2-10%HRM			38.9	49.9	66.3	70.6	3.38	4.35	5.46	5.75
MR2-15%HRM			39.6	56.3	70.6	74.7	3.45	4.55	5.62	6.1
Ref. -MR1	IQ	1.0	35.5	45.1	57.2	60.5	3.00	3.8	4.58	4.62
MR1-5%HRM			36.4	46.1	60.0	63.1	3.2	4.01	4.75	4.81
MR1-10%HRM			37.7	48.7	63.2	64.5	3.29	4.04	5.05	5.11
MR1-15%HRM			38.4	54.0	67.5	69.8	3.35	4.18	5.11	5.22
Ref.-MR2	SA		35.7	45.7	57.6	61.5	3.05	3.9	4.75	4.78
MR2-5%HRM			36.6	47.0	60.8	65.0	3.11	4.07	5	5.11
MR2-10%HRM			37.5	48.7	63.6	66.1	3.23	4.3	5.18	5.21
MR2-15%HRM			38.8	54.6	67.1	68.9	3.34	4.48	5.42	5.47
Ref. -MR1	IQ	1.5	35.2	43.9	55.8	53.7	2.94	3.81	4.35	4.31
MR1-5%HRM			36.0	45.1	58.5	56.6	3	3.88	4.48	4.46
MR1-10%HRM			37.2	46.9	61.2	59.8	3.15	3.95	4.62	4.6
MR1-15%HRM			38.5	50.2	65.4	60.2	3.21	4.2	4.75	4.71
Ref.-MR2	SA		35.4	43.6	56.1	54.8	3	3.78	4.41	4.37

MR2-5%HRM			36.2	45.8	58.7	57.5	3.08	4	4.58	4.54
MR2-10%HRM			37.4	47.0	62.5	58.9	3.15	4.18	4.71	4.7
MR2-15%HRM			38.3	52.6	66.0	59.2	3.28	4.36	4.88	4.81
Ref. -MR1	IQ	2.0	34.8	42.5	53.5	48.1	2.88	3.6	4.1	3.91
MR1-5%HRM			35.7	43.2	56.8	52.2	2.95	3.68	4.15	4.01
MR1-10%HRM			36.8	45.5	58.0	54.1	3.06	3.79	4.28	4.12
MR1-15%HRM			37.9	47.4	60.5	56.8	3.16	4.02	4.41	4.36
Ref.-MR2	SA		34.6	42.2	55.2	49.6	2.91	3.65	4.13	4.01
MR2-5%HRM			33.9	43.6	57.1	53.1	3.01	3.68	4.2	4.02
MR2-10%HRM			32.7	45.9	60.9	56.4	3.11	3.86	4.35	4.27
MR2-15%HRM			32	50.7	62.7	59.1	3.21	4.09	4.47	4.33

* By wt. of sand

Table 13. Ultrasonic pulse velocity results for all SCC mixes.

Mixes No.	Cement Type	Total SO_3 (%)	SO_3(%) by wt. of sand	Ultrasonic Pulse Velocity (Km/s)			
				7-day	28- day	90-day	180-day
Ref. -MR1	Iraqi	3.002	0.5	4.650	4.742	4.805	4.822
MR1-5%HRM				4.662	4.758	4.842	4.858
MR1-10%HRM				4.675	4.772	4.871	4.885
MR1-15%HRM				4.681	4.795	4.895	4.910
Ref.-MR2	Saudi Arabia	3.372		4.658	4.745	4.812	4.831
MR2-5%HRM				4.675	4.762	4.853	4.865
MR2-10%HRM				4.686	4.781	4.878	4.882
MR2-15%HRM				4.695	4.802	4.902	4.913
Ref. -MR1	Iraqi	3.652	1.0	4.641	4.732	4.792	4.801
MR1-5%HRM				4.655	4.781	4.826	4.841
MR1-10%HRM				4.668	4.758	4.851	4.871
MR1-15%HRM				4.672	4.788	4.878	4.888
Ref.-MR2	Saudi Arabia	4.052		4.651	4.741	4.800	4.808
MR2-5%HRM				4.669	4.755	4.832	4.848
MR2-10%HRM				4.675	4.762	4.856	4.861
MR2-15%HRM				4.684	4.785	4.888	4.882
Ref. -MR1	Iraqi	4.302	1.5	4.622	4.715	4.771	4.762
MR1-5%HRM				4.638	4.728	4.803	4.791
MR1-10%HRM				4.649	4.741	4.844	4.831
MR1-15%HRM				4.660	4.772	4.851	4.842
Ref.-MR2	Saudi Arabia	4.672		4.638	4.73	4.786	4.778
MR2-5%HRM				4.645	4.742	4.810	4.701
MR2-10%HRM				4.658	4.754	4.831	4.822
MR2-15%HRM				4.671	4.805	4.866	4.851
Ref. -MR1	Iraqi	4.952	2.0	4.601	4.728	4.758	4.739
MR1-5%HRM				4.615	4.741	4.781	4.762

MR1-10%HRM				4.622	4.762	4.812	4.788
MR1-15%HRM				4.642	4.79	4.836	4.801
Ref.-MR2	Saudi Arabia	5.322		4.612	4.735	4.768	4.745
MR2-5%HRM				4.628	4.752	4.792	4.770
MR2-10%HRM				4.641	4.768	4.828	4.790
MR2-15%HRM				4.652	4.781	4.851	4.818

Effect of Construction Joints on the Behavior of Reinforced Concrete Beams

Hussain Askar Jabir
Lecture
E-mail: haskar@uowasit.edu.iq

Thaar Sauid Salman
Assistant Professor
College Engineering - University of Wassit
E-mail: thaar@uowasit.edu.iq

Jasim Mahmood mhalhal
Assistant Lecture
E-mail: eng_ jasem67@yahoo.com

ABSTRACT

In this study, the effect of construction joints on the performance of reinforced concrete beams was experimentally investigated. Seven beam specimens, with dimensions of 200×100×1000 mm, were fabricated. The variables were considered including; the location and configuration of the joints. One beam was cast without a joint (Reference specimen), two specimens were fabricated with a one horizontal joint located either at tension, or compression zone. The fourth beam had two horizontal joints placed at tension, and compression area. The remaining specimens were with one or two inclined joints positioned at the shear span or beam's mid-span. The specimens were subjected to a monotonic central concentrated loading until the failure. The results of the experimental program indicated that the best location of the construction joint is at the compression zone. The presence of the horizontal construction joint at tension zone resulted in a reduction in strength of beams, about 5% - 7.5%, relative to the reference beam. However, the inclined construction joint had a little effect on the collapse load of beams, about 1.25% - 2.5%.

Key words: construction joint, cold joint, reinforced concrete, beams, crack, monotonic.

تأثير المفاصل الانشائية على تصرف العتبات الخرسانية المسلحة

حسين عسكر جابر
مدرس
كلية الهندسة-جامعة واسط

ثائر سعود سلمان
استاذ مساعد
كلية الهندسة-جامعة واسط

جاسم محمود مهلهل
مدرس مساعد
كلية الهندسة-جامعة واسط

الخلاصة

في هذا البحث تم دراسة تأثير المفاصل الانشائية على اداء العتبات الخرسانية المسلحة عن طريق فحص النماذج عمليا في المختبر.تم أنشاء سبعة نماذج بأبعاد (100×200×1000) ملم. ان المتغيرات التي تم اعتمادها هي مواقع و تشكيل المفاصل الانشائية. النموذج المصدري لم يحتوي على مفصل و نموذجين حتوى على مفصل افقي في منطقة الشد أو الضغط. النموذج الرابع أحتوى على مفصلين افقيين في منطقتي الشد والضغط. النماذج المتبقة تم أنشائها مع مفصل او مفصليين افقيين تقع في منطقة القص او في منتصف العتبة. بينت النتائج العمليه الى ان افضل موقع للمفصل الانشائي هو في منطقة الانضغاط، وتشير ايضا الى ان المفصل الافقي ذو تأثير واضح على مقاومة النماذج حيث ان نسبة الانخفاض جاءت بين (5%-7.5%). بينما يوجد نقصان طفيف على مقاومة النماذج ذات المفصل الانشائي المائل بحدود (1.25%-2.5%).

الكلمات الرئيسية: المفصل الانشائي، العتبات الخرسانية المسلحة، التشقق، التحميل الساكن.

1. INTRODUCTION

Construction joints (or cold joints) can be defined as stopping positions in the concrete casting, and they are needed because of impracticality to cast concrete in one continuous process. The concrete quantity, produced at one time, is dominated by the capacity of mixers and the formworks' strength. Thus, the concrete casting process may be stopped and resumed several times leading to initiate the construction joints **Aziz, 2006**.

Clark and **Gill, 1985** investigated the shear capacity of 60 plain concrete prisms having smooth construction joints at their mid-span. These joints were inclined at various angles ranged from 13.9^o and 75.1^o. The results showed that the shear resistance was developed by a combination of friction and cohesion. The specimens were failed either by sliding over the cold joint or by crushing monolithically if the joint is very strong. Moreover, an empirical equation for estimating the shear strength was presented.

Mo and **Lai, 1995** evaluated experimentally the influence of the casting procedure on the structural response of nine reinforced concrete beams. The beams were (300×500mm) in the cross section, and their compressive strength was 34 MPa. Two-step casting procedures (two layers) were achieved. Three specimens were concreted monolithically; the others were concreted to the high of (360mm) on the first day and the remaining part of (140mm) on the next day. An inconsiderable difference between the two casting procedures was observed.

Patnaik, 2001, presented an experimental study of the behavior of composite concrete beams of a smooth interface. The beams were fabricated in the T and rectangular cross- sectional area. The cold joints were located between the web and the flange in the T-beams. In the rectangular beams, construction joints were positioned at (150mm) below the upper face. The specimens were constructed with effective depth (d) ranged from (277mm) and (317mm). The compressive concrete strength of the specimens was varied from (17MPa) to (38MPa). The tests showed that the concrete strength of a composite concrete beam with a smooth interface and that the effective depth to tie spacing ratio (d/s) did not influence the horizontal shear strength of such beams.

The influence of construction joints and the existing flange openings on strength of reinforced concrete T-beams was studied by **Aziz** and **Ajeel, 2010**. Eight T-specimens of simply supported were tested under a concentrated loading applied at their mid-span. The test's parameters were the position and number of construction joints and flange openings. The results observed that the shear strength dropped about (27%) for the specimen having cold joint.

Camille A. Issa et. al., 2014, correlated experimentally the concrete compressive strength to the modulus of rupture for plain concrete beams with a vertical construction joint placed at their center. The experimental results indicate that for monolithic beams, the ACI Code always underestimates the modulus of rupture. The presence of a vertical construction joint yielded a significant loss in the modulus of rupture of concrete varying between 24% and 83%.

2. RESEARCH SIGNIFICANCE

The purpose of this experimental study is to understand the effect the construction joints on the structural behavior beams. Seven beam specimens were fabricated and subjected to a three-point loading until failure. The tests focused on the influences of the types and locations of the construction joints.

3. TEST SPECIMENS

Seven reinforced concrete beams were manufactured to study the effect the construction joints on behavior of RC beams. They were similar in the geometry and reinforcement ratio. Their dimensions and steel reinforcement ratios were selected according to **ACI 318M-2014** requirements for the reinforced concrete structures. The total length of the tested beams was (1000) mm and with cross-section of (100×200) mm. The flexural reinforcement composed of two deformed bars of 10mm diameter located in the beam bottom, and the shear reinforcements were 6mm diameter deformed bars forming closed stirrups spaced at the 75mm center to center. Two bars of 6mm diameter were used in the top of the beams to support the stirrups as shown in **Fig. 1**.

The study parameters were the locations and the types of the construction joints. One beam was fabricated without construction joint (Reference specimen) as shown in **Fig. 2**. Other six specimens had the construction joints with various types and locations as shown in **Fig. 3**. Four of them were made with one construction joints and concreted into two layers. The primary layer was cast on a first day, and a second one was done on the next day. The other two specimens were with two joints and cast in three layers on three consecutive days.

A total of seven specimens (**SR**, **SHT**, **SHC**, **SHTC**, **SIM**, **SIS**, and **SISM**) were tested as a simply supported and subjected to a concentrated loading applied at their mid-span. The specimen's designation can be explained as follows; the first symbol indicates the (Specimen); the second one refers to the type of construction joint (R=reference without construction joint, H= horizontal construction joint, I=inclined construction joint); and the third and fourth symbols indicate the location of construction joint (T= tension zone, C= compression zone, M= maximum moment (mid-span) and S= shear span). The entire characteristics and details of the tested specimens are listed in **Table 1**. Finally, the beams were categorized into two groups depending on the joints' type as shown in Table **2**.

The properties of steel used in the reinforcing of the beams are listed in **Table 3**. One specimen for each bar size was tested according to **ASTM A 615M- 2005.** The samples were produced using a normal density concrete with 30 MPa target compressive strength. The concrete mixing consisted of; ordinary Portland cement, sand, and 12mm maximum size crushed coarse aggregate in the following weight proportion 1; 2.05; 2.2, respectively. The water to cement ratio was 0.55 for all specimens. These raw materials were mixed using a mechanical mixer according to the procedure of **ASTM C192-2002**. **Table 4** lists the final strengths based on the average values from the tests performed on at least three 150 x 300mm cylinders for each test specimen. The tensile strength of concrete was determined by performing the split cylinder tests.

4. TEST PROCEDURE

The beam samples were tested using a testing rig at Engineering College of Wasit University. The specimens were positioned inside the testing rig and supported simply as shown in **Fig. 4**. They were subjected to a centrally concentrated loading, three-points loading, applied gradually at an increment of 5 kN until specimens' failure. The loading was subjected through a hydraulic jack of 500 kN capacity, and its value was recorded using a load cell that inserted between the jack strike and specimen's surface. A dial gauge of 0.01 mm accuracy was located directly under the bottom beam surface at mid-span to measure the maximum deflection at each a loading increment.

At each loading stage, the test measurements included the magnitude of the applied load and deflection of the beam at mid-span was recorded. At the end of each test, the cracks developed

were marked and the crack pattern and mode of failure for each specimen were carefully investigated.

5. TEST RESULTS AND DISCUSSION

5.1 General Behavior and Crack Patterns

For all specimens except for **SIS** and **SISM,** the first crack initiated from the bottom of the beam in the mid-span where the maximum bending moment occurred, just the tensile stresses exceeded the concrete rupture modulus. In samples **SIS** and **SISM,** the primary crack was observed at the inclined construction joints in the shear span, and in the maximum moment region, respectively.

As the applied loading increased, the first cracks widened and propagated vertically upward. Moreover, other flexural cracks also developed and separated along the beam's length. Diagonal cracks were noticed near the supporting points, some of these cracks connected with the flexural cracking shaping the shear-flexural cracks. It is worth mentioning that horizontal cracks were noted at the horizontal cold joints in the beams **SHT** and **SHTC.**

In general, all specimens were failed in a ductile mode by an excessive yielding of tension steel reinforcement and a concrete crushing at the top surface. **Fig. 5** shows the crack patterns of the testing specimens.

5.2 Cracking and Failure Loads

The experimental results for cracking and ultimate loads of all specimens are listed in **Table 5**. The test results show that the cracking loading was (20.5% to 25.6%) of the ultimate load capacity of these specimens.

The existing of a cold joint in the horizontal form in the tension zone decreased the cracking load about 15% to 20% for specimens **SHT** and **SHTC**, respectively with respect to the beam **SR**. Whereas it had no effect on the cracking load of specimens whose horizontal joint positioned at the compression zone. Furthermore, the inclined joint constructed at the specimens' mid-span led to a considerable dropping in the cracking load, reached 20% comparing with specimen **SR**. On the contrary, the inclined joints, located at the shear span, did not affect the cracking load as shown in specimen the **SIS**.

Generally, the construction joint leverage on the ultimate load was more tenuous than that on the cracking load. For specimens with horizontal construction joints, the joints influenced the ultimate load only when they located in a tension zone near the flexural reinforcement. However, the reduction in the ultimate load was relatively slight about 5%, and 7.5% for specimens **SHT**, and **SHTC,** respectively compared to the control one **SR**. The beam **SHC** with joint, located in the compression fiber, failed at the same load of the specimen **SR**.

The beams, made with inclined joints, showed the smallest drop in the failure load compared with the reference beam without joints. Where the specimens SIM**, SIS** and **SISM** collapsed at loads 1.25%, 2.5% and 2.5% less than that of the control sample **SR**, respectively. The limited effect of the inclined joints was due to the flexural failure of these beams.

5.3 Load-Deflection Response

Vertical deflection at the mid-span was recorded at each load step of the test program. Two groups were adopted in the presentation of the load-deflection relations as described in **Table 2**. The load-deflection response of the specimens is compared to that of the reference specimen, at two loading levels as listed in **Table 6**: a service load level and the failure load level. The

serviceability load is approximately (70-75%) of the peak load **Tan** and **Zhao**, **2004**. In the current illustration of deflections, the service loads are assumed to be 70% of the collapse load of reference specimens. The failure loads of samples are equal to the recorded load, in **Table 5**.
Generally, when a beam is progressively loaded, the deflection linearly augmented at an elastic juncture. Thereafter, the first crack appeared; the deflection rose rapidly. After developing of cracks in the beam, the load-deflection response remained somewhat linear even yielding of tensile reinforcement. Beyond this, the deflection largely grew without a considerable boost in applied load.
The influence of the horizontal and inclined construction joints on load- central deflection behavior is demonstrated in **Fig. 6** and **Fig. 7,** respectively. As shown in the figures, there is a significant effect for inclined joints on the deflection measured at the service stage. Since it reduced the inertia moment of the specimens, the deflection increased compared with the specimen **SR**. The increments in the deflection were 22.2%, 43.7% and 29.6% for the specimens **SIM**, **SIS** and **SISM** respectively. It is worth mentioning that the reduction in the deflection was trivial (4.8%, 1.9%) for one horizontal joint specimens **SHT**, and **SHC**, correspondingly. The specimen SHTC, which had two horizontal joints at tension and compression zones, exhibited 16.7% rising in the deflection compared with the reference beam.
Finally, at failure all specimens showed ultimate deflection smaller than that of the control specimen (specimen without construction joint).

6. CONCLUSIONS

The major conclusions of current experimental investigation are listed as follows;

1. All specimens exhibited a ductile failure. The first cracks developed at a load range of about (20.5% to 25.6%) of the ultimate load capacity of the specimens.
2. The beams, having construction joints at the compression zone parallel to the main reinforcement, performed structurally better than the beams with construction joints at the tension zone.
3. The load carrying capacity of specimens with horizontal construction joints at a tension zone was reduced about (5% -7.5%) with respect to the reference specimen.
4. The location of horizontal joints at a compression zone did not influence the ultimate strength of specimens.
5. Inclined construction joints had a trivial effect on the overall behavior of reinforced concrete beams displayed the flexural failure. The load carrying capacity for the tested beam with inclined construction joints dropped about (1.25% - 2.5%) comparing to the reference specimen.
6. The existing of construction joints led to a reduction in the inertia moment of beams, and therefore, dropping in the beams' stiffness.
7. If the existing of construction joints is impossible to avoid in beams, the best location for joints is at the compression zone in the horizontal configuration. For beams, designed to fail in the flexural, the presence of inclined construction joints does not affect the beams strength.

REFERENCES

- ACI Committee 318, 2014, *Building Code Requirements for Structural Concrete ACI 318M-14 and commentary*, American Concrete Institute, Farmington Hills, 519 pp.

- ASTM Designation A615, 2005, *Standard Specification for Testing Method and Definitions for Mechanical Testing of Steel Products*, Annual Book of ASTM Standards, American Society for Testing and Material, Philadelphia, Pennsylvania, Section 1, Vol. 1.01, pp. 248-287.

- ASTM Designation C192/C192M-02, 2002, *Making and Curing Concrete Test Specimens in Laboratory*, Annual Book of ASTM Standards, American Society for Testing and Materials, Philadelphia, Pennsylvania, Vol. 4, 02.

- Aziz, A. H., (2006), *Flexural and Shear Behavior of Hybrid I-Beams with High - Strength Concrete and Steel Fibers*, Ph.D. Thesis, Department of Civil Engineering, Al-Mustansirya University, (10) p.

- Aziz A. H. and Ajeel A. E. 2010, *Effect of Existing Flange Opening and Cold Joints on Strength of RC T-Beams*, Journal of Engineering, Collage of Engineering, University of Baghdad, Iraq, Volume 16, Number 1, March, pp. 4535-4546.

- Camille A. Issa , Nagib N. Gerges , Samer Fawaz, 2014, *The Effect of Concrete Vertical Construction Joints on the Modulus of Rupture*, Construction Materials Jornal, Vol.1, pp. 25–32.

- Clark, L. A. and Gill, B. S., 1985, *Shear Strength of Smooth Unreinforced Construction Joints*, Magazine of Concrete Research, V. 37, No. 131, June, pp. 95-100.

- Mo, Y. L. and Lai, H. C., 1995, *Effect of Casting and Slump on Ductilities of Reinforced Concrete Beams*, ACI Structural Journal, V. 92, No. 4, July-August, pp. 419-424.

- Patnaik, A. K., 2001, *Behavior of Composite Concrete Beams with Smooth Interface*, ASCE-Journal of Structural Engineering, V. 127, No. 4, April, pp. 359-366.

- Tan, K. G. And Zhao, H. , 2004, *Strengthening of Openings in One-Way Reinforced-Concrete Slabs Using Carbon Fiber-Reinforced Polymer Systems*, Journal of Composites for construction ,ASCE, Vol. 8, No. 5, pp. 393-402.

Table 1. Characteristics of the tested beams.

No.	Specimen designation	Beam depth (mm)	Beam width (mm)	Tension steel ratio (ρt)	Shear reinforcement details	Location of construction joint
1	SR	200	100	0.0092	$\emptyset 6\ mm\ at\ 75\ mm\ c/c$	Without construction joint
2	SHT	200	100	0.0092	$\emptyset 6\ mm\ at\ 75\ mm\ c/c$	Tension zone
3	SHC	200	100	0.0092	$\emptyset 6\ mm\ at\ 75\ mm\ c/c$	Compression zone
4	SHTC	200	100	0.0092	$\emptyset 6\ mm\ at\ 75\ mm\ c/c$	Tension and compression
5	SIS	200	100	0.0092	$\emptyset 6\ mm\ at\ 75\ mm\ c/c$	Shear span (min. moment)
6	SIM	200	100	0.0092	$\emptyset 6\ mm\ at\ 75\ mm\ c/c$	Maximum moment (mid-span)
7	SISM	200	100	0.0092	$\emptyset 6\ mm\ at\ 75\ mm\ c/c$	Shear span & maximum moment

Table 2. Details of beams groups.

Group	Description	Specimens
I	$b = 100mm, \quad h = 200mm$ $\rho t = 0.009$ Horizontal Construction Joint (Variable)	1. SR 2. SHT 3. SHC 4. SHTC
II	$b = 100mm, \quad h = 200mm$ $\rho t = 0.009$ Inclined Construction Joint (Variable)	1. SR 2. SIM 3. SIS 4. SIMS

Table 3. Properties of steel reinforcement.

Nominal diameter (mm)	Measured diameter (mm)	Yield stress fy MPa	Ultimate strength fu MPa	Elongation %
6	5.83	724.4	777.4	16
10	9.87	648.2	721.34	13

Table 4. Mechanical properties of concrete.

Specimen ID	Layer Description	Compressive Strength at Time of Specimen Testing (MPa)		Modulus of rupture (MPa)	Splitting tensile strength (MPa)
		f_{cu}	f'_c	fr	ft
SR	Casting one part	44.72	36.76	4.03	3.72
SHT	The first layer of beam	44.72	36.76	4.03	3.72
	The second layer of beam	41.87	33.16	3.64	3.13
SHC	The first layer of beam	43.35	33.92	3.7	3.42
	The second layer of beam	41.87	33.16	3.64	3.13
SHTC	The first layer of beam	44.72	36.76	4.03	3.72
	The second layer of beam	41.87	33.16	3.64	3.13
	The third layer of beam	38.86	30.82	3.36	3.32
SIS	The first part of beam	45.84	35.82	3.92	3.18
	The second part of beam	43.15	35.68	3.73	3.44
SIM	The first part of beam	45.84	35.82	3.92	3.18
	The second part of bean	43.15	35.68	3.73	3.44
SISM	The first part of beam	45.84	35.82	3.92	3.18
	The second part of beam	43.15	35.68	3.73	3.44
	The third part of beam	41.02	31.64	3.45	3.22

Table 5. Cracking and ultimate loads of the tested beams.

Specimens		First crack load (Pcr) (kN)	Ultimate load (Pu) (kN)	% Pcr/Pu	%Decrease in first cracking load with respect to Ref.	%Decrease in ultimate load with respect to Ref.
Group I	**SR**	20	80	25	Ref.	Ref.
	SHT	17	76	22	15	5
	SHC	20	80	25	0.0	0.0
	SHTC	16	74	21.6	20	7.5
Group II	**SR**	20	80	25	Ref.	Ref.
	SIM	17	79	21.5	15	1.25
	SIS	20	78	25.6	0	2.5
	SISM	16	78	20.5	20	2.5

Table 6. Central deflections of the tested beams at service and ultimate loads.

Specimens		**Deflection at Service Load of Ref. Specimen (mm)**	**% Increase in Deflection at Service Load**	**Deflection at Ultimate Load of Ref. Specimen (mm)**	**% Decrease in Deflection at Ultimate Load**	**Ultimate Deflection of each Specimens (mm)**
Group I	**SR**	2.7	Ref.	16.98	Ref.	16.98
	SHT	2.83	4.8	**	**	11.98
	SHC	2.75	1.9	15.99	5.8	15.99
	SHTC	3.15	16.7	**	**	13.69
Group II	**SR**	2.7	Ref.	16.98	Ref	16.98
	SIM	3.3	22.2	**	**	13.26
	SIS	3.88	43.7	**	**	14.8
	SISM	3.5	29.6	**	**	14.47

**Ultimate load of control specimen SR (80 kN) is beyond the failure load of these specimens.

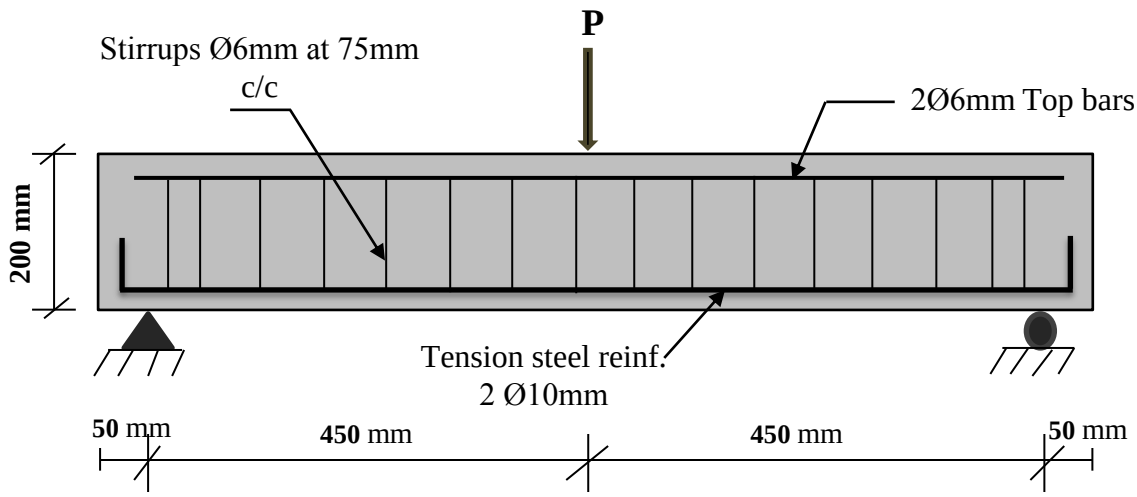

a. Longitudinal section of the beams

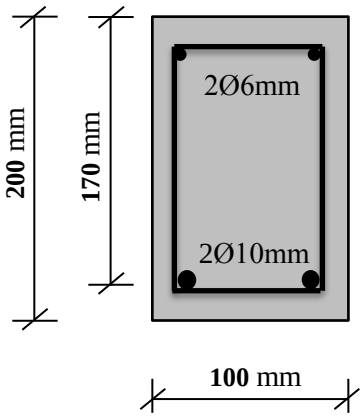

b. Cross Section in Beams

Figure 1. Typical dimensions and reinforcement details of the beams

Figure 2. Longitudinal section of the control specimen (without construction joint)

a. SHT specimen

b. SHC specimen

c. SHTC specimen

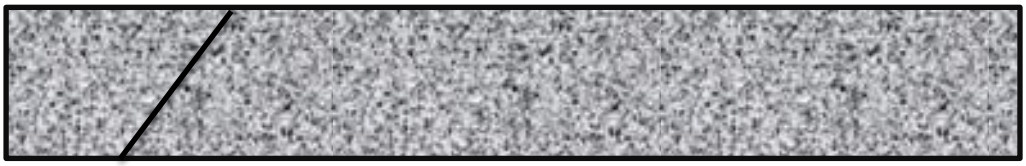

d. SIS specimen

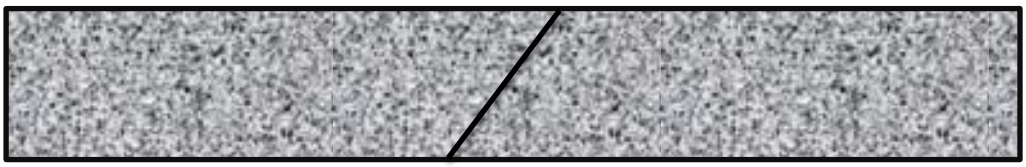

e. SIM specimen

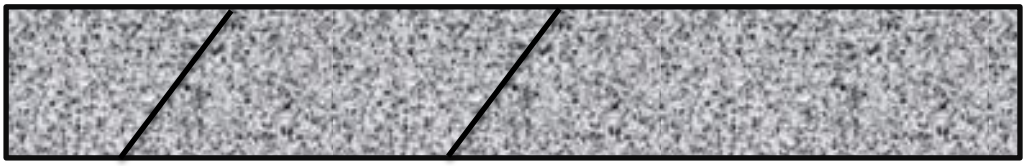

f. SISM specimen

Figure 3. Locations of the construction joints for the tested specimens.

Figure 4. Photograph of specimen setup.

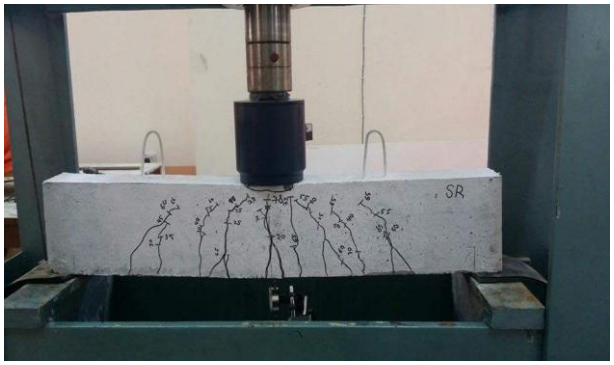

a. SR specimen

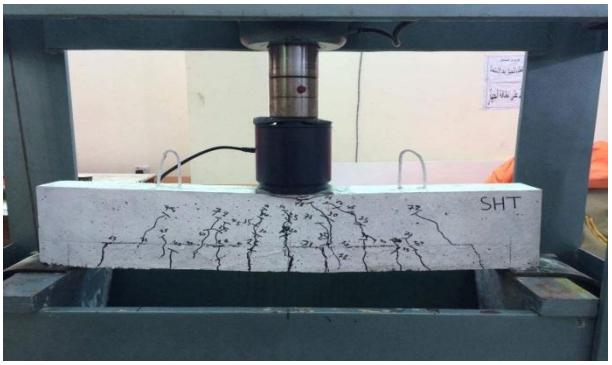

b. SHT specimen

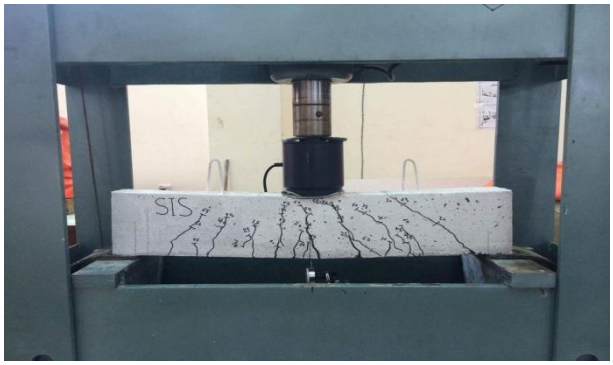

e. SIS specimen

c. SHC specimen

f. SIM specimen

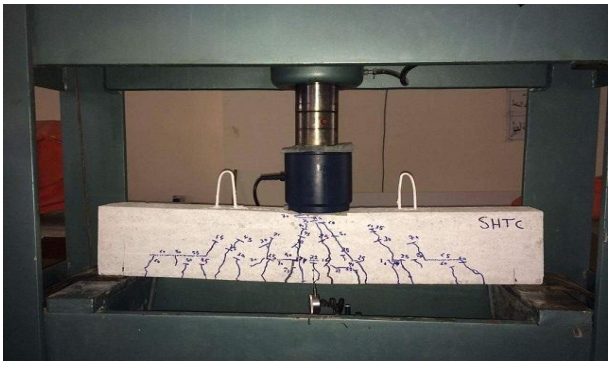

d. SHTC specimen

g. SISM specimen

Figure 5. Cracks pattern for the specimens tested after failure.

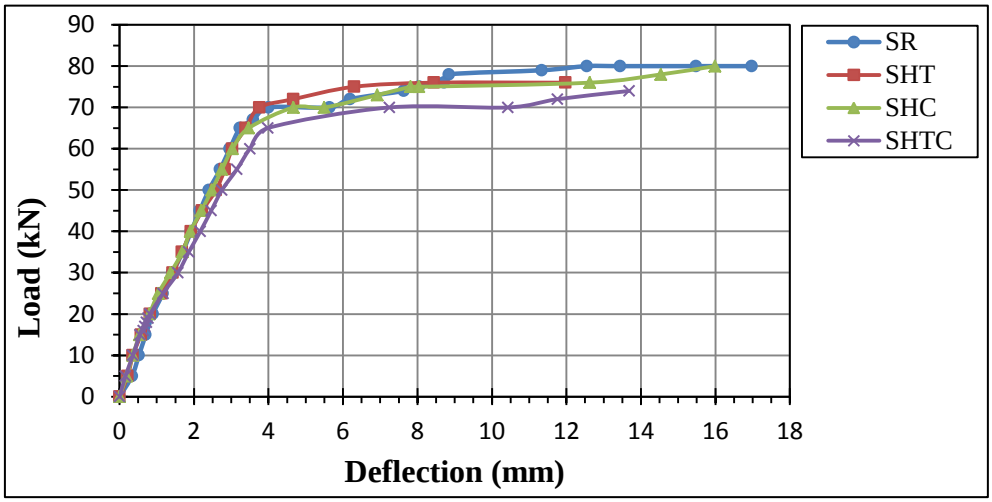

Figure 6. Influence of the horizontal construction joint on load-central deflection behavior of the specimens of group (I).

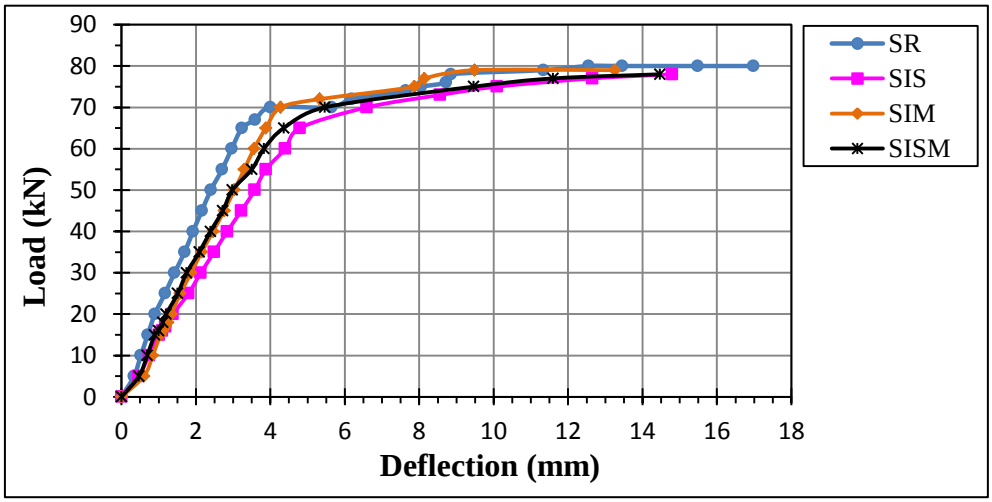

Figure 7. Influence of the inclined construction joints on load-central deflection behavior of the specimens of group (II).

Sustainable Roadway Planning: A Model for a Proposed Rating System in Iraq

Angham Ezzulddin Alsaffar
Professor Doctor
College of Engineering-University of Baghdad
Email: anghamalsaffar@yahoo.com

Dua'a Mouiad Lafta
Researcher
College of Engineering-University of Baghdad
Email: duaamouiad@yahoo.com

ABSTRACT

The goal of the research is to develop a sustainable rating system for roadway projects in Iraq for all of the life cycle stages of the projects which are (planning, design, construction and operation and maintenance). This paper investigates the criteria and its weightings of the suggested roadway rating system depending on sustainable planning activities. The methodology started in suggesting a group of sustainable criteria for planning stage and then suggesting weights from (1-5) points for each one of it. After that data were collected by using a closed questionnaire directed to the roadway experts group in order to verify the criteria weightings based on the relative importance of the roadway related impacts that each credit addresses. Statistical analysis for expert's answers have been evaluated by using factor analysis method to ensure the compatibility and validity of credits selected for the rating system and the actual weights conducted for each criteria by using the factor analysis method by using SPSS program V.19. Finally the researcher put the details for each criterion that contain from aim, requirements and strategies. The researcher reached to that the study of the all life cycle stages is important to make a clear comparison between the roles of the criteria in different stages.

Keywords: rating system; sustainable criteria; sustainable planning.

التخطيط المستدام لمشاريع الطرق: نموذج نظام تقييم مقترح في العراق

أنغام عزالدين الصفار
استاذ دكتور
كلية الهندسة /جامعة بغداد

دعاء مؤيد لفته
باحث
كلية الهندسة /جامعة بغداد

الخلاصة

الهدف من هذا البحث هو تطوير نظام تقييم مستدام لمشاريع الطرق في العراق لجميع مراحل دورة حياة المشاريع التي تشمل (التخطيط والتصميم والبناء والتشغيل والصيانة). يتضمن البحث تحديد المعايير والأوزان لنظام تقييم الطرق المقترح اعتمادا على فعاليات مرحله التخطيط المستدام . بدأت المنهجية في اقتراح مجموعة من المعايير المستدامة لمرحلة التخطيط ثم اقتراح الأوزان من (1-5) نقاط لكل معيار منها، بعد أن تم جمع البيانات باستخدام استبيان مغلق موجه الى مجموعة خبراء مختصين من أجل التحقق من الأوزان و المعايير التي تقوم على اهمية المعيار وتأثيره على المشروع . تم عمل التحليل الإحصائي بعد الحصول على إجابات الخبراء باستخدام طريقة تحليل العوامل لضمان التوافق وصحة الاعتمادات المحددة لنظام التصنيف والأوزان الفعلية التي أجريت لكل المعايير باستخدام أسلوب تحليل العوامل بواسطه برنامج التحليل الاحصائي (SPSS,V.19) وأخيرا تم وضع التفاصيل لكل المعايير والتي تتكون من الهدف والمتطلبات والاستراتيجيات. توصل الباحث الى ان دراسة دورة حياة المشروع كامله في مثل هذه المواضيع مفيدة جدا من الناحية العملية لأن المقارنة بين ادوار المعايير في المراحل المختلفة ستكون اوضح.

الكلمات المفتاحية: نظام التقييم , المعايير المستدامة , التخطيط المستدام

1. INTRODUCTION

In earlier decade, sustainable development idea has grown up from numerous environmental movements. Recently sustainable issues have been widely discussed especially in construction industry.

Sustainable development is a key issue in order to meet the environmental objectives and fulfills the demand of the large infrastructure projects due to increasing numbers of population growth and urban density, **Constandopoulos,** and **Nation, 2010**.

The decisions regarding the location, type, timing, feasibility or other planning level ideas are excluded. While planning is fundamental to roadway and community sustainability, these decisions are often too complex or political to be adequately defined by a point-based performance metric, **Stephen**, and **Jeralee, 2009**.

The green highway rating system was introduced to determine the level of greenery and environmental friendly of the highway. Since roads run through the landscape, road have point source impact and linear effect. Greenroads is the first green highway rating system that has been established in United States. It is a voluntary third party rating system for road project which seeks to recognize and reward the roadway projects that exceed the public expectation for environmental, economic and social performance. Washington Internship for Students Engineering (WISE) has introduced the green highway rating system. The rating system is to make sure the highway design is sustainable, environmental friendly and giving less impact of environment damage which can be used for developing and classifying an environmentally and economically sustainable highway, **WISE**, **2011**.

Nowadays, green rating system becomes a popular tool to confirm the green credential of building. Most countries have developed their own green building rating system. The countries that already have the rating system are United States, Canada, Australia, United Kingdom, Hong Kong, Japan, Taiwan, Singapore, Philippine, European, Korea, India and Australia. Malaysia also owns the green building rating system which is GBI. With the successful implementation of green building rating system, the rating system has been widened into the highway. There are three rating system for the highway that has been found which is Greenroads, Green Leadership in Transportation and Sustainable (GreenLITES) and Illinois-Livable and Sustainable Transportation (I-LAST), **Raffia,** and **Rooshdi**, **2013**.

Sustainable planning could minimize the impacts of the roadway projects on the environment. Costing, safety, health, management, siting, water, energy are the most important factors that should be highlighted in the sustainable rating system through the project life cycle. The evaluation for the sustainable roadway is not yet available in Iraq and this paper seeks to address this problem.

2. CRITERIA

As development of criteria for green highway, there were several green rating tools which are Greenroads, GreenLITEs, I-LAST and INVEST that had been reviewed as a summary of green highway criteria.

The above rating systems have similarities and differences. Specifically, all of sustainability rating systems are applicable to the planning and design phases of projects. Only GreenLITES, Greenroads and INVEST are applicable to the construction phase; and only GreenLITES and INVEST are applicable to the operations and maintenance phases of a project. I-LAST is

currently developing a sub-system applicable to the construction phase. The all rating systems are only applicable to highway projects, **Caroline, et al., 2013**.

There are some common criteria that can be found in every green rating system such as sustainable site, water efficiency, energy efficiency, materials and resources and innovation. The sustainable criteria includes of geometrics and alignment, earthworks, pavement, drainage, slope protection, landscape ecology, transportation facilities, maintenance, sound insulation, electrical, mechanical and lighting. These criteria were different in every project according to the country circumstances, **Raffia,** and **Rooshdi, 2013**.
The rating system consist the explanation of different certification levels and the total points that are needed to obtain them. Starting with the least green to exceptional green, most of the certifications are distinguished by four different levels, **Clark, et al., 2009**.

For Greenroads the certification levels are as follows:
Certified: All Project Requirements + 32 - 42 Voluntary Credit points
Silver: All Project Requirements + 43- 53 Voluntary Credit points
Gold: All Project Requirements + 54- 63 Voluntary Credit points
Evergreen: All Project Requirements + 64+ Voluntary Credit points

For GreenLITES the certification levels are (GreenLITES Certified, GreenLITES Silver, GreenLITES Gold and GreenLITES Evergreen awards) and so on.

Therefore, this paper attempts to identify the criteria for sustainable planning stage according to the most popular rating system manuals and (the World Bank reports) by depending on their working concepts in road projects and also criteria identification depend on roadway experts' opinions.

3. METHODOLOGY

3.1 The Closed Questionnaire

The absence of a system depends on the application of the sustainability concepts in the evaluation of the lifecycle of roadway projects in Iraq was the reason for thinking through this research to find the appropriate method for the selection of the main criteria and sub-criteria in a suggested rating system specifically planning stage. The development of these criteria is largely based on conducting a comprehensive literatures review and reports for sustainable roadway. Criteria related to sustainable project in planning stage activities in many green roadway rating systems have been chosen depending on literature review and the country circumstances that are related to the environmental, social and economical impacts. The criteria selected in the questionnaire have been discussed among the experts to select the most appropriate criteria by making the questionnaire checklist flexible and the expert can add, remove or modify on any criteria according to his/her opinion. They would share their experience, opinion and suggestion on the best criteria in sustainable planning stage activities. **Table 1** shows the profile of the respondents. The survey indicates that, 17.5% of respondents have more 21 years' experience followed by 82.5% of them has at least 7 years' experience. This shows that the respondents have an extensive experience, which helps to provide this study with reliable data.

World Bank reports in addition to other references have been used as a guide for the similar criteria in indicating the criteria for this research. **Table 2** shows the suggested criteria and sub criteria for sustainable planning stage activities and the weights suggested by the researcher.

3.2 Discussion of the Questionnaire Results

After returning the questionnaire results, the researcher tried to organize the weights that most of the experts agreed on it, for each criterion during the planning stage to present an initial idea for the weights for each criterion before the statistical analysis which is made by using SPSS program V.19. **Table 3** shows the percentage of the maximum respondent answers for each criterion and the weight that most of the experts agreed on it in planning stage.

3.3 Statistical Analysis of Criteria Weightings

Once the criteria had been finalized through questionnaires and expert opinions, the data had been analyzed using factor analysis method to produce mean index and factor loading for each criterion to have the actual weight at the end of the analysis process. The final model of the suggested rating system consisted of 11 criteria for planning stage. Reliability test were done in the beginning of the section analysis due to check the reliability of data to be analyzed for planning stage where the Cronbach's Alpha computed in Eq. (1):

$$Alpha = [n/(n - 1)] \times [(Vart - \Sigma Vari)/Vart] \quad (1)$$

where Alpha = estimated reliability of the full-length test, n = number of items, Vart = variance of the whole test (standard deviation squared), and ΣVari = sum the variance for all n items.
This data set show Cronbach's Alpha is 0.834 for planning stage.
There is high internal consistency for the data set which the Cronbach's Alpha is more than 0.7, **Hair, et al., 2010**.
Then the data were analyzed by using Kaiser-Meyer-Olkin measure of sampling (KMO) to test the sampling adequacy where KMO index computed in Eq. (2):

$$KMO = (\sum\sum r^2\_ij) / (\sum\sum r^2\_ij + a^2\_ij),\ i \neq j \quad (2)$$

where the correlation matrix is $R = [r_{ij}]$ and the partial covariance matrix is $A = [a_{ij}]$.
The KMO ranges from (0-1) with higher values indicating greater suitability, and greater than 0.750 is much better, **Raffia,** and **Rooshdi**, **2013**. The KMO value is 0.853 for the data of planning stage.
As suggested that accepting values greater than 0.5 is acceptable, **Kaiser, 1974**. And the values of KMO between 0.7 until 0.8 is good, **Hutcheson,** and **Sofroniou, 1999**
Planning stage has three factors had eigenvalues over Kaiser's criterion of 1. **Table 4** shows the factor loadings for planning stage.
In weighting the criteria, the factor loading had been multiplied with mean index as shows in Eq.(3):

$$Actual\ weight = factor\ loading * mean\ index \quad (3)$$

Factor loading shows the important of these criteria in the planning stage and the mean index shows the level agreement of respondents towards those criteria. By combining the important and level of agreement of each criterion, **Table 5** shows the mean and the weightage of each criterion.

4. SUGGESTED ACTIONS FOR ROADWAY RATING SYSTEM "PLANNING STAGE"

The planning stage contained 11 criterion that the researcher conducted depending on the researches and the world bank reports that are compatible with Iraq circumstances as much as sustainable planning need for roads projects and each one of it consisted from aim of it, requirements that need to meet this criteria and strategies that could conduct it to have this criteria and also the actual weight that the researcher reached to it after the statistical analysis for each criterion. **Fig.1** to **Fig. 10** shows the details for the criteria of planning stage.

5. ROADWAY RATING SYSTEM "PLANNING STAGE" VERIFICATION

The verification process based on the questionnaire attached with the suggested rating system for sustainable roads project "planning stage" that the researcher suggested it previously with the criteria details, weights of it, and the amount of the criteria suitability.

The survey process contains fifteen evaluator (five experts from Iraq and ten experts from outside of Iraq) who has related to the fields of roads projects, the verification process contains seven questions to evaluate the suggested SRSI for planning stage; the answering of these questions contain three answers (Yes, No and Yes with suggestion) to reflect the experts (evaluators) opinions about the applicability of the system and system components, the required modification through the suggestions pointed out by the respondents, or the system components not applicable or unrealistic for planning stage.

Table 6 shows the verification process for planning stage.

6. CONCLUSIONS

1. The study of the all life cycle in this type of subjects is necessary because the comparison between the criteria in more than one stage must be the clearest.

2. Green highway classifications will help transportation planning officials to have a clearer understanding of techniques and incentives for maximizing sustainable efforts.

3. From the verification process the following conclusions founded:

   - The costing criteria should study planning, construction and operation and maintenance stages.
   - The risks criteria should be considered later in planning stages.
   - The quality management system is important criterion and it should be highlighted in all the life cycle stages

7. RECOMMANDATIONS

1. It's recommended to dependence the suggested rating system (SRSI) by one of the establishment who has relevant with the roads projects such as the Iraqi directorate for roads and bridges.

2. The sustainability aspects should be adopted during the construction of the roadway projects, because of its importance on environment, economic and social life in Iraq.

REFRENCES

- Caroline, M. C., Mehmet, E. O., and Sherona, S., 2013, *Review of Sustainability Rating Systems used for Infrastructure Projects*, Colorado State University Fort Collins, Colorado.

- Clark, M., Paulli, C., Tetreault, Z., Thomas, J., 2009, *Green Guide for Roads Rating System (S. S. D. P. Site, Trans.): A major Qualifying Project Report for the Stantec Sustainable Design Project Site*, Worcester: Worcester Polytechnic Institute.

- Constandopoulos, J., and Nation, M., 2010, *Towards Sustainable Roadways*, Sinclair Knight Merz, Insights/AchieveMagazine/Issue1-2010/article9.aspx

- Hair JR., J., F., William C., Barry J., Rolph E., 2010, *Multivariate Data Analysis: Overview of Multivariate Method*, seventh edition.

- Hutcheson, G., Sofroniou, N., 1999, *The Multivariate Social Scientist: Introductory Statistics Using Generalized Linear Models*, Thousand Oaks, CA: Sage Publications.

- Kaiser, H., F., 1974, *An Index of Factorial Simplicity*, Psychometrical, Vol. 39, PP. 31-36.

- Raffia, R., Rooshdi, M., R., 2013, *An Evaluation of Sustainable Design and Construction Criteria for Green Highway*, 4th International Conference on Sustainable Future for Human Security.

- Stephen, T. M., Jeralee, L. A., 2009, *Greenroads: A sustainability performance metric for roadway design and construction*, Transportation Northwest: University of Washington.

- WISE, 2011, *Greenroads Manual V1.5*, Washington: Washington Internship for Students Engineering.

Table 1. Respondent's designation and years of experience.

Position	**Experience**			
	Less than 7 years	7-14 years	15-21 years	More than 21 years
Manager	0	0	5	2
Consultant	0	0	4	3
Resident Engineer	0	14	10	2
	0.0%	35%	47.5%	17.5%

Table 2. Criteria and sub criteria for planning stage.

Planning Stage			
Criteria	Sub Criteria	Suggested Weights	Description
1. Costing plan	Costing plan	1 point	To analysis the cost during the life cycle of the project at the early stage of the plan
	Life cycle cost analysis	1 point	
2. Safety and Health	Risks management plan	1 point	To show the amount of reduction in risks during the project life
	Safety improvements	1 point	
	Workers safety audit	1 point	
3. Management and Planning	Environmental and social impact analysis	1- 3 points	To describe the management facilities that should provide in the planning concepts
	Quality control plan	1 point	
4. Siting-position selection		1 point	To describe the accuracy in alignment selection during the planning stage
4. Energy		1 point	To describe the amount of reduce in material energy emissions and try to encourages the efficient use of energy resources

Table 2. Continued .

Planning Stage			
Criteria	Sub Criteria	Suggested Weights	Description
6. Water		1 point	Improve stormwater quality from the impacts of the project and control the flow to minimize their erosive effects on receiving water bodies and related water resources
7. Waste management plan	Construction and demolition Waste management plan	1 point	Create an accounting and management plan for roadway construction and demolition waste materials

Table 3. Maximum respondent answers for planning stage.

Max. Percentage Respondents Answers		Planning Criteria
57.50%	1 point	Life cycle cost analysis
57.50%	1 point	Costing plan
52.50%	1 point	Risks management plan
55%	1 point	Safety improvements
50%	1 point	Workers safety audit
100%	3 points	Environmental and social impact analysis
57.50%	1 point	Quality control plan
100%	1 point	Sitting position selection
100%	1 point	Energy
100%	1 point	Water
60%	2 points	Construction and demolition waste management plan

Table 4. The factor loading for the sub criteria of planning stage.

Criteria	Categories		
	1	2	3
Safety improvements	.960	.069	—
Costing plan	.927	.140	—
Life cycle cost analysis	.890	-.116-	—
Quality control plan	.889	.005	—
Risks management plan	.886	.050	—
Workers safety audit	.752	-.159-	—
Construction and demolition waste management plan	-.021-	.990	—
Siting position selection	—	—	—
Energy	—	—	1
Water	—	—	1
Environmental and social impact analysis	—	—	1
			1

Table 5. The mean and the actual criteria weights for planning stage.

Criteria	Mean	Actual weighting = Factor loading * Mean
Safety improvements	1.4500	1
Costing plan	1.4250	1
Life cycle cost analysis	1.4250	1
Quality control plan	1.4250	1
Risks management plan	1.5250	1
Workers safety audit	1.5500	1
Construction and Demolition Waste Management Plan	1.6000	1
Siting position selection	1.0000	1
Energy	1.0000	1
Water	1.0000	1
Environmental and social impact analysis	3.0000	3

Table 6. Summary of evaluating planning stage verification results.

Verification Questions	**Yes**	**No**	**Yes with suggestion**	**Suggestions**
Are the four project requirements discussed for planning stage complementary for the roads projects in that stage?	86%	14%	__	
About the costing criteria, can it found otherwise planning stage for more benefits?	21%	13%	66%	According to sustainability aspects this criterion should found in construction and O&M
For safety and health criteria in planning stage, Are the sub criteria of it from the sustainability seen adequate or not?	67%	33%	__	
For the siting position selection criteria in planning stage, are the requirements of it comprehensive for the sustainability needs in that side or not?	75%	10%	15%	Agreed, but it should has sub division for more details and benefits
Are the requirements and strategies of the energy criterion in planning stage achieving the sustainability requirements or not?	80%	20%	__	
For water criterion in planning stage, is the best management practice strategies of this criterion adequate or not?	54%	16%	30%	Agreed and it prefer to link with the sustainable strategies
Is the planning stage criteria's conducted the important sides of sustainability that can found in this stage?	73%	13%	14%	Agreed, but the researcher could discuss the risks in planning stage.

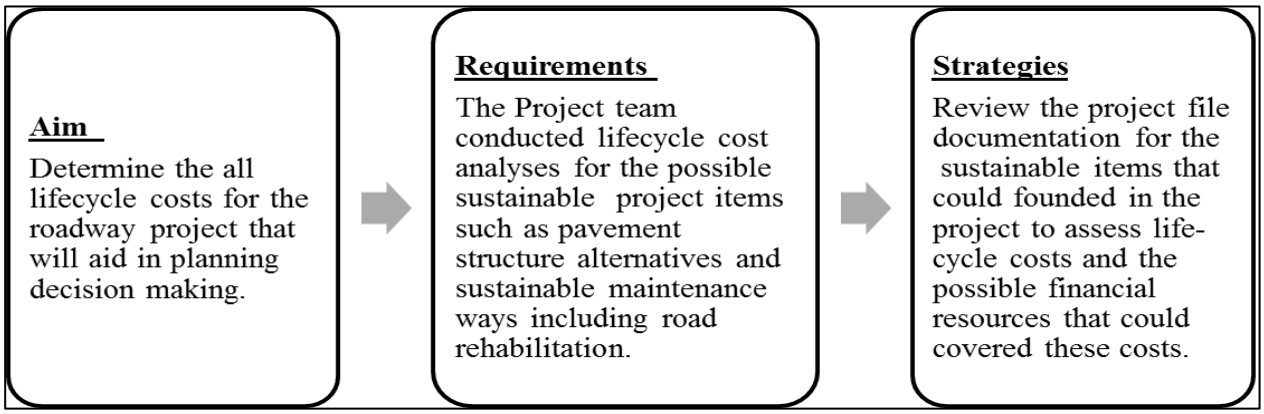

Figure 1. The details for life cycle cost analysis criterion in planning stage.

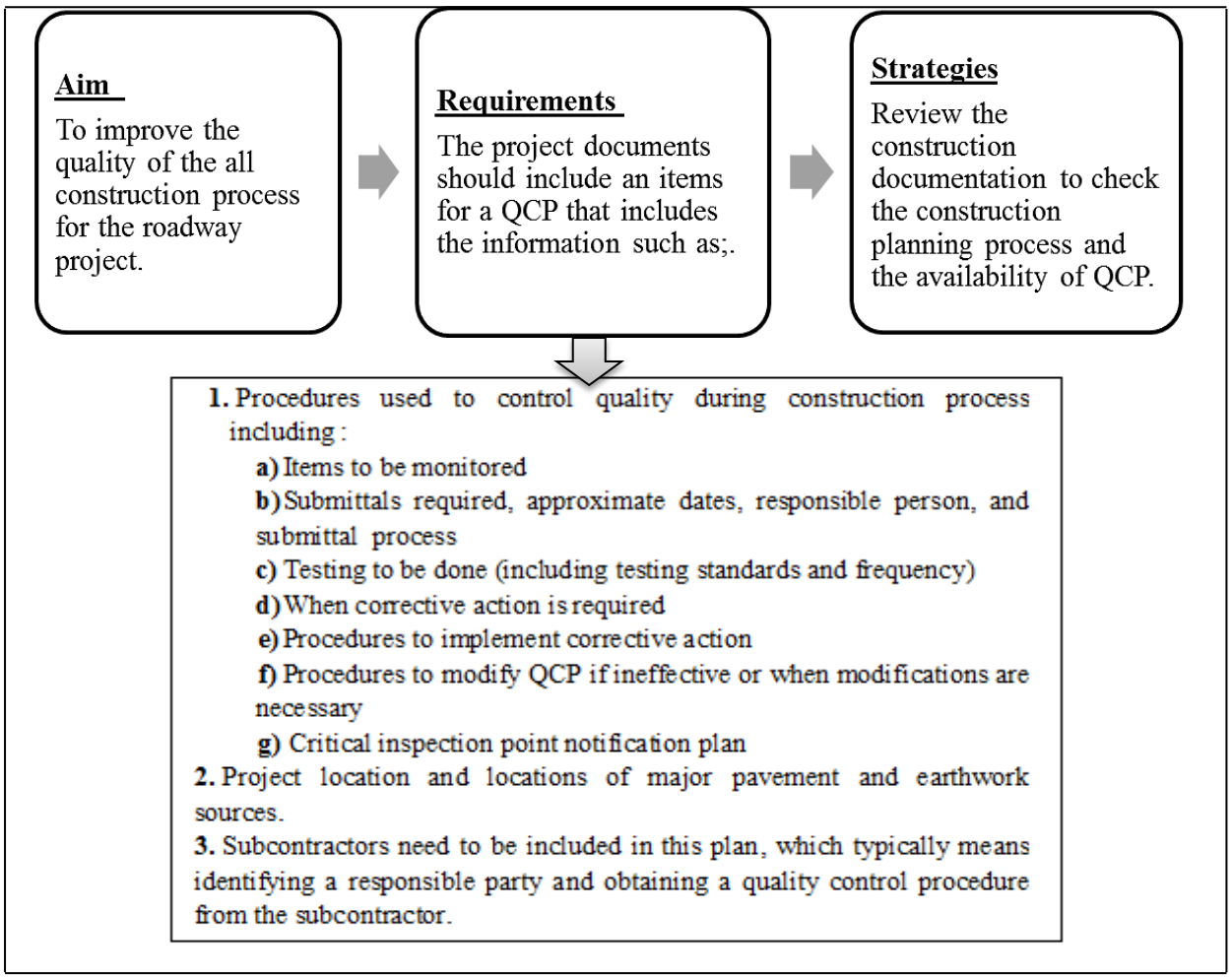

Figure 2. The details for quality control plan criterion in planning stage.

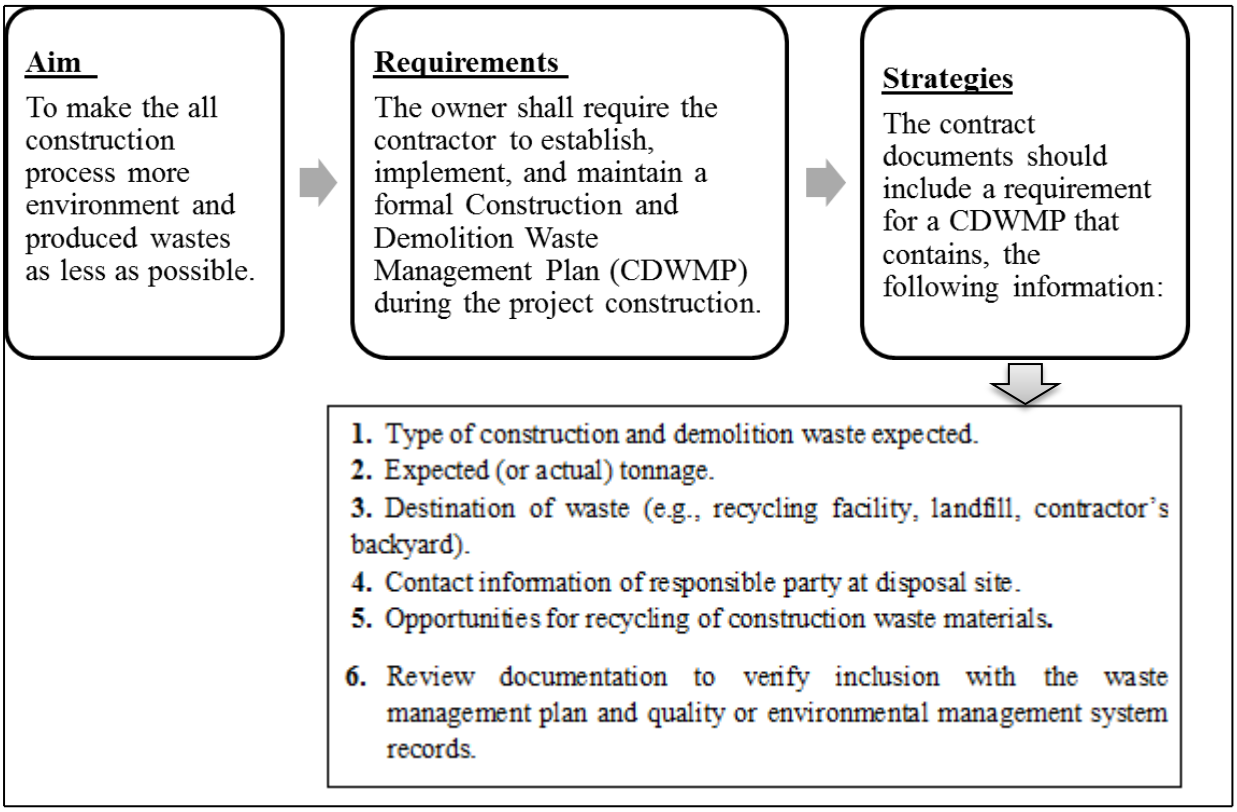

Figure 3. The details for construction and demolition waste management plan criterion in planning stage.

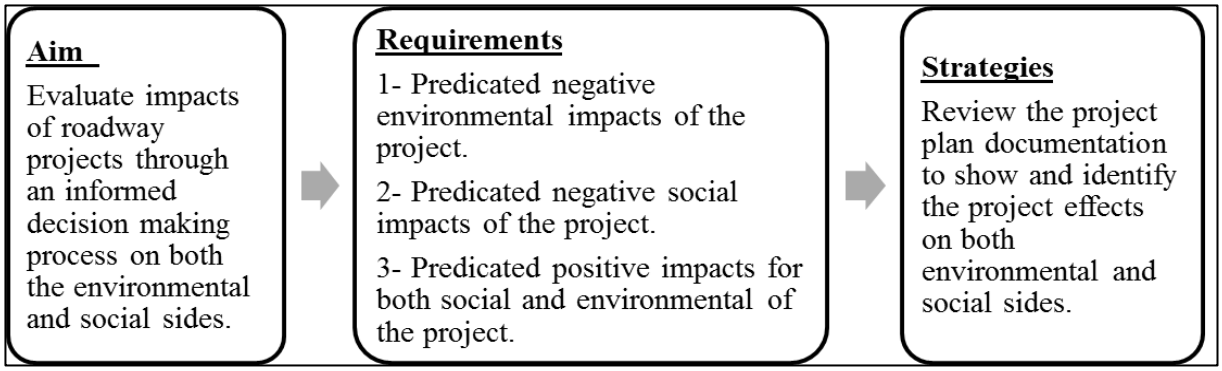

Figure 4. The details for environmental and social impact analysis criterion in planning stage.

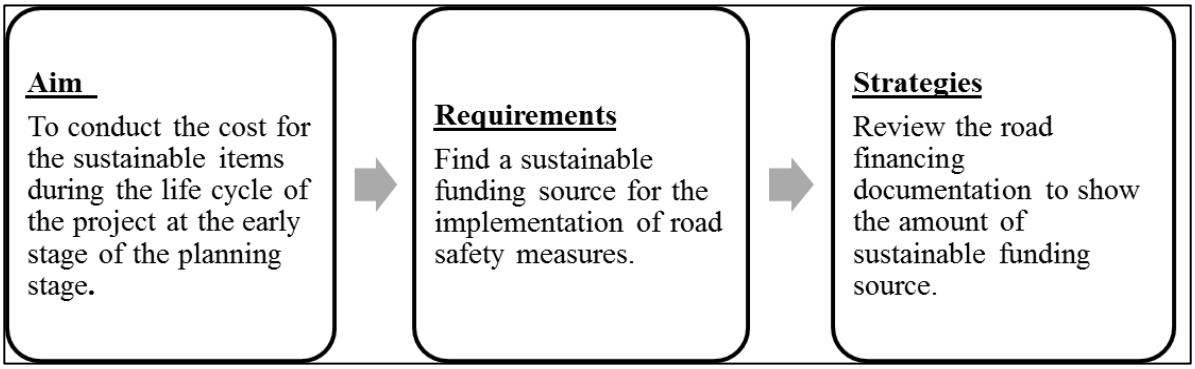

Figure 5. The details for costing plan criterion in planning stage.

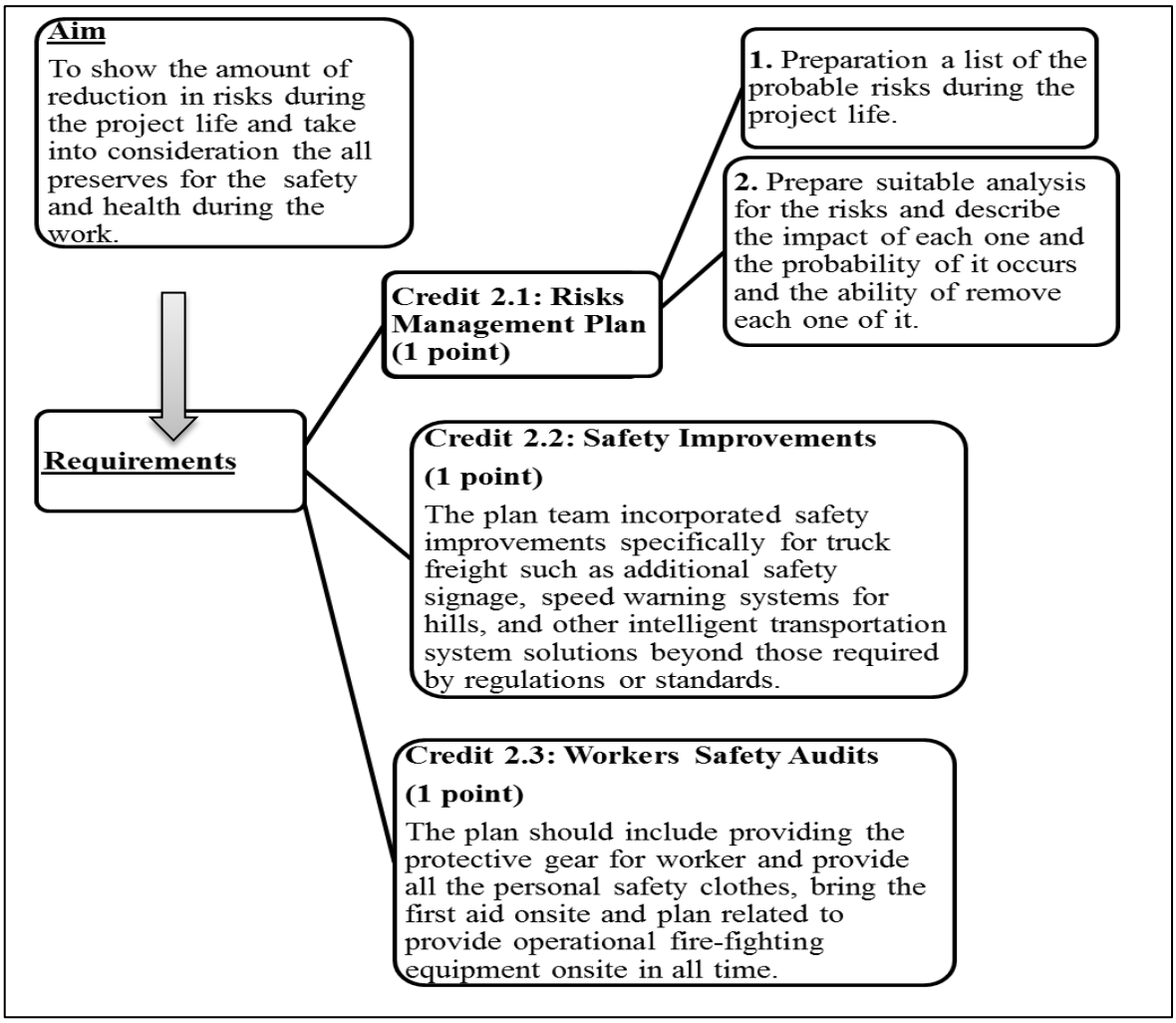

Figure 6. The details for safety and health criteria in planning stage.

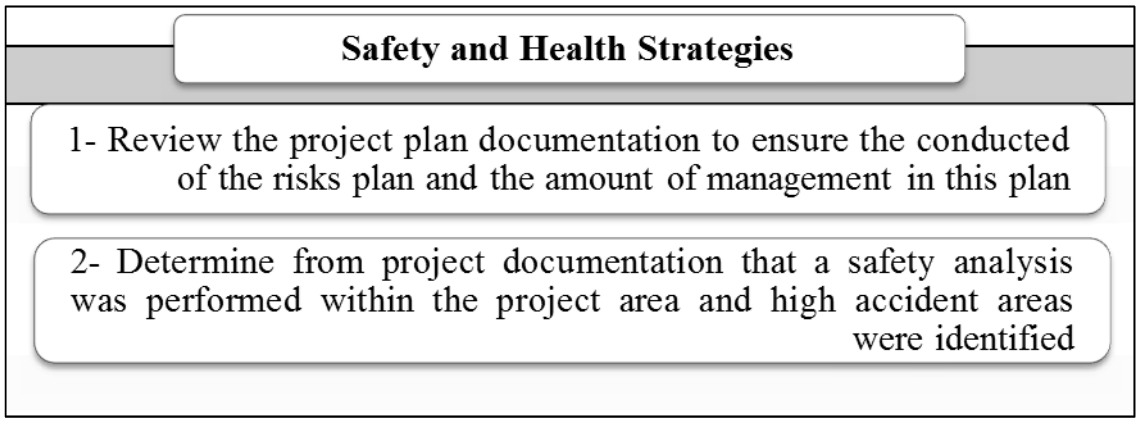

Figure 7. Strategies details for safety and health criteria in planning stage.

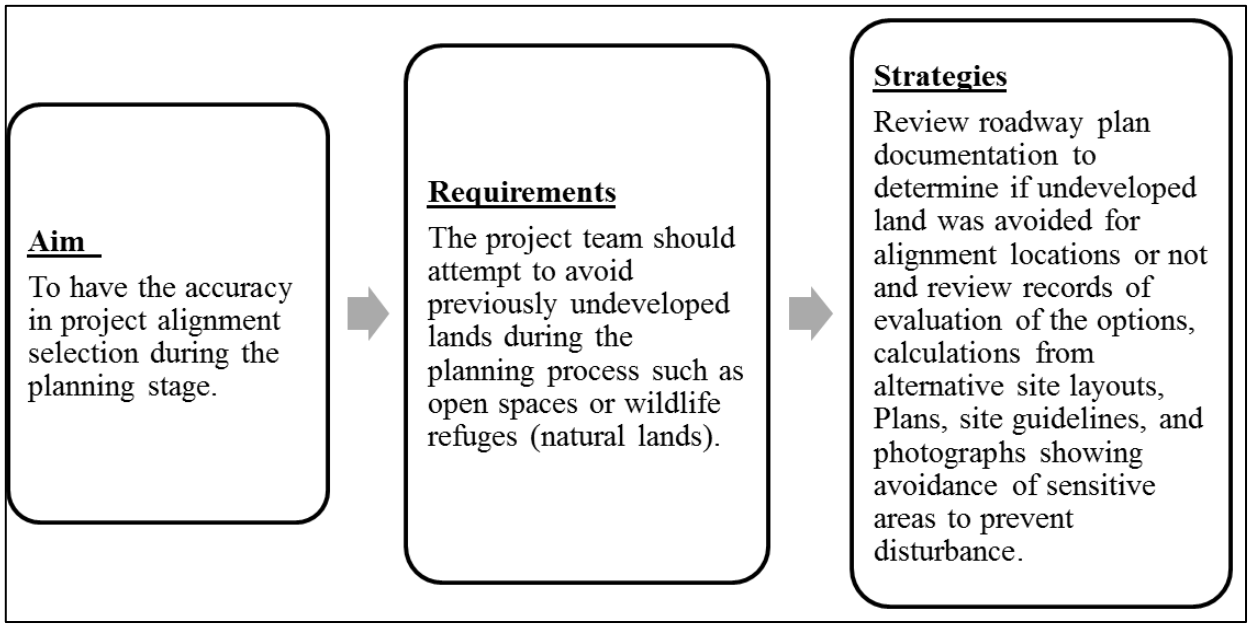

Figure 8. The details for siting position selection criterion in planning stage.

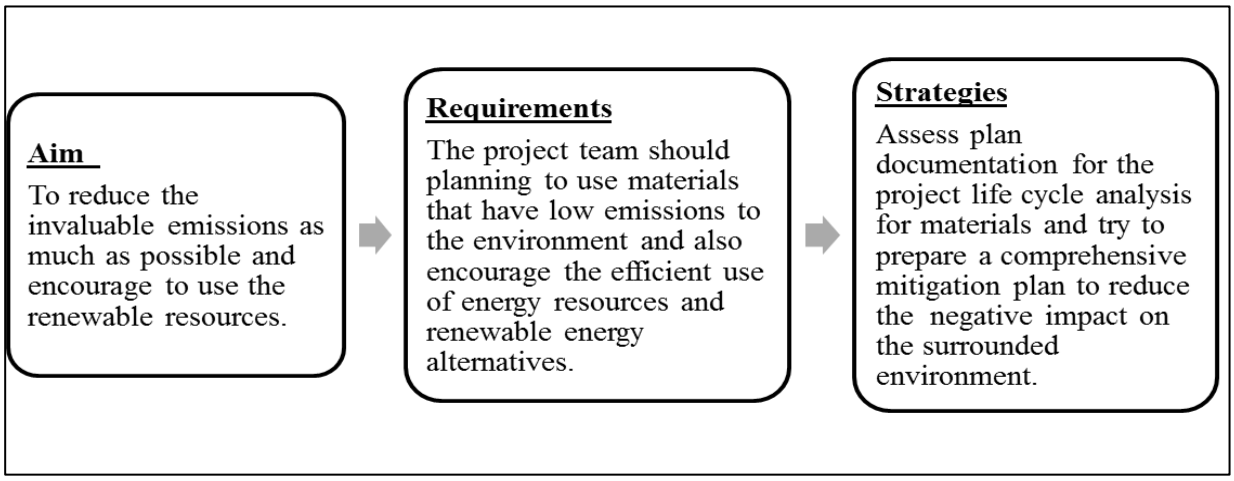

Figure 9. The details for energy criterion in planning stage.

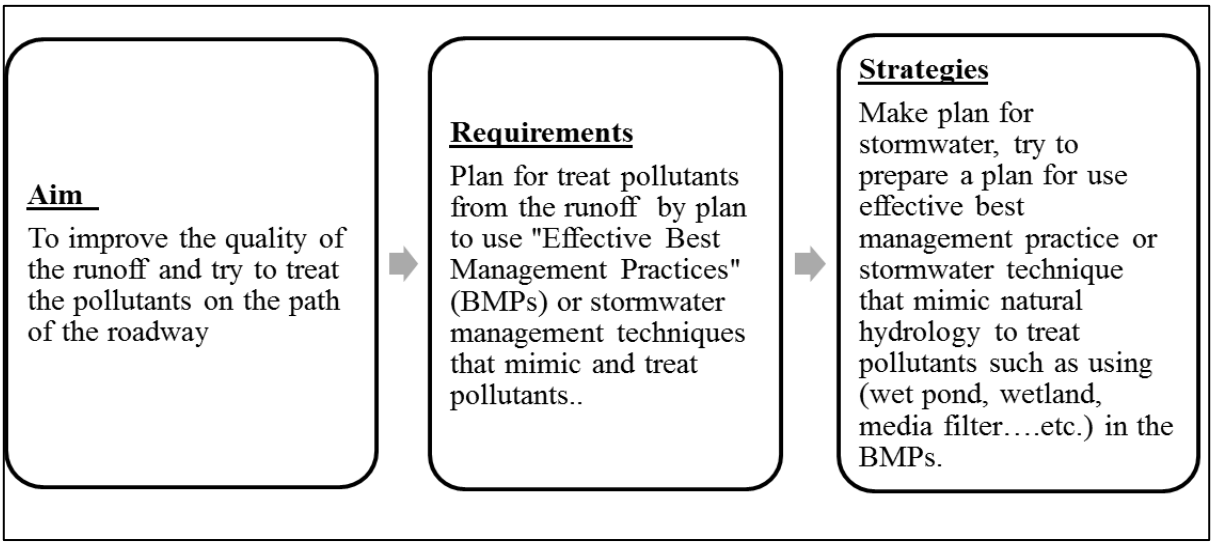

Figure 10. The details for water criterion in planning stage.

Implementation of a Proposed Load-Shedding System Using Altera DE2 FPGA

Bashar Adel Esttaifan
Assistant Lecturer
Electronics and Communications Dept.
University of Baghdad
Email: bashar_stephan@yahoo.com

Mohammed Kasim Al-Haddad
Assistant Professor
Electronics and Communication Dept.
University of Baghdad
Email: mkmih12@gmail.com

ABSTRACT

A load-shedding controller suitable for small to medium size loads is designed and implemented based on preprogrammed priorities and power consumption for individual loads. The main controller decides if a particular load can be switched ON or not according to the amount of available power generation, load consumption and loads priorities. When the maximum allowed power consumption is reached and the user want to deliver power to additional load, the controller will decide if this particular load should be denied receiving power if its priority is low. Otherwise, it can be granted to receive power if its priority is high and in this case lower priority loads are automatically switched OFF in order not to overload the power generation. The main idea of the proposed LS controller is to minimize the amount of the isolated load without overloading the power system. In this paper, three versions of load shedding controller were implemented using Altera DE2-115 FPGA; with number of loads equal 32, 64 and 128 for each controller.

Keywords: Power Systems, Load shedding, Overload, FPGA.

بناء منظومة مقترحة لعزل الاحمال باستعمال مصفوفة البوابات المنطقية القابلة لإعادة البرمجة

بشار عادل اسطيفان
مدرس مساعد
قسم الهندسة الالكترونية والاتصالات
جامعة بغداد

محمد قاسم محمد
أستاذ مساعد
قسم الهندسة الالكترونية والاتصالات
جامعة بغداد

الخلاصـــــة

في هذا البحث تم تصميم مسيطر لعزل الاحمال يتناسب مع احمال صغيرة الى متوسطة الحجم ويكون اساس العمل على أولويات ومقدار استهلاك قدرة مُبرمجة مسبقا ولكل حمل. المسيطر الرئيس يتحكم بتشغيل او اطفاء اي من الاحمال حسب ما متوفر من قدرة متولدة واستهلاك الحمل واولوية عمله. عند طلب المستفيد بتشغيل حمل اضافي وكانت القدرة المستهلكة عند الحد الاقصى المسموح بها عندها يقوم المسيطر باتخاذ قرار بمنع تجهيز القدرة الى الحمل إذا كان الحمل ذو اولوية واطئة او السماح بتجهيز القدرة لذلك الحمل إذا كان الحمل ذو اولوية عالية وفي هذه الحالة يقوم المسيطر بإطفاء الاحمال ذات الاولوية الواطئة لكيلا يحدث تحميل زائد على قدرة التوليد. الفكرة الرئيسة من منظومة عزل الاحمال المقترحة هي تقليل مقدار الحمل المعزول مع تجنب التحميل الزائد لمنظومة القدرة. خلال. في هذا البحث تم بناء ثلاثة نماذج لمنظومة عزل الاحمال باستعمال مصفوفة البوابات المنطقية القابلة للبرمجة من نوع DE2 من شركة Altera، لعدد احمال يساوي 23 و 64 و128 لكل مسيطر.

كلمات مفتاحية: أنظمة القدرة، عزل الاحمال، التحميل الزائد، مصفوفة البوابات المنطقية القابلة للبرمجة.

1. INTRODUCTION

Load shedding is a procedure to disconnect parts of the load from the power system when the load demand exceeds the amount the power generation can deliver. Such situation occurs due to different conditions such as hours of peak demand, disturbances causing tripping of lines connecting power plants to the main grid and disturbances causing load islanding. **Fig. 1** explains the situation of islanding, where, the load is isolated from the main generation and left connected with the cogeneration, which can be a small diesel generation, solar panels, inverters or any other small-scale power source. In any of these conditions, the power system will have poor conditions where the voltage and frequency will drop significantly below nominal values that can lead to a total shutdown. This happens when the frequency continues to decrease until it goes below the 47.5 Hz which is the under frequency limit value for the generation protection, **Rudez and Mihalic, 2011**. To avoid this undesirable condition, power utility authorities resort to load shedding where controlled isolation of loads is implemented. The optimum load shedding procedure should make a balance between two requirements; the first is to maintain the operation of the power system by shedding load in a timely manner, in this way the drop of frequency below the 47.5 Hz limit is avoided. The second is that sometimes-conservative load shedding can shed more loads than it is actually required and this may leads to unnecessary blackouts, which is also undesirable. Therefore, the optimum load shedding is when the amount of the isolated load is as low as possible while maintaining the continuity of the power system.

2. OVERVIEW OF LOAD SHEDDING SCHEMES

There are different load shedding schemes, all share the same purpose that is, when the power system is faced with the condition where input generation power is less than the output-consumed power. The following is a brief review of the basic schemes used in load shedding.

2.1 Breaker Interlock Scheme

This is the simplest method to implement load shedding where some of the load breakers are interlocked by hardwiring with the main source beaker. When the main source breaker is tripped for some reasons, the interlocked breakers are directly tripped without any time delay. The advantage of this scheme is that it is simple and fast since there is no processing required. The disadvantage is that, the choice, amount of the interlocked loads is fixed by the hardwiring, and it is not easy to change. Also, there is only one stage for load shedding which makes the designer work on the worst case scenario and in many situations this will shed more loads than it is actually necessary, **Shokooh, et al., 2011**.

2.2 Under Frequency Scheme

Under Frequency load-shedding (UFLS) is the most common scheme used in load shedding. Its idea is such that, in situations when the available generation is overloaded either because of losing a part of the generation due to a disturbance or because of high load demand at peak hours, the frequency starts to decay and the under frequency load shedding scheme detect the condition of power system overload by measuring the frequency or its derivative. The schemes that rely on frequency value as a criteria for load shedding work on a multistage tripping of loads with each stage having a frequency value and a time delay settings. **Table 1** shows an example of settings of a two stage under frequency load shedding, **Rudez and Mihalic, 2011**.

According to these settings when the frequency goes below 49.5Hz but still above 49.0Hz (due to loss of part of the generation), the UFLS waits for 0.5s time delay and then trips the 100MW load. If the frequency stabilizes above the 49.0Hz, no more load shedding is required, but if the frequency continues to drop below the 49.0Hz limit, the UFLS waits for the 2.0s before it trips the 300MW load. The time delay in the conventional UFLS can lead to power system collapse due to situations when fast frequency deterioration that the time delays in the UFLS cause the load shedding to be made when it is too late. **Rudez and Mihalic, 2011,** proposed an under frequency

load shedding that relies on the second derivative of the frequency as a source of information to estimate future values of frequency (frequency forecast), and when the calculated forecast frequency goes below the 47.5Hz value the system starts shedding loads according to the value of the forecasted frequency. Performance analysis showed that this method could maintain the operation of the power system by shedding loads less than the conventional under frequency load shedding.

2.3 Under Voltage Scheme

The under voltage load shedding (UVLS) scheme relies on voltage measurement as a criterion instead of frequency to monitor the condition of the power system, the main difference between the two schemes is that frequency value is the same throughout the entire power system grid, so, different nodes in the power grid measure the same frequency value. While for the voltage, the situation is not the same, different nodes measure different values of voltage due to drops across transmission lines. In general, nodes closer to generation units measure higher values of voltage and nodes far from generation measure lower values of voltage. **Otomega, et al, 2007**, proposed an UVLS system where distributed controllers are used around the power system. Each controller monitors the transmission voltage and controls a group of loads. The decision of one controller is made by measuring the voltage V at the controller's node and comparing to a certain threshold V_{th}, if V goes below V_{th}, an amount ΔP of load is shed after a time T. The values of ΔP and T are dynamically determined according to the measured value of V. In this system, the choice of the load to be shed is better determined because the nodes with the lowest voltage are expected to shed loads more than the nodes that have higher values of voltage. since the load is expecting the power utility to deliver the voltage at its nominal value, it will make more sense when the power system isolate the load that it can't provide the proper voltage level to it.

2.4 Power Based Load Shedding

The power-based load shedding (PLS) works on gathered information about the amount of available generation and consumed power and it reacts when there is a detection of deficiency between the actually generated and the consumed power. In order to optimize the performance of this scheme (PLS), it only requires that the information gathering technique to be optimal in terms of accuracy about how much is the generated and consumed power as well as the time delay required to deliver this information to the LS system. Therefore, such systems are only useful for small to medium scale power systems like isolated industrial plants, oil fields, mines, etc. **Giroletti, et al, 2012**, proposed a hybrid LS system were power based scheme is combined with frequency based LS.

2.5 Controller Based Load Shedding

In Controller based load shedding (CLS), either a programmable logic controller (PLC) or a microcontroller is used as a main controller of LS. This is to make the LS system configurable to a specific small-scale application. This scheme can be considered as a simplified version of the PLS scheme where the difference between the available power and the consumed power is monitored and the load shedding is scheme is performed according to the calculated power shortage. It has the advantage of being fast and optimal in terms of amount load shedding. The proposed LS scheme of this work falls under this category and further details will be provided in the next section.

2.6 Intelligent Load Shedding Scheme

Intelligent load shedding (ILS) is different from the previously mentioned schemes in its concept where system has the capability of predicting the behavior of the power system in terms of frequency and voltage values in cases of contingencies that cause loss of generation, increase of load demand or any change in the power system configuration. The capability of predicting the

behavior of the power system necessitate several requirements to be provided for the ILS system, **Shokooh, et al., 2011**,

- The power system configuration should be defined to the ILS system as a knowledge base.
- The ILS system should acquire information in the form of self-training and automatic learning to update the system knowledge base due to system changes.
- The ILS system should have sufficient (but still limited) number of data collecting points to map the complex power system to a proper model.
- Making fast and reliable decision on priority load shedding based on actual loading of status of each breaker.

Intelligent load shedding scheme is complex system where load-shedding tables are built according to previous knowledge of the power system status during contingencies and these tables are constantly updated through the real-time monitoring and simulation of the power system. As a result, when the ILS detects a power shortage and thus a need for load shedding, it will be equipped with the necessary knowledge to be correctly decide the optimal load to be shed in terms of amount and location with minimum time delay. Works that are based on ILS philosophy can be found in **Shi and Liu, 2014; Novikov and Karatayev, 2015 and Tamilselvan and Jayabarathi 2015**.

3. THE PROPOSED SCHEME

In this work, a controller-based load shedding (CLS) system is suggested, designed and implemented for small to medium scale load size like a large building, hospital, industrial plant… etc. The general idea is that the controller compares the total sum of the consumed power P_s with maximum allowable power consumption P_{max}. Before going into details, it is worth mentioning that powers measured and calculated can be either active power or apparent power, the apparent power which is simply $S=IV$ gives more indication about the load current I, this is important since the overload protections are based on current measurements. However, it should be noted that the apparent power S is a vector (complex value) quantity and in order to calculate the total apparent power as the sum of individual loads apparent powers, the power factor $\cos\phi$ of each load should be considered. An alternative way would be to use measurement to find the total load current I to calculate $S=IV$ but this requires additional hardware for current measurement like a current transformer (CT) which would increase the cost of the system. Alternatively the active power $P=IV\cos\phi$ which is the real part of S can be used and the active power of the individual loads can be added directly. However, this choice does not give a direct indication about the total current because power factor is required in the calculations. Another alternative is to deal with load currents that is equivalent to the choice of the apparent power S because the voltage can be considered constant for all loads and hence becomes just a scale factor between current and apparent power. If the apparent power or the current quantity is adopted an approximation calculation approach can be used to avoid the need of the power factor which is adding the magnitude of the individual loads apparent power or current. This will give total sum greater than the actual sum, due to the triangle inequality **Eq. (1)**.

$$|S_1| + |S_2| \geq |S_1 + S_2| \tag{1}$$

This is equivalent to assuming that all loads power factors are equal which is considered as a worst-case scenario and can be adopted when simplicity and cost reduction is required. It will be up to the designer to choose the appropriate scheme depending on the specific application and/or the customer requirement. In this work, quantities are summed as real numbers and referred to a load power that can be either active power or apparent power with the approximation of equal power factors.

Each load that should be controlled by the shedding rules is assigned two index values and these two values are stored in the main load-shedding controller as lookup tables. The first is the power index value which defines the amount of power the specific load consumes, the second is the priority index which defines how much the load is important and hence whether it should be isolated first (for low priority loads) or kept connected (for high priority loads) in case of power shortage. In this system, the user does not have direct control on the load; instead, the user can only give the command of switching ON or OFF to the LS controller. The LS controller continuously poles all the load ON/OFF switches as the system input and the controller will process this input and decides which of the individual ON inputs should pass to the output as ON value (logic 1), so that their respective loads are actually switched ON, and which load are switched OFF even if their respective input switches are actually ON. **Figure (3)** shows a typical block diagram for the system hardware. The inputs to LS controller can be classified to two types; software and hardware. The software type is the entries of the power index and priority lookup tables **PIT** and **PRT** that are entered to the controller as user defined input settings values. The hardware input is the $\mathbf{L_{IN}}$ vector that represents the load status according to the user request (which load is to be ON and which to be OFF).

There is one more important parameter of the system, which is the P_{max} value. This value is defined both by hardware and software. It is assumed that the source of power is not a single source, which is generally the case where multiple generations are synchronized and connected in parallel. Therefore, for each source of generation, the nominal generation power is defined in the vector **PG** to the LS controller as user input settings. These generation sources can be either a standalone generator or a transformer connected to the main grid. The status of each source is defined to the LS controller by the vector $\mathbf{G_{IN}}$ as hardware input, both vectors **PG** and $\mathbf{G_{IN}}$ have length of N_G, which is the number of generation sources. Therefore, when a generation source is connected to the system, the respective bit in the $\mathbf{G_{IN}}$ vector is set and when that generation source is lost, the respective bit is cleared. This bit can be connected directly to an auxiliary contact of the circuit breaker connecting the generation source to the system. According to the above, the value of P_{max} is given by Eq. (2).

$$P_{\max} = \sum_{n=1}^{N_G} \mathbf{G_{IN}}(n).\mathbf{PG}(n) \qquad (2)$$

The nth components of the power index table **PIT** are measure of the nth load power consumption. Since there is a wide range of values of the power for all loads the storage space for these values will unnecessarily be large, therefore, the power index **PIT**(n) defined as the integer value of the ratio of the nth load to the smallest load as given in Eq. (3)

$$\mathbf{PIT}(i) = \left\lceil \frac{\alpha P(n)}{\min\{P(n)\}} \right\rceil \quad n = 1,2...N_L \qquad (3)$$

Where ⌈ ⌉ equals the smallest integer greater than x and α is a factor depending on the maximum and minimum load powers to make the range of load power index suitable for the storage space allocated for each entry of the power index. For example if the maximum load power is 3kW (or kVA) and the smallest load power is 100W (or VA) and the memory allocation space for the power index is 8 bits then the maximum index would be 255 then α should be 255×100/3000=8.5. It is important to note that the minimum load power does not mean the absolute minimum power because there are loads with small powers, in domestic applications such loads can be chargers of battery-operated devices, economic lightings…etc. Such loads do not need to be under the control of load shedding. It is up to the user to determine the minimum load power that should be under the

control of the load-shedding controller because obviously the complexity of the system depends on the number of loads that the LS controller can handle.

The priority table **PRT** defines the importance of the load, upon which the LS controller will decide if the load should be isolated or not in case the power demand exceeds the available power. For a given load, the value of **PRT**(n) is not related to the respective power index value **PIT**(n) it is only related to the type of load, for example a refrigerating load may be considered a higher priority load than a water heating load although the water heating load has a higher power index than the refrigerating load. The priority values can be either all distinct or there can be multiple loads of equal priority according to the user choice.

The typical algorithm used for the load shedding is explained by the flowchart shown in Fig. (4). Assuming the number of loads equals to N_L, the inputs are read as a vector of logic values $\mathbf{L_{IN}}$. The input vector is passed to another vector of equal size that is called the status vector **ST**. After that, the controller starts to calculate the sum of the power indices of the loads that have logic 1 in the status vector **ST**.

$$P_s = \sum_{n=1}^{N_L} \mathbf{PIT}(n).\mathbf{ST}(n) \qquad (4)$$

The power index sum P_s will be compared to the maximum allowable power consumption P_{max} which is a value provided by the power system authority above which the power generation cannot supply and if the sum of power indices is less than the maximum available power ($P_s \leq P_{max}$), the status vector will be passed to the output vector $\mathbf{L_{out}}$ and all loads that the user required to switch on will be switched on by the LS controller. If the power consumption is more than this value ($P_s > P_{max}$), the load shedding is activated and the LS controller starts resetting the entry in the status vector **ST**(x) that correspond to the lowest priority loads and the value of P_s is updated according to eq. (2) and the process is repeated until ($P_s \leq P_{max}$). Mathematically, this can be describes be the equation

$$P_s = \sum_{\mathbf{PRT}(n) \leq K} \mathbf{PIT}(n).\mathbf{ST}(n) < P_{\max} \qquad (5)$$

Where K is the minimum priority allowed by the load condition such that

$$P_s = \sum_{\mathbf{PRT}(n) \leq K+1} \mathbf{PIT}(n).\mathbf{ST}(n) > P_{max} \qquad (6)$$

This is a typical algorithm whose flowchart is shown in a simplified form in Fig. (4). The algorithm although works just fine and is adopted in many LS applications but it is not adopted in this work, the reason is that it has a disadvantage where in some situations the amount of load shedding is not optimal!

Consider the situation where a load with high value of power index and a low priority and that the LS situation required switching OFF that particular load due to its low priority, this can leave a gap between P_s and P_{max} i.e. P_{max}-P_s is not minimized, because high power index load has been eliminated in order to keep $P_s < P_{max}$. While on the other hand there can be loads of lower priority and lower power indexes that can be switched ON while maintaining the condition $P_s < P_{max}$ which is the ultimate objective of the LS system. The cause of the pitfall of this algorithm is that the **ST** vector is initialized with the $\mathbf{L_{IN}}$ vector and the priority processing is carried out in down-up direction. An alternative approach would be to initialize the **ST** vector with all zeros vector and starting filling the **ST** vector according to the $\mathbf{L_{IN}}$ vector with the priority processing in the up-down direction. This approach is adopted in this work and its flowchart is shown in Fig. (5).

This flowchart shows two nested loops the outer loop is the priority index (p) loop and the inner loop is the load number (n) loop. The idea of this flowchart is that the controller starts processing

the highest priority loads first giving them the advantage of being switched ON before the low priority loads. In each iteration of the outer priority loop, i.e., for a particular value of p, the priority table is checked for the loads that have this particular value of priority. This is achieved by running the inner loop for all values of n to check the condition PRT(n)=p. The design allows multiple loads to have equal priorities or the user can have all loads with different priorities. When the condition PRT(n)=p is satisfied, the status vector **ST** is updated according to the flowchart shown in Fig. (6), where the input vector $\mathbf{L_{IN}}$ is checked if the user has requested the nth load to be switched ON which is given by the condition $\mathbf{L_{IN}}$(n)=1. If not then nothing is done and the value of n is incremented, if so, then the controller checks if the respective load power is less than the difference of the maximum allowable power P_{max} and the updated value of the power sum P_s, which is given by the condition PIT(n)<P_{max}-P_s. If this condition is satisfied then the LS controller grants permission to the respective load to be switched ON by setting its respective bit in the power status vector **ST** to 1, i.e., **ST**(n)=1 and the power sum is updated by P_s=P_s+PIT(n).
A mathematical description of this algorithm is described by the equation

$$P_{max} - \sum_{n} \mathbf{ST}(n).\mathbf{PIT}(n) < \min_{\mathbf{ST}(n)=1} \{\mathbf{PIT}(n)\} \qquad (7)$$

Where summation is run over the values of n such that all values of **PIT** are considered starting from 1 (highest priority) to N_L (lowest priority) excluding the values of n that violates the condition of eq. (5) and the values of n where **ST**(n)=0. This algorithm guarantees that P_{max}-P_s is minimized.

4. SYSTEM IMPLEMENTATION

The proposed system of LS was implemented on FPGA platform. The Altera DE2-115 board shown in Fig. (7), was used to implement the proposed system. The board hosts, the Altera Cyclone IV 4CE115 FPGA device, which contains 114,480 logic elements (LE's). The main components of the implemented LS system are shown in block diagram of Fig. (8), Fig. (9) shows the result of project compilation.

The top-level entity of the implemented project is a schematic file type (as shown in Fig. (10)), but all other entities are (.hdl) file type. The written VHDL code compiled and transferred to create a symbol. The created symbols can be put on the top-level entity and route easily.
The input ports of the top-level entity are the user load input vector, $\mathbf{L_{IN}}$, the generator input vector, $\mathbf{G_{IN}}$, system clock, ***clk***, as well as the push buttons and slide switches for the user editing.
The output ports of the top-level entity are the loads output $\mathbf{L_{OUT}}$, the generator output vector, $\mathbf{G_{OUT}}$, and the data and control signals to derive LCD.
There are two main processes in the top-level entity; the first process is editing the power index and priority tables that saved in memory. This part also includes accessing the LCD embedded inside the DE2-115 board where the user's entered values are displayed before storing in the memory block that represents the look up tables of power index and priority. The second part of the code is the LS controller described earlier.
The LS controller is designed to control 32, 64 or 128 loads (i.e. N_L=32, 64 or 128), and it has been show earlier that the LS controller body is in the form of two nested loops of size N_L. Therefore, the total delay for a complete loop will be proportional to N_L^2. The total time that the LS controller needs to pole the users' inputs, makes decision and updates the outputs is about 0.1 second, which is small enough that the user cannot notice. Therefore, the clock frequency of the **clk** signal must be chosen to be 10.24 kHz or more to maintain 0.1-second criteria for a system that shed 32 load according to eq.(8). If the controller is designed to control more loads, the clock frequency should be increased in order maintain the acceptable time delay given by eq. (8).

$$f_{clk} = \frac{N_L^{\ 2}}{\tau} \qquad (8)$$

Where f_{clk} is the controller clock frequency, τ is the acceptable controller time delay and N_L is the number of loads. **Table 2** summarize the required clock frequency to achieve 0.1-second criteria with different number of loads. So, the clock frequency would be about 655.36 kHz for 256 loads system which is considered moderate in today's technologies so there will be no major concerns regarding power consumption, heat dissipation, etc.

5. SYSTEM TESTING AND RESULTS VERIFICATION

A priority based load-shedding controller is implemented to deals with small to medium power systems applications. In the implemented design, the amount of load to be shed is minimal unlike the traditional controllers based load shedding systems. The system was implemented and tested on FPGA platform and timing analysis showed that the system delay time is quite manageable.
To verify the implemented system, different case studies are presented as follow:

- The controller will shed 32 loads.
- The power delivered from FIVE different generators each with 200 KVA. (Totally 1000 KVA)
- The priorities and power consumption of each load are initially assumed as in **Table 2**.

The controller will calculate total required current due to the switched ON loads. If the total required power is less than maximum available power then there is no need to enter load-shedding algorithm. If not, the load shedding algorithm start to check the status of loads depending their priority level.
The controller will shutting down or starting generators depending on the required power. Therefore, if the total required current less than 800 KVA, then one of the five generators will shut down, and so on.

Input switches panel are used as a user load input vector (L_{IN}) (Device 1 to device 32) will connected to DE2-115. To verify the output of the controller (32 loads output L_{OUT}) we need 32 LED, and if the load is switched ON by LS controller then the corresponding LED will shine.
Table 3 lists four different cases to test the LS controller, for simplicity, the devices rearranged according their priorities from higher to weaker priority.

In the first case, the sum of the required power (calculated by controller) are less than the maximum available power (i.e. 970 KVA < 1000 KVA delivered by 5 generators), so no load shedding needed.

In case 2, the required power (1070 KVA) is higher than the maximum available power (1000 KVA), so, the controller starts LS algorithm, the controller take a decision to turn Device (28) OFF, which has weaker priority between the turned ON devices. The consumed power after LS algorithm be 950 KVA.

The main advantage of the proposed LS controller is founded in case 2. The user need to switch devices (18 and 20) ON which has the lowest priorities between the turned ON devices (lower than D28 priority). As mentioned in the previous case, Device (28) and any other devices with lower priorities will turned OFF, so the rest power (not used) will be 50 KVA. The extra power required to derive D18 and D20 is 25 KVA so the controller will support them with power and the rest power (not used) will be 25 KVA and the total consumed power be 975 KVA.
The last case (i.e. case 5), the user need to switch device (26) ON as well as the other needed loads. The controller will shut down D28, D20 and D18, and the total required power will be 990 KVA, but the rest power (10 KVA) is enough to derive D18 only (which need 6 KVA) and the rest power become just (4 KVA) and total power consumed will be 996 KVA.

6. CONCLUSION

A priority based load-shedding controller is implemented suitable for small to medium power systems applications. In the suggested approach- as shown in **Table 3**- the amount of load to be shed is minimal unlike the traditional controller based load-shedding systems. The main difference is that the proposed LS system allow power to be delivered to a lower priority loads under the condition that the total power delivered is less than the maximum available power. The system was implemented and tested on FPGA platform. The hardware implementation produced small time-delay that is quite suitable for LS application.

7. REFERENCES

- *Altera DE2-115 User Manual*. 2010, Altera Company.
- Benyun Shi and Jiming Liu, 2015, Decentralized control and fair load-shedding compensations to prevent cascading failures in a smart grid, Elsevier Electrical Power and Energy Systems research 67-582–590.
- Faranda, R., Pievatolo, A., and Tironi, E., 2007, *Load Shedding: A New Proposal*, IEEE Transactions on Power Systems, Volume. 22, Number 4, pp 2086-2093.
- Girgisa, A., and Mathure, S., 2010, *Application of Active Power Sensitivity to Frequency and Voltage Variations on Load Shedding*, Elsevier Electric Power Systems Research, Volume 80, Issue 3, pp 306-310.
- Giroletti, Farina and Scattolini, 2012, *A Hybrid Frequency/Power Based Method for Industrial Load Shedding*, Elsevier Electrical Power and Energy Systems, Volume 35, Issue 1, pp 194–200.
- Hsu, C., Chuang, H., and Chen, C., 2011, *Adaptive Load Shedding for an Industrial Petroleum Cogeneration System*, Elsevier, Expert Systems with Applications, Vol. No. 11, pp 13967–13974.
- Moors, LeCebvre and Van Cutsem, 2000, *Design of Load Shedding Schemes Against Voltage Instability*, IEEE Conference of Power Engineering Society, Singapore.
- Mozina, C., 2007, *Undervoltage Load Shedding*, IEEE Power Systems Conference, Advanced Metering, Protection, Control, Communication, and Distributed Resources, USA.
- Navabi, Z., 2007, ***VHDL Modular Design and Synthesis of Cores and Systems***, McGraw Hill.
- Rudez, U., and Mihalic, R, 2011, *A Novel Approach to Under-frequency Load Shedding*, Elsevier Electric Power Systems Research, Volume 81, Issue 2, pp 636-643.
- Otomega, B., Glavic, M., and Cutsem, T., 2007, *Distributed Under-voltage Load Shedding*, IEEE Transactions on Power Systems, Volume. 22, Number. 4.

- Shokooh, F., Dai, Shokooh, S., Tastet, J., Castro, H., Khandelwal, T., and Donner, G., 2011, *An Intelligent Load Shedding (ILS) System Application in a Large Industrial Facility*, IEEE Industry Applications Magazine, Volume 17, Issue 2, pp 4-53.

- Tamilselvan, V and Jayabarathi, 2016, T, *A hybrid method for optimal load shedding and improving voltage stability*, Ain Shams Engineering Journal–Elsevier, 7- 223–232.

- Voropai , Efimov and et al, 2015, *Distributed Adaptive Load Shedding Scheme to Maintain Transient Stability and Prevent Overload*, IFAC –Elsevier, OnLine 48-30 (2015) 554–559.

- Xu Fu and Wang, X., 2011, *Determination of Load Shedding to Provide Voltage Stability*, Elsevier International Journal of Electrical Power & Energy Systems, Volume 33, Issue 3, pp 515-521.

- Zhant, and et al, 1999, *An Adaptive Microcomputer Based Load Shedding Relay*, IEEE Conference of Industry Applications, USA.

Figure 1. The situation when part of the load is islanded.

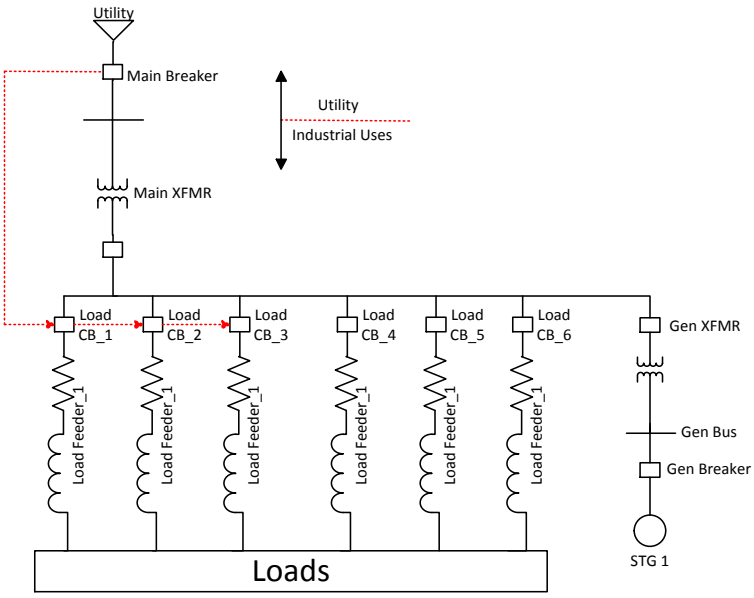

Figure 2. Breaker interlock scheme.

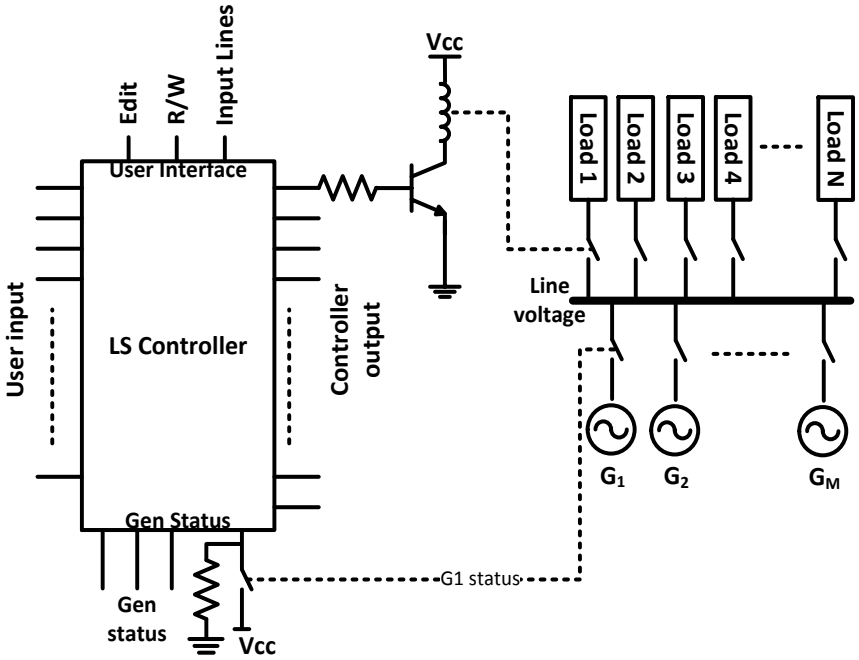

Figure 3. Block diagram of the proposed LS system.

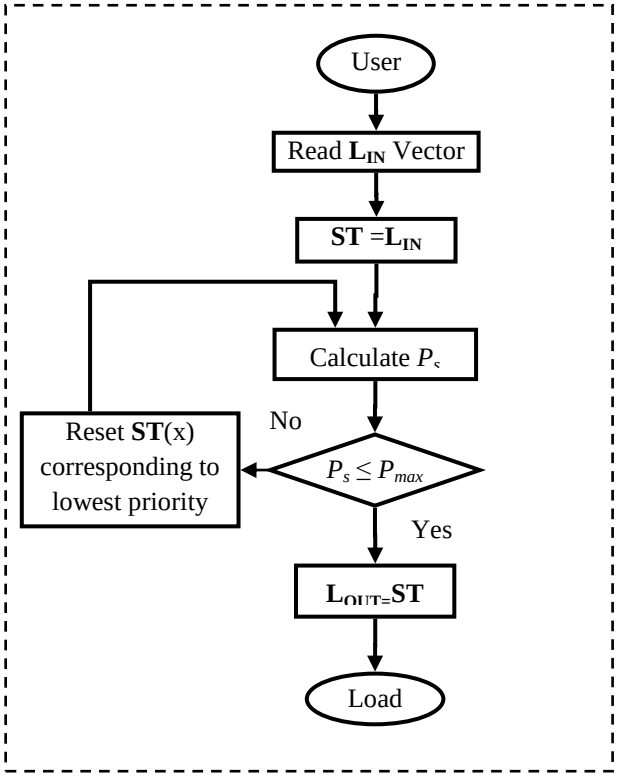

Figure 4. Flow diagram of a typical priority based LS.

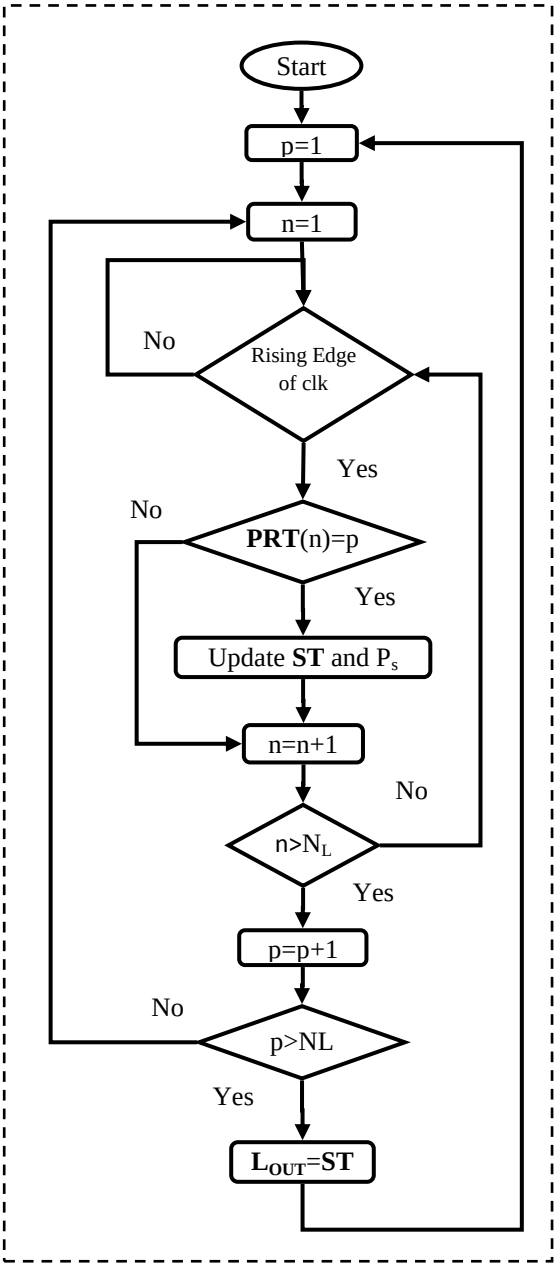

Figure 5. A flowchart of the implemented LS algorithm.

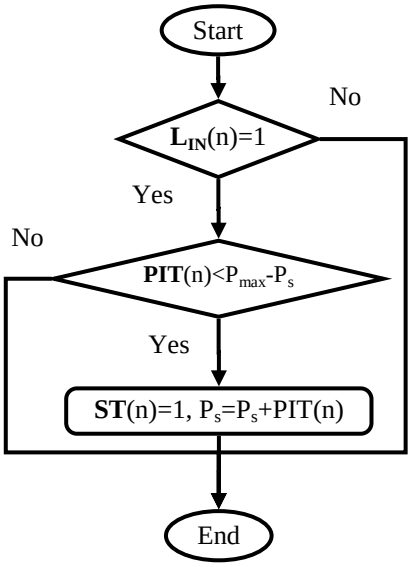

Figure 6. Details of updating ST and P_s.

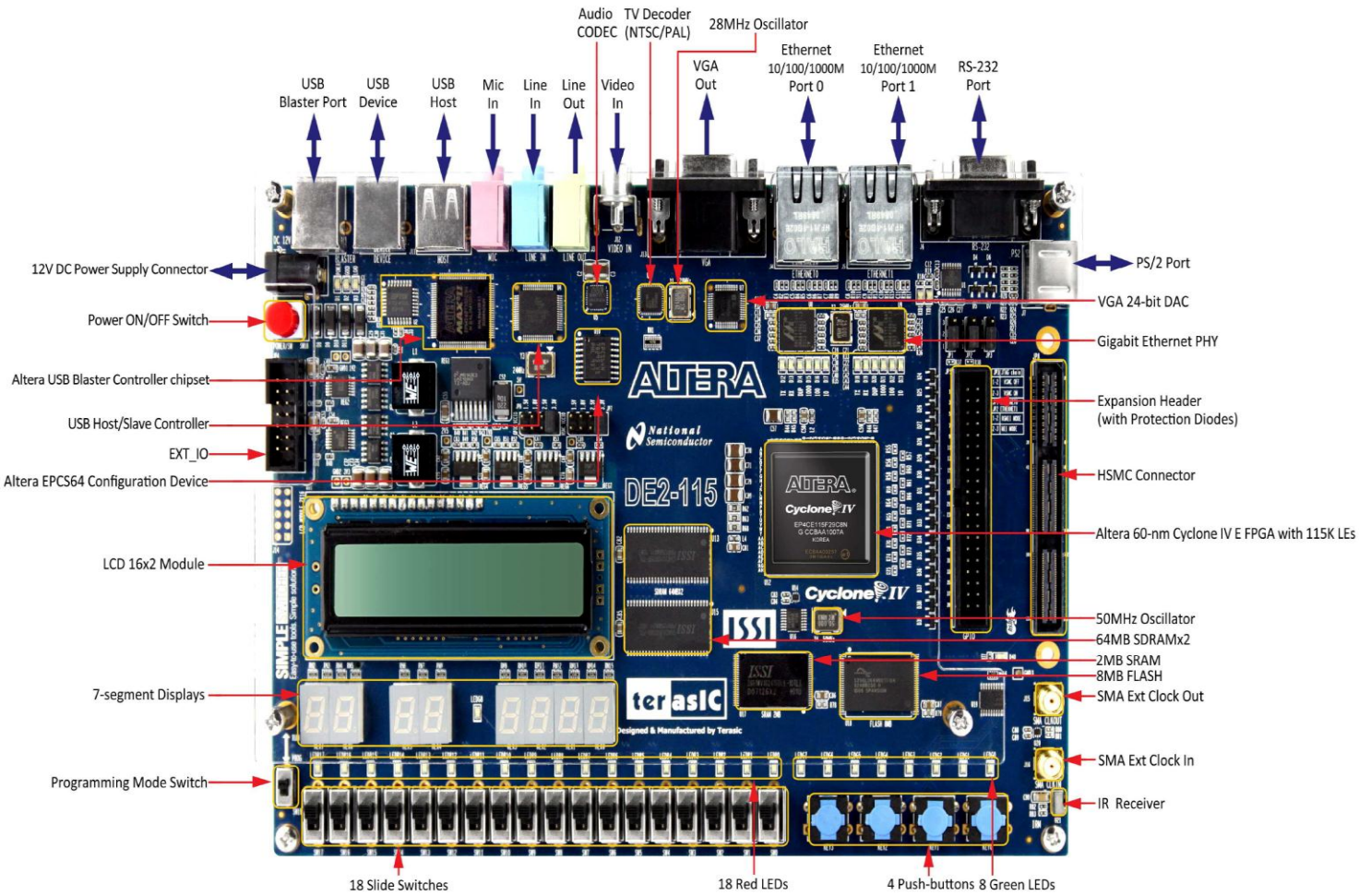

Figure 7. Altera DE2-115 FPGA (Top view).

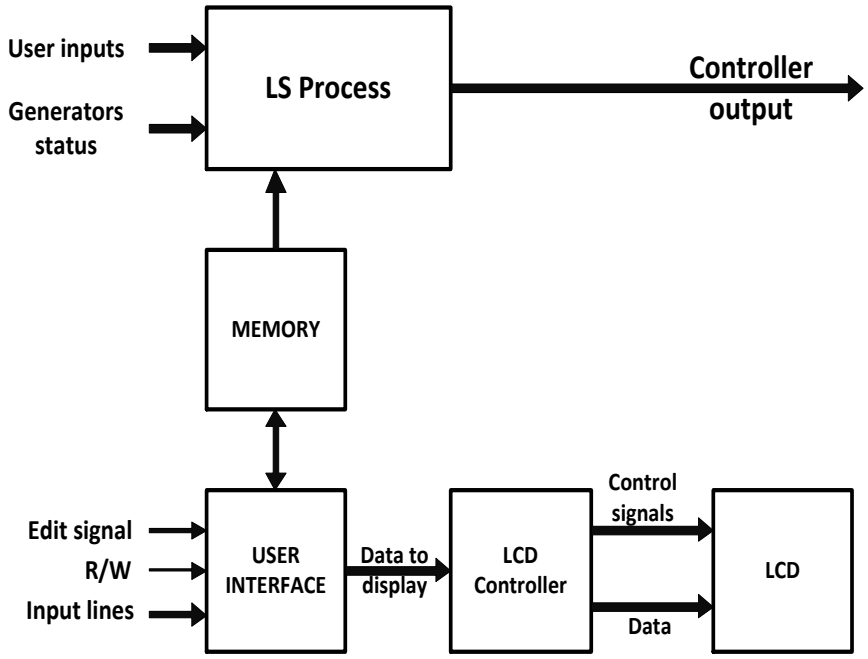

Figure 8. Block diagram showing the internal logic of the implemented LS system.

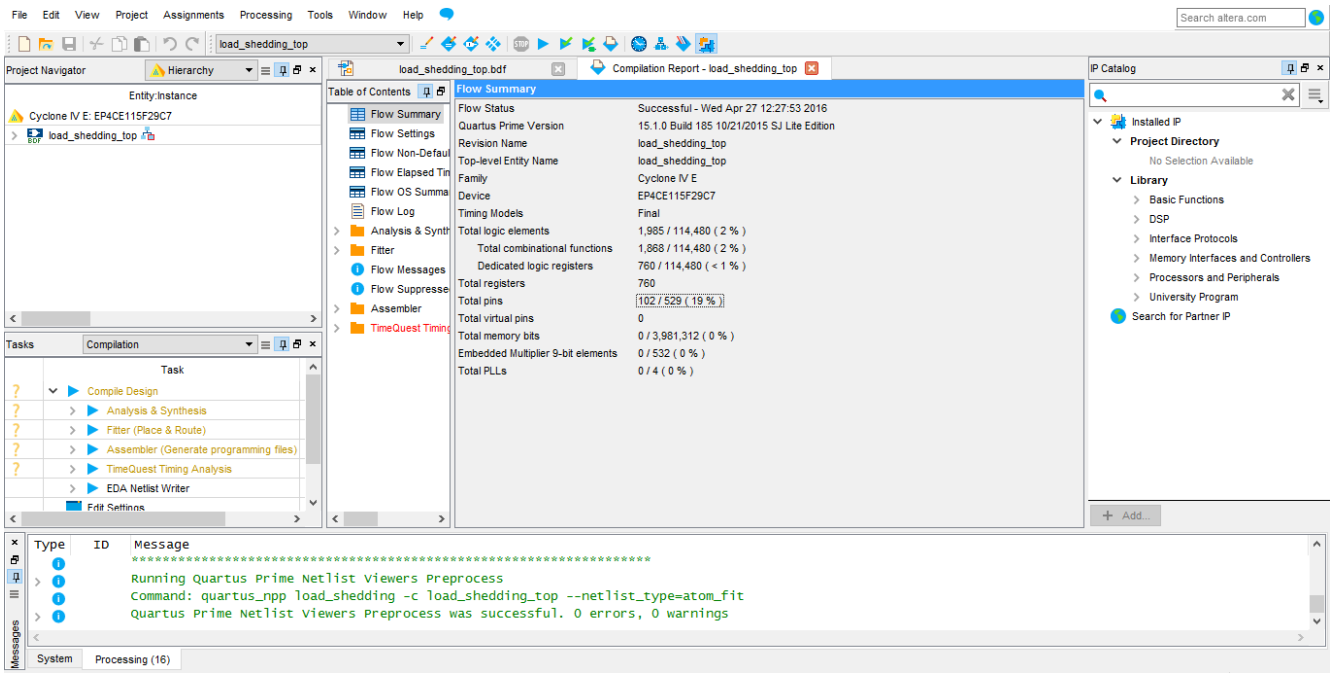

Figure 9. The result of project compilation.

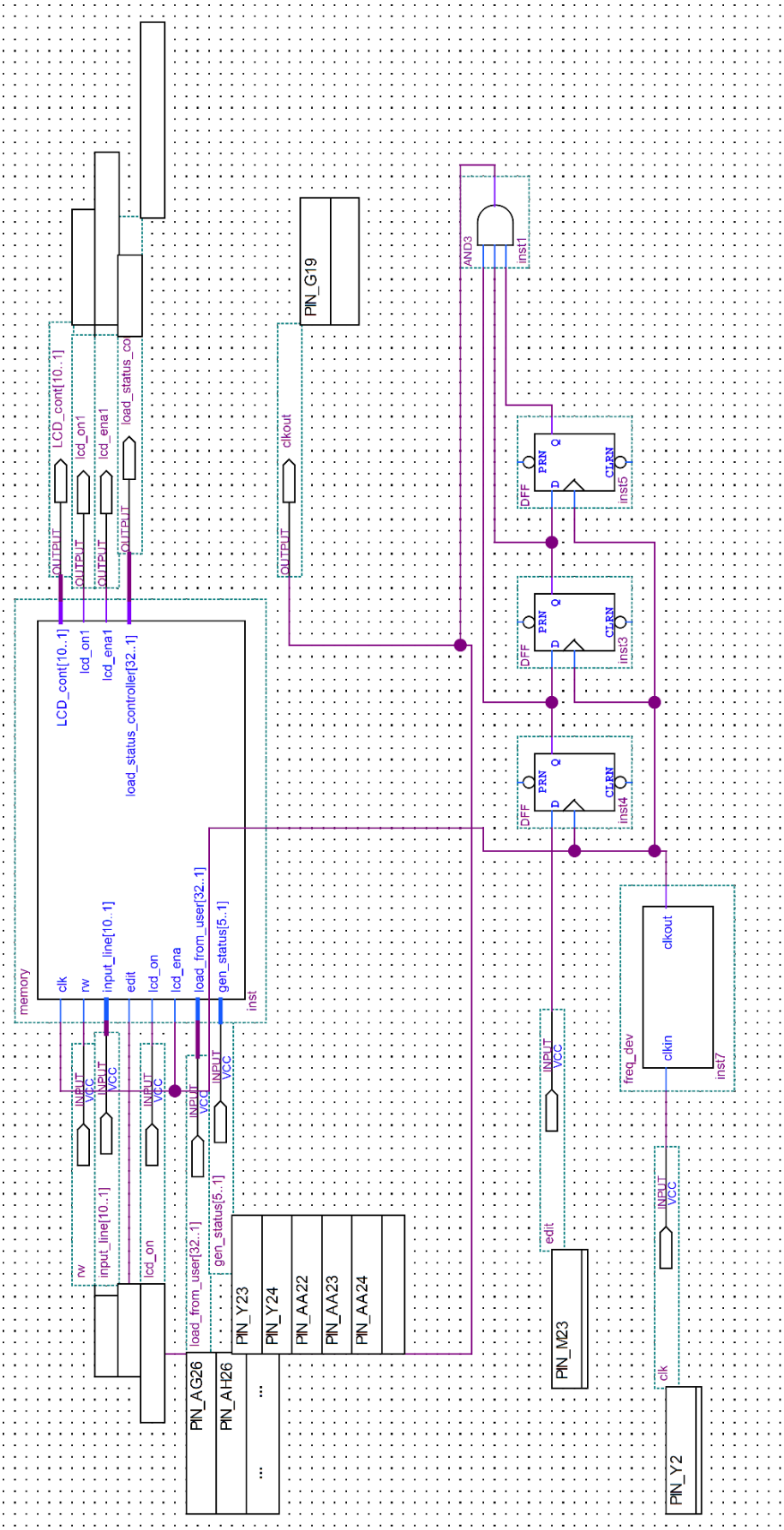

Figure 10. Schematic diagram of the implemented controller using Quartus.

Table 1. Example of Under Frequency Load Shedding (UFLS) Settings

Stage	Frequency	Time Delay	Load Shed
1	49.5 Hz	0.5 s	100 MW
2	49.0 Hz	2.0 s	300 MW

Table 2. Clock frequency of the implemented system with respect to number of loads

No. of loads	Frequency	Time Delay
32	10.24 KHz	0.1 s
64	40.96 KHz	0.1 s
128	163.84 KHz	0.1 s
256	655.36 KHz	0.1 s

Table 3. Priorities and power consumption of each load (arranged according device index)

Device name	Device Index	Devise Priority	Consumed Power
D1	1	25	10
D2	2	17	10
D3	3	26	70
D4	4	8	200
D5	5	24	50
D6	6	18	15
D7	7	23	65
D8	8	2	350
D9	9	19	20
D10	10	1	100
D11	11	12	15
D12	12	22	40
D13	13	6	5
D14	14	16	500
D15	15	7	25
D16	16	27	5
D17	17	13	100
D18	18	32	6
D19	19	9	35
D20	20	31	20
D21	21	15	90
D22	22	14	55
D23	23	30	10
D24	24	4	180
D25	25	20	70
D26	26	11	20
D27	27	3	40
D28	28	29	120
D29	29	10	110

D30	30	21	20
D31	31	28	90
D32	32	5	10

Table 4. Several cases to verify features of implemented LS controller (Rearranged according device priority).

Device name	Device Index	Devise Priority	Consumed Power	Case 1			Case 2			Case 3			Case 4		
				L_{IN}	L_{OUT}	conv	L_{IN}	L_{OUT}	conv	L_{IN}	L_{OUT}	conv	L_{IN}	L_{OUT}	conv
D10	10	1	100	0	0	0	1	100	100	1	100	100	1	100	100
D8	8	2	350	0	0	0	0	0	0	0	0	0	0	0	0
D27	27	3	40	0	0	0	0	0	0	0	0	0	0	0	0
D24	24	4	180	0	0	0	0	0	0	0	0	0	0	0	0
D32	32	5	10	0	0	0	0	0	0	0	0	0	0	0	0
D13	13	6	5	0	0	0	0	0	0	0	0	0	0	0	0
D15	15	7	25	0	0	0	0	0	0	0	0	0	0	0	0
D4	4	8	200	1	200	200	1	200	200	1	200	200	1	200	200
D19	19	9	35	0	0	0	0	0	0	0	0	0	0	0	0
D29	29	10	110	0	0	0	0	0	0	0	0	0	0	0	0
D26	26	11	20	0	0	0	0	0	0	0	0	0	1	20	20
D11	11	12	15	0	0	0	0	0	0	0	0	0	0	0	0
D17	17	13	100	1	100	100	1	100	100	1	100	100	1	100	100
D22	22	14	55	0	0	0	0	0	0	0	0	0	0	0	0
D21	21	15	90	0	0	0	0	0	0	0	0	0	0	0	0
D14	14	16	500	1	500	500	1	500	500	1	500	500	1	500	500
D2	2	17	10	0	0	0	0	0	0	0	0	0	0	0	0
D6	6	18	15	0	0	0	0	0	0	0	0	0	0	0	0
D9	9	19	20	0	0	0	0	0	0	0	0	0	0	0	0
D25	25	20	70	0	0	0	0	0	0	0	0	0	0	0	0
D30	30	21	20	0	0	0	0	0	0	0	0	0	0	0	0
D12	12	22	40	0	0	0	0	0	0	0	0	0	0	0	0
D7	7	23	65	0	0	0	0	0	0	0	0	0	0	0	0
D5	5	24	50	1	50	50	1	50	50	1	50	50	1	50	50
D1	1	25	10	0	0	0	0	0	0	0	0	0	0	0	0
D3	3	26	70	0	0	0	0	0	0	0	0	0	0	0	0
D16	16	27	5	0	0	0	0	0	0	0	0	0	0	0	0
D31	31	28	90	0	0	0	0	0	0	0	0	0	0	0	0
D28	28	29	120	1	120	120	1	0	0	1	0	0	1	0	0
D23	23	30	10	0	0	0	0	0	0	0	0	0	0	0	0
D20	20	31	20	0	0	0	0	0	0	1	20	0	1	20	0
D18	18	32	6	0	0	0	0	0	0	1	6	0	1	6	0
Power KVA				970	970	970	1070	950	950	1096	976	950	1136	996	970
				Required	suggested LS	Traditional LS	Required	suggested LS	Traditional LS	Required	suggested LS	Traditional LS	Required	suggested LS	Traditional LS

Total Load shed	---	---	---	---	---	---	---	120	146	---	120	146
No. of isolated loads	---	---	---	---	1	1	---	1	3	---	1	3
Unused power because of shedding	---	---	---	---	50	50	---	24	50	---	4	30

Biotreatment of Slaughterhouse Wastewater Accompanied with Electrcity Generation and Nutrients Recovery in Microbial Fuel Cell

Zainab Ziad Ismail
Professor
Dept. of Environmental Engineering
College of Engineering
Baghdad University
Email: zismail9@gmail.com

Ali Jassim Mohammed
Chief Engineer
Saad State Company
Ministry of Construction and Housing and public municipality
Email: Alijassim_70@yahoo.com

ABSTRACT

In recent years and decades, there is a great need for developing new alternative energy sources or renewable sustainable energy. On the other hand, new technology approaches are growing towards benefits from the valuable nutrients in wastewater which are unrecoverable by traditional wastewater treatment processes. In the current study, a novel integrated system of microbial fuel cell and anoxic bioreactor (MFC-ANB) was designed and constructed to investigate its potential for slaughterhouses wastewater treatment, nitrogen recovery, and power generation. The system consisted of a double-chamber tubular type MFC with biocathode inoculated with freshly collected activated sludge. The MFC-ANB system was continuously fed with real-field slaughterhouse wastewater, with initial concentrations of COD and ammonium were 990 mg/L and 200 mg-N/L, respectively. The MFC-ANB system was operated for a total period of 43 days. Maximum removal efficiencies of COD, ammonium, nitrate, nitrogen recovery, Columbic efficiency, and power generation were 99%, 99.3%, 100%, 100%, 13.37% and 162.22 mW/m^2, respectively.

Key words: Microbial fuel cell**,** slaughterhouse wastewater, ammonium, and nitrate.

المعالجة البايولوجية للمطروحات السائلة من المجازر مع توليد الطاقة الكهربائية وأسترجاع المغذيات في خلية الوقود الأحيائية

زينب زياد اسماعيل
أستاذ
قسم الهندسة البيئية
كلية الهندسة-جامعة بغداد

علي جاسم محمد
رئيس مهندسين
شركة سعد العامة
وزارة الاعمار والاسكان والبلديات العامة

الخلاصة

خلال السنوات والعقود الماضية ظهرت حاجة ماسة لتطوير مصادر جديدة بديلة للطاقة اواللجوء للطاقة المتجددة او المستدامة. من ناحية اخرى، ان المسلك التكنولوجي الحديث يتجه نحو استغلال القيمة العالية للمغذيات في المياة الملوثة والتي من غيرالممكن استرجاعها بأستخدام الطرق التقليدية في المعالجة. في هذه الدراسة تم تصميم وتنفيذ منظومة معالجة جديدة قائمة على اساس الدمج بين خلية الوقود الاحيائية (MFC) مع المفاعل الاحيائي اللاهوائي (ANB) وهذه المنظومة "MFC-ANB" تقوم بمعالجة مياه المجازر واسترجاع النتروجين بالاضافة الى توليد الطاقة الكهرائية المستدامة في آن واحد. ان شكل وتصميم خلية الوقود الاحيائية (MFC) في هذه الدراسة هو انبوبي ذو حجرتين، حجرة الانود والتي تحتوي على قطب الانود الاحيائي وحجرة الكاثود التي تحتوي على قطب الكاثود الاحيائي ، وقد تم تغذيتها بألحمأة النشطة كمصدر للبكتريا النشيطة. تم تغذية منظومة المعالجة "MFC-ANB" بشكل مستمر بمياه المجازر الحقيقية لمدة 43 يوم. علما ان التركيز الابتدائي لمحتوى الطلب الكيمياوي للاوكسجين (COD) وتركيز الأمونيوم في حدود 990 ملغم/لتر، و 200 ملغم-نيتروجين/

لتر على التوالي. اظهرت النتائج المختبرية ان اقصى ازالة للطلب الكيمياوي للاوكسجين،، الامونيوم، النترات، استرجاع نتروجين، كفاءة كولومبية، وتوليد طاقة كانت 99٪، 99.3٪، 100٪، 100٪ ، 13.37٪ و 162.22 ملي واط/م^2 على التوالي.

الكلمات الدالة: خلية الوقود الاحيائية، مياه المجازر، الامونيوم،النترات، واسترجاع النتروجين.

1. INTRODUCTION

The technology of microbial fuel cells (MFCs) represents the latest approach of generating electricity from biomass using active living bacteria with wastewater treatment. MFC is one of the sustainable alternatives for renewable energy production. This process happens when the biofilm of bacteria on the anode surface oxidizes organic matter in the wastewater and produce electrons and protons, which generates electrical current through an external circuit **Arora, 2012; Janicek, et al., 2014**.

The slaughterhouses are the most important agro-industrial facility that has a direct impact on public health and the environment. Meat processing in slaughterhouses produces large amounts of organic wastewater during the manufacturing process, including, stunning, bleeding, hide or hair removal, carcass washing, cleaning process and trimming **Wang, 2004**; **Yordanov, 2010.** The slaughterhouse wastewater has a high strength, in terms of biochemical oxygen demand (BOD), and chemical oxygen demand (COD), suspended solids (SS), nitrogen and phosphorus, as compared with domestic wastewater **Wang, 2004**.

Typical concentration parameters of slaughterhouse wastewater such as BOD, COD, and nitrogen are 1900, 2579-6650, and 80 mg/L, respectively **Wiesmann, et al., 2007**.

However, primary and/or chemical treatments are not appropriate to reduce the pollutants in slaughterhouse wastewater to meet the discharge standards. Therefore, biological treatment is widely used for partial or complete stabilization of biologically degradable substances **Cheremisinoff, 1996**. On the other hand, anaerobic-aerobic treatment is an efficient way to treat highly COD loaded industrial and municipal wastewater **Chan, et al., 2009.**

Nitrification and denitrification are common processes to remove ammonia from slaughterhouse wastewater **Mousavi et al., 2012**. MFCs can be applied as a novel technique for bioelectrochemical nitrogen recovery, which can be accomplished by the nitrification process in an aerated biocathode **Yan, et al., 2012.**

Malaeb et al., 2013, developed a system consisting of a microbial fuel cell combined with membrane bioreactor (MFC-MBR) for simultaneous wastewater treatment and power generation. The achieved COD and NH_3−N removals were 97% and 91%, respectively.

Lin, et al., 2015 studied high-strength animal manure wastewater treatment and electrical energy recovery by air-cathode microbial fuel cells (MFCs). The MFC system was fed with swine wastewater and under external resistor of 2.2 kΩ, the observed energy production efficiency, columbic efficiency, and generated power were 0.37%, 1.5% 28.2 μW, respectively. **Zhu et al., 2016,** investigated the simultaneous nitrification and denitrification of cyanobacteria solution accompanied with power generation using a dual-chamber MFC. Removal of 0.064 ± 0.005 kg TN/m^3.day and 0.063 ± 0.005 kg NH_4^+/m^3.day were achieved. **Hiegemann et al., 2016,** evaluated the performance of pilot scale MFC system of 45 L volume consisting of 4 single-chamber membrane-less MFCs integrated into a full-scale wastewater treatment plant. Results revealed that COD, TSS, nitrogen removal, and columbic efficiency of 24.8% of 24%, 40% and 28%, respectively were achieved.

The present study looks forward to experimentally and theoretically investigate the performance of a sequential-flow tubular microbial fuel cell integrated with external anoxic bioreactor (MFC-ANB) for simultaneous treatment of real-field slaughterhouse wastewater,

sustainable power generation, and nitrogenous-nutrient recovery. The MFC-ANB system was fed with real-field slaughterhouse wastewater and inoculated with activated sludge.

2. MATERIALS AND METHODS

2.1. MFC-ANB integrated system

MFC

An integrated complete system mainly consisted of tubular type microbial fuel cell associated with internal aerobic bioreactor and external anaerobic bioreactor was set up as given in Fig. 1. The tubular dual-chamber MFC consisted of three concentric Plexiglas cylinders. The internal, mid, and external cylinders represent the anodic section, cathodic compartment, and the extended aerobic bioreactor, respectively. The diameter of anode, cathode and bioreactor chambers were 60 mm, 160 mm, and 200 mm, respectively with height of 420 mm. The anode compartment was occupied with graphite rod. The graphite rod diameter and the effective length were 20 and 290 mm, respectively, resulted in a total effective surface area of 185.35 cm^2. The cylindrical perforated anode chamber had 169 holes, each hole of 11 mm diameter. The effective volume of anode was 680 mL. The anodic chamber was wrapped with a rectangular (410 mm x 200 mm) sheet of cationic membrane (CMI7000s). Graphite granules were used as contact material in the cathode compartment. This material had a bulk density of 1660 kg/m^3, surface area of 0.0832 m^2/g, and granular size diameter range of 2-4 mm. The total mass of the granular graphite electrode in the cathode compartment was 2200 g. It was placed in a perforated basket made of stainless steel (304) mesh 14.

Denitrification bioreactor

Continuous up flow mixed bed bioreactor was designed and installed to carry out the denitrification process, the bioreactor was made of Plexiglas cylinder (outside diameter 60 mm, height 420 mm).The active volume of the reactor was 680 mL.

2.2. Preparation of the MFC integrated system

Prior to construction and set up of the MFC integrated system, all its components were cleaned well with an appropriate detergent, then repeatedly rinsed with tap water and deionized water. Cation exchange membrane (CEM) was subjected to a course of pre-conditioning by immersion in a 5% sodium chloride solution for 24 h to allow for membrane hydration and expansion, and then washed with deionized water.

2.3. Acclimation and enrichment of biomass

To start up and operate the MFC, 680 mL of the activated sludge was placed in the anode compartment, and was sparged with nitrogen gas for a period of 10 min to maintain anaerobic environment. During the enrichment period, the anode was periodically fed by nutrient salt solution. After 45 days, the MFC was fed with a real field slaughterhouse wastewater at a rate of 0.38 mL/min.

2.4. Substrate, Inoculum and Chemicals

The real slaughterhouse wastewater was freshly collected from Al-Shoula slaughterhouse in Baghdad. The quality of wastewater is given in Table 1. The activated sludge which was obtained from the aeration tanks of Al-Rustamia third extension municipal treatment plant, Baghdad was used to inoculate the anode, cathode, and the denitrification bioreactor.
In order to develop and enrich the growth of microorganisms in the MFC, a mineral salt media was used for this purpose. This MSM solution was prepared according to the procedure outlined in **Ghangrekar, et al., 2005**. The media solution was prepared by dissolving; 0.56 g $(NH_4)2SO_4$, 0.20 g $MgSO4{\bullet}7H_2O$, 15 mg $CaCl_2$, 1 mg $FeCl_3{\bullet}6H_2O$, 20 mg $MnSO_4{\bullet}H_2O$, 0.42g $NaHCO_3$ in liter distilled water, and then the solution was autoclaved at 121°C for 20 minutes and cooled under oxygen-free nitrogen gas before use.

2.5. Start up and operation of MFC integrated system

After 45 days of inoculating the MFC, wastewater was continuously fed to the anodic chamber of the MFC at a flow rate of 0.38 mL/min to achieve hydraulic retention time (HTR) of 30 h. Nitrogen gas was purged into the wastewater feed tank to eliminate oxygen content and provide anaerobic environment. At the same time, an air compressor with a maximum flow rate of 10 mL/min was connected to the cathode compartment to supply oxygen in a continuous manner. Also, the pH of the solution in the MFCs was monitored continuously and adjusted to 7-7.2 using 1M HCl or 1M NaOH solution. The MFC integrated system was operated at ambient temperature.

3. Data acquisition system and analysis

3.1. Wastewater and treated effluent analysis

Chemical oxygen demand (COD), biological oxygen demand (BOD), dissolved oxygen (DO), pH, NO_3^-, NH_4^+, and TDS tests were carried out by the researcher on a daily basis. The tests were conducted every day in accordance to the procedures outlined in the *Standard Methods* **APHA, 1998,** and the **ASTM Manual of Water and Environmental Technology, D1426-92.** Instruments and measuring devices used in this study were; COD reactor (model RD 125, Lovibond, Germany, COD test (model MD 200 COD vario, Lovibond, Germany), Multidirect (Lovibond,Germany), pH meter (model portable HI-83141, Hanna Instruments, Romania), Voltage data logger (model: Lascar EL-USB-3, USA), Multimeter (model MT1233C, pro'skit, Taiwan), Peristaltic pump (Model Mini-Pump Variable Flow Control, USA), Air compressor (model ACO-318, HAILEA, China), Resistance box (0-100,000 Ohm), Multiparameter Photometer bench type (Model C200, Hanna Instruments, Romania), BOD Measurement System (Model OxiDirect, Lovibond, Germany), Dissolve Oxygen meter (model HI9147-04, Hanna Instruments, Romania),Gas Chromatographs (Packard Models 438A, Packard instrument company, USA), Micromeritics analyzer (model: Micromeritics ASAP 2020, Micromeritics Instrument Corporation, USA).

3.2. Power density

The MFC voltage was continuously monitored via USB data logger. This data was converted to current by using Ohm’s law Eq. (1):

$$I=E_{cell}/R_{ext} \quad (1)$$

The power density was calculated according to Eq. (2):

$$P = (E_{cell})^2/R_{ext}*A_{an} \quad (2)$$

where: P is the power (W/m^2), I is the current (Amp.), R_{ext} is the external resistance (Ω), and E_{cell} is the cell voltage (V), A_{an} is the projected surface area of anode (m^2).

3.3. Coulombic efficiency

The columbic efficiency was carried out according to Eq. (3) for continuous flow:

$$\epsilon_{cb} = \frac{MI}{Fbq\Delta COD} \quad (3)$$

Where: M is the molecular weight of oxygen (32 g/ mol), F is the Faraday constant (96485 C/mol of e^-), I is the current (Amp.), b is the number of electrons exchanged per mole of oxygen (4 mol/mol), q is the volumetric influent flow rate (m^3/sec), ΔCOD is the difference COD between the influent and effluent.

4. RESULTS AND DISCUSSION

4.1. Substrate (as COD) removal

The MFC-ANB system was continuously fed for 43 days with real-field slaughterhouse wastewater having average COD concentration of 1000 mg/L at organic loading rate of 0.8 kg COD /m^3.d. As shown in Fig. 2. , steady state condition was directly achieved in MFC-ANB fed with real-field slaughterhouse wastewater. This behavior could be due to the favorable and significant growth of previous acclimated microorganisms in the anodic and cathodic biofilm.

The slight fluctuation in COD removal was observed and was well expected when using real-field wastewater due to the variation in COD concentration, as well as the existence of different species which may affect the substrate biodegradation. Inspite of this fluctuation, maximum and average COD removal efficiencies were 98% and 94%, respectively. These results were comparable, or in fact relatively higher than 92% reported by **Min et al., 2005,** for the treatment of swine wastewater by MFC.

4.2. Ammonium ions removal

The ammonium concentrations in each part of the MFC–ANB system were examined during the entire period of the system operation. As given in Fig. 3, the influent average ammonium concentration was 200 mg-N/L. The removal efficiency of ammonium ions achieved 97.9% after 14 days of continuous operation, and then a steady state condition was observed with a maximum ammonium removal of 99.3%. However, a relatively moderate fluctuation in the ammonium removal ranged from 88.5% to 99.3% was observed. The removal of NH_4^+ occurred in the biocathodic section by the activity of nitrifying bacteria growing within the cathodic biofilm. The transfer of ammonium ions from the anodic section to the biocathodic section occurred by diffusion through the cation permeable membrane (CMI7000s). On the other hand, the small remaining concentrations of NH_4^+ ions will transfer from the anode via the sequential flow of the anodic effluent to the cathode.

4.3. Nitrate removal

The ammonium ions were converted to nitrate ions by the nitrifying bacteria in the aerobic biocathodic section and the subsequent extended aerobic bioreactor. Then after, the resulted nitrate ions were converted to nitrogen in the anoxic bioreactor (ANB) by the activity of denitrifying bacteria at steady state of continuous operation. Nitrate removal efficiency increased achieving 92.69% after19 days as shown in Fig.4. After 21 days, maximum removal efficiency of nitrate achieved 100%. The slight fluctuation in nitrate removal could be attributed to the limited supply of COD to the denitrifying bacteria to reduce nitrate to nitrogen in the anoxic bioreactor, **Schipper, et al., 2010**. The nitrate removal efficiency remained within a range from 90.3% to 95.5% after 35days.

4.4. MFC Voltage

The MFC voltage was regularly monitored and directly measured using the data logger during the entire period of continuous operation. As shown in Fig.5, the voltage sharply increased to achieve a maximum value of 350 mV after the first day of operation. Then, a decline of voltage was observed to a value of 300mV which lasted for about 8 days, and then the voltage was re-stabilized at 350 mV until the end of the operation period at the day 43. This short period-voltage drop could be related to the sudden existence of complex organic matter accompanied with other forging species and high ammonium concentration that may inhibit and adversely affect the growth and reproduction of bacteria and a subsequently lower electrons generation. The re-stabilization of voltage to its original maximum value was most likely due to the re-acclimation of active microorganisms to this type of substrate.

4.5. Polarization curve

In order to investigate the performance of MFC during a stable phase of operation, the output voltage was recorded under various external loads from 10 to 1000 Ω. In order, to get the polarization curve, the current density was plotted against voltage and power density. As given in Fig.6, maximum power and current densities were 165.22 mW/m^2 and 472 mA/m^2, respectively obtained at 40 Ω external resistances.

4.6. Power and current density

Profiles of the generated current and power are presented in Fig. 7. A sharp increase in the current and power were observed after the first day of operating the MFC-ANB system. After 10 days, the current and power densities were stabilized at 472 mA/m^2 and 165.22mW/m^2, respectively and steady state conditions were observed. Then the current and the corresponding power exhibited unsteady state condition for a period of 40 days.

5. CONCLUSIONS

This study demonstrated and evaluated the performance of an integrated system of dual chamber tubular microbial fuel cell (MFC) with extended aerobic bioreactor and anoxic bioreactor for real field slaughterhouse wastewater treatment, ammonium removal, and power generation. Results revealed that maximum efficiencies of COD removal, ammonium oxidation, nitrate reduction, Columbic efficiency, and power generation were 99%, 99.3%, 100%, 13.37% and 162.22 mW/m^2, respectively.

6. REFERENCES

- APHA, 1998.*Standard methods for examination of water and wastewater*, 20th ed. American Public Health Association, Washington, DC.
- Arora, R., 2012. *Microbial biotechnology.* Wallingford, Oxford shire: CAB International.
- ASTM Manual of Water and Environmental Technology, D1426-92., Nessler method.
- Chan, Y., Chong, M., Law, C., Hassell, D., 2009. *A review on anaerobic–aerobic treatment of industrial and municipal wastewater.* Chemical Engineering Journal, 155(1-2), 1-18.
- Cheremisinoff, N., 1996. *Biotechnology for waste and wastewater treatment.* Westwood, N.J.: Noyes Publications.
- Ghangrekar, M.M., Joshi, S.G., Asolekar, S.R., 2005. *Characteristics of sludge developed under different loading conditions during UASB reactor start-up*. Water Research, 39 (6), 1123–1133.
- Hiegemann, H., Herzer, D., Nettmann, E., Lübken, M., Schulte, P., Schmelz, K., Gredigk-Hoffmann, S., Wichern, M., 2016. *An integrated 45L pilot microbial fuel cell system at a full-scale wastewater treatment plant*. Bioresource Technology, 218, 115-122.
- Janicek, A., Fan, Y., Liu, H., 2014. *Design of microbial fuel cells for practical application: a review and analysis of scale-up studies*. Biofuels, 5(1), 79-92.
- Lin, H., Wu, X., Nelson, C., Miller, C., Zhu, J., 2015. *Electricity generation and nutrients removal from high-strength liquid manure by air-cathode microbial fuel cells*. Journal of Environmental Science and Health, Part A, 51(3), 240-250.
- Malaeb, L., Katuri, K., Logan, B.E., Maab, H., Nunes, S., Saikaly, P., 2013. *A Hybrid Microbial Fuel Cell membrane bioreactor with a conductive ultrafiltration membrane biocathode for wastewater treatment*. Environmental Science & Technology, 47(20), 11821-11828.
- Min, B., Kim, J., Oh, S., Regan, J., Logan, B.E., 2005. *Electricity generation from swine wastewater using microbial fuel cells.* Water Research, 39(20), 4961-4968.
- Mousavi, S., Ibrahim, S., Aroua, M., 2012. *Sequential nitrification and denitrification in a novel palm shell granular activated carbon twin-chamber upflow bio-electrochemical reactor for treating ammonium-rich wastewater*. Bioresource Technology, 125, 256-266.
- Schipper, L., Robertson, W., Gold, A., Jaynes, D., Cameron, S., 2010. *Denitrifying bioreactors—an approach for reducing nitrate loads to receiving waters*. Ecological Engineering, 36(11), 1532-1543.
- Wang, L., 2004. *Handbook of industrial and hazardous wastes treatment*. New York: Marcel Dekker, Inc., New York, NY.
- Wiesmann, U., Choi, I., Dombrowski, E., 2007. *Fundamentals of biological wastewater treatment.* nheim: Wiley-VCH.

- Yan, H., Saito, T., Regan, J., 2012. *Nitrogen removal in a single-chamber microbial fuel cell with nitrifying biofilm enriched at the air cathode*. Water Research, 46(7), 2215-2224.
- Yordanov, D., 2010.*Preliminary study of the efficiency of ultrafiltration treatment of poultry slaughterhouse wastewater*. Journal of scientific & industrial, 69, 727-73.
- Zhu, G., Chen, G., Yu, R., Li, H., Wang, C., 2016. *Enhanced simultaneous nitrification/denitrification in the biocathode of a microbial fuel cell fed with cyanobacteria solution.* Process Biochemistry, 51(1), 80-88.

7. NOMENCLATURE

BOD =biochemical oxygen demand, mg/l
COD= chemical oxygen demand, mg/l
SS =suspended solids, mg/l
MFC= microbial fuel cell.
MFC-ANB= microbial fuel cell integrated with external anoxic bioreactor
MCL=maximum contamination level, mg/l
TDS= total dissolved solid, mg/l

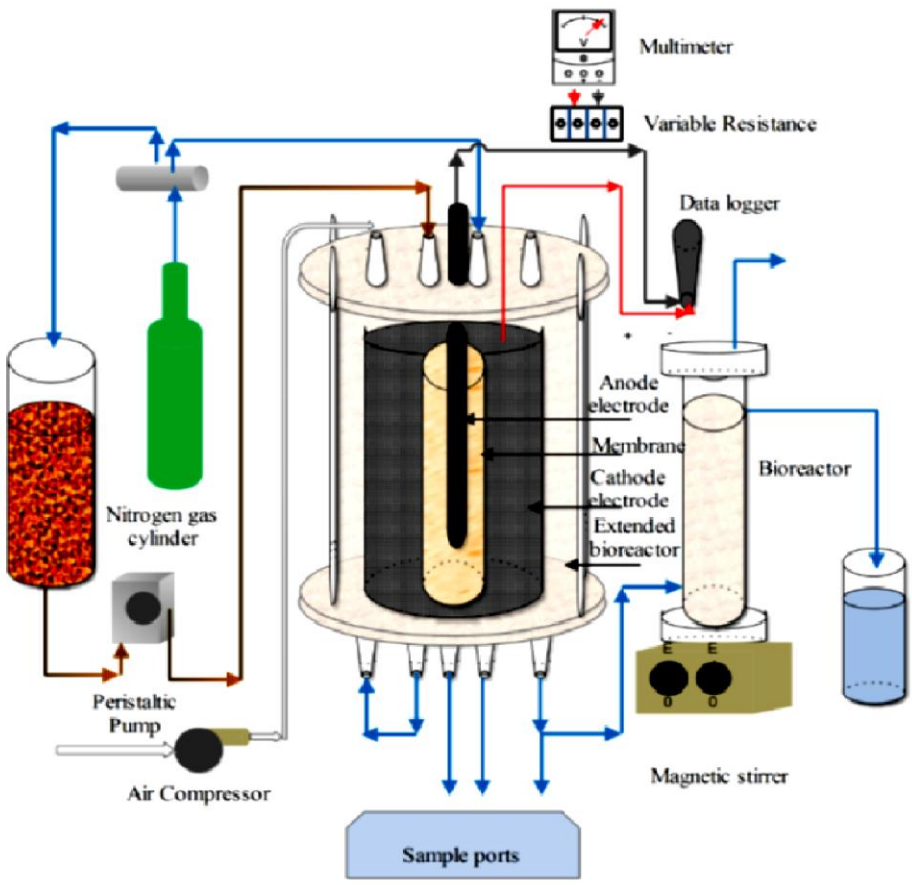

Figure 1. Schematic diagram of microbial fuel cell integrated with anoxic bioreactor .

(MFC-ANB)

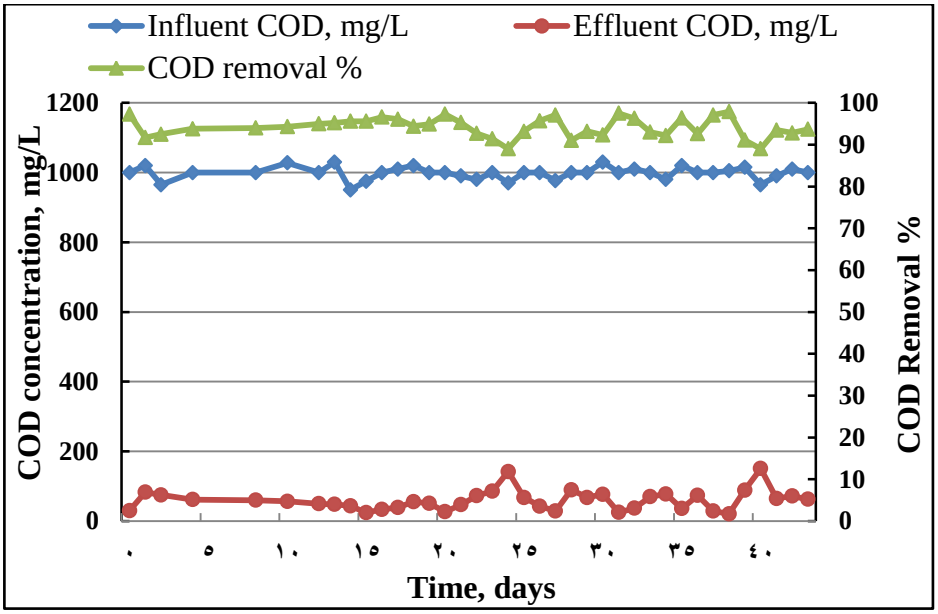

Figure 2. Profile of COD removal in the MFC-ANB system.

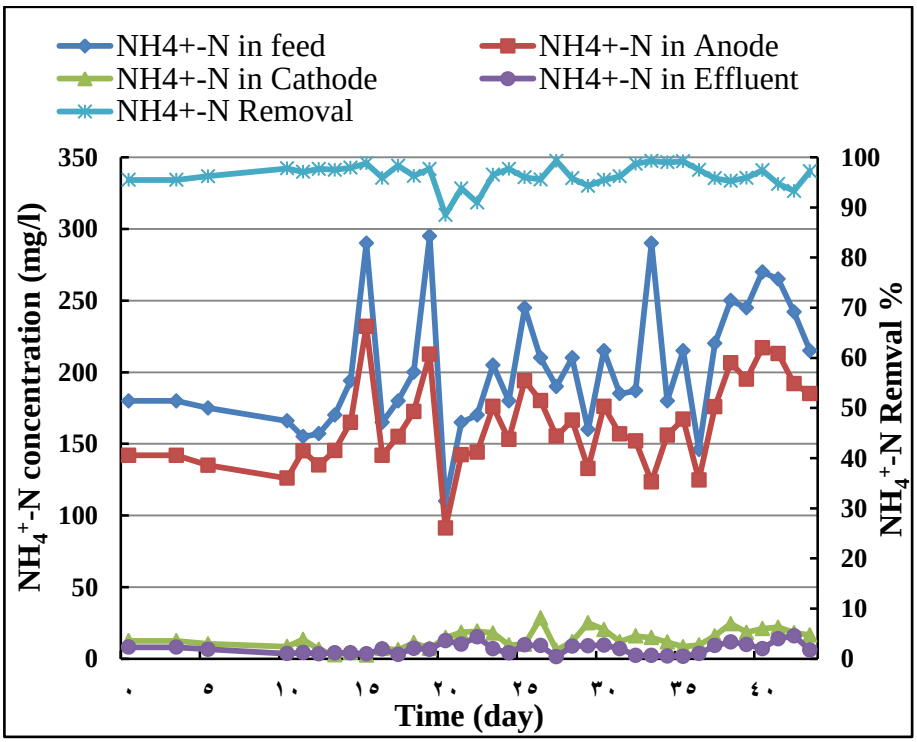

Figure 3. Profile of ammonium ions removal in MFC-ANB.

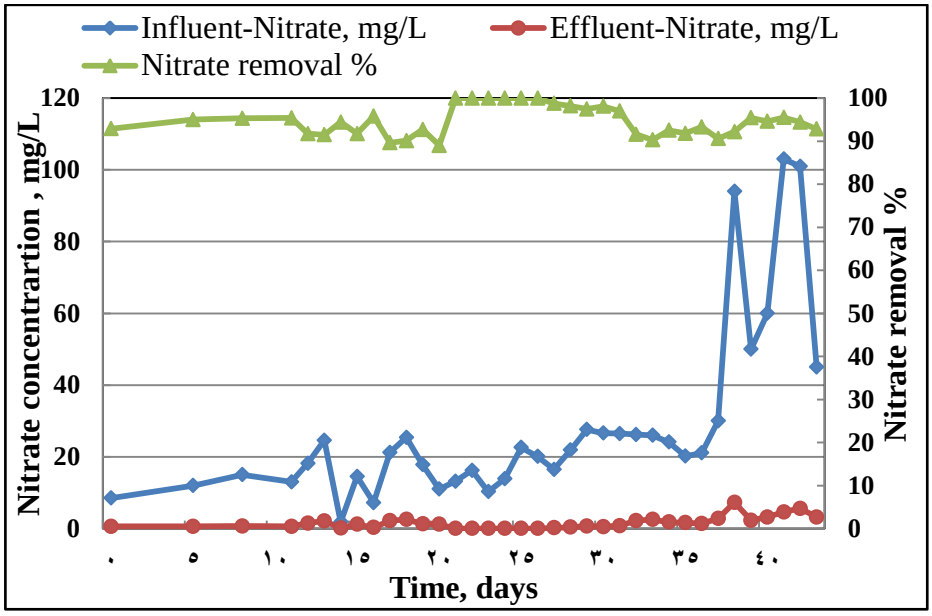

Figure 4. Profile of nitrate ions removal in the MFC-ANB.

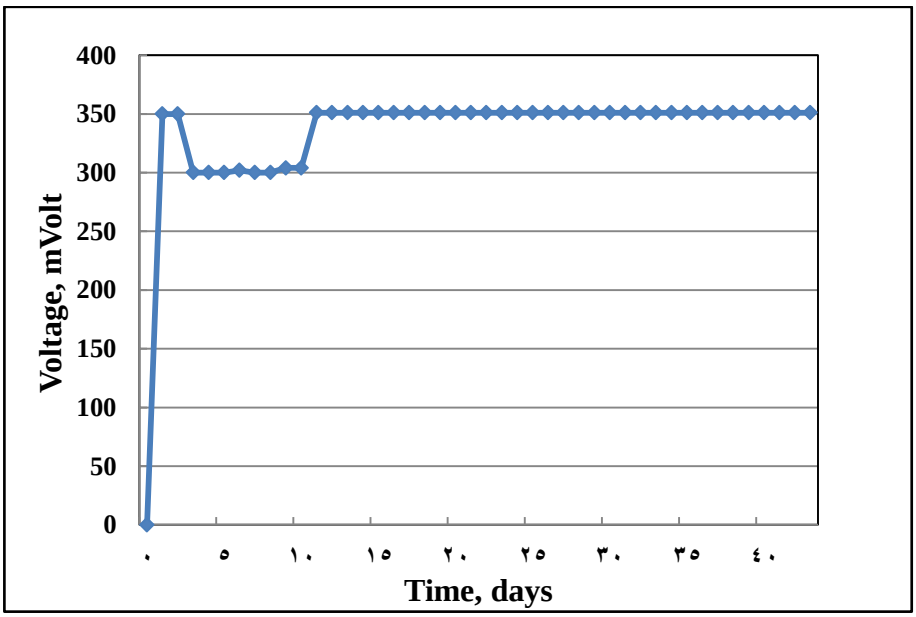

Figure 5. Voltage profile in the MFC at external resistance of 40 Ω.

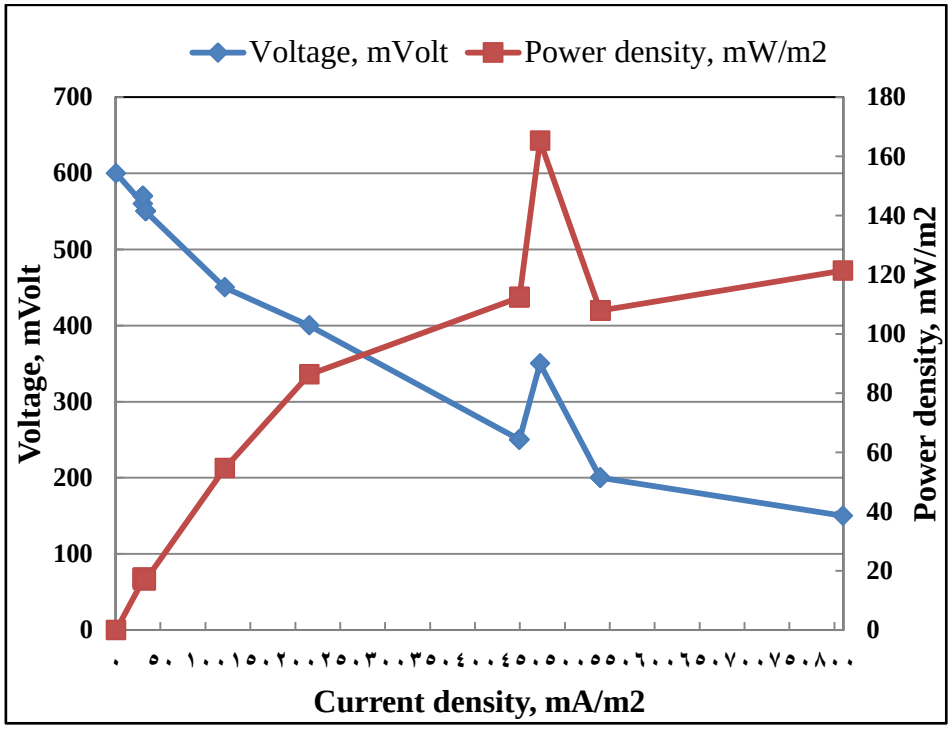

Figure 6. Polarization curve in MFC.

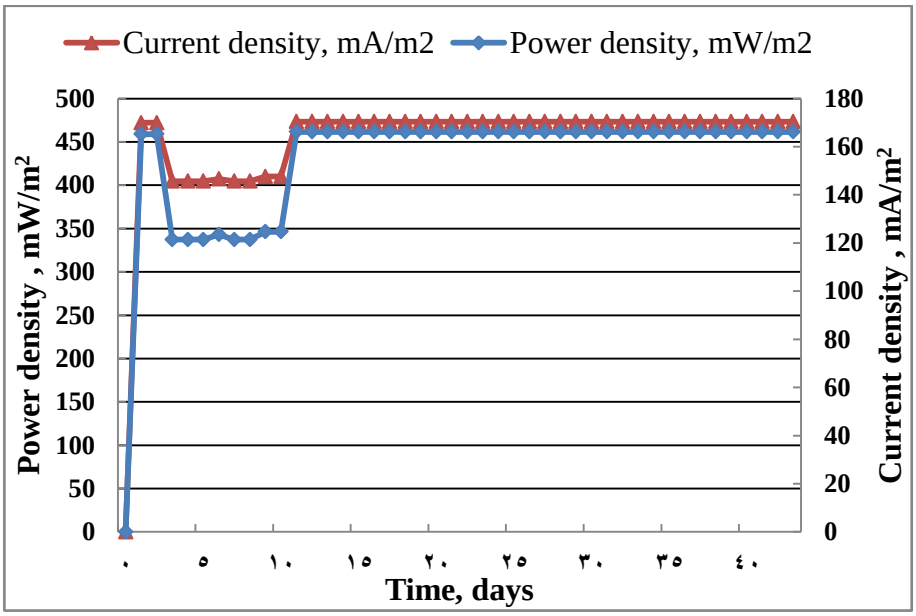

Figure 7. Power density and current density profiles in MFC.

Table 1. Quality of real-field slaughterhouse wastewater.

Constituents	Units	Average concentration
COD	mg/L	1000
BOD	mg/L	550
Ammonium (NH_4^+)	mg/L	75.05
Sulfate(SO_4^{-2})	mg/L	69.5
Nitrate (NO_3^-)	mg/L	13.5
Nitrite (NO_2^-)	mg/L	9.0
Chloride (Cl^-)	mg/L	49.0
Total dissolved solids (TDS)	mg/L	501
Phosphate (PO_4^{-3})	mg/L	3.07
pH	-	6.7

Experimental Study on Heat Transfer and Friction Factor Characteristics of Single Layer Graphene Based DI-water Nanofluid in a Circular Tube under Laminar Flow and Different Heat Fluxes as Boundary Conditions

Prof. Dr. Najdat N. Abdullah
Department of Mechanical Engineering
University of Baghdad
E mail: najdat_abdulla@yahoo.co.uk

Hussein A. Ibrahim
Department of Mechanical Engineering
University of Baghdad
E mail: hussain1983ali@gmail.com

ABSTRACT

An experimental study was performed to estimate the forced convection heat transfer performance and the pressure drop of a single layer graphene (GNPs) based DI-water nanofluid in a circular tube under a laminar flow and a uniform heat flux boundary conditions. The viscosity and thermal conductivity of nanofluid at weight concentrations of (0.1 to 1 wt%) were measured. The effects of the velocity of flow, heat flux and nanoparticle weight concentrations on the enhancement of the heat transfer are examined. The Nusselt number of the GNPs nanofluid was enhanced as the heat flux and the velocity of flow rate increased, and the maximum Nusselt number ratio ($Nu_{nanofluid}/Nu_{base\ fluid}$) and thermal performance factor was (1.45) and (1.24) respectively, by using (1wt%) concentration and $q=6104 W/m^2$ heat flux. Finally, an analysis of the thermal performance factor shows that the GNPs nanofluids could work as a good alternative conventional working fluid in thermal heat transfer applications.

Key words: convective heat transfer, graphene nanofluid, laminar flow, pressure drop, performance factor

دراسة تجريبية على خصائص انتقال الحرارة ومعامل الاحتكاك لمائع نانوي احادي الطبقة (كرافين-ماء) في انبوب دائري تحت الجريان الانسيابي واحمال حرارية مختلفة كشروط حدودية

أ.د. نجدت نشأت عبدالله
قسم الهندسة الميكانيكية
جامعة بغداد

حسين علاوي ابراهيم
قسم الهندسة الميكانيكية
جامعة بغداد

تم اجراء دراسة تجريبية لحساب خصائص انتقال الحرارة القسري وانخفاض الظغط لمائع نانوي احادي الطبقة (كرافين-ماء) في انبوب دائري لجريان انسيابي وحمل حراري منتظم كشروط حدودية. اللزوجة والموصلية الحرارية للمائع (0.1-1wt%) النانوي تم قياسها.تأثير سرعة الجريان،الحمل الحراري وتركيز الجزيئات النانوية على تعزيز انتقال الحرارة تم تحريها.النتائج

بينت ان عدد نسلت للمائع النانوي (كرافين-ماء) يزداد بزيادة الحمل الحراري وسرعة الجريان.واعظم نسبة عدد نسلت (عدد نسلت مائع نانوي/عدد نسلتمائع اساسي) ومعامل الاداء الحراري كان (1.45) و(1.24) على التوالي، باستخدام تركيز (1wt%) وحمل حراري ($6104W/m_2$). واخيرا تحليل معامل الاداء يبين ان المائع الانوي كرافين يمكن ان يعمل كبديل جيد للموائع التقليدية في تطبيقات انتقال الحرارة.

الكلمات الرئيسية: انتقال الحرارة بالحمل، مائع نانوي كرافين، الجريان الانسيابي، انخفاض الضغط، معامل الاداء

1. INTRODUCTION

Most heat transfer applications use conventional fluids like ethylene glycol (EG), DI-water and engine oil as heat transfer working fluids. The efficiency of these fluids is often limited so the efficiency of the conventional fluids can be enhanced by improving the heat transfer properties and thermal conductivity. These heat transfer fluids have low thermal conductivity with respect to solid materials. Therefore, solid particles with high thermal conductivity are generally added to traditional heat transfer fluids to increase their thermal conductivity. However, the addition of micrometer or millimeter particles sized can cause problems as sedimentation and agglomeration. **Choi, 1995,** avoided these problems by introducing a new type of heat transfer medium referred to nanofluid where the nanoparticles are dispersed in base fluids like EG, water and oil.

A nanofluid is a new kind of heat transfer fluid prepared by dispersing metallic or non-metallic nanomaterials with typical size less than (100 nm) which are stably distributed in conventional fluids. These suspended nanomaterials in the liquid improve the thermal conductivity of conventional liquid. Nanofluids have been considered as innovative heat transfer fluids for numerous applications

The benefits of nanofluids technologies are expected to be large due to the heat transfer characteristic of cooling devices or heat exchangers in many applications. Nanofluids can show many advantages besides the abnormal high effective thermal conductivity. These advantages involve, **Murshed et al., 2008**: Reduction in pumping power, improving heat transfer and stability, miniaturizing systems, micro channel cooling without clogging and savings cost and energy.

Recently, several investigations were devoted to study of thermal properties such as thermal conductivity and viscosity as well as convective heat transfer characteristics of the nanoparticles based nanofluid prepared from different carbonic structures, like single-wall, multiwall carbon nanotubes, graphite nanoparticles, and diamond nanoparticles, graphene oxide, graphene. Among all of these structural forms, single layer graphene is a 2-D material with one carbon atom thickness layer was discovered **by Novoselov** in **2004**. It has unique thermal characteristics due to large specific surface area and high thermal conductivity compared with other carbonic forms. **Balandin, 2008,** reported values thermal conductivity single-layer graphene in-plane up to 5200W/mK which sounds impressive when compared to the axial thermal conductivity of carbon nanotubes, that is, 3000W/mK **,Chen, 2010**. Further, the thermal properties of graphene were expected to be much different from one dimension carbon nanotube and zero dimension nanoparticles. Because the graphene itself is a very good thermal conductor, so the graphene based nanofluid was normally expected to show important thermal conductivity improvement.

However, according to literature, theoretical and experimental studies on the heat transfer thermal properties such as viscosity and thermal conductivity as well as heat transfer improvement of graphene based nanofluids are scarce.

Rashidi, et al., 2014, studied experimentally the force convection heat transfer characteristics laminar flow of graphene nanosheets nanofluid through the shell and tube heat exchanger. The convective heat transfer coefficients of (GNP) graphene nanosheets based on water nanofluids under laminar conditions were measured. Also the effects of weight concentration and temperature on convective heat transfer coefficients of (GNP) graphene nanosheets nanofluid were discussed. Results of added 0.075wt% of (GNP) graphene nanosheets to the base fluid contributed to an improvement of thermal conductivity about 31.83% and the convective heat transfer coefficient up to 35.6% at 38 ºC compared with pure water.

Mehrali, 2015, investigated experimentally the heat transfer performances laminar forced convection for (GNP) nanofluid with 750m^2/g of specific surface area inside a circular tube under constant heat flux at different weight fraction concentrations (0.025-0.1wt.%). The effect of the nanoparticles concentration on thermal properties, thermal performance factor and convective heat transfer coefficient was examined. Thermal conductivity of GNP nanofluid enhancement from 12% to 28% was noticed compare to the base fluid. The heat transfer coefficient for the GNP nanofluid was found about 15% higher than the distilled water. The thermal performance factor for 0.1wt.% was found to be increased about 1.15.

Akhavan-Zanjani, et al., 2014, studied experimentally the convective heat transfer of graphene based water nanofluids in turbulent flow through a uniformly heated circular tube with various concentrations. Experiments were conducted to measure viscosity, thermal conductivity, heat transfer coefficient and pressure drop. Adding a small amount of nanoparticles led to moderate increment of viscosity and enhancement of thermal conductivity. Furthermore, heat transfer coefficient showed relatively high enhancement, and pressure drop remained without change. Results showed that the maximum augmentations were 4.95%, 6.04% and 10.30%, for viscosity, heat transfer coefficient and thermal conductivity, respectively.

The aim of this work is to investigate experimentally the effect of single layer of graphene DI-water nanofluid concentration on heat transfer enhancement and pressure drop through a circular tube under fully developed laminar flow and different uniform heat fluxes boundary conditions

2. EXPERIMENTAL APPARATUS AND PROCESS

The rig was built at convective heat transfer laboratory of **Texas A&M** University and it was composed of the following main parts and measuring apparatus. **Figs. 1** and **2** show the photo and schematic diagram of the experimental apparatus.

Copper pipe with length, inner and outer diameter of (90, 0.789, 0.9525) cm respectively is connected to the entrance length and other parts by polypropylene compression straight adapter to reduce the axial heat loss conduction as shown in **Fig. 3**. Nichrome wire is used to uniformly heat the copper pipe. The copper pipe is painted with a fine spray before the Nichrome wire is wrapped up around it to avoid electrical conduction. Five thermocouples (T-type) are soldered in the small cavity at the copper pipe surface before the heater wires are wrapped around it. Whole

copper pipe is enveloped with fiberglass insulation and aluminum tape to minimize heat losses to the surrounding.
Programmable (LAMBADA) Variable voltage and current transformer (0-600V, 0-2.6A) was used to adjust the input heater power as required. A variable speed magnetic pump (5-12V DC) is used to circulate the nanofluid inside the heat transfer loop. The pump is connected with variable voltage power supply to get desired speed.

An electromagnetic (Megameter) low flow from Seametrics (PE202 Megameter) is utilized to measure the velocity and volume flow rate of the working fluid flowing through the heat transfer rig. The accuracy of the measurement is +/- 1%. **Fig. 4** shows the electromagnetic flow meter.
An electromagnetic Wet/Wet Differential Pressure Transmitters (PX154) from Omega is used to measure the pressure drop of the working fluid across test section. The output of the pressure transmitter ranges from 4 to 20 mA. The accuracy of the pressure transmitter is +/- 0.75% of the full scale.
Nanofluid is purchased from (US Research Nanometarials, Inc USA) as single layer of graphene DI-water dispersion at weight fraction Concentration (1wt%) and to dilute it only add DI water and shake it up to desired concentration **Figs. 5** and **6** show a visual inspection of GNP nanofluids after 2 months of the nanofluid purchased. Although two months from preparation passed no sedimentation and agglomeration was observed.

The experiments include the study forced convection heat transfer performance and the pressure drop of a of single layer of Graphene DI-water nanofluid, with concentrations of (φ=1, 0.8, 0.6, 0.4, 0.2, 0.1 and 0 wt%) in plain tube. All the tests were carried out under fully developed laminar flow with mass flow rate of (0.36, 0.4, 0.468 0,526, 0.58, 0.65, 0.72) kg/min and uniform heat fluxes range (4292-6104 W/m^2).
Cleaning the test rig after finishing the readings for each concentration of the nanofluid is done by using the draining valve for preventing clogging and sedimentation.

3. EXPERIMENTAL CALCULATIONS

3.1 Heat Transfer Calculation

Comparisons of the Nusselt numbers at equal Reynolds number is unreliable and is uninteresting from a practical perspective. The comparison of nanofluids at the same Reynolds number is common in the literature for nanofluid fields. Based on many literatures, comparing the heat transfer at the same flow rates (pumping power) is considered a more appropriate method in a nanofluids study (**France,2010, Haghighi,2014 and Mehirli,2014**), therefore, the better choice is the constant velocity instead of constant Re number.

The actual heat flux is calculated from the two evaluations as follows:

1) The total amount of heat transfer created by the electrical heater is given as:

$$Q_1 = \zeta VI \quad (1)$$

where, I and V represent the current and voltage which generated by programmable power supply and pass through electrical heater as well as the factor ζ=0.97 represents the accounts of the heat lost to environment, **Akhavan-Behabadi, 2012**.

2) The amount of heat input is estimated from the sensible heat gained by the nanofluid as follow:

$$Q_2 = \dot{m}\, c_p\, (T_{out} - T_{in}) \quad (2)$$

where, T_{in} ,T_{out} , $\dot{m}$ and cp represent the temperature of the bulk fluid at inlet and outlet of the test section, mass flow rate and specific heat of working fluid respectively.

The actual heat flux is then estimated as follow:

$$q'' = \frac{0.5\,(Q1 + Q2)}{\pi d_o L} \quad (3)$$

The local heat transfer a characteristic was defined in terms of the Nusselt number Nu(x) and heat transfer coefficient h(x) as given below.

$$h(x) = \frac{q''}{(Tw - Tf)X} \quad (4)$$

$$Nu(x) = \frac{h(x)di}{k} \quad (5)$$

where T_f and T_w are the fluid and wall temperatures respectively, q'' is the actual heat flux, k is the thermal conductivity of fluid, d_i is the inlet tube diameter and x is the axial distance from the test section inlet.

The temperature profile of fluid was obtained in the test section from the energy balance as follows:

$$T_{f\,(x)} = T_{f\,in} + \frac{q''Px}{\rho c_p uA} \quad (6)$$

Where P is the perimeter and A is cross-sectional area of the test section tube respectively, and u is the velocity of average fluid.

The average heat transfer coefficient and Nusselt number are calculated as follow:

$$h = \frac{q''}{(\bar{T}_w - \bar{T}_f)} \quad \text{and } Nu = \frac{hd}{k}$$

Here, $\bar{T}_w$ is the average temperature of the wall and $\bar{T}_f$ is the average bulk temperature of fluid.

Specific heat capacity and density of nanofluids are calculated from:

$$C_p=\frac{q''}{\dot{m}(T_{in}-T_{out})} \quad (7)$$

$$(\rho C_p)_{nf}=\varphi(\rho C_p)_p+(1-\varphi)(\rho C_p)_f \quad (8)$$

3.2 Friction Factor Calculation

Friction factor based on practically measured pressure drop can be evaluated by using Darcy friction factor equation, **Frank, 2001**.

$$f=\frac{\Delta P}{(hu^2/2)}\frac{d}{L} \quad (9)$$

Where Δp is the pressure drop through the test section measured by using an electromagnetic pressure transducer.

4. MEASURMENT OF VISCOSITY AND THERMAL CONDUCTIVITY

The viscosity of the GNPs based DI-water nanofluids at different weight fractions concentrations (1, 0.9, 0.8, 0.7, 0.6, 0.5, 0.4, 0.3, 0.2 and 0.1wt%) were measured by using a rotational type low viscosity DV-I prime digital viscometer. Measurements are taken at different shear rates and temperatures range from (5, 10, 15, 20, 25, 30 and 35°C) and were repeated four times for each experiment to obtain an accurate results.

Thermal conductivity of GNPs based DI-water nanofluids with six various weight fraction concentrations (1, 0.8, 0.6, 0.4, 0.2, 0.1 wt%) at temperatures range from (5-35ºC) is measured by using a KD2 Pro instrument from (Decagon devices, Inc. USA). The measurements were taken under different temperature conditions by using a temperature-controlled container connected with chiller to maintain constant temperature of sample.

5. RESULTS AND DISCUSSION

At first the experiments were conducted for DI- water. The results of experiments for DI-water under constant and uniform heat flux condition were compared with the data from the traditional standard equations, like the Shah and Darcy equations for laminar flow **Jang, 2009** as flowing:

$$Nu=\begin{cases} 1.302x_*^{-\frac{1}{3}}-1 & x_*\leq 0.00005 \\ 1.302x_*^{-\frac{1}{3}}-5 & 0.00005\leq x_*\leq 0.0015 \\ 4.346+8.68\left(10^3 x_*\right)^{-0.506}\exp\left(-41x_*\right) & x_*\geq 0.001 \end{cases} \quad (10)$$

where

$$Nu_* = h(x)d_i/k$$

$$x_* = \left[\frac{\frac{x}{di}}{RePr}\right]$$

$$f = \frac{64}{Re} \quad (11)$$

Fig. 7 illustrates the comparison between the average Nusselt number from experiments results and the results from Shah Equation. Data from this classical correlations and the experimental Nusselt number for DI- water agrees well and shows the precision of the experimental-setup with an error rate of less than 1.5%. To verify the friction factor data, **Fig. 8** shows the friction loss validation for DI-water from the experimental study, and the Darcy equation with an error rate of less than 3%.

Fig.9 shows reduction in the viscosity of the DI-water and GNPs nanofluid when the temperature is increasing. This is due to that, when the temperature is rising that causes the weakening of the adhesion forces for inter-particles intermolecular and that reducing the average forces of intermolecular. Subsequently, the viscosity reduces when the temperature increases that which noticed for the most kinds of nanofluids as shown in previous work**. Fig. 10** shows the maximum increment in viscosity of GNPs based DI-water is 111% at 1 wt% weight concentration and temperature 35 ºC compared with base fluid.
Thermal conductivity of the GNPs nanofluids with various weight fraction concentrations and temperature ranging from (5 to 35°C) are shown in **Fig. 11**. It is clear from this figure that the thermal conductivity enhancement was obtained with increasing weight concentrations and temperature. **Fig. 12** shows the thermal conductivity enhancement ratio. The maximum enhancement ratio in thermal conductivity for 1 wt% of GNPs was 22% at 35 ºC and 10% for 0. 1 wt % concentration was compared with base fluid.

Figs. 13, 14 and **15** reveal the variation of the average Nusselt number with velocity flow rate for GNPs nanofluid in a plain tube at different weight fraction concentrations (0.1-1wt%) and heat fluxes of 6104, 5040 and 4292W/m^2, respectively. The Nusselt numbers were largely influenced by the thermophysical properties (viscosity and thermal conductivity), the Brownian motion of nanoparticles, and the specific surface area of the nanoparticles. Therefore, the high concentration, heat flux, and nanofluid velocity causes an increase in the values of the Nusselt number. The enhanced heat convection performance of the GNPs nanofluid was resulted from the disordered movement of the nanoparticles and the high thermal conductivity of the GNPs nanofluid. As the nanoparticles concentration and fluid velocity increase the Nusselt number increases because the effective thermal conductivity of GNPs nanofluid increases with increasing weight concentration of the nanoparticles, which is explained by Brownian motion of the nanoparticles, molecular-level layering of the liquid at particle/liquid interface. Improved thermal conductivity reduces resistance to thermal diffusion in the laminar sublayer of boundary layer.

From figures, it can be seen that, the largest enhancement of the Nusselt number were 17.9%, 22.19%, 28.16%, 32.5%, 39.6% and 45.28% for the φ_m= 0.1, 0.2, 0.4, 0.6, 0.8 and 1wt %, respectively at a heat flux of 6104 W/m^2.

The augmentation in the heat transfer (the Nusselt number ratio) ($Nu_{nanofluid}/Nu_{plain\ tube}$) is shown in **Figs. 16, 17** and **18**. The maximum enhancement in the heat transfer for GNPs was (1.528) at velocity (0.25 m/s) heat flux (6104 W/m^2) and concentration (1wt%).

Fig. 19 shows the Nusselt number at different heat fluxes for the (1wt %) GNPs nanofluids. The Nusselt number had an enhancement of 33.9%, 40.9%, and 45.2% for the heat fluxes of 4292, 5040, and 6104 W/m^2, respectively.

The improvement in heat transfer coefficient in nanofluid is attributed to the effective thermal conductivity of nanofluid solution. The heat transfer coefficient is given as (k/δt), where (δt) is the thermal boundary layer thickness. This means that the decreasing thermal boundary layer thickness and/or improvement of nanofluid thermal conductivity increases the heat transfer coefficient and lead to increase the Nusselt number. Also, it seems that, the thermal boundary layer thickness of nanofluids is less than that of the DI-water. Furthermore, the thermal dispersion contributes to this improvement is because of the inherent irregular and random motion of graphene nanoparticles. Therefore, the temperature gradient at the wall becomes steeper, and that cause increasing in heat transfer rate.

The variation in friction factor at different velocities and weight fraction concentrations for GNPs nanofluid for plain tube is shown in **Fig. 20**.
Fig. 21 shows the effect of different studied parameters on friction factor ratio ($f_{nanofluid}/f_{plain\ tube}$). Maximum increase in ($f_{nanofluid}/f_{plain\ tube}$) for GNPs nanofluid was (1.74) at velocity flow rate of (0.25 m/s) and concentration of (1wt%).
The thermal performance factor of the GNPs nanofluid can be used to determine the usefulness of GNPs nanofluids for application in thermal systems.

$$\eta = \left(\frac{Nu_{\mathrm{nf}}}{Nu_{\mathrm{bf}}}\right) / \left(\frac{f_{\mathrm{nf}}}{f_{\mathrm{bf}}}\right)^{1/3} \qquad (12)$$

The results showed that the thermal performance factor of the GNPs nanofluid is high at a high heat flux and increased as the velocity and heat flux increased as shown in **Figs. 22, 23** and **24**. This is a result of the superior efficiency of the fluid disturbance and thus the heat transfer caused by the high values of thermal conductivity at the same pumping power. The maximum thermal performance of the GNPs nanofluid increased up to 1.25, 1.22, and 1.18 for 1 wt % of GNPs nanofluid at heat fluxes of 6104, 5040, and 4292W/m^2, respectively as shown in **Fig. 25.** Finally, an analysis of the pressure drop and the heat transfer result via the thermal performance factor shows that in spite of the pressure losses and the pumping power penalty, the GNPs based DI-water nanofluid is an excellent alternative for traditional working thermal fluids in heat transfer applications.

Nusselt number and friction factor can be related with Reynold number, Re, Prandel number, Pr, and nanofluid weight concentration, φm, with GNPs based DI-water nanofluids through the following correlations:

$$Nu=a_1 Re^{a_2} Pr^{a_3} (1+\varphi_m)^{a_4} \quad (13)$$

The limitations for this correlation are (Re=563-2158), (Pr=6.1-11.3) and nanofluid concentration (φ_m=0.1-1 wt%). The value of constants and the deviations are given in **Table 2.**

$$f=b_1 Re^{b_2} (1+\varphi_m)^{b_3} \quad (14)$$

The limitations for this correlation are (Re=563-2158), (Pr=6.1-11.3) and nanofluid concentration (φ_m=0.1-1 wt%).The value of constants and the deviations are given in **Table 3**.

Figs. 26 and **27** give the representation of the above correlations.

The comparison of the present experimental results of GNPs based water nanofluid with the published work, of **Mehrali, 2015**, is shown in **Fig. 28** for Nusselt number. This comparison shows a reasonable agreement with an error not exceeds 17%.

6. CONCLUSIONS

The following conclusions were obtained:

1. Thermal conductivity enhances as the nanofluid temperature and concentrations increase, and maximum enhancements was around 11.9% to 22.2% with weight concentration of 1wt % and temperature range from 5 to 35ºC.

2. Viscosity of the GNPs nanofluid was dependent on the concentration and temperature. It decreases with increases the temperature, and their increment was 80−111% of 1wt % compared with DI-water when the temperature increased from 5 to 35 ºC.

3. The Nusselt number enhances as the heat flux and velocity flow rate increase and maximum Nusselt number ratio ($Nu_{nanofluid}$/ $Nu_{plain\ tube}$) was (1.45) by using (1wt%) GNPs based DI-water nanofluid and the maximum thermal performance factor was (1.24). The GNPs nanofluid provides a good choice for the replacement of the traditional working fluids in heat transfer applications.

REFERENCE

- Akhavan-Behabadi M.A., Saeedinia M. and Nasr M.,2012 *"Experimental study on heat transfer and pressure drop of nanofluid flow in a horizontal coiled wire inserted tube under constant heat flux"*, Experimental Thermal and Fluid Science Vol.36, P.158–168.
- Akhavan-Zanjani, 2014, *Turbulent Convective Heat Transfer and Pressure Drop of Graphene–Water Nanofluid Flowing inside aHorizontal Circular Tube*, Journal of Dispersion Science and Technology,35 P. 1230–1240.

- Balandin A., Ghosh S., Bao W., Calizo I. and Teweldebrhan D.,2008, "*Superior Thermal Conductivity of Single-Layer Graphene"*, Nano Letters Vol.8, P.902-907.
- Chen L. and Xie H.,2010, "*Surfactant-Free Nanofluids Containing Double- and Single-Walled Carbon Nanotubes Functionalized by a Wet-Mechanochemical Reaction"*, Thermochim. Acta Vol.497, P.67–71.
- Choi S. and Eastman A.,1995,*"Enhancing thermal conductivity of fluid with nanoparticles"* , in: D.A. Siginer, Developments and Applications of Non-Newtonian Flows, Vol.66, P.99–105.
- France, Timofeeva E. and Singh, D.,2010,*"Thermophysical property-related comparison criteria for nanofluid heat transfer enhancement in turbulent flow"* Appl. Phys. Lett., Vol.96(21), P.213109.
- Frank M, White,2001,*"Fluid Mechanics"*, Fourth edition, MacGraw-Hill books.
- Jang S., Hwang K. and Choi U.,2009, *Flow and Convective Heat Transfer Characteristics of Water-Based Al2O3 Nanofluids in Fully Developed Laminar Flow Regime*, International Journal of Heat and Mass Transfer Vol.52, P.193–199.
- Haghighi E., Saleemi, M., Muhammed, M. and Palm B.,2014,*"Accurate basis of comparison for convective heat transfer in nanofluids"*, International Communications in Heat Mass Transfer, Vol.52, P.1−7.
- Murshed S.M.S, Leong K.C. and Yang C.,2008,*"Thermophysical and electrokinetic properties of nanofluids" – A critical review*, Vol.28, P.2109-2125.
- Mehrali M., Sadeghinezhad E. and Rose A.,2015,"*Heat Transfer and Entropy Generation for Laminar Forced Convection Flow of Graphene Nanoplateletsnano fluids in a Horizontal Tube"*, International Commun. in Heat and Mass Transfer Vol.66, P.23-31.
- Mehrali M.,Sadeghinezhad E., Mehrali M. and KaziS. N.,2014,*"Experimental investigation of convective heat transfer using graphene nanoplatelet based nanofluids under turbulent flow conditions"*, Industrial & Engineering Chemistry Research, Vol.53, P.12455−12465.
- Novoselov K., Geim A., Morozov S., Dubonos S. and Firsov A.,2004,*"Electric field effect in atomically thin carbon films"*, Science Vol.306, P. 666.

- Rashidi A.,Ghozatloo A. and Shariaty-Niassar M.,2014,"*Convective Heat Transfer Enhancement of Graphene Nanofluids in Shell and Tube Heat Exchanger"*, Experimental Thermal and Fluid Science Vol.53, P.136–141.

NOMENCLATURE

ρ= density, kg/m^3

f= friction factor

nf= Nanofluid

bf= Base fluid

η= thermal performance factor

φ_m= mass or weight friction concentration

Q_1=total heat power, W/m^2

Q_2=sensible heat gained by the nanofluid,W/m^2

$\bar{P}$=perimeter, m

u= velocity, m/s

I=current,omh

V=voltage,Volt

T=temperature, ˚C

L= length of tese section, m

$\dot{m}$=mass flow rate,kg/s

q"=actual heat flux,W/m^2

ζ= factor of heat loss to ambient

d= diameter, m

Cp= specific heat, KJ/kg.K

h= heat transfer coefficient, W/m^2.k

Table 1. Graphene nanoparticles properties.

Properties	Specifications
Color	black liquid
Shape of particle	single layer nanoplatelets
Content of carbon	>99.3 wt%
Surface area	500 - 1200m^2/g
Bulk density	0.2–0.4 g/cm3
diameter of particle	1µm - 12µm
Thickness of particle	0.55nm - 1.2nm
Thermal conductivity (vertical to surface)	6 W/m K
Thermal conductivity (parallel to surface)	5000 W/m K

Table 2. Values of factors for Eq.(13).

Nanofluid	a_1	a_2	a_3	a_4	a_5	Deviation
GNPs DI-water	0.6451	0.4180	-0.3730	6.9672	0	± 7.5%

Table 3. Values of factors for Eq.(14).

Nanofluid	b_1	b_2	b_3	b_4	Deviation
GNPs DI-water	54.450	-0.9752	-2.2072	0	± 10.5%

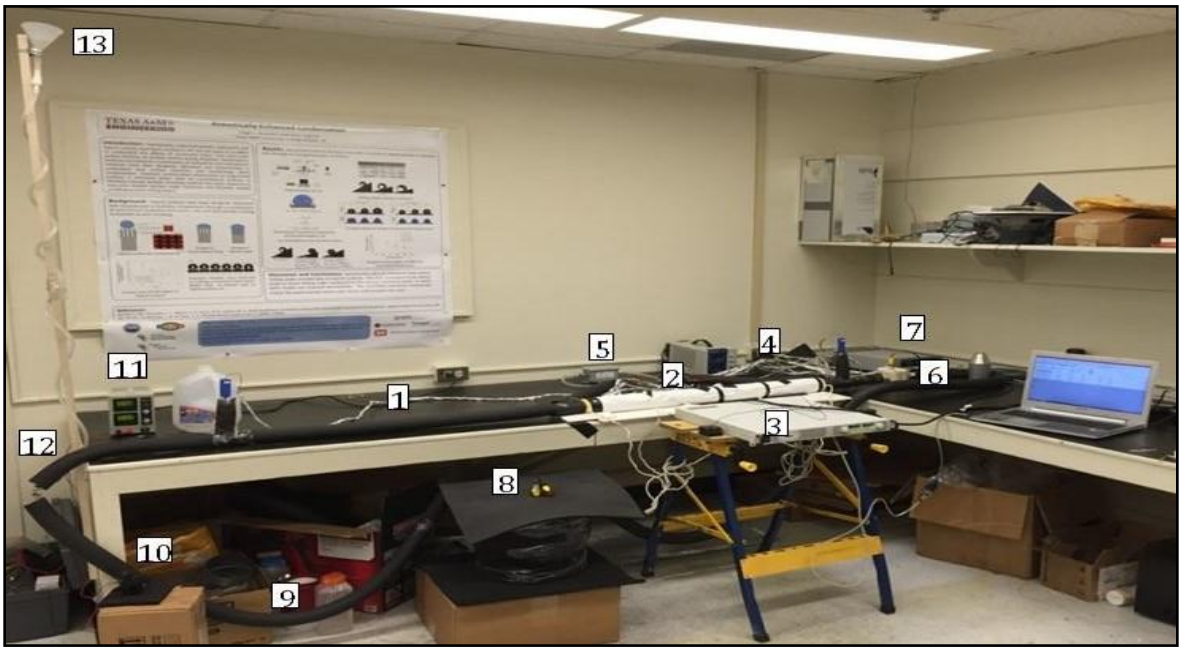

Figure 1. Heat Transfer loop at convective laboratory.

1. Entrance length **2.** Test section **3.**Variable voltage transformer **4.** Thermocouples **5.** Pressure transducer **6.** Flow meter **7.** Data acquisition system **8.** Heat exchanger **9.** Silicone Rubber Tubing **10.** Pump **11.** Power supply **12.** Control valve **13.** Plastic funnel

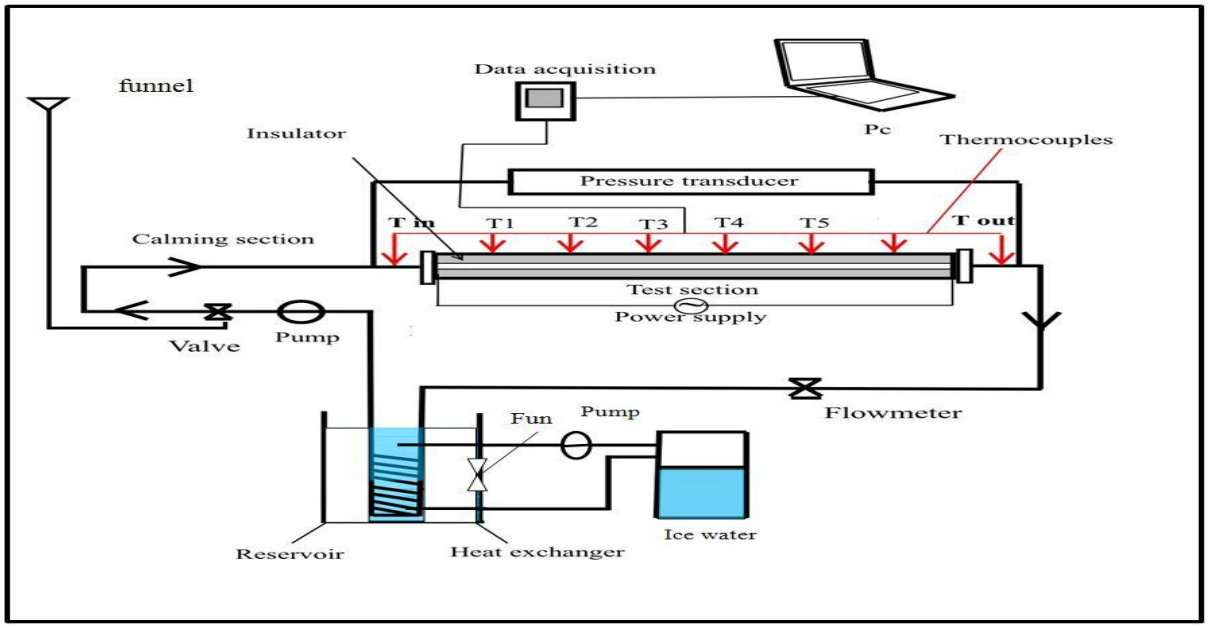

Figure 2. Schematic diagram of experimental apparatus.

Figure 3. Polypropylene compression straight adapter to reduce the axial heat loss conduction.

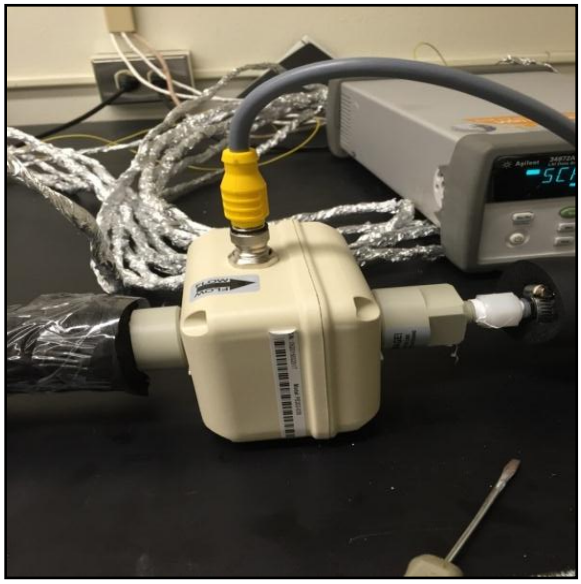

Figure 4. Electromagnetic flow meter.

Figure 5. Nanofluid samples.

Figure 6. Nanofluid samples after two months.

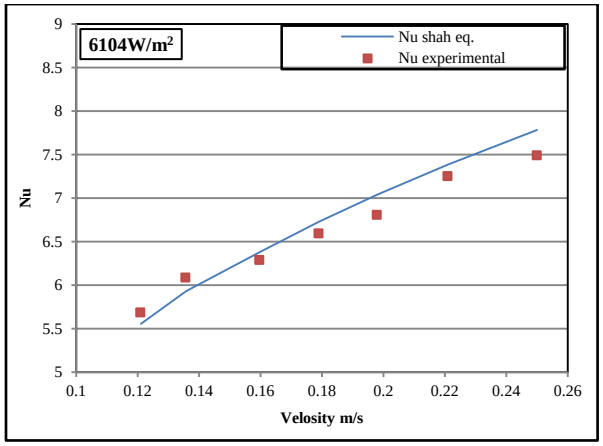

Figure 7. Measured average Nusselt number and the prediction correlations for DI-water versus the velocity.

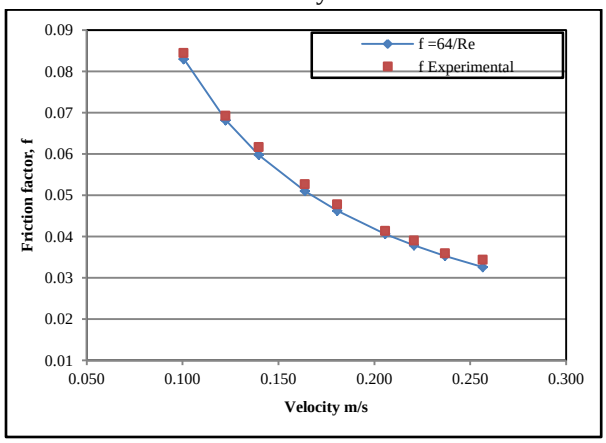

Figure 8. Frictional head loss as a function of the velocity for DI-water.

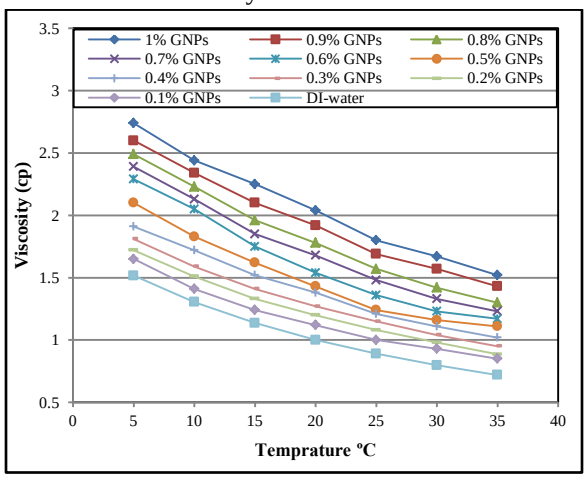

Figure 9. Viscosity of GNPs nanofluid with different weight fraction concentrations.

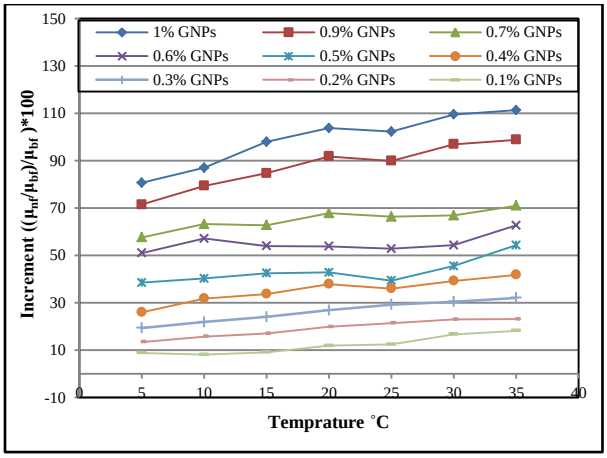

Figure 10. Viscosity of GNPs nanofluid increment percentage compared with DI-water.

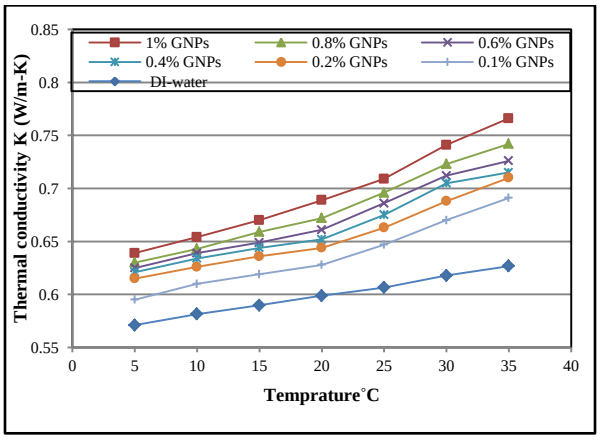

Figure 11. Thermal conductivity of GNPs with different weight concentrations.

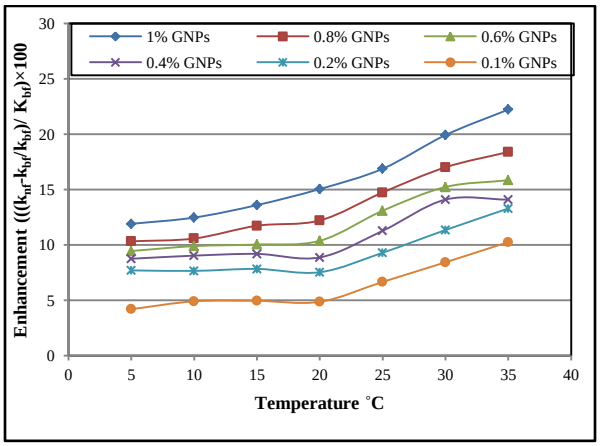

Figure 12. Thermal conductivity enhancement percentage compared with DI-water.

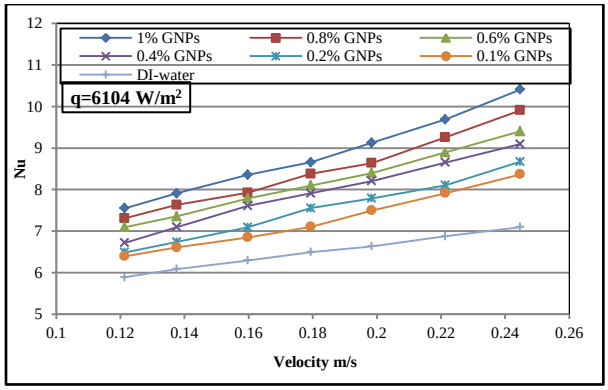

Figure 13. Effect of velocity of GNPs nanofluid on Nusselt number for different weight concentrations at q=6104 W/m^2.

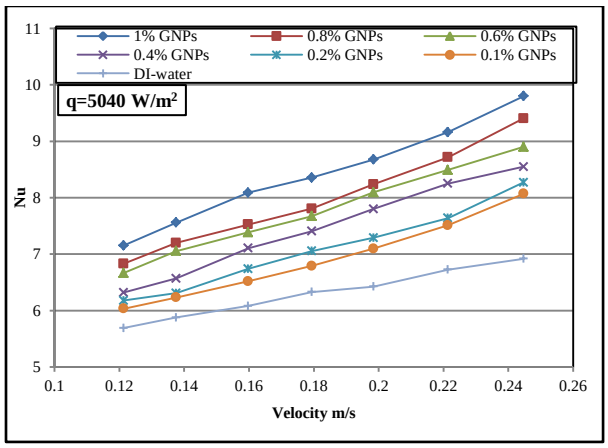

Figure 14. Effect of velocity of GNPs nanofluid on Nusselt number for different weight concentrations at q=5040 W/m^2.

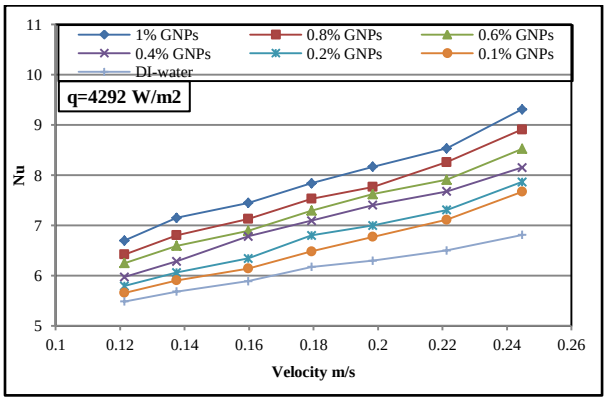

Figure 15. Effect of velocity of GNPs nanofluid on Nusselt number for different weight concentrations at q=4292 W/m^2.

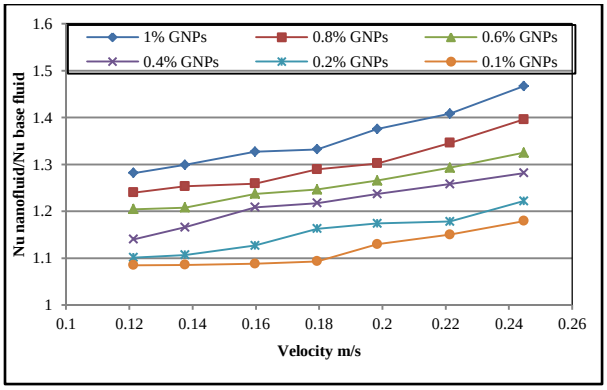

Figure 16. Effect of velocity of GNPs nanofluid on Nusselt number ratio ($Nu_{nanpfluid}/Nu_{DI\text{-}water}$)for different weight concentrations at q=6104 W/m^2.

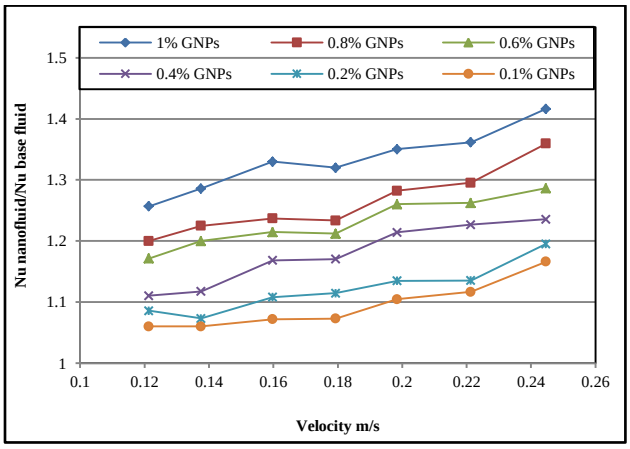

Figure 17. Effect of velocity of GNPs nanofluid on Nusselt number ratio ($Nu_{nanofluid}/Nu_{DI\text{-}water}$)for different weight concentrations at (q=5040 W/m^2).

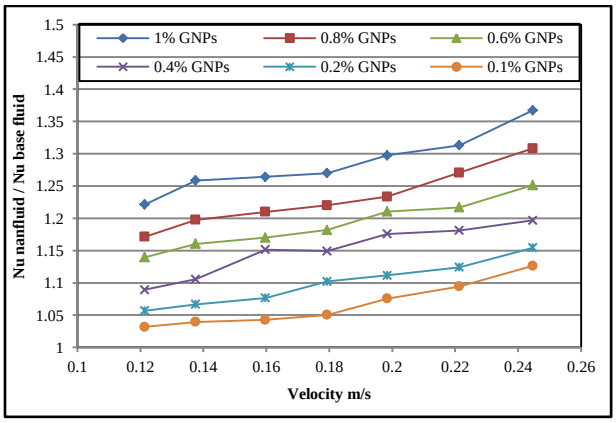

Figure 18. Effect of velocity of GNPs nanofluid on Nusselt number ratio ($Nu_{nanpfluid}/Nu_{DI\text{-}water}$)for different weight concentrations at q=4292 W/m^2.

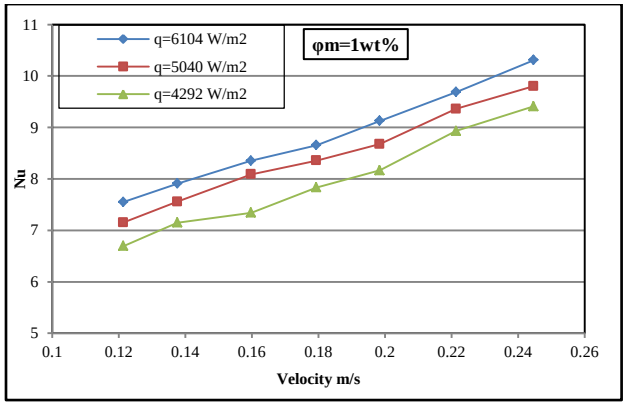

Figure 19. Effect of heat flux on Nusselt number for GNPs nanofluid for different weight concentrations.

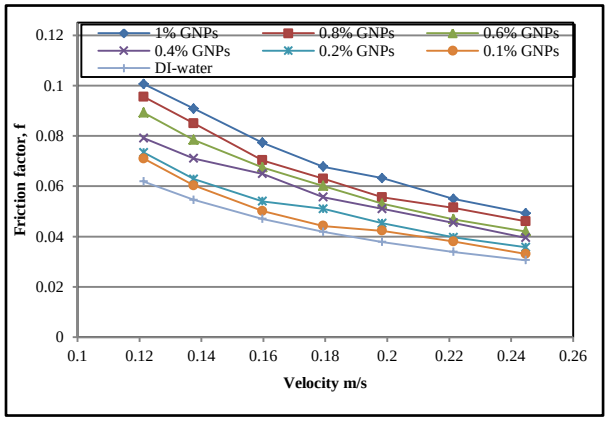

Figure 20. Variation of friction factor at different velocities and weight concentrations for GNPs nanofluid.

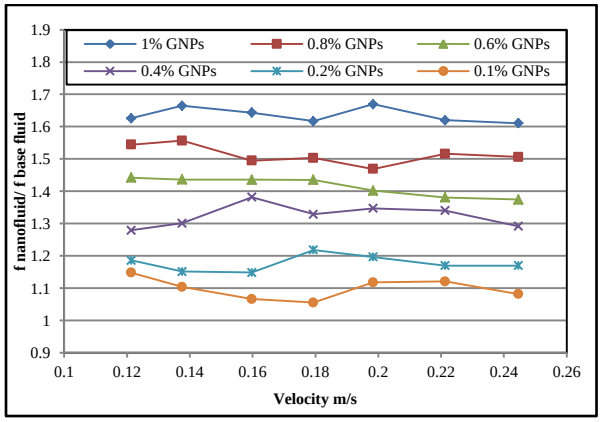

Figure 21. Variation of friction factor ratio ($f_{nanofluid}$/ $f_{plain\ tube}$) at different velocities and weight concentrations for GNPs.

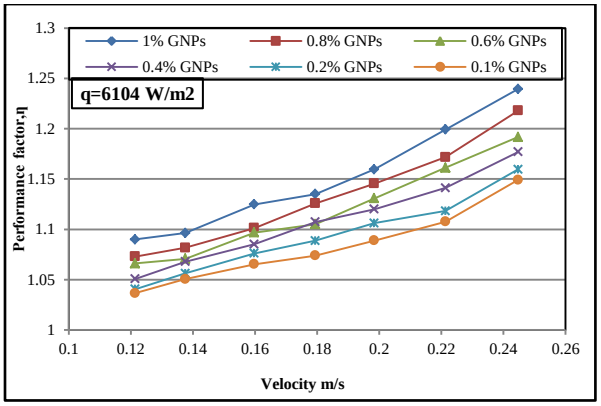

Figure 22. Effect of velocity and concentration on performance factor (η) for GNPs nanofluid at q=6104 W/m^2.

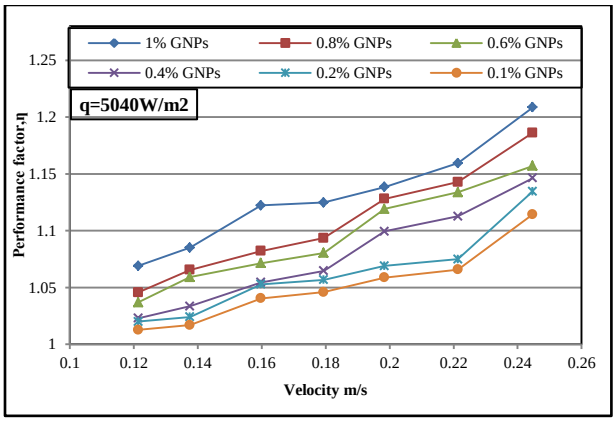

Figure 23. Effect of velocity and weight concentration on performance factor (η) for GNPs nanofluid at q=5040 W/m^2.

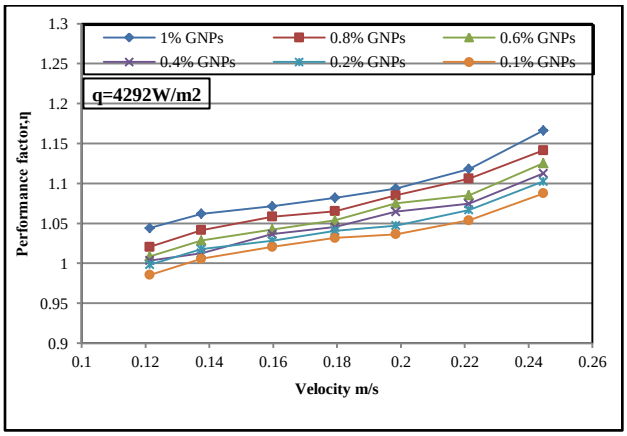

Figure 24. Effect of velocity and weight concentration on performance factor (η) for GNPs nanofluid at q=4292 W/m^2.

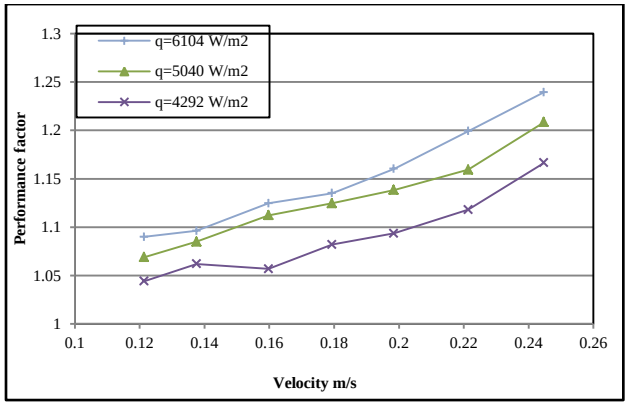

Figure 25. Effect of velocity on performance factor (η) for (1wt%) concentration of GNPs nanofluid at different heat flux.

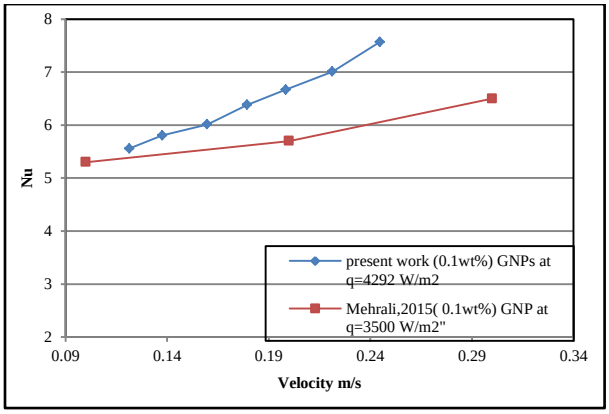

Figure 28. Comparison of experimental result of Nusselt number for present work with the published data of **Mehrali, 2015**.

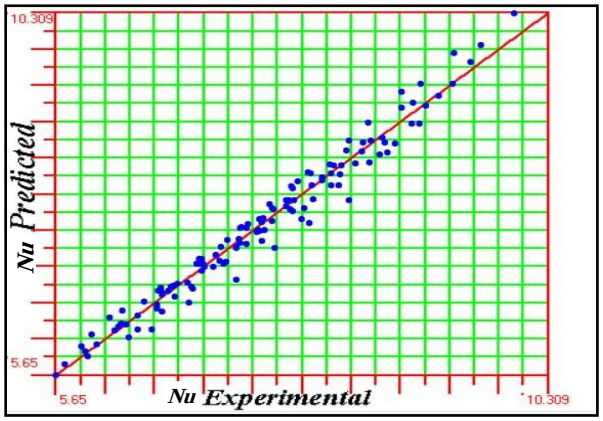

Figure 26. Comparison of experimental data with regression equation of Nusselt number for GNPs nanofluid.

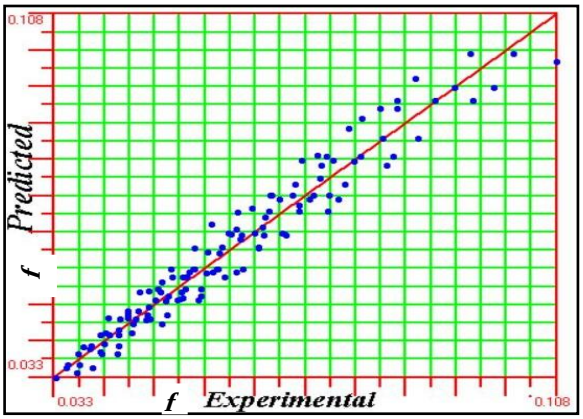

Figure 27. Comparison of experimental data with regression equation of friction factor for GNPs nanofluid.

The Effect of Fin Design on Thermal Performance of Heat Sink

Hayder Mohammad Jaffal
Assistant Professor
Faculty of Engineering -Al-Mustansiriyah University
E-mail:hayder.jaffal@yahoo.com

ABSTRACT

An experimental and computational study is conducted to analyze the thermal performance of heat sinks and to pick up more profound information in this imperative field in the electronic cooling. One important approach to improve the heat transfer on the air-side of the heat exchanger is to adjust the fin geometry. Experiments are conducted to explore the impact of the changing of diverse operational and geometrical parameters on the heat sink thermal performance. The working fluid used is air. Operational parameters includes: air Reynolds number (from 23597 to 3848.9) and heat flux (from 3954 to 38357 W/m^2). Conformational parameters includes: change the direction of air flow and the area of conduction/convection. Six parallel plate heat sinks are fabricated and tested in small wind tunnel: flat plate, cross-cut, perforated, perforated cross-cut, zigzag and serpentine. Three-dimensional numerical simulations using commercial available FLUENT 15 software, based on the Navier–Stokes equations standard k-ε applied turbulence model and energy equation, are acquired for forced convection of air in same heat sinks under the same experimental conditions. It is found that the numerical prediction of base temperature is in good agreement with experimental data. Results show that the Reynolds number has a significant effect on the thermal performance of the system. With increasing free stream velocity, the heat transfer coefficient increases and consequently the thermal resistance decreases. Furthermore, it is found that the heat transfer coefficient and thermal resistance are depending on heat flux. From the comparison analysis of various geometries of heat sinks, the perforated-cut heat sink showed the best thermal performance indicated heights Nusselt number and heat transfer coefficient, lowest thermal resistance.

Key words: Heat sink, fins, CFD, Numerical simulation, thermal performance.

تأثير تصميم الزعنفة على أداء المشتت الحراري

حيدر محمد جفال
استاذ مساعد
كلية الهندسة-الجامعة المستنصرية

الخلاصة

اجريت دراسة عملية وحسابية لتحليل الاداء الحراري للمشتات الحرارية لاكتساب المعرفة في هذا المجال الهام في تبريد الاجهزة الالكترونية. احد الطرق المهمة لتعزيز انتقال الحرارة على جانب الهواء من المبادل الحراري هي تطوير شكل الزعانف. وقد أجريت تجارب للتحقق من أثر تغيير متغيرات تشغيلية وتصميمة متنوعة على الأداء الحراري لمشتت الحرارة. مائع العمل المستخدم هو الهواء. تضمنت المتغيرات التشغيلية: عدد رينولدز (23597 - 3848.9) الفيض الحراري (3954 - 38357 واط/م^2) المتغيرات التصميمة هي: تغيير اتجاه تدفق الهواء ومساحة التوصيل/الحمل. ستة مشتتات حرارية مسطحة متوازية تم تصنيعها واختبارها في نفق هوائي صغير وهي : لوحة مسطحة، قطع، مثقب، ثقب - قطع، متعرج واعوج. المحاكاة العددية باستخدام برنامج FLUENT 15 ، بالاعتماد على معادلات نافير - ستوكس تم تطبيق نموذج الاضطراب k-ε ومعادلات الطاقة طبقت للحمل القسري للهواء لنفس الظروف التجريبية للمشتات الحرارية. تبين أن التنبؤ العددي لدرجة الحرارة القاعدة في توافق جيد مع البيانات التجريبية. أظهرت النتائج أن عدد رينولدز للهواء له تأثير كبير على الأداء الحراري للنظام. مع زيادة سرعة تيار الهواء، معامل انتقال الحرارة يزداد وبالتالي تقل المقاومة الحرارية. علاوة على ذلك، وجد أن

معامل انتقال الحرارة والمقاومة الحرارية يعتمدان على الفيض الحرري. من بين مختلف المشتتات المستخدمة، لوحظ ان افضل اداء حراري للمشتت الحراري ثقب- قطع له اعلى عدد نسلت ومعامل انتقال الحرارة، واقل مقاومة حرارية .
الكلمات الرئيسية: مشتت حراري، زعانف، CFD، تنبوء عددي، أداء حراري.

1. INTRODUCTION

The day by day increment in power dissipation of electronic segments sets increasingly elevated requests on the execution of the heat sinks. Two basic sorts of heat sinks which are generally utilized in the industry: plate fin heat sinks and pin fin heat sinks. Plate fin heat sinks are usually utilized as gadgets for upgrading heat transfer in electronics parts. The selection of an ideal heat sink relies upon various geometric parameters, for example, fin height, fin length, fin thickness, number of fins, base plate thickness, space between fins, fin shape or profile, material and so forth. Fins must be intended to accomplish the most extreme heat evacuation with least material consumption, considering, be that as it may, the simplicity of assembling of the fin shape. Extensive number of studies has been directed on enhancing fin shapes. S**ikka, et al., 2002,** experimentally investigated the effect of geometry rearranging the surface area of a finned heat sink on heat transfer. Heat sinks with fluted and wavy fin configurations are designed and fabricated together with conventional longitudinal-plate and pin fin heat sinks. **Arularasan and Velraj, 2008**, have developed CFD modeling and simulation on the fluid flow and heat transfer characteristics of a parallel plate heat sink to choose an ideal design of heat sink. The simulation is accomplished with a commercial package provided by Fluent Inc. The geometric parameters considered in this study were fin height, fin thickness, base height and fin pitch. **Tae, and Sung, 2009**, experimentally investigated the impacts of the cross-cut on the thermal performance of heat sinks. Tests outcomes additionally demonstrate that the cross-cut length basically impacts the thermal performance of heat sinks among the majority of the outline parameters of the cross-cut. The results also show that solitary cross-cut heat sinks are better than numerous crosscut heat sinks under the parallel flow condition. **Kavita, et al., 2014,** have displayed an experimental study to examine the heat transfer enhancement over horizontal flat surface with rectangular fin arrays with lateral, square and circular perforation by forced convection. The impacts of Reynolds number and perforation on the characteristics of heat transfer were resolved. It is watched that the Reynolds number and size aperture largely affect Nusselt number for the both sorts of holes. **Mohamed, 2015**, analytically explored the impact of fins number and fin thickness on the performance of heat sink. The results demonstrated that both the increase in fins number and thickness leads to an increase in heat transfer rate, however the increase in fins numbers essentially has more impact on the heat transfer rate than the increase in fin thickness. The increased in the thickness of the fin results in an increase in the heat transfer rate, yet more increment of the fin thickness results in abatement out there between fins. **Mehedi, et al., 2015,** analyzed experimentally the turbulent heat transfer performance of rectangular fin arrays. They assessed and thought about both solid and circular perforations along the length of the fin. They found that for increasingly and bigger holes, pressure drop and thermal resistance diminish while the fin efficiency and effectiveness are increased. **Ali and Abbas, 2015**, performed a numerical study for free convective heat transfer from introduced intruded rectangular fins. The continuity, Naver-Stockes and energy equations were solved for steady-state, incompressible, two dimensional and laminar flow with Boussiuesq approximation by Fluent 15 software. The different geometric parameters of project are assumed such as ratio of interrupted length to the fin length and the ratio of thickness to the fin length at different temperature. They found an enhancement in the thermal performance of the fin with reduction of its weight as a result of adding interruption to a vertical fin.

To the best of the author's knowledge, no previous studies have been conducted based on the following fins shape design: flat plate, cross-cut, perforated, perforated cross-cut, zigzag and serpentine. Therefore, numerical simulation and experimental study is conducted to investigate the thermal performance of the heat sinks. This study will advantage the outline engineers involved in electronic cooling.

2. EXPERIMENTAL APPARATUAS AND PROCEDURE

2.1 Description of Test Rig

A test apparatus is composed and manufactured, in which various operating parameters could be varied and tried, in the research facilities of Al-Mustansiriyah University, Faculty of Engineering. The general arrangement of the equipment is indicated photographically in **Fig. 1,** and schematically in **Fig. 2**. The experimental system incorporated at a wind tunnel, power supply, flow rate controller, blower, heat input unit and several thermocouples. The wind tunnel shown in **Fig. 3** is constructed of galvanized steel sheet of 1.5 mm thickness and has an interior cross-section of area 150 mm × 200 mm with an aggregate channel length of 800 mm. The face of the wind conduit is made of transparent Plexiglas glass sheet of 4 mm thickness to give a clear perspective of the activities inside the passage. The plate sort heater is utilized to provide uniform heat flux to the fins. Fins are fitted on a heater plate with help of bolts. The heater is placed inside insulation box to insulate thermally by 30 mm thickness glass wool. The regular was utilized to control the electric power contribution of the heating coil to get constant heat flux along the test section. The heater voltage drops and the current are measured by a multi-meter. The tests were conducted at heat input of 500 W. Air enters the single stage centrifugal blower at a rate which is controlled by the butterfly valve. Air is drawn through the duct. The mass flow rate of air is measured by utilizing an orifice plate with associated ducting and differential manometer. Thermocouples, K-type were inserted before and after the heat sink through two holes in test section to measure inlet and outlet air temperature in the wind tunnel. To measure the base plate temperatures at intermediate location inside heat sink, an exceptional hole have been assembled to embed thermocouple. In this work, to enhance the performance, selection of heat sink design depended on two factors: the first is to change the area of conduction – convection (cross-cut, perforated, perforated cross-cut) and the second is to change the direction of flow inside the heat sink (zigzag and serpentine). Six different aluminum fin arrays are constructed in training and laboratory center / University of Technology. All parallel plate fins with thickness of 2.5 mm, base plate of 18.5 mm and 114 mm long. The height of fins is 45 mm with pitch of 12 mm. The details of these arrays are shown in **Fig. 4,** and **Fig.5.**

2.2 Test Procedure

1- The fin put on heater inside the wind tunnel.

1- The electrical heater is switched on, and the desired voltage is maintained by using the regulator.

2- The blower is switched on, and air velocity is adjusted by butterfly valve.

3- For about (30 minutes) the steady state condition was accomplished, the voltage, current and local temperatures at difference points is recorded.

4- Repeat steps above with various air velocities (Reynolds number range is 23597- 3849) and various heat fluxes (heat flux range is 3954 - 38357 W/m^2).

5-The first third steps are repeated for various fin types.

2.3 Data Reduction

The convective heat transfer rate from electrically heated test surface is calculated by utilizing a relation:

$$Q_N = Q_{(electrical)} + Q_{(conduction)} + Q_{(radiation)} = \dot{m_a}\, C_{pa}(T_{out} - T_{in}) \quad (1)$$

The electrical heat input is calculated from the electrical potential and current supplied to the surface. In comparable studies, investigators reported that aggregate radiation and conduction heat losses from a similar test surface would be about 0.5% and 1.1% of the aggregate electrical heat input and therefore Q_{cond} and Q_{rad} are neglected in the present work.

The heat transfer from the test section by convection can be expressed as:

$$Q_N = h_{av} A_T \left[T_s - \left(\frac{T_{out}+T_{in}}{2}\right)\right] \quad (2)$$

The area A_T in equation 2 is total area of fin that touches fluid passing through the duct; it is equal to the sum of projected area and total surface area contribution from the blocks **Kavita, et al., 2014**.

For flat plate fin:

$$A_T = WL + 2N_f H[L+t] + 2B[L+W] \quad (3)$$

For perforated fin, this area includes outer surfaces of fin and also inner surfaces of perforations.

$$A_T = WL + 2N_f H[L+t] + 2B[L+W] + N_p N_f dt - N_p N_f \frac{\pi}{4} d^2 \quad (4)$$

For cross-cut fin:

$$A_T = WL + 2N_f H[L+t] + 2B[L+W] + N_f CH - 2N_f tH \quad (5)$$

Hence average convection heat transfer coefficient h_{av} can be finding as **Kavita, et al., 2014**:

$$h_{av} = \frac{Q_N}{A_T\left[T_s - \left(\frac{T_{out}+T_{in}}{2}\right)\right]} \quad (6)$$

Now, the thermal resistance is calculated as **Mehedi, et al., 2015:**

$$R_{th} = \frac{1}{h_{av}A_T} \quad (7)$$

The dimensionless groups are calculated as follows:

The Nusselt number, N_u is defined as:

$$N_u = \frac{h_{av}D_h}{k_a} \quad (8)$$

In order to better reflect the actual effective velocity at the measurement section in the test section, the average velocity is calculated using the effective fluid flow area, $A\text{-}A_{front}$, such as:

$$V_{av} = \frac{V}{A-A_{front}} \quad (9)$$

The duct Reynolds number, Re is defined as:

$$R_e = \frac{\rho_a V_{av} D_h}{\mu_a} \quad (10)$$

The hydraulic diameter of rectangular section of wind tunnel is defined as:

$$D_h = 4\frac{A_w}{P_w} \quad (11)$$

where A_w is the wind tunnel cross-sectional area, and P_w the wind tunnel perimeter.

Fin Performance: for evaluating the effectiveness of new configuration fin arrays, it is required to find out fin performance. To determine effectiveness of fin, the ratio of the actual heat transfer rate from the fin arrays (Q_f) to heat transfer rate of plate fin arrays (Q_{fp}).

$$\varepsilon_{fin} = \frac{Q_f}{Q_{fp}} \quad (12)$$

Percentage improvement of fins: the comparison of percentage effectiveness of fin arrays to plate fin arrays can calculate using following equation:

$$\%\varepsilon_{fin} = \frac{Q_f - Q_{fp}}{Q_{fp}} \quad (13)$$

In all calculations, the values of thermo physical properties are obtained at the bulk mean temperature, which is:

$$T_{mean} = \left(\frac{T_{out}+T_{in}}{2}\right) \quad (14)$$

A MATLAB program was written to compose the accompanying parameters: heat transfer coefficient, Nusselt number, Reynolds number, heat flux and heat dissipation. The input data to this program is the deliberate parameters taken from the trial runs.

3. DESCRPTION NUMERICAL SIMULATION

Steady state computational fluid dynamics (CFD) formulation is utilized to model this issue in ANSYS FLUENT. In CFD calculations, there are three principle steps: Pre-Processing, Solver Execution, Post-Processing. Pre-Processing is the progression where the displaying objective are resolved and computational grid is made. Numerical models and boundary conditions are set to start up the solver in the second step. Solver keeps running until the convergence is come to. At the point when solver is ended, the outcomes are inspected which is the post processing part. The Navier–Stokes and energy equations are utilized to model the convective heat transfer process with the accompanying presumptions: (i) steady 3D fluid flow and heat transfer; (ii) turbulent flow and incompressible fluid; (iii) physical properties of air, such as thermal conductivity, density, and specific heat are temperature dependent; and (iv) negligible radiation heat transfer. According to the above assumptions, the 3D governing equations are:

The continuity equation:

$$\nabla(\rho\vec{U}) = 0 \tag{15}$$

The X, Y, Z Momentum Equations

$$\nabla(\rho\vec{U}u) = -\frac{\partial p}{\partial x} + \frac{\partial \tau_{xx}}{\partial x} + \frac{\partial \tau_{yx}}{\partial y} + \frac{\partial \tau_{zx}}{\partial z} + \beta_x \tag{16}$$

$$\nabla(\rho\vec{U}v) = -\frac{\partial p}{\partial y} + \frac{\partial \tau_{xy}}{\partial x} + \frac{\partial \tau_{yy}}{\partial y} + \frac{\partial \tau_{zy}}{\partial z} + \beta_y \tag{17}$$

$$\nabla(\rho\vec{U}w) = -\frac{\partial p}{\partial z} + \frac{\partial \tau_{xz}}{\partial x} + \frac{\partial \tau_{yz}}{\partial y} + \frac{\partial \tau_{zz}}{\partial z} + \beta_z \tag{18}$$

The Energy Equation

$$\nabla(\rho h\vec{U}) = -p\nabla\vec{U} + \nabla(k\nabla T) + \Phi + S_h \tag{19}$$

Where ρ is the fluid density, V is the fluid velocity vector, τ_{ij} is the viscous stress tensor, p is pressure, β is the body forces, t is time, Φ is the dissipation term, h is the aggregate enthalpy , u, v and w are velocity components, $\vec{U}$ is the velocity vector. No-slip boundary conditions are imposed on the walls of the wind tunnel. At the inlet, mass flux and temperature are indicated. At the outlet, pressure is specified and temperature gradient is assumed to be zero. A uniform heat flux condition is imposed over the lower wall, and the heat flux is zero at all other walls. A typical computational domain and mesh distribution of the duct and the flat plate heat sink based on the experimental rig are shown in **Fig. 6**.

4. RESULTS AND DESCUSSION

4.1 Experimental validation of numerical simulation

In order to validate the CFD simulation results, experimental study is completed by keeping up the same working conditions. As can be seen from the **Fig.7** and **Fig.8** test results are in good agreement with the CFD results with most extreme deviation of 11%. **Fig.7** presents the variety of base temperature with heat flux. As the heat flux increases, the base temperature goes expanding in light of fact that the heat sink gets heated up increasingly because of conduction heat transfer from heat source. **Fig.8** presents the variation of base temperature with Reynolds number. As the Reynolds number expands, the base temperature goes diminishing because the fluid gets heated up increasingly because of convection heat transfer.

4.2 Experimental Results

4.2.1 The impact of heat flux

Figs.9 to **12** shows the impact of heat flux on the heat transfer coefficient, Nusselt number and thermal resistance for six heat sinks: flat plate, cross-cut, perforated, perforated cross-cut, zigzag and serpentine. To determine the appropriate heat flux for the heat sink, it is necessary to inspect the performance of heat sink with the change of the imposed heat flux. **Fig.9** shows the relationship between heat transfer coefficient with the imposed heat flux for flat and cross-cut heat sinks. From this figure, it is indicated that the heat transfer coefficient firstly increases with the increase of heat flux until the value of heat flux reached 23924 W/m^2 then it decreases with the increases of heat flux after this value. It can be concluded from this figure that the maximum heat flux for this heat sink is about 23924 W/m^2 or the heat sinks with these dimensions are appropriated to dissipate 272.734W to the surrounding. **Fig.10** indicates the impact of the heat flux upon the heat transfer coefficient for different heat sinks. The heat transfer coefficient increases as heat flux increases for all heat sinks. Also, it is indicated that the largest heat transfer coefficient can be achieved in the perforated-cut heat sink as a result of higher heat dissipation compared with other types. The variation of Nusselt number with heat flux is illustrated in **Fig.11**. Form this figure, it is seen that for all heat sinks, as the heat flux increased, the Nusselt number is increased. It is clear that the increase of Nusselt number is because of the increasing in amount of heat transfer. For instance, for perforated-cut heat sink, and at het flux of 23924 and 3954.38 W/m^2, the Nusselt number is calculated as 570.5467 and 117.2693 respectively. The effect of heat flux on thermal resistance for constant Reynolds number is illustrated in **Fig.12**. The thermal resistance diminishes with the increase of heat flux for all heat sinks as a result of increasing in heat transfer between the heat sink and air.

4.2.2 The impact of Reynolds number

Figs. 13 to **15** indicate the impact of Reynolds number on the heat transfer coefficient, Nusselt number and thermal resistance for six heat sinks: flat plate, cross-cut, perforated, perforated cross-cut, zigzag and serpentine. The heat transfer coefficient corresponding to different Reynolds number for different heat sinks is shown in **Fig.13**. For each heat sink, as the Reynolds number increase, the heat transfer coefficient increases. The most important reason for increasing heat transfer coefficient with Reynolds number when increasing the amount of air, the flow potential of heat removed will increase and caused an increased heat transfer coefficient. It is also indicated that the largest heat transfer coefficient is achieved in the perforated-cut heat sink as a result of change the area of heat transfer by conduction/convection that achieved more

heat exchange with the air. The variation of Nusselt number with Reynolds number is illustrated in **Fig.14**. For each heat sink, as the Reynolds number increased, the Nusselt number is increased. It is apparent that the increase of Nusselt number is due to the increasing in heat transfer coefficient that was caused by increased air flow rate. For instance, for perforated-cut heat sink, as air Reynolds number of 23597 and 3848.9, the Nusselt number is calculated as 456.1123and 215.4555 respectively. The relationship between the thermal resistance and Reynolds number are illustrated in **Fig.15**. It can be noticed that the thermal resistance is inversely proportional to the Reynolds number for all heat sinks.

4.3 Simulation Results

The conjugate heat transfer investigation of fins is done by utilizing commercial available FLUENT 15 software and turbulence module is utilized to represent for turbulence wonder. Standard k-ε model is utilized for turbulence model. Conjugate heat transfer simulation work consists of analysis of both conduction and convection heat transfer processes. The air flows over the fins at the interface regions of fluid and solid. The momentum equations and turbulence-modeling equations are main equations solved for fluid flows are. Solution of these Navier-Stokes equations gives the velocity vectors and pressures in the fluid flow region. FLUENT 15 have ability to solve Navier-Stokes equations with standard k-ε applied turbulence model. By applying the interface boundary conditions at the coupled region, temperature distribution along the length of the fin obtain by solving the energy equation for both fluid (air) and solid (aluminum) regions. The effects of heat flux and Reynolds number on the temperature distribution in the heat sinks have been presented by Fluent through series of numerical calculations. The results are committed to the local temperature distribution in heat sinks. **Fig.16** presents the filled contour of temperature of heat sink at heat flux of 23924 W/m^2 and air velocity of 2 m/s in a wind tunnel for different configuration of fins. The temperature is least at heat sink's upper right and left parts when contrasted to center part of the heat sink due to more air flow circulation in sides of heat sink. For all of the heat sinks, it is seen that their centers are the hottest spots since the intensity of heat transfer between aluminum and air is in its peak near the heat source at the bottom plate. For genuine cases, the middle would not be as hot as the present simulations predict, due to the swirl. The cooling becomes less efficient at other sides of the heat sink. The performance of cross-cut, perforated and perforated-cut fin heat sinks model are better when compared to all fill fin heat sink models due to quickly heat dissipation to atmosphere as an after effect of increment surface area exposed to air and exasperates air flow. **Figs. 17** to **22** show the velocity vectors of flow in the fluid computational domain for all simulated heat sinks for a heat flux of 23924 W/m^2 and air velocity of 2 m/s in a wind tunnel. It is clear that the higher velocity of flow exists on the top and around the heat sink. This common phenomenon for all heat sinks was observed. It can also be seen that the maximum velocity at the top of heat sink causes temperature changes at the height of fin. From the comparison of different heat sinks it is also observed that the highest velocity of flow exists at the top of the perforated and perforated-cut heat sinks. The numerical variation of heat transfer coefficient with the heat flux and Reynolds number are shown in **Fig. 23** and **Fig. 23** respectively. To compare the results with experimental values, the heat flux and Reynolds number similar to the experimental tests. The comparisons with experimental results in **Fig. 10** and **Fig. 13** show similar thermal performances. The difference in the value of heat transfer coefficient between the numerical and experimental results is due to assumptions of the numerical simulation and uncertainty of measurement. For future work in the experimentation, to decrease the test errors that are brought about measurements, it is proposed that temperatures must be measured at more locations in the base of heat sink as well as at exit of the wind tunnel.

5. CONCLUSIONS

In this paper, thermal performance of different arrangements heat sinks were evaluated numerically and experimentally. The results acquired in the numerical simulation were in good agreement with the experimental results for the same operating conditions that was considered for this investigation. The heat transfer coefficient and Nusselt number are increased as heat flux and Reynolds number are increased for all heat sinks. Therefore, for each heat sink, as the heat flux and the Reynolds number increase, the thermal resistance decreases. The perforated-cut heat sink demonstrates the greatest heat transfer coefficient and the minimal thermal resistance. The percentage effectiveness of fin arrays to plate fin arrays are: 19.51%, 16.60%, 6.90%, -1.47% and -6.52% for perforated-cut, cut, perforated, serpentine and zigzag fins respectively.

REFERENCES

- Ali A. F. Al- Hamadani. and Abbas Jassim Jubear .,2015, *Numerical Simulation of Natural Convection Heat Transfer from Interrupted Rectangular Fins,* Journal of Engineering, Vol.21, pp(55–69).

- Amol B. Dhumne. and Hemant S. Farkade .,2013, *Heat Transfer Analysis of Cylindrical Perforated Fins in Staggered Arrangement,* International Journal of Innovative Technology and Exploring Engineering (IJITEE), Vol.2, Issue.5, pp(225–230).

- Arularasan R. and Velraj R .,2008, *CFD Analysis in a Heat Sink for Cooling of Electronic Devices,* International Journal of The Computer, the Internet and Management, Vol. 16,No.3 , pp(1–11).

- -Kamal K.Sikka, Kenneth E. Torrance, C. U. Scholler and P. I. Salanova .,2002**,** *Heat Sinks with Fluted and Wavy Fins in Natural and Low-Velocity Forced Convection***,** IEEE Transactions on Components and Packing , Vol.25, No.2, pp(283–292).

- Kavita H. Dhanawade, Vivek K. Sunnapwar and Hanamant S. Dhanawade .,2014, *Thermal Analysis of Square and Circular Perforated Fin Arrays by Forced Convection,* International Journal of Current Engineering and Technology, Vol. 2 , pp(109–114).

- Mehedi Ehteshum, Mohammad Ali, Md.Quamrul Islam, Muhsia Tabassum.,20015, *Thermal and Hydraulic Performance Analysis of Rectangular Fin Arrays with Perforation Size and Number,* Procedia Engineering, Vol.105 , pp(184–191).

- Mohamed H.A. Elnaggar.,2015, *Heat Transfer Enhancement by Heat Sink Fin Arrangement in Electronic Cooling,* Journal of Multidisciplinary Engineering Science and Technology (JMEST), Vol.2 , Issue 3, pp(457–460).

- Tae Young Kim, Sung Jin Kim.,2009, *Fluid Flow and Heat Transfer Characteristics of Cross-Cut Heat Sinks,* International Journal of Heat and Mass Transfer, Vol.52 , pp(5358–5370).

NOMENCLATURE

A=heat transfer area, m^2
B=base height, m
C=cross-cut length, m
D_h=hydraulic diameter, m
d=perforated diameter, m
H=height of fins, m
h=connection heat transfer coefficient, $W/m^2\ ^oC$
k=thermal conductivity, $W/m\ ^oC$
L=length of heat sink, m
$\dot{m}$=mass flow rate, kg/s
Nu=Nusselt number
N_f= number of fins
N_p= number of perforated
Re=Reynolds number
Rth=thermal resistance, $^oC/W$
S= channel width, m
T=temperature, ^oC
t=fin thickness, m
V=velocity, m/s
W=width of heat sink, m

GREEK SYMBOLS

ρ= density, kg/m^3
μ =dynamic viscosity, $N\ s/m^2$
ε = Percentage improvement of fins

SUBSCRIPTS

a=air
av=average
in=inlet
N=convection
out=outlet
S= base
T=total
w=win tunnel

Figure 1. Photographic picture for the experimental apparatus.

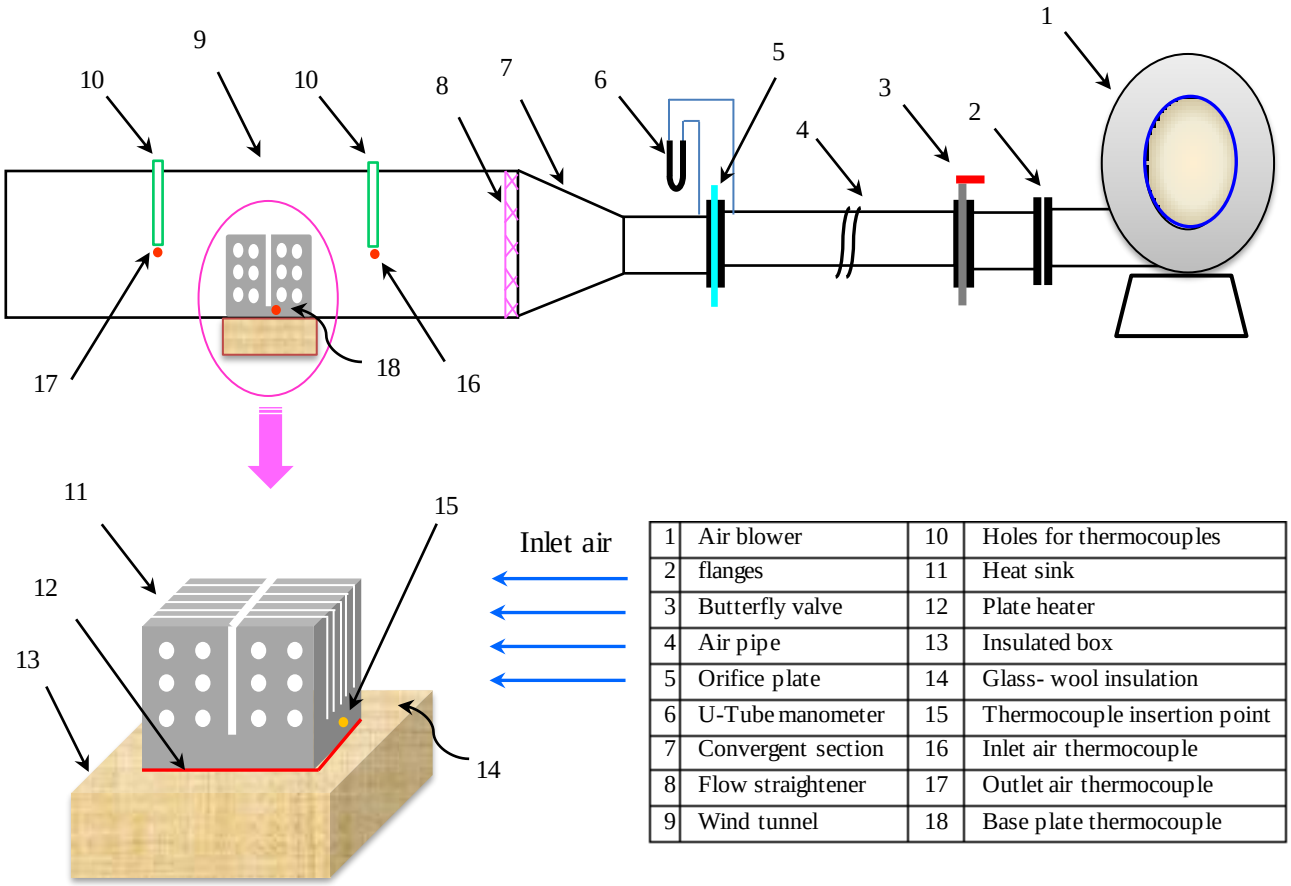

1	Air blower	10	Holes for thermocouples
2	flanges	11	Heat sink
3	Butterfly valve	12	Plate heater
4	Air pipe	13	Insulated box
5	Orifice plate	14	Glass- wool insulation
6	U-Tube manometer	15	Thermocouple insertion point
7	Convergent section	16	Inlet air thermocouple
8	Flow straightener	17	Outlet air thermocouple
9	Wind tunnel	18	Base plate thermocouple

Figure 2. Schematic diagram for experimental setup.

Figure 3. Wind tunnel.

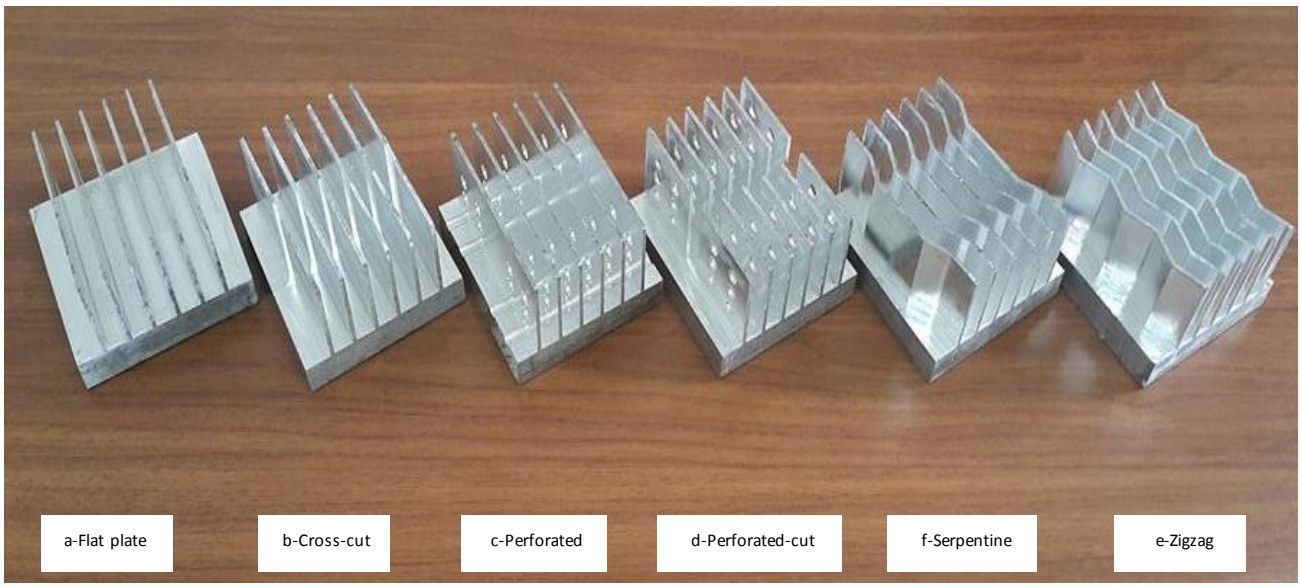

Figure 4. The configurations of all heat sinks.

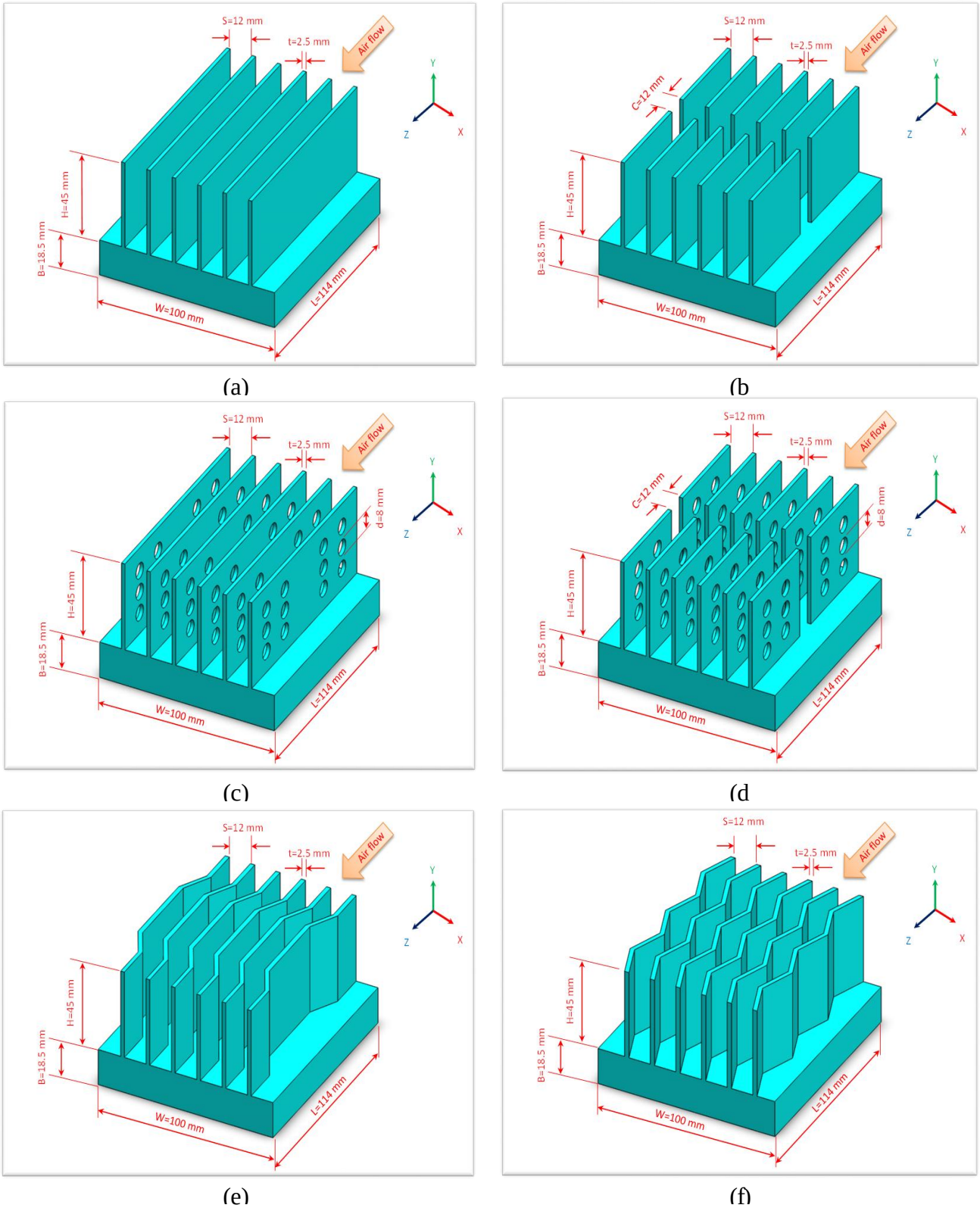

Figure 5. The geometry of the heat sinks: a-flat plate, b- cross-cut, c- perforated, d- perforated cross-cut, e- serpentine and f- zigzag.

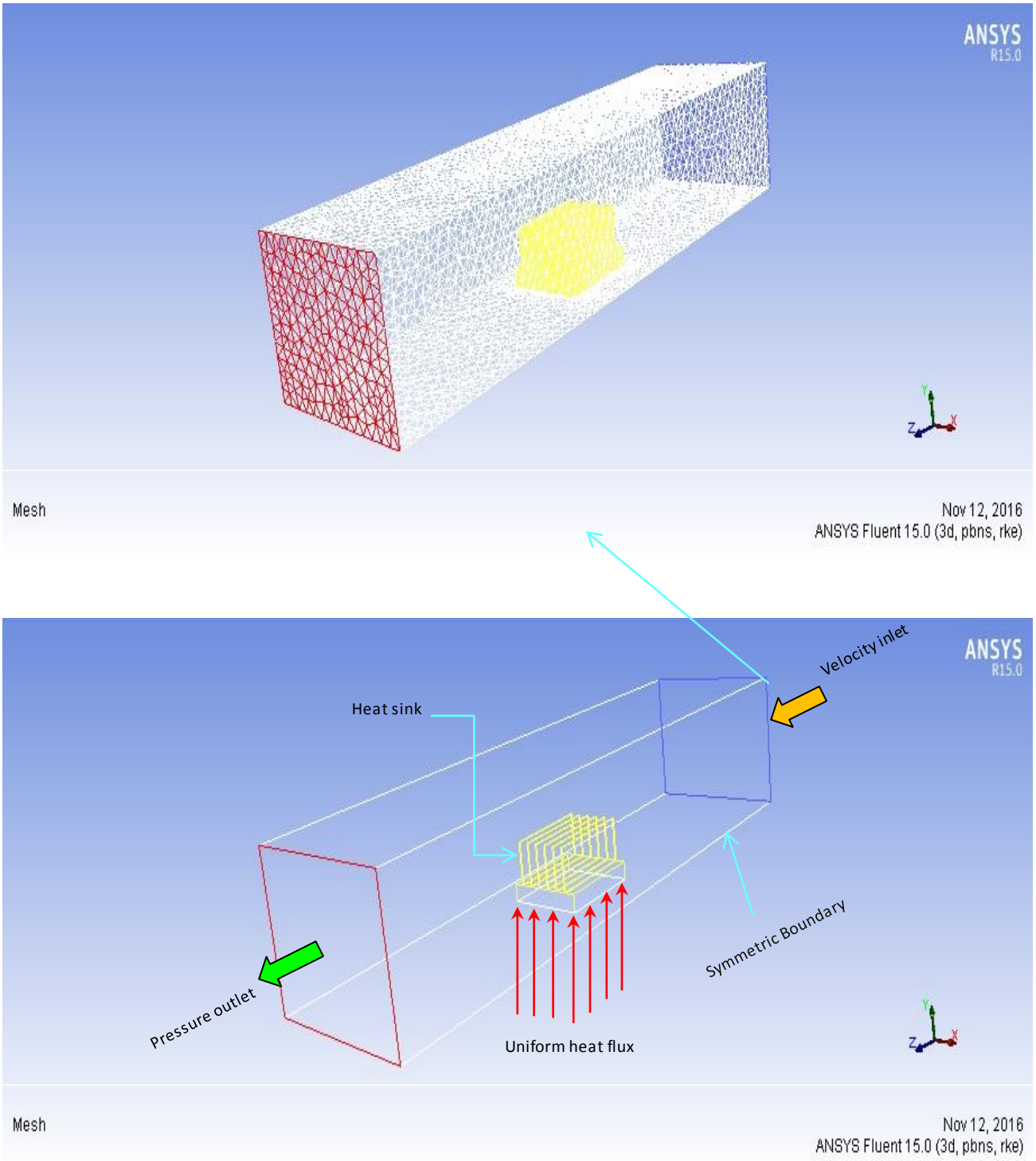

Figure 6. Computational domain and mesh distribution of the modeling.

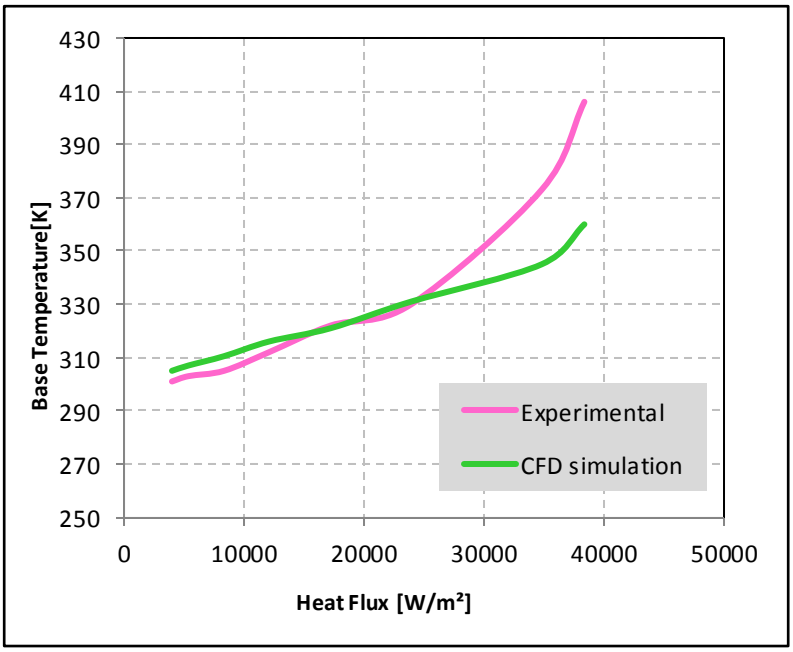

Figure 7. Comparison of experimental and numerical analysis.

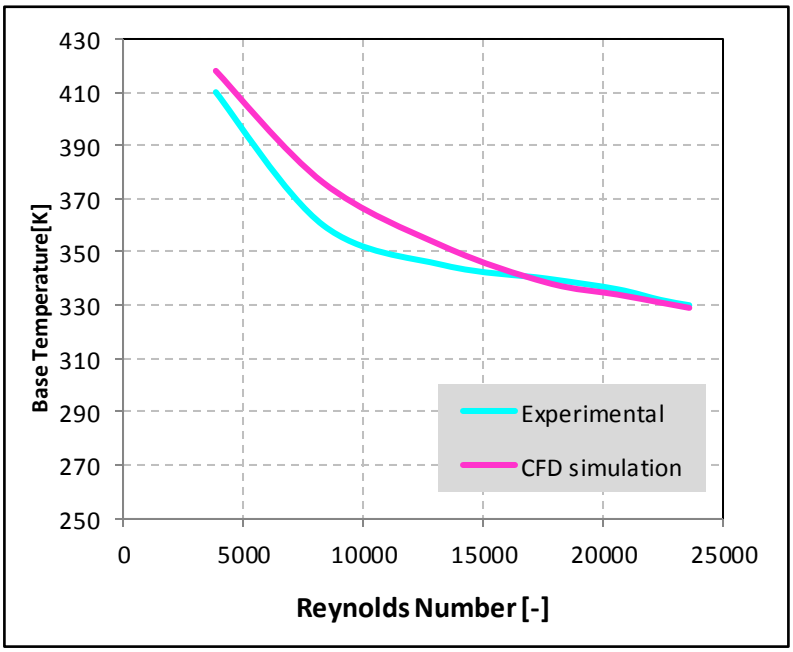

Figure 8. Comparison of experimental and numerical analysis.

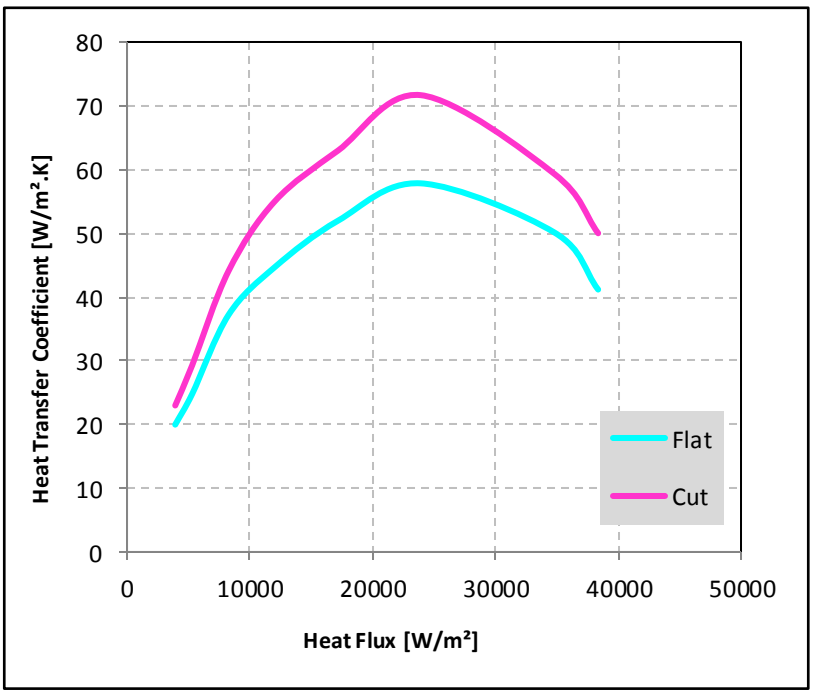

Figure 9. Variation of heat transfer coefficient with different heat fluxes for flat palte and cross-cut heat sinks.

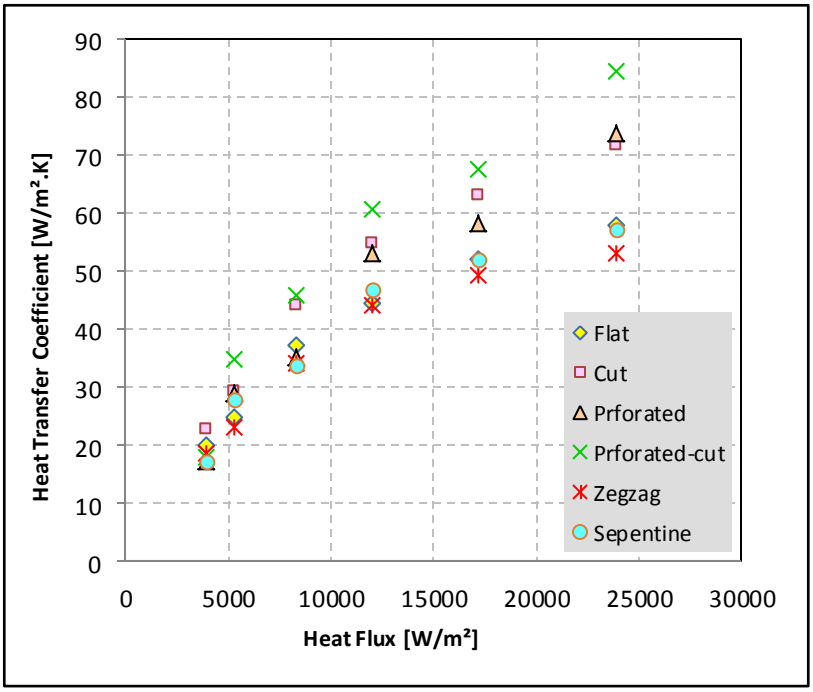

Figure 10. Variation of heat transfer coefficient with different heat fluxes for all heat sinks.

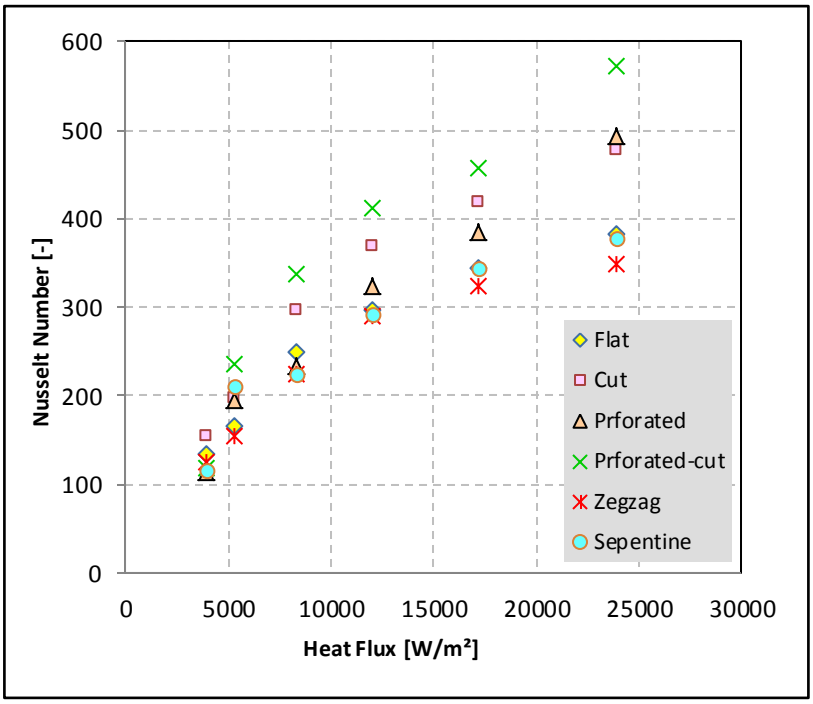

Figure 11. Variation of Nusselt number with different heat fluxes for all heat sinks.

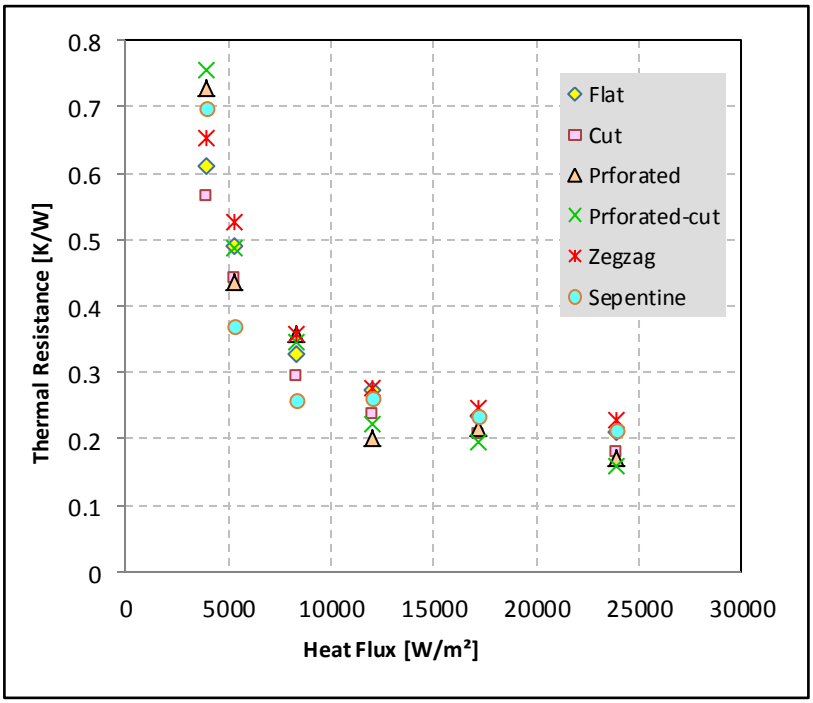

Figure 12. Variation of thermal resistance with different heat fluxes for all heat sinks.

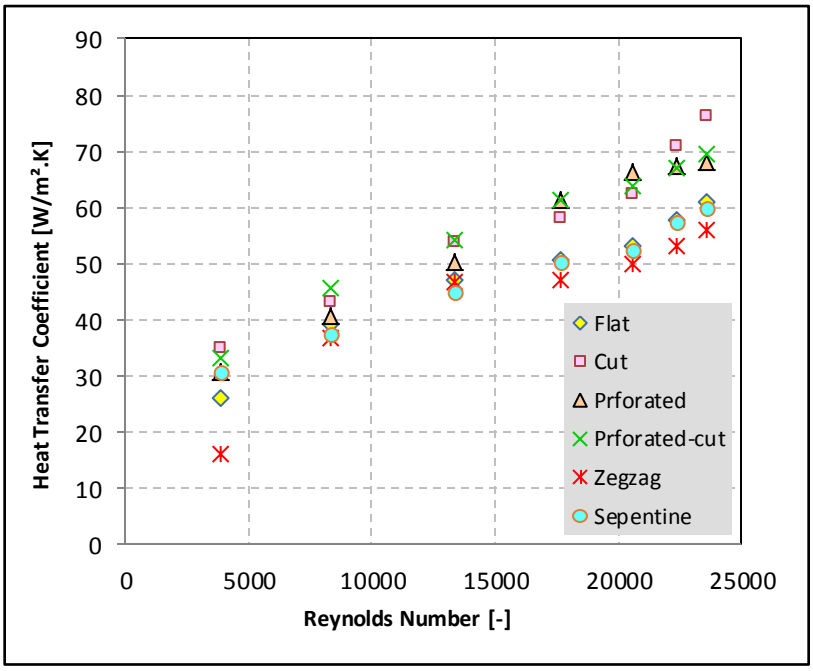

Figure 13. Variation of heat transfer coefficient with Reynolds number for all heat sinks.

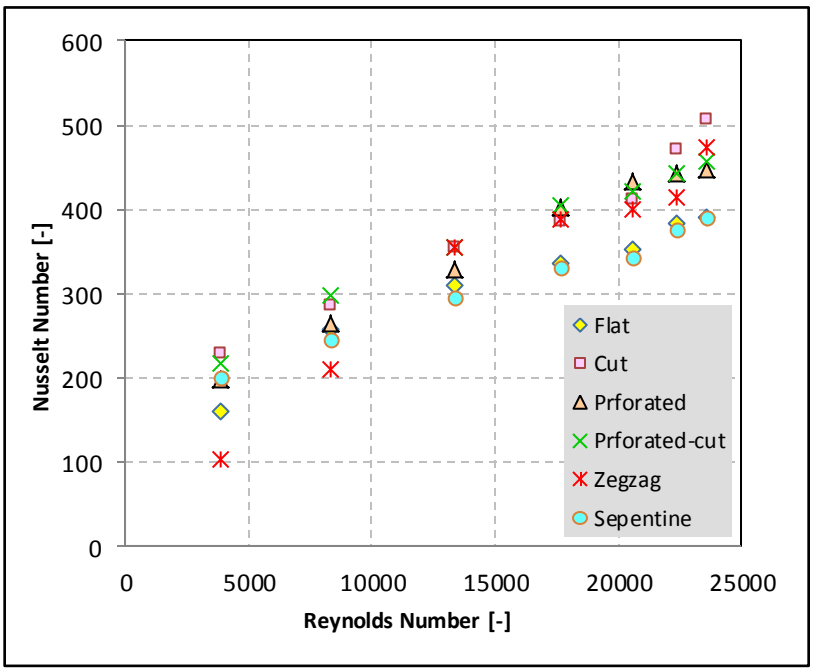

Figure 14. Variation of Nusselt number with Reynolds number for all heat sinks.

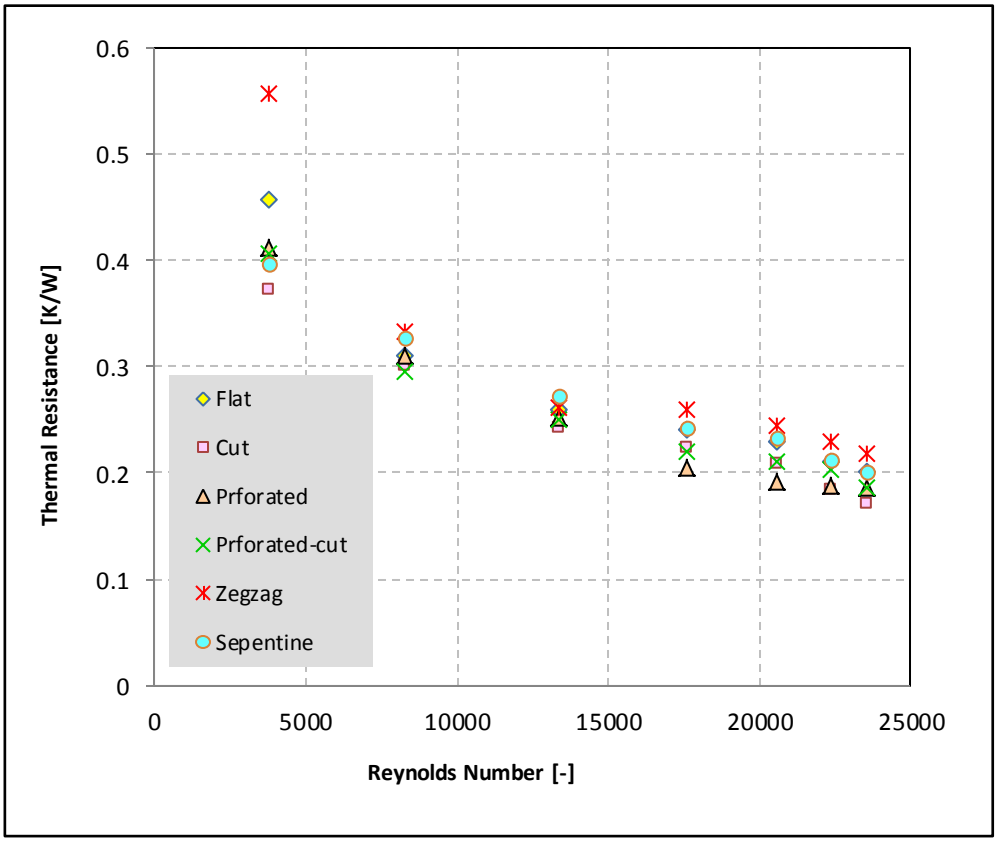

Figure 15. Variation of thermal resistance with Reynolds number for all heat sinks.

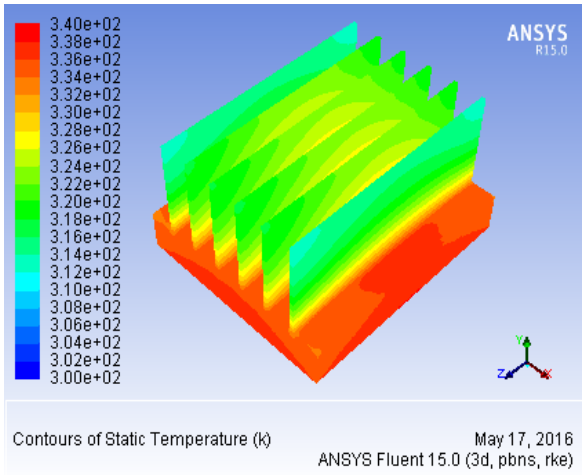

(a)

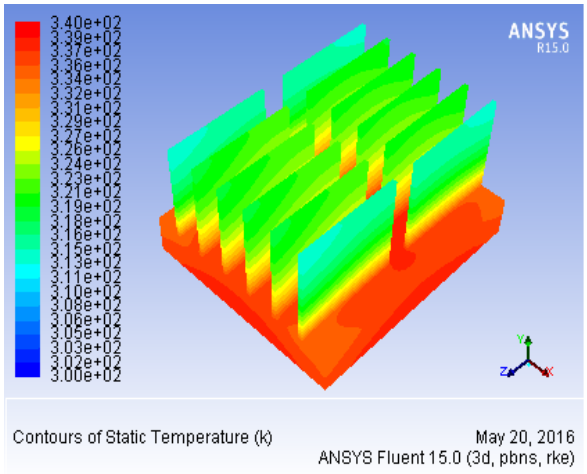

(b)

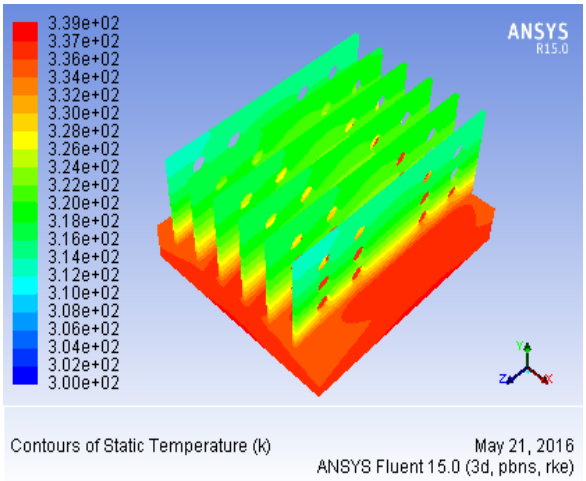

(c)

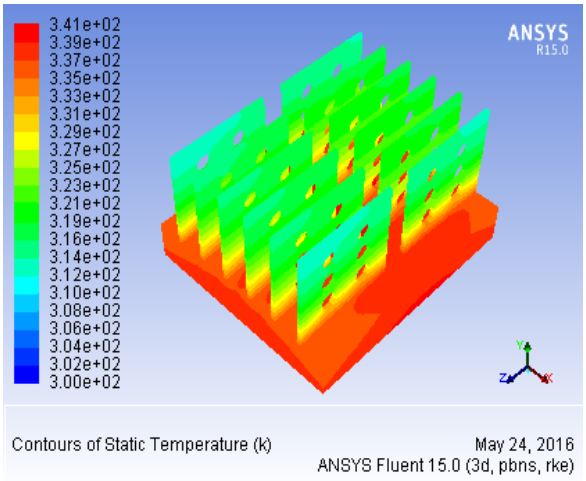

(d)

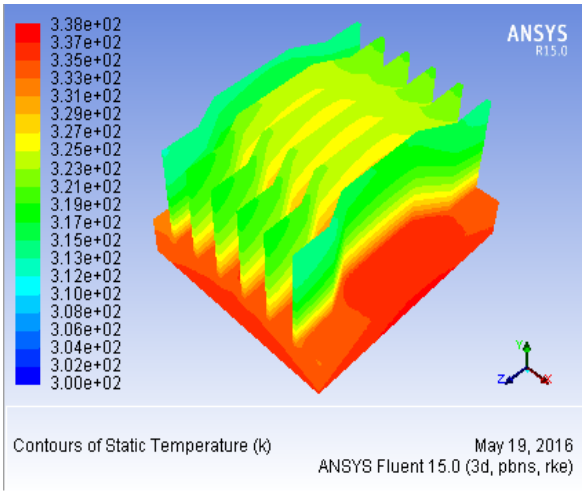

(e)

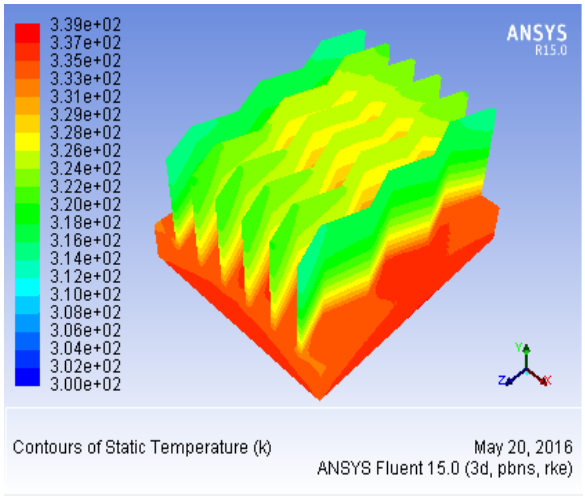

(f)

Figure 16. Temperature contour of the heat sinks: a-flat plate, b- cross-cut, c-perforated, d-perforated cross-cut, e- serpentine and f- zigzag.

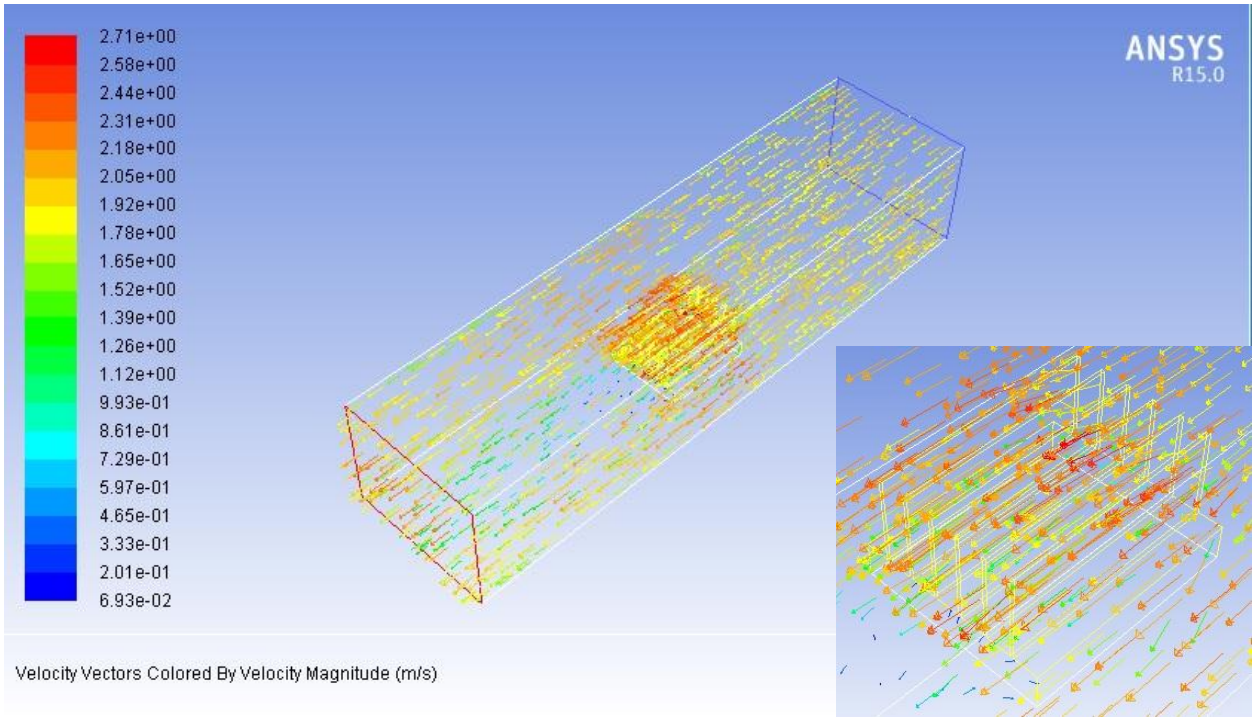

Figure 17. Velocity vectors for flat plate heat sink.

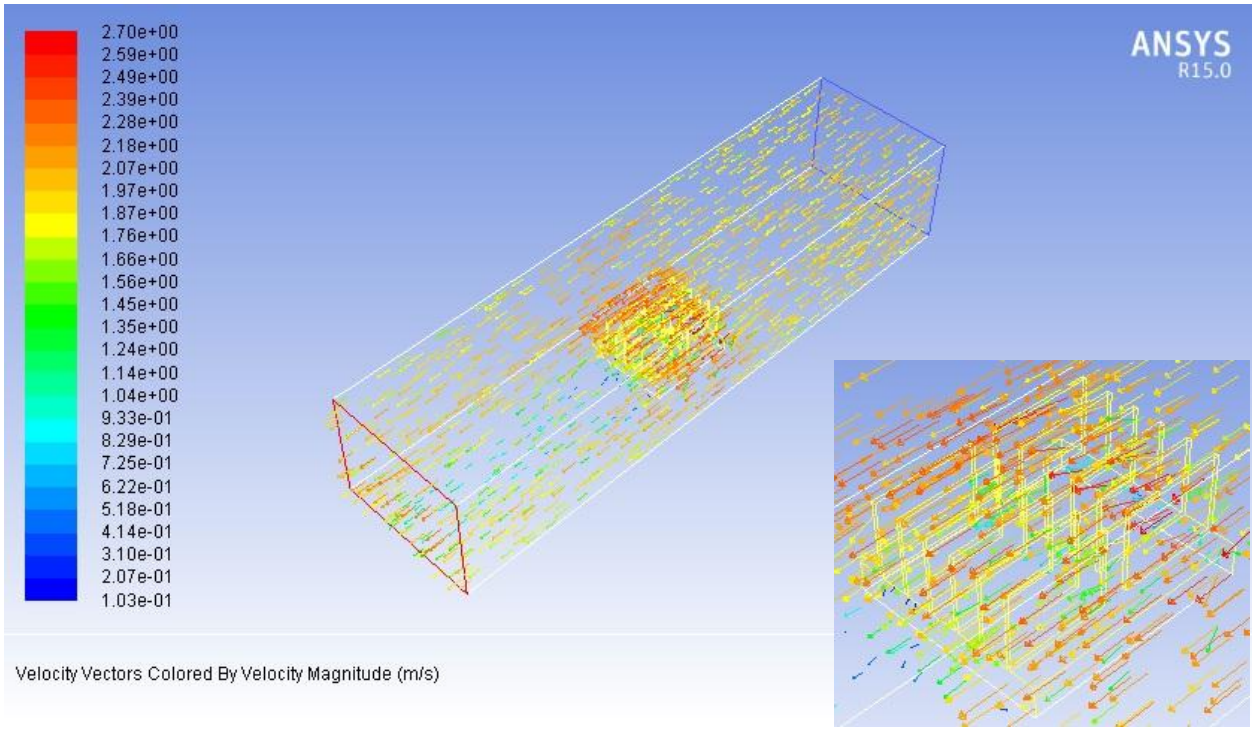

Figure 18. Velocity vectors for cross-cut heat sink.

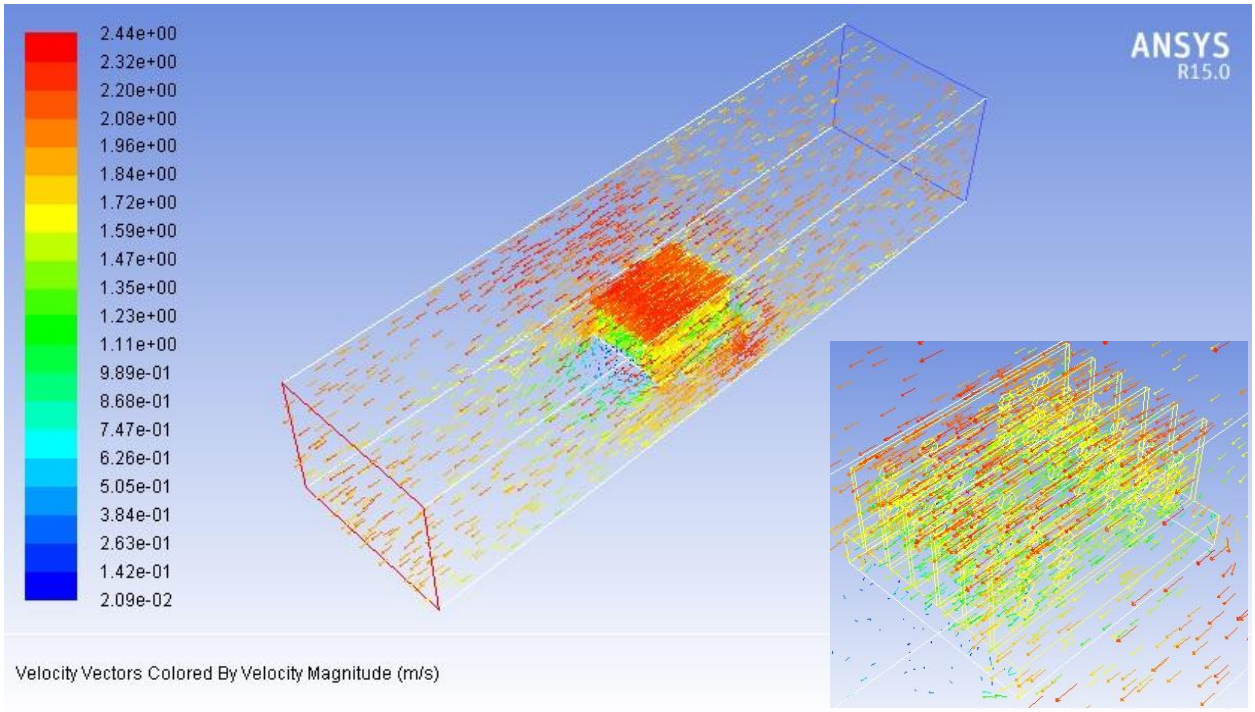

Figure 19. Velocity vectors for perforated heat sink.

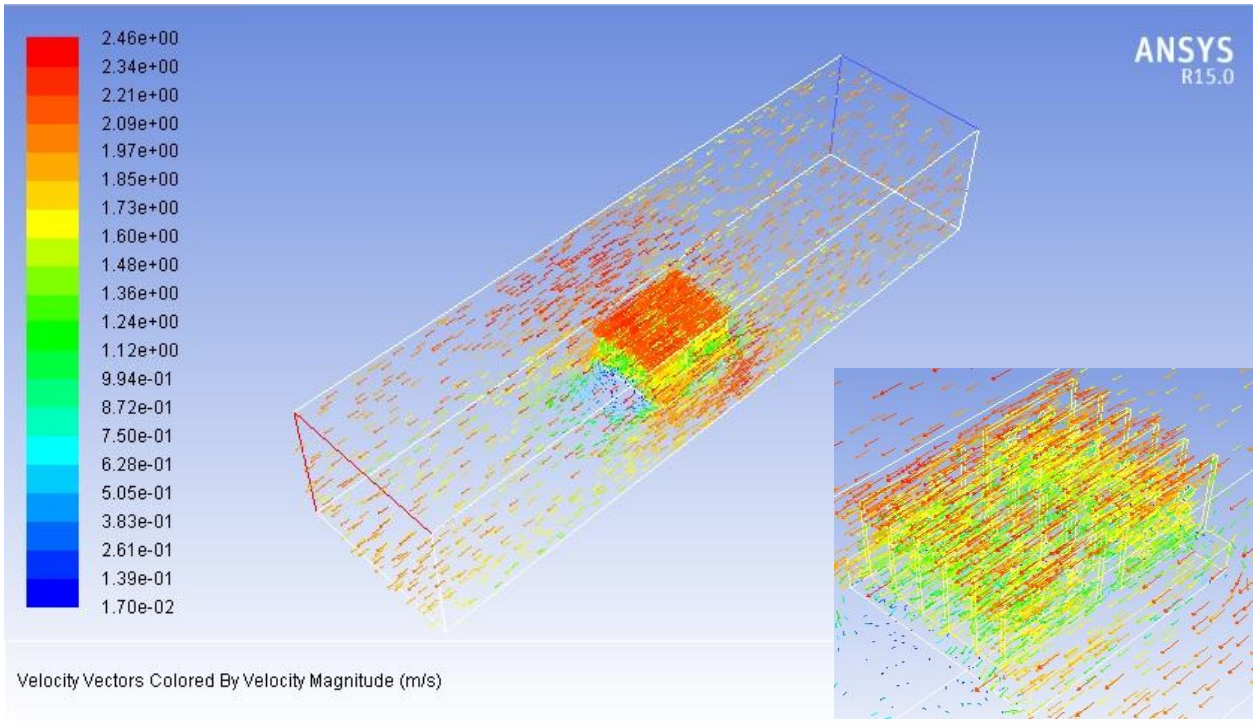

Figure 20. Velocity vectors for perforated-cut heat sink.

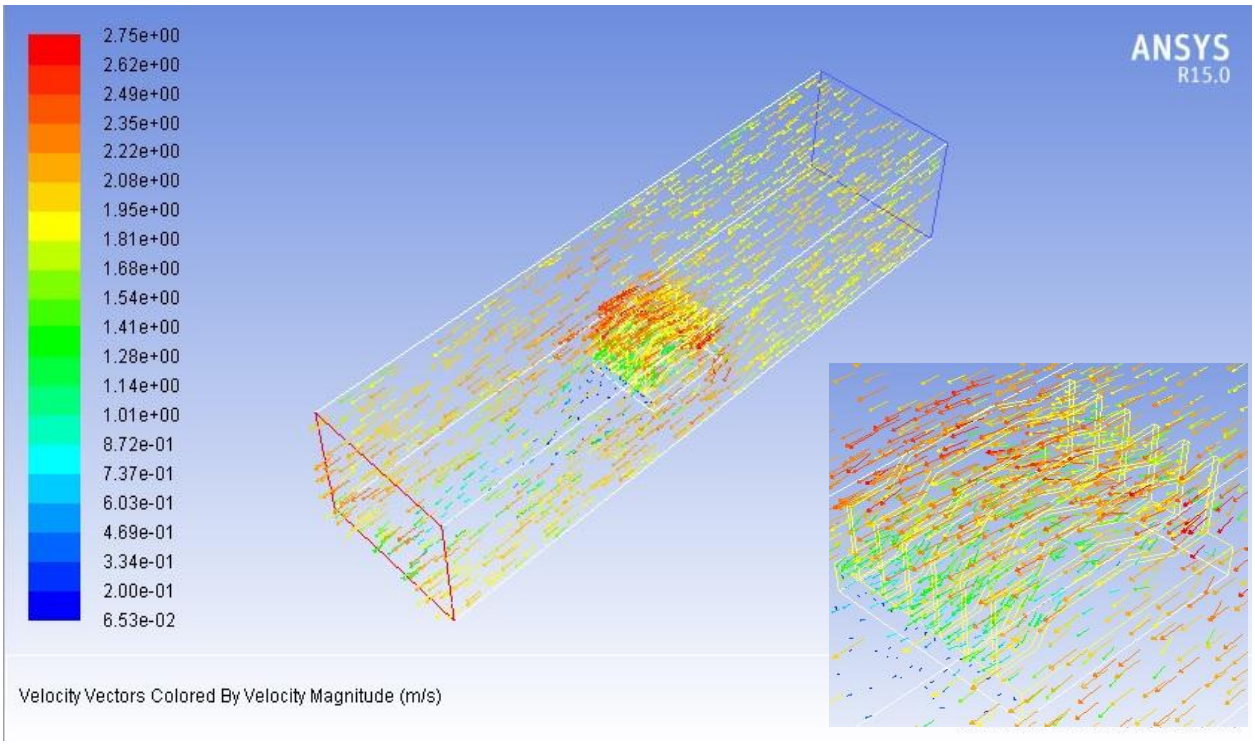

Figure 21. Velocity vectors for serpentine heat sink.

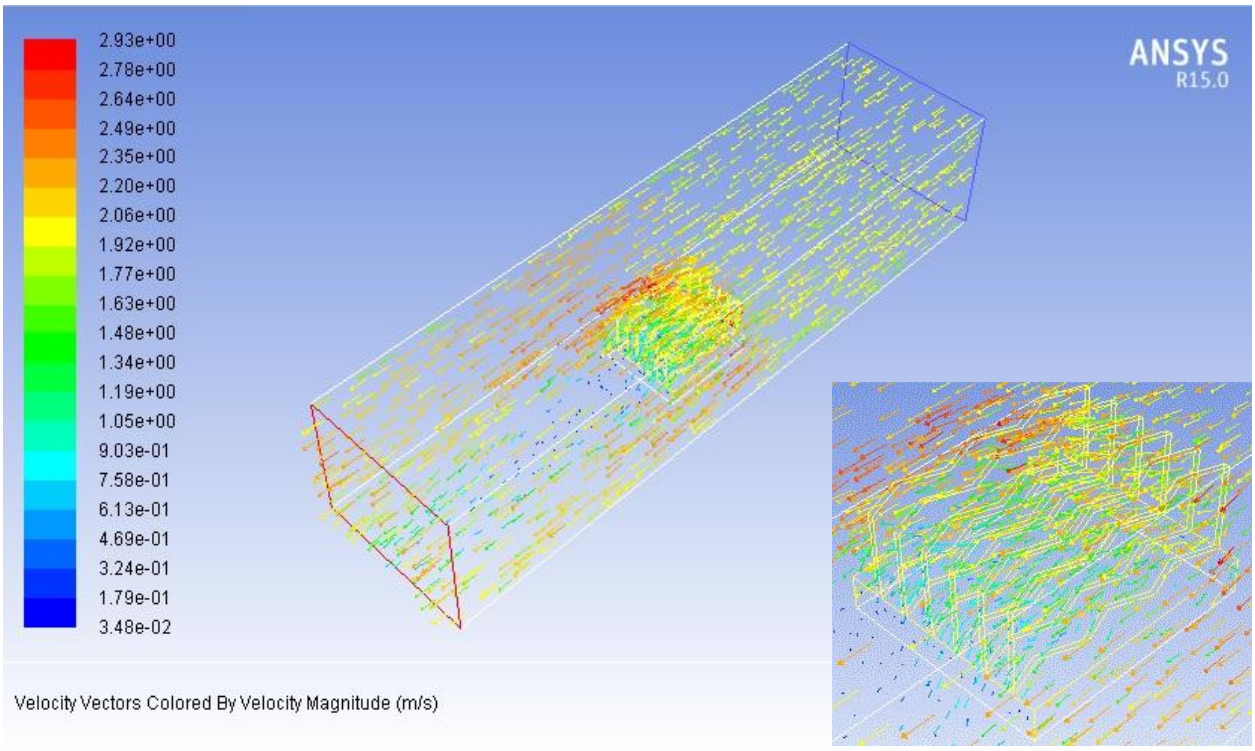

Figure 22. Velocity vectors for zigzag heat sink.

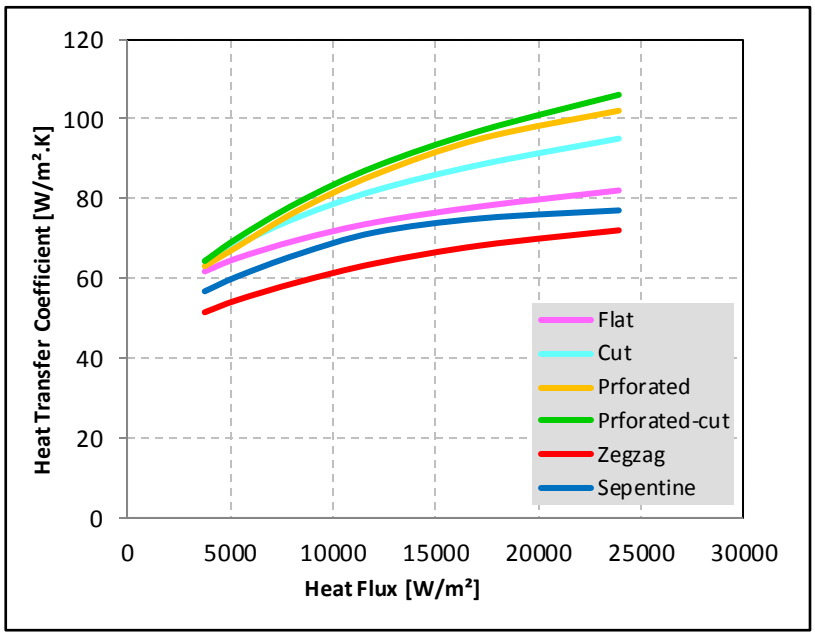

Figure 23. Numerical variation of heat transfer coefficient with different heat fluxes for all heat sinks.

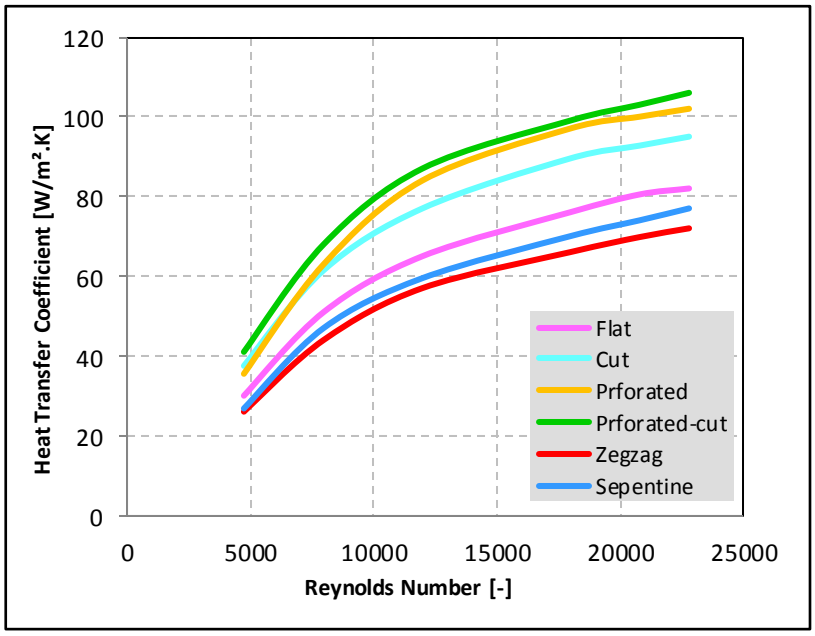

Figure 24. Numerical variation of heat transfer coefficient with Reynolds number for all heat sinks.

Compatibility between Hydraulic and Mechanical Properties of Ceramic Water Filters

Dr. Riyadh Z. Al Zubaidy
Professor
College of Engineering
University of Baghdad
azzubaidi@hotmail.com

Dr. Mahmoud S. Al-Khafaji
Assistant professor
Department of Building and Construction Engineering
University of Technology
41100@uotechnology.edu.iq

Riyadh J. M. Al-Saadi
Assistant lecturer
College of Engineering
University of Karbala
riyadhj62@yahoo.com

ABSTRACT

In this paper, ceramic water filters were produced by using ten mixtures of different ratios of red clay and sawdust under different production conditions. The physical properties of these filters were tested. The production conditions include five press pressures ranged from 10 to 50*MPa* and a firing schedule having three different final temperatures of 1000, 1070, and 1100˚*C*. The tests results of the physical properties were used to obtain best compatibility between the hydraulic and the mechanical properties of these filters.

Results showed that as the press pressure and the firing temperature are increased, the bulk density and the compressive and bending strengths of the produced filters are increased, while, the porosity and absorption are decreased. As the sawdust content is increased the bulk density and the compressive and bending strengths are decreased, while, the porosity and absorption are increased. High hydraulic conductivity is obtained at a firing temperature of 1070˚*C* when the sawdust content is less than 10%. Otherwise, it is increased as sawdust content and the firing temperature are increased. Filters made of mixture 92.5% red clay and 7.5% sawdust formed under a press pressure of 20*MPa* and a firing temperature of 1070˚*C* gave the best compatibility between hydraulic and mechanical properties. In this case, the hydraulic conductivity was 50*mm/day*, the compressive strength was 14*MPa*, and the bending strength was 10.8*MPa*.

Key words: ceramic water filters, water filtration, hydraulic conductivity, compressive strength, bending strength.

توافق الخصائص الهيدروليكية والميكانيكية لمرشحات الماء الخزفية

أ.د. رياض زهير الزبيدي
كلية الهندسة/ جامعة بغداد

أ.م.د. محمود صالح الخفاجي
قسم البناء والانشاءات/ الجامعة التكنولوجية

م.م. رياض جاسم محمد السعدي
كلية الهندسة/ جامعة كربلاء

الخلاصة

هدف هذا البحث انتاج مرشحات ماء خزفية باستخدام عشر خلطات بنسب مختلفة من الطين الاحمر ونشارة الخشب كمضاف وتحت ظروف انتاج مختلفة وليتم فحص خواصها الفيزيائية. تضمنت ظروف الانتاج خمسة ضغوط للكبس تراوحت بين 10 و 50 ميكا باسكال وجدول للحرق بثلاث درجات نهائية مختلفة 1000 و 1070 و 1100°م. استخدمت نتائج فحص الخواص الفيزيائية في تحديد افضل توافق بين الخواص الميكانيكية والهيدروليكية لهذه المرشحات.

اشارت نتائج الاختبارات بان زيادة كل من ضغط الكبس وحرارة الحرق تؤدي الى زيادة كثافة ومقاومتي الانضغاط والانحناء للمرشحات المنتجة بينما تقل كل من المسامية والامتصاص لها. تقل كثافة ومقاومتي الانضغاط والانحناء للمرشحات المنتجة وتزداد كل من المسامية والامتصاص بزيادة محتوى نشارة الخشب. تم الحصول على أعلى ايصالية هيدروليكية عند درجة حرق مقدارها 1070°م عندما يكون محتوى نشارة الخشب أقل من 10% وبخلاف هذه النسبة تزداد الايصالية الهيدروليكية بزيادة نسبة نشارة الخشب ودرجة الحرارة. وجد بان المرشحات المنتجة باستخدام خلطة مكونة من 92.5% من الطين الاحمر و7.5% من نشارة الخشب والمشكلة تحت ضغط كبس مقداره 20 ميكا باسكال ودرجة حرق مقدارها 1070°م تعطي أفضل توافق بين الخواص الهيدروليكية والميكانيكية. وفي هذه الحالة كان مقدار الايصالية الهيدروليكية 50ملم/يوم ومقاومة الانضغاط 14 ميكا باسكال ومقاومة الانحناء 10.8 ميكا باسكال.

1. INTRODUCTION

The characteristics of ceramic filters are affected by mixture ratios of raw materials that are used to produce these filters and the process of production. Ceramic filters are made of mixtures of raw materials such as clay, additives, fluxes, and water. Different methods are used to form the shape of these filters such as pressing, slip casting, and extrusion. Firing is the final process for producing ceramics. It is important to select a suitable time schedule program of firing to produce ceramic suitable for water filtration.

Many studies and researches were conducted to obtain the characteristics of ceramic filters produced under different conditions. Most of these are focused on the materials and additives used in their production and their applications. There is a lack in studies that relates the mechanical with the hydraulic properties of the produced filters.

This study aims to produce ceramic water filters discs made of different ratios of red clay and sawdust as an additive under different production conditions and to test their physical properties. The tests results will be used to obtain the best compatibility between the hydraulic and the mechanical properties of ceramic water filters.

A composition of clay materials was tested by using X-Ray diffractions and chemical tests. Sawdust was selected as an additive that was added with different ratios to the ceramic mixture to manipulate the final product porosity. Hydraulic and mechanical properties of the produced ceramic filters were tested and analyzed. The main physical properties that were tested include porosity, hydraulic conductivity, compressive strength, and bending strength.

2. RAW MATERIALS

Ceramic filters were produced from different mixtures of red clay, sawdust and water. The used red clay is the type that is widely used in ceramic artworks and is available at local markets and is of low cost. The red clay was well washed in a container to wash out salts content and then it was left to dry in a room temperature for two days. The clay was then dried by using an oven at $110^{\circ}C$ for $24hr$. A rubber hummer was used to crash the dried clay and then grinded by using a grinding machine. The graded clay was sieved by using $1mm$ sieve size and then it was ready to be used for the production of ceramic filters mixtures. X-Ray diffractions test was carried out on samples of the prepared clay. The results of this test are presented in **Fig. 1**. The major clay minerals of these samples are Mica and Kaolinite, and the non-clay minerals are Quartz, Orthoclase, and Calcite minerals. A chemical analysis was carried out on the red clay samples by the laboratories of the Iraqi State of Geological Survey by using the gravimetric wet analysis. The results of this analysis and of the normative minerals analysis are listed in **Table 1**. All contents of oxides in this analysis are presented as a weight percent. The percentage of clay minerals in the samples is 63%, including 49% Mica (Biotite) and 14% Kaolinite. The percentage of non-clay minerals is 37%, including 21.5% Calcite, 11.5% Quartz, and 4% Orthoclase. A particle size analysis was carried out on samples of red clay soil by using a laser particle size analyzer device. The granular analysis curve is shown in **Fig. 2**. The range of particle size of red clay is between $0.4\mu m$ and $30\mu m$. The reflection of the pulses of laser rays indicated that the particles size of the red clay has overall two main gradations, the first one is $0.8\mu m$ with percentage of about 31% and the second one is $4\mu m$ with percentage of about 69%.

Sawdust was selected to be used as an additive material that is widely used to control the porosity of the ceramic water filters. Sawdust can be easily grinded into fine and loose particles, available, and is cheap. A well grinded sawdust was brought from a local market. Results of the sieve analysis of this sawdust, **Fig. 3**, show that the grain size of sawdust varies between 75 and

425μm. Percentages of finer particles size of sawdust within the range of 75 and 90μm, 90 and 180µm, 180 and 425μm, are about 20, 60, and 20%, respectively.

Water is required to improve workability and plasticity of ceramic mixtures. Distilled water was added to mixtures of red clay and sawdust.

3. DESIGN OF MIXTURES

The weight ratios of red clay and sawdust as an additive and the water content can play a key role in the hydraulic and mechanical properties. To investigate the effect of adding sawdust as a percentage by weight to red clay, ten different mixtures were prepared with sawdust content varying between 0% and 25%. Details of these mixtures are presented in **Table 2**. Each mixture was coded starting from M1 to M10.

Each mixture was prepared carefully by mixing specific weight red clay and sawdust as a weight percentage by using a mixer until it becomes homogeneous. Then water is added at a ratio of 10% of the total weight of both the red clay and the sawdust. This water is added gradually to all mixtures with a good mixing. The mixture was then forced to pass through a sieve of 1*mm* in size to prevent any agglomerate that may occur during mixing. The mixture was stored in a sealed plastic bag for at least 24*hours* in refrigerator to prevent water evaporation and ensure uniform water distribution through the mixture.

To test the effect of particle size of sawdust on the porosity and hydraulic conductivity of ceramic filter disc, sawdust was divided into two categories. The first, having a particle size less than 90μm and the second having a particle size greater than 212μm. 10% sawdust of the first and second particle size category were used to prepare the M9 and M10 mixtures, respectively.

4. MOLDS

Steel molds were designed according to required shapes of ceramic filters. The required ceramic filters have three shapes, the first, has a disc shape of 3*cm* in diameter, which was used to test the physical properties of ceramic filters. The second one has solid cylindrical shape of 1*cm* diameter and 2*cm* height that was used for compression strength tests of ceramic materials according to **ASTM-C773-88 standards, 2006**. The third one has rectangular shape of 114*mm* length, 25.4*mm* width, and 12.7*mm* height which was used for bending strength (modulus of rupture) test of ceramic materials according to **ASTM-C674-88 standards, 2006**. Specific weight of a mixture is placed into the mold and then pressed until the required press pressure of forming is reached.

5. PRESS PRESSURES

A test was made to indicate roughly upper limit of press pressure required to form the ceramic discs. The test was made on a ceramic mixture sample of 90% red clay, 10% sawdust and 10% water content. The cylindrical steel mold was used and the range of the press pressures ranged between 10 to 170*MPa*. The press pressures were increased by an increment of 10*MPa* each time until reaching 170*MPa*. For each pressure, three cylindrical filters were produced. The filters were left for drying in the free air for more than 24*hours*. Then the compaction test was carried out for each filter. The average of three filters formed by the same press pressure was calculated. Results of these tests are presented in **Fig. 4**. The compressive strength increased generally when increasing the press pressure until reaching press pressure of 140*MPa*. After this value, increasing the press pressure tends to weaken the bonding of ceramic mixture body structure and reduce its compressive strength and ability of forming without flaws. Some trials on hydraulic tests were carried out on samples of ceramic filters obtained under different pressures shows that

very low hydraulic conductivity was obtained as the press pressure is more than 50*MPa*. Accordingly, the selected press pressures in this study have the values 10, 20, 30, 40, 50*MPa*.

Press pressure is applied to the mixture inside the mold by using an automatic compression machine at a constant rate of loading of 0.1*KN/sec* until the required pressure is reached.

6. FIRING TEMPERATURE

Firing temperature controlled the sintering behavior on the body of ceramic materials. The sintering process has two major phases; the first one is called a solid state phase of sintering that occurred below the firing temperature of 950˚C, and the second phase is called the liquid phase of sintering that occurred above the firing temperature of 950˚C, **Hettiarachchi, et al., 2010**. The liquid phase of sintering is affecting the densification of clay more than the solid state phase. The amount and viscosity of liquid phase are controlled by the firing temperature and the content of quartz and fluxes oxides such as calcium oxide in the red clay material. The quartz has unstable behavior and has different effect than fluxes oxides on the liquid phase with increasing of firing temperature. So, the temperature is considered the main control on the amount and viscosity of liquid phase. Therefore, it is important to indicate carefully the program of firing temperature. The firing program used in this study is shown in **Table 3**. The program includes three final firing temperatures 1000, 1070, and 1100˚*C* and twelve levels of rising and soaking temperatures. The temperature is increased from room temperature to 80˚*C* in 15*minutes* and a soaking time at 80˚*C* for 30*minutes*. During this period, all trapped water inside pores of ceramic filter is evaporated. Then the temperature was increased from 80˚*C* to 180˚*C* in 15*minutes* and soaking at 180˚*C* for 30*minutes*. During this period the samples are completely dried. The temperature is then increased from 180˚*C* to 330˚*C* in 15*minutes* and soaking at 330˚*C* for 30*minutes*. The water which is chemically combined with the molecular structure is completely derived out during this period. By rising the temperature from 330˚*C* to 550˚*C* in 15*minutes* and soaking at 550˚*C* for 45*minutes*, an irreversible change of chemical occurred that is known as dehydration. By rising the temperature from 550˚*C* to 800˚*C* within 15*minutes* and soaking at 800˚*C* for 45*minutes*, the organic and inorganic materials are burnt. All sawdust will be burnt during this period. By rising the temperature from 800˚*C* to *1000˚C*, to 1070˚*C* or to 1100˚*C* for 15*minutes* and soaking at each of these last temperatures for 60*minutes*, vitrification of the red clay components will be occurred.

7. PRODUCTION OF FILTERS

In order to produce ceramic water filter discs, cylindrical form of filters, and rectangular form of filters, the mixture samples were weighted in electrical sensitive balance and then pressed inside a specified mold using automatic compression machine. The specimens were left to dry during minimum 72*hours* and then fired inside a programmed electrical kiln to a specified temperature according to firing program mentioned in **Table 3**. The ceramic filters were left inside the kiln to cool gradually.

Three hundred and sixty-six ceramic discs of 3*cm* diameter were produced with different thicknesses made of mixtures M1 to M10. Twenty hundred and seventy of both cylindrical and rectangular shapes ceramic filters were produced using mixtures M1 to M6. Samples of these filters are shown in **Fig. 5**.

Table 4 shows the produced ceramic filter discs for all test mixtures. Three samples were fired for each ceramic filter disc of mixtures M1 to M6 and the average was considered for each disc. All samples of ceramic filter disc of mixtures M7 and M8 were broken after firing due to the high percent of sawdust content which makes them weak. The same details in **Table 4** for mixtures M1 to M6 are used to produce ceramic filters of cylindrical and rectangular shapes for

mechanical tests. Also three samples were fired for each ceramic filter of cylindrical and rectangular form and the average was taken for each shape. Only three samples of ceramic filter discs for each of mixtures M9 and M10 were produced to test the effect of particle size of sawdust on its porosity and hydraulic conductivity. The porosity was measured according to the **ASTM-C 373-88 standards, 2006**. The hydraulic conductivity was measured by the constant head method.

8. TESTING OF PHYSICAL PROPERTIES

The tested physical properties of ceramic filters were the change of dimensions, the bulk density, the apparent porosity, the absorption, the hydraulic conductivity, the compressive strength, and the bending strength.

The change in diameter before and after firing was used as a measure of the percentage of change in the dimension of the filter discs. This change is calculated according to the following equation:

$$P_d = \left|\frac{d_a - d_b}{d_b}\right| \times 100 \quad (1)$$

where:

P_d= percentage of change in diameter of ceramic filter disc,
d_b= the diameter of ceramic filter disc before firing, mm, and
d_a= the diameter of ceramic filter disc after firing, mm.

The bulk density, apparent porosity and absorption of the ceramic filter discs were tested according to **ASTM-C 373-88 standards, 2006**. The following equations are used to determine these properties:

$$\rho_a = \frac{M_d}{M_{sa} - M_s} \quad (2)$$

$$n = \frac{M_{sa} - M_d}{M_{sa} - M_s} \times 100 \quad (3)$$

$$W_a = \frac{M_{sa} - M_d}{M_d} \times 100 \quad (4)$$

where:

M_d= the dry mass, gm
M_{sa}= the saturated mass, gm
M_s= the suspended mass in water, gm
ρ_a= bulk density, gm/cm^3,
n= apparent porosity, $\%$, and
W_a= water absorption, $\%$

The hydraulic conductivity (K) of the ceramic water filter discs is measured using laboratory test known as constant head method. This test was conducted by using a local manufactured device shown in **Fig. 8**. The hydraulic conductivity is calculated according to Darcy law as follows:

$$K = \frac{V\,T_a}{A_c\,h\,t} \quad (5)$$

where:

K= hydraulic conductivity, *cm/min*.
V = collected volume of water, cm^3.
T_a = thickness of ceramic filter disc, *cm*,
Ac = cross sectional area of ceramic filter disc, cm^2,
h = head difference (constant head), *cm*, and
t = time required to collect volume of water, *min*.

The standard hydraulic conductivity, Ks was calculated for the ceramic filter discs of 3cm by using the following equation, **Lamb, 1969**:

$$K_s = K\frac{\mu}{\mu_{20}} \tag{6}$$

where:

K=measured saturated hydraulic conductivity, *cm/min*,
μ=dynamic viscosity of water at any temperature, *Pa.s*, and
μ_{20} =dynamic viscosity of water at 20˚*C*, *Pa.s*.

The compression test procedure was applied on the cylindrical ceramic filters according to **ASTM-C773-88 standards, 2006**. The compressive strength is calculated according to the following equation:

$$\sigma_c = \frac{F_c}{A_b} \tag{7}$$

where:

σ_c= compressive strength of the cylindrical ceramic filter, *MPa*.,
F_c = total load on the cylindrical ceramic filter at failure, *N*, and
A_b = area of the bearing surface of the cylindrical ceramic filter, mm^2.

The bending test (modulus of rupture test) procedure was applied on rectangular ceramic filters according to **ASTM-C674-88 standards, 2006**. The bending strength (modulus of rupture) is calculated according to the following equation:

$$M = \frac{3F_b L}{2b\,d^2} \tag{8}$$

where:

M = modulus of rupture (bending strength), *MPa*.,
F_b = load at rupture, *N*,
L = distance between supports, *mm*,
b = width of the rectangular ceramic filter, *mm*, and
d = thickness of the rectangular ceramic filter, *mm*.

9. RESULTS ANALYSIS

The ceramic filters produced by using the M7 and M8 mixtures were so soft and can be disintegrated easily by hand. This is referred to their high content of sawdust, which is 20 and 25% in M7 and M8 mixtures, respectively. Produced filters made of these two mixtures were excluded from further tests.

Table 5 presents the results of tests that were carried out to investigate the effects of sawdust particles size on the porosity and hydraulic conductivity of the ceramic filter disc. These tests were carried out on filters made of the M9 and M10 mixtures. Results indicate that there is no significant effect of the sawdust particle size categorizing into particle size less than 90μm and greater than 212μm on both the porosity and hydraulic conductivity of ceramic filter disc.

The results of all tested physical properties carried on filters made of M1 to M6 mixtures are presented in **Table 6** that include the change in the dimensions due to firing and their bulk density, porosity, absorption capacity, hydraulic conductivity, compressive strength, and bending strength.

Generally, there was a reduction in the dimensions of the ceramic filter discs compared to their original values before firing. This reduction is increased as firing temperature and percentage of sawdust content are increased and is remained constant as the press pressure is increased. The overall range of the reduction in their dimensions varies between 0.33% and 2.67%. The overall average of this reduction in dimensions was 1.59%. The maximum value of reduction in dimensions was observed in all filters made of M6 mixture under a firing temperature of 1100$^{\circ}C$ and whatever the press pressures are. This is referred to the high percentage of sawdust content and high firing temperature used in producing these filters. The minimum value of reduction in dimensions was noticed in all filters made of M1 mixture under the firing temperature of 1000$^{\circ}C$ and whatever the press pressures are. This may be referred to the absence of sawdust in this mixture and to the low firing temperature.

The bulk density of filter discs is increased as the press pressure and firing temperature are increased and it is decreased as the percentage of sawdust content is increased. The range of the bulk density of all tested ceramic filter varies between 1.16gm/cm^3 and 1.91gm/cm^3. The overall average of this variation in bulk density was 1.44gm/cm^3. The bulk density is affected simultaneously by the change in dimension and the final weight of the filters. Firing temperature and press pressure affect both the dimension, as was presented in the above, and the final dry weight of the filters. The dry weight of filter discs is decreased as the firing temperature is increased for the same conditions of press pressure and sawdust content. This is expected due to losing of some materials of the filters during firing. Different phases of chemical reactions that release gases and vapours take place at different temperatures. The maximum value of bulk density was observed in filter number 15 made of the M1 mixture under the firing temperature of 1100$^{\circ}C$ and the press pressure of 50MPa. This may be referred to the absence of sawdust in this mixture and to losing more weight, the reduction of dimension, and the densification due to the used high press pressure. The minimum value of bulk density was observed in filter number 76 made of the M6 mixture under the firing temperature of 1000$^{\circ}C$ and the press pressure of 10MPa. This may be a cause of losing less weight of the filter material and less reduction in dimension under low firing temperature and press pressure.

The porosity and absorption of filter discs are decreased as the firing temperature and the press pressure are increased and are increased as the percentage of sawdust content is increased. The porosity varied in an overall range of 30.17% and 67.33%. The overall average of this variation in porosity was 47.84%. Its maximum value was measured in the filter number 76 made of M6 mixture under a firing temperature of 1000$^{\circ}C$ and the press pressure of 10MPa. This is expected due to high sawdust content, and low press pressure and firing temperature. The minimum value of porosity was measured for the filter number 15 made of the M1 mixture under a firing temperature of 1100$^{\circ}C$ and the press pressure of 50MPa. This is due to the absence of sawdust in this mixture and due to the high press pressure and firing temperature. The overall average of the variation in absorption was 34.34%. Its measured maximum and minimum values were 58.82% and 15.75%, respectively. The maximum value of absorption was found in filter number 76 made of M6 mixture under a firing temperature of 1000$^{\circ}C$ and the press pressure of 10MPa. This is referred to the high sawdust content, and low press pressure and firing temperature. The minimum value of absorption is measured in filter number 15 made of M1 mixture under the firing temperature of 1100$^{\circ}C$ and the press pressure of 50MPa. This is due to the absence of sawdust in this mixture and to the high press pressure and firing temperature.

In the hydraulic conductivity tests, all the filters made of M6 mixture under a press pressure of 10*MPa* and at all firing temperatures were weak to withstand the applied water head. This also happened in filters made of M5 mixture expect filters that were produced under a firing temperature of 1100˚*C*. In general, the hydraulic conductivity of filter discs is decreased as the press pressure is increased. It was noted that the sawdust affects the value of the hydraulic conductivity depending on its percentage. High hydraulic conductivity is obtained at a firing temperature of 1070˚*C* when the sawdust content is less than 10%. Otherwise, the hydraulic conductivity is increased as sawdust content and the firing temperature are increased. When the firing temperature is 1070˚*C*, as the sawdust content is increased from 0 to 7.5%, the hydraulic conductivity is increased and then it was reduced when the sawdust content is 10%. Then the hydraulic conductivity is increased when increasing the sawdust content to 12.5 and 15%. The overall range of the variation in hydraulic conductivity varied between 0*mm/day* and 189*mm/day*. The overall average of this variation in hydraulic conductivity was 37.23*mm/day*. The maximum value of hydraulic conductivity was obtained when testing filter number 87 made of M6 mixture under a firing temperature of 1100˚*C* and the press pressures of 20*MPa*. This is due to the high percentage of sawdust and low press pressure. The minimum value of hydraulic conductivity obtained in the filters numbers 4, and 5 made of the M1 mixture under the firing temperature of 1000˚*C* and the press pressure of 40, and 50*MPa*, respectively. This is due to the absence of sawdust in this mixture and to the high press pressure.

Generally, the compressive and bending strengths of the ceramic filters are increased as the press pressure and firing temperature are increased and the percentage of sawdust content is decreased. The overall range of the variation in compressive and bending strengths varies between 0.1*MPa* and 71.3*MPa*, and 2.4*MPa* and 14.95*MPa*, respectively. The overall average of this variation in compressive and bending strengths was 17.16*MPa* and 8.05*MPa*, respectively. The maximum values of compressive and bending strengths were obtained when testing filter number 15 made of the M1 mixture under a firing temperature of 1100˚*C* and a press pressure of 50*MPa*. This is referred to high values of the press pressure and the firing temperature, and the low percentage of sawdust content that were used in producing these filters. The minimum values of compressive and bending strengths were found in filter number 76 made of M6 mixture under a firing temperature of 1000˚*C* and a press pressure of 10*MPa*. Low press pressure and firing temperature, and a high percentage of sawdust content were the reason behind these minimum values. Moreover, filters made of mixtures with the percentage of sawdust content less than 10% under all the press pressures and firing temperatures have in general a compressive strength greater than bending strength. While, filters made of mixtures with the percentage of sawdust content greater than 10% have bending strength greater than compressive strength.

The range of the properties of the produced ceramic filters was categorized according to the percentage of sawdust content in their mixture, the press pressure, and the firing temperature. **Table 7** presents the range of the physical properties of ceramic filters that are categorized according to the percentage of sawdust content. Generally, the reduction in dimensions, porosity, absorption, and the hydraulic conductivity are increased as the percentage of sawdust content is increased. While, the bulk density, and compressive and bending strengths are decreased as the percentage of sawdust content is increased.

Table 8 lists the range of the physical properties of ceramic filters that are categorized according to the firing temperature. In general, the reduction in dimensions, bulk density, and compressive and bending strengths are increased as the firing temperature is increased. While the porosity and the absorption are reduced as the firing temperature is increased.

The ranges of the physical properties of ceramic filters that are categorized according to the press pressure are presented in **Table 9**. The range of reduction in dimensions of all the produced

filters remains the same whatever the press pressure is. This may be referred to the same loss of material during firing process. In general, as the press pressure is increased, the bulk density, and compressive and bending strengths are increased. While the porosity, the absorption, and the hydraulic conductivity are decreased.

In practical water filtration applications, it is required to select a filter among all of the produced filters based on a hydraulic conductivity that ensures suspended materials of the filtrated water to be within the standard limits for drinking water, and acceptable compressive and bending strengths. In this study, the selection is based on acceptable compressive and bending strengths, and a high hydraulic conductivity as possible. How the selected hydraulic conductivity is related to the filtration efficiency is recommended to be tested in a further study. According to the results presented above, filters produced under the press pressure of 20*MPa* have the highest value of hydraulic conductivity and acceptable compressive and bending strengths. The highest hydraulic conductivity and compressive and bending strengths are obtained under a firing temperature of 1100˚*C*. The highest hydraulic conductivity is obtained in filters made of the mixture having 15% of sawdust content. Under this content of sawdust, both of compressive and bending strengths are low. This is true also for filters made of mixture with 12.5% of sawdust content. Acceptable compressive and bending strengths are obtained in filters made of mixture with sawdust content of 7.5% and 10%. But the hydraulic conductivity of ceramic filters made of mixture with 7.5% of sawdust content under a firing temperature of 1070˚*C* are higher than that obtained with 10% of sawdust content. Accordingly, filter number 37 made of mixture M3, with 7.5% of sawdust content, produced under press pressure of 20*MPa* and firing temperature of 1070˚*C* gave a good balance between the hydraulic conductivity and the compressive and bending strengths. This filter disc has hydraulic conductivity of 50*mm/day*, compressive strength of 14*MPa*, and bending strength of 10.8*MPa*.

10. CONCLUSIONS

The purpose of the current study aims to test the physical properties of the ceramic water filters discs produced from different mixtures of local raw materials under different production conditions of press pressures and temperatures. The conclusions of this research are listed below:

1. Filters made of mixtures with high content of sawdust greater than 15% are so soft and can be easily disintegrated.
2. Within the range of particle size of the used sawdust, there is no significant effect of the sawdust particle size categorizing into particle size less than 90μm and greater than 212μm on both the porosity and hydraulic conductivity of ceramic filter disc.
3. There was a reduction in the dimensions of the ceramic filter discs compared to their original values before firing. This reduction is increased as firing temperature and percentage of sawdust content are increased and is remained constant as the press pressure is increased. The overall average of this reduction in dimensions is 1.59%.
4. The bulk density of filter discs is increased as the press pressure and firing temperature are increased and it is decreased as the percentage of sawdust content is increased. The range of the bulk density of all tested ceramic filter varies between 1.16gm/cm^3 and 1.91gm/cm^3.
5. The porosity and absorption of filter discs are decreased as the firing temperature and the press pressure are increased and are increased as the percentage of sawdust content is increased. The porosity varied in an overall range of 30.17% and 67.33%. The overall average of the variation in absorption is 34.34%.
6. Filters made of mixtures with 15% of sawdust content produced under a press pressure of 10*MPa* are weak to withstand the applied water head of the hydraulic conductivity test.

7. High hydraulic conductivity is obtained at a firing temperature of 1070 ˚*C* when the sawdust content less than 10%. Otherwise, the hydraulic conductivity is increased as sawdust content and the firing temperature are increased.
8. The overall range of the variation in hydraulic conductivity varied between 0*mm/day* and 189*mm/day*. The overall average of this variation in hydraulic conductivity is 37.23*mm/day*.
9. The compressive and bending strengths of the ceramic filters are increased as the press pressure and firing temperature are increased and the percentage of sawdust content is decreased. The overall range of the variation in compressive and bending strengths varies between 0.1*MPa* and 71.3*MPa*, and 2.4*MPa* and 14.95*MPa*, respectively.
10. The reduction in dimensions, porosity, and absorption are increased as the percentage of sawdust content is increased. While, the bulk density, and compressive and bending strengths are decreased as the percentage of sawdust content is increased.
11. The reduction in dimensions, bulk density, and compressive and bending strengths are increased as the firing temperature is increased. While the porosity and the absorption are reduced as the temperature is increased.
12. As the press pressure is increased, the bulk density, and compressive and bending strengths are increased. While, the porosity, absorption, and the hydraulic conductivity are decreased.
13. Filter number 37 made of mixture M3, with 7.5% of sawdust content, produced under press pressure of 20*MPa* and temperature of 1070 ˚*C* gave a good balance between the hydraulic conductivity and the compressive and bending strengths.

REFERENCES

- ASTM-C373-88 standards, 2006, *Standard Test Method for Water Absorption, Bulk Density, Apparent Porosity, and Apparent Specific Gravity of Fired Whiteware Products*, ASTM, USA.

- ASTM-C674-88 standards, 2006 *Standard Test Methods for Flexural Properties of Ceramic Whiteware Materials*, ASTM, USA.

- ASTM-C773-88 standards, 2006, *Standard Test Method for Compressive (Crushing) Strength of Fired Whiteware Materials*, ASTM, USA.

- Hettiarachchi, P., Motha, J. T. S., and Pitawala, H. M. T. G. A., 2010, *Identification of an appropriate body composition for red clay products*, Cerâmica 56: 285-290.

- Lamb, T. W., and Whitman, R. V., 1969, *Soil Mechanics*, John Wiley and Sons, Inc., USA.

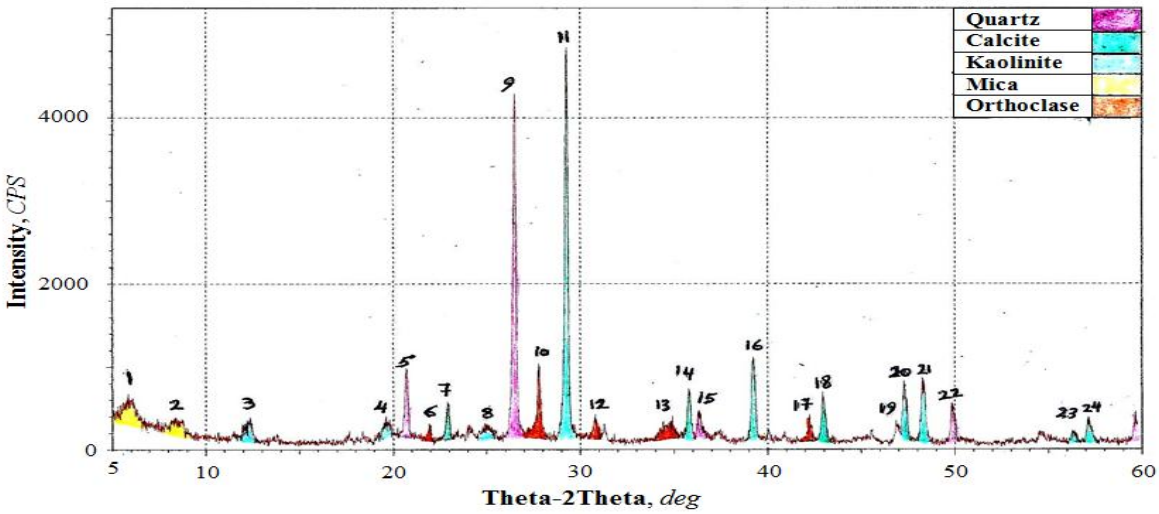

Figure 1. X-ray diffractions of red clay.

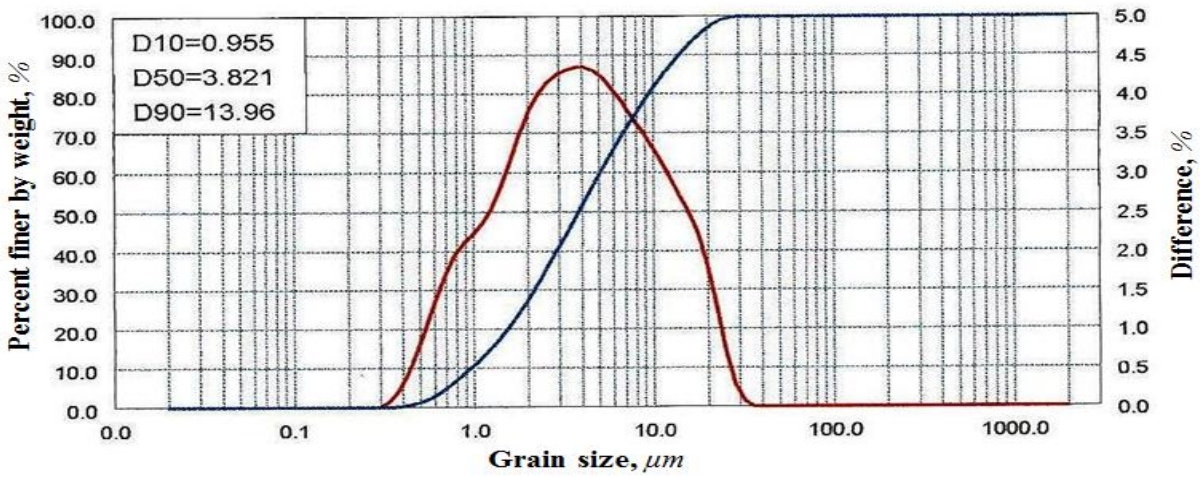

Figure 2. Particle size analysis of red clay.

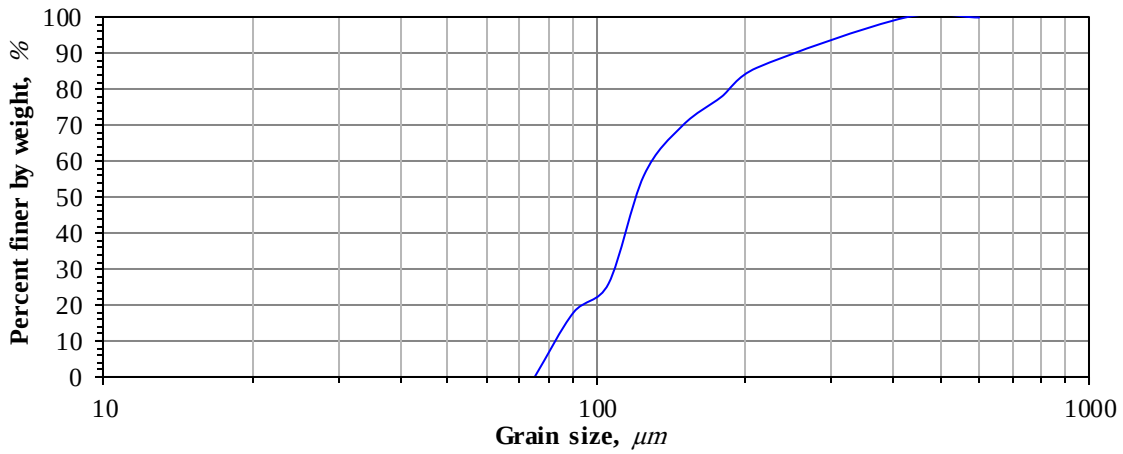

Figure 3. Particle size analysis of sawdust.

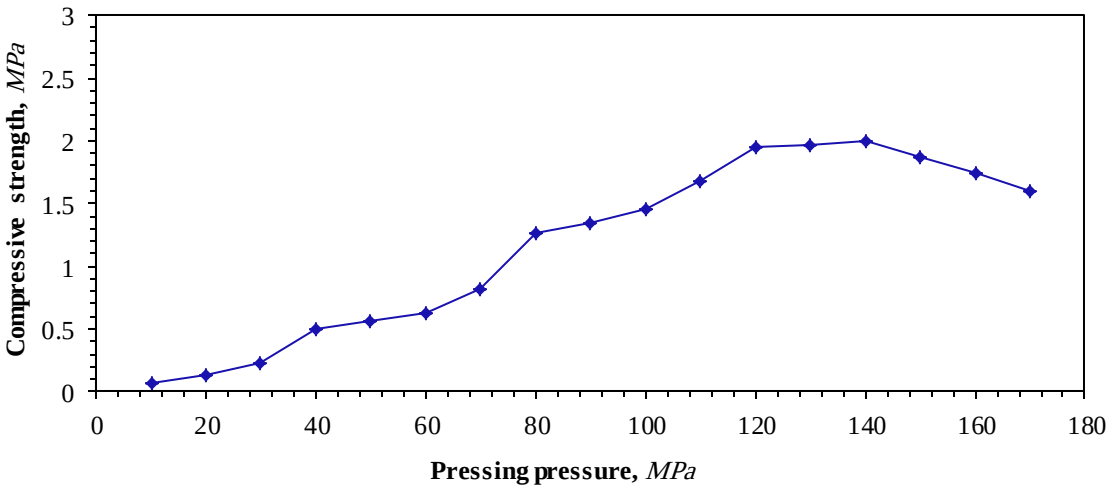

Figure 4. Relation between press pressure and compressive strength of ceramic before firing.

a- Samples of disk shape filters.

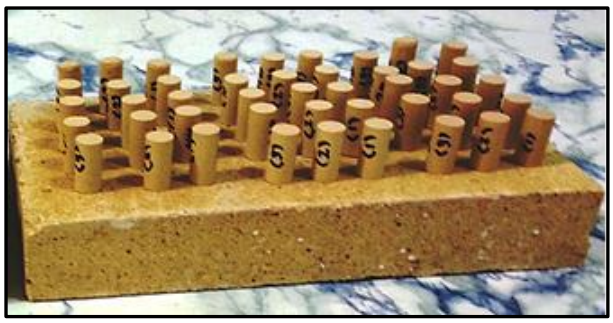

b- Samples of cylindrical shape filters.

c- Samples of rectangular shape filters.

Figure 5. Ceramic filters of discs, cylindrical and rectangular shapes.

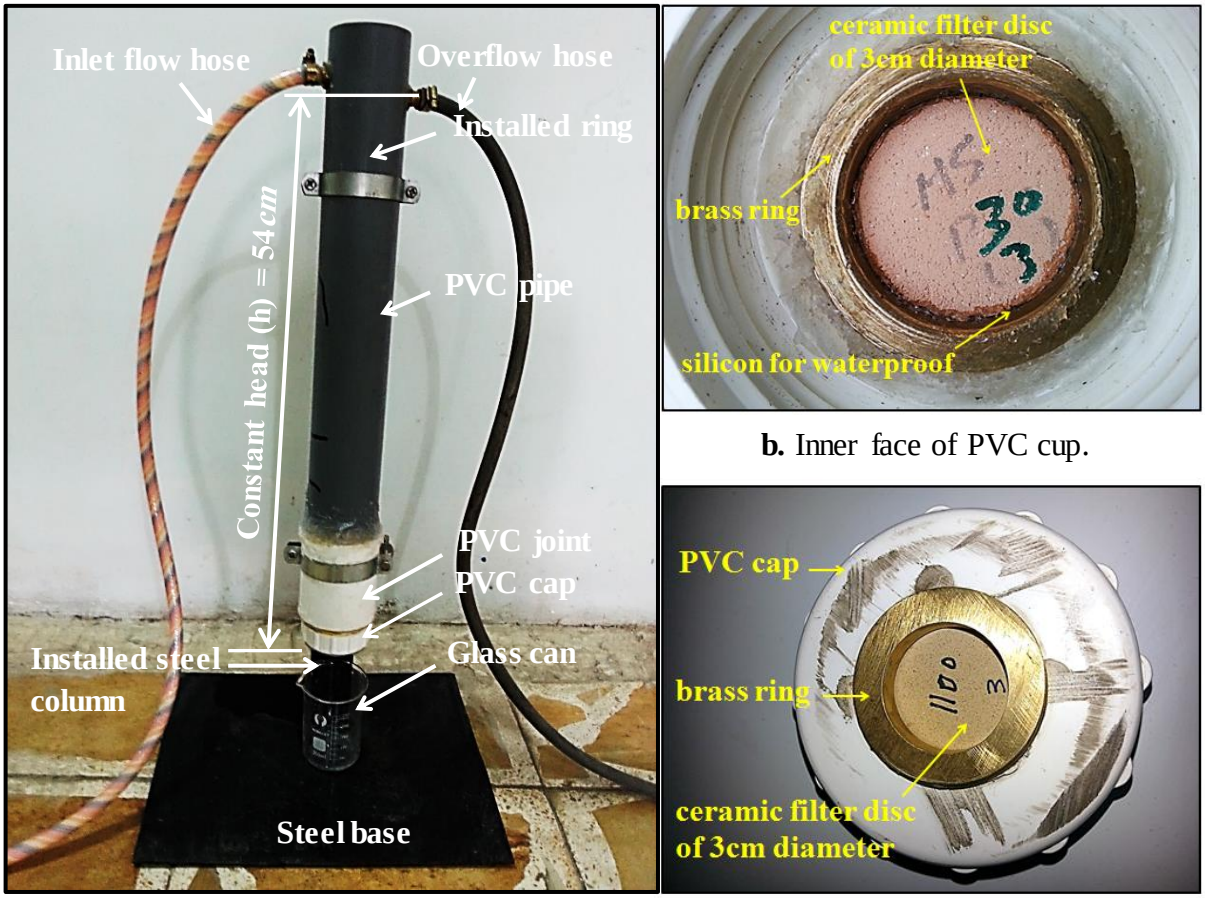

b. Inner face of PVC cup.

a. General view. **c.** Outer face of PVC cap.

Figure 6. Test rig of the hydraulic conductivity of the ceramic water filter disc.

Table 1. Composition analysis of red clay soil and mineral content.

Oxides	Percentage, %	Minerals contents	
SiO2	37.14	Clay minerals	Mica(Biotite) = 49%
Fe2O3	5.33		
Al2O3	11.31		Kaolinite = 14%
TiO_2	0.37		
CaO	18.0	Non-clay minerals	Calcite = 21.5%
MgO	4.95		
SO3	0.62		Quartz = 11.5%
Na2O	1.01		
K2O	1.4		Orthoclase = 4%
LOI	19.31		
Total	**99.44**		

Table 2. Different mixtures of red clay and sawdust.

Code of Mixture	Red Clay, %	Sawdust, %	Particle size of sawdust, μm
M1	100	0	75 - 425
M2	95	5	
M3	92.5	7.5	
M4	90	10	
M5	87.5	12.5	
M6	85	15	
M7	80	20	
M8	75	25	
M9	90	10	< 90
M10	90	10	>212

Table 3. Time schedule program of firing temperature for ceramic.

Level	Time, min.	Temperature, ˚C	
		From	To
1	15	Room	80
2	30	80	soaking
3	15	80	180
4	30	180	soaking
5	15	180	330
6	30	330	soaking
7	15	330	550
8	45	550	soaking
9	15	550	800
10	45	800	soaking
11	15	800	1000 or 1070 or 1100
12	60	1000 or 1070 or 1100	soaking

Table 4. The Details of the Produced Ceramic Filters.

Code of Mixture	Disc no.	Applied		Code of Mixture	Disc no.	Applied	
		Press Pressure *MPa*	Firing Temperature *ºC*			Press Pressure *MPa*	Firing Temperature *ºC*
M1	1	10	1000	M3	42	20	1100
	2	20	1000		43	30	1100
	3	30	1000		44	40	1100
	4	40	1000		45	50	1100
	5	50	1000	M4	46	10	1000
	6	10	1070		47	20	1000
	7	20	1070		48	30	1000
	8	30	1070		49	40	1000
	9	40	1070		50	50	1000
	10	50	1070		51	10	1070
	11	10	1100		52	20	1070
	12	20	1100		53	30	1070
	13	30	1100		54	40	1070
	14	40	1100		55	50	1070
	15	50	1100		56	10	1100
M2	16	10	1000		57	20	1100
	17	20	1000		58	30	1100
	18	30	1000		59	40	1100
	19	40	1000		60	50	1100
	20	50	1000	M5	61	10	1000
	21	10	1070		62	20	1000
	22	20	1070		63	30	1000
	23	30	1070		64	40	1000
	24	40	1070		65	50	1000
	25	50	1070		66	10	1070
	26	10	1100		67	20	1070
	27	20	1100		68	30	1070
	28	30	1100		69	40	1070
	29	40	1100		70	50	1070
	30	50	1100		71	10	1100
M3	31	10	1000		72	20	1100
	32	20	1000		73	30	1100
	33	30	1000		74	40	1100
	34	40	1000		75	50	1100
	35	50	1000	M6	76	10	1000
	36	10	1070		77	20	1000
	37	20	1070		78	30	1000
	38	30	1070		79	40	1000
	39	40	1070		80	50	1000
	40	50	1070		81	10	1070
	41	10	1100		82	20	1070

Table 4. Cont.

Code of Mixture	Disc no.	Applied		Code of Mixture	Disc no.	Applied	
		Press Pressure *MPa*	Firing Temperature *ºC*			Press Pressure *MPa*	Firing Temperature *ºC*
M6	83	30	1070	M7	103	30	1100
	84	40	1070		104	40	1100
	85	50	1070		105	50	1100
	86	10	1100	M8	106	10	1000
	87	20	1100		107	20	1000
	88	30	1100		108	30	1000
	89	40	1100		109	40	1000
	90	50	1100		110	50	1000
M7	91	10	1000		111	10	1070
	92	20	1000		112	20	1070
	93	30	1000		113	30	1070
	94	40	1000		114	40	1070
	95	50	1000		115	50	1070
	96	10	1070		116	10	1100
	97	20	1070		117	20	1100
	98	30	1070		118	30	1100
	99	40	1070		119	40	1100
	100	50	1070		120	50	1100
	101	10	1100	M9	121	20	1000
	102	20	1100	M10	122	20	1000

Table 5. Effects of sawdust particles size on the porosity and hydraulic conductivity of the ceramic filter disc.

Mixture code	Sawdust particle size	Sample no.	Porosity %	Average porosity %	Hydraulic conductivity *mm/day*	Average hydraulic conductivity *mm/day*
M9	< 90 µm	1	54	54.7	36	35
		2	55		34	
		3	55		35	
M10	>212 µm	1	56	56	34	34
		2	57		33	
		3	55		35	

Code of the mixture	Disc no.	Firing temp. °C	Press pressure MPa	Average of three samples for each ceramic filter							
				Change in dimensions of disc due to firing, %	Bulk density gm/cm³	Porosity %	Absorption %	Hydraulic conductivity mm/day		Compressive strength MPa	Bending strength MPa
								Observed	Standard at 20 °C		
M1	1	1000	10	0.33	1.57	37.51	23.89	5	4	54.3	12.5
	2		20	0.33	1.65	35.75	21.67	2	2	57.3	12.5
	3		30	0.33	1.73	35.37	20.45	2	1	63.2	12.5
	4		40	0.33	1.78	34.34	19.28	0	0	63.6	12.7
	5		50	0.33	1.85	32.39	17.51	0	0	64.9	12.7
	6	1070	10	1	1.6	36.81	23	10	7	52.6	12.5
	7		20	1	1.72	35.37	20.56	5	4	53.9	12.5
	8		30	1	1.78	34.5	19.39	3	2	55.2	12.5
	9		40	1	1.82	32.66	17.95	2	1	58.1	13.1
	10		50	1	1.88	30.82	16.39	1	1	60.7	13.3
	11	1100	10	1.33	1.66	36.24	21.83	4	3	61.1	12.82
	12		20	1.33	1.77	35.14	19.83	3	2	65.8	12.82
	13		30	1.33	1.81	33.84	18.7	1	1	66.2	12.82
	14		40	1.33	1.85	31.98	17.3	1	1	68.7	13.2
	15		50	1.33	1.91	30.17	15.75	1	1	71.3	14.95
M2	16	1000	10	0.57	1.38	55.78	40.43	8	7	5.1	4.6
	17		20	0.57	1.4	51.91	37.08	4	4	13.6	5
	18		30	0.57	1.41	49.72	35.26	4	3	15.7	5.5
	19		40	0.57	1.45	44.77	30.87	3	2	16.1	8.6
	20		50	0.57	1.48	39.98	27.02	2	1	19.5	9.7
	21	1070	10	1.33	1.41	54.89	38.92	60	54	7.2	5.6
	22		20	1.33	1.44	49.11	34.11	42	38	14.4	10.9
	23		30	1.33	1.49	46.27	31.05	31	28	16.1	11
	24		40	1.33	1.53	41.61	27.2	14	13	19.9	11.1
	25		50	1.33	1.55	39.61	25.56	8	7	23.3	11.2

Table 6. Physical properties of ceramic water filters.

Table 6. Cont.

Code of the mixture	Disc no.	Firing temp. °C	Press pressure MPa	Average of three samples for each ceramic filter							
				Change in dimensions of disc due to firing, %	Bulk density gm/cm^3	Porosity %	Absorption %	Hydraulic conductivity mm/day		Compressive strength MPa	Bending strength MPa
								Observed	Standard at 20 °C		
M2	26	1100	10	1.67	1.45	53.69	37.03	40	35	8.1	10.8
	27		20	1.67	1.5	46.89	31.24	27	23	15.7	11.1
	28		30	1.67	1.53	42.41	27.72	20	17	19.5	11.3
	29		40	1.67	1.58	40.88	25.87	11	9	24.6	11.6
	30		50	1.67	1.6	37.2	23.25	5	4	27.6	14.4
M3	31	1000	10	0.87	1.35	57.99	42.96	37	30	4.2	4.5
	32		20	0.87	1.37	53.44	39	24	19	13.1	4.5
	33		30	0.87	1.38	50.27	36.42	14	12	14.6	5.5
	34		40	0.87	1.41	45.38	32.17	9	7	15.7	6.5
	35		50	0.87	1.43	42.31	29.59	7	6	17.8	8.6
	36	1070	10	1.5	1.38	56.56	40.98	71	61	5.5	4.9
	37		20	1.5	1.4	50.81	36.3	50	43	14	10.8
	38		30	1.5	1.44	47.77	33.16	40	33	14.8	10.8
	39		40	1.5	1.49	44.86	30.11	33	27	16.9	10.8
	40		50	1.5	1.51	41.38	27.4	18	15	18.2	10.9
	41	1100	10	2	1.42	54.08	38.07	64	58	6.4	10.6
	42		20	2	1.46	48.95	33.53	43	39	14.9	10.8
	43		30	2	1.5	45.92	30.61	27	25	16.9	10.8
	44		40	2	1.55	42.73	27.57	16	14	18.7	10.8
	45		50	2	1.58	38.59	24.42	8	7	20	11.1
M4	46	1000	10	1.17	1.3	58.8	45.22	42	34	0.6	4.1
	47		20	1.17	1.34	55.53	41.44	34	27	4.7	4.2

	48		30	1.17	1.36	51.01	37.51	17	14	9.3	4.6
	49		40	1.17	1.4	45.84	32.73	11	9	9.8	5.6
	50		50	1.17	1.42	42.42	29.87	9	8	10.2	5.6

Table 6. Cont.

Code of the mixture	Disc no.	Firing temp. *°C*	Press pressure *MPa*	Average of three samples for each ceramic filter							
				Change in dimensions of disc due to firing, *%*	Bulk density *gm/cm³*	Porosity *%*	Absorption *%*	Hydraulic conductivity *mm/day*		Compressive strength *MPa*	Bending strength *MPa*
								Observed	Standard at 20 *°C*		
M4	51	1070	10	1.67	1.35	57.31	42.47	55	49	1.3	4.6
	52		20	1.67	1.37	53.25	38.87	35	31	6.8	10.6
	53		30	1.67	1.41	49.26	34.94	20	18	9.5	10.6
	54		40	1.67	1.44	45.28	31.45	17	14	10	10.8
	55		50	1.67	1.47	41.91	28.51	13	11	10.6	10.8
	56	1100	10	2.33	1.38	55.89	40.49	71	65	1.5	5.6
	57		20	2.33	1.42	51.36	36.17	54	50	7.2	8.7
	58		30	2.33	1.47	48.47	32.97	33	32	9.77	9.7
	59		40	2.33	1.52	44.64	29.37	24	24	10.2	10.8
	60		50	2.33	1.56	41.71	26.75	14	15	11.47	10.8
M5	61	1000	10	1.5	1.19	59.43	50.11	B	B	0.3	4
	62		20	1.5	1.23	56.95	46.33	45	35	0.6	4.2
	63		30	1.5	1.28	53.8	42.05	34	27	2.1	4.5
	64		40	1.5	1.3	49.9	38.46	26	19	3.8	4.5
	65		50	1.5	1.33	47.62	35.84	22	17	3.8	4.9
	66	1070	10	1.93	1.23	57.75	47.39	B	B	0.5	4
	67		20	1.93	1.27	55.77	43.93	56	44	1.3	5.2
	68		30	1.93	1.3	51.93	39.94	49	39	3.4	5.6
	69		40	1.93	1.32	49.01	37.13	39	31	3.8	5.6
	70		50	1.93	1.35	46.26	34.27	32	26	3.8	5.6
	71	1100	10	2.5	1.25	56.94	45.7	78	59	0.6	4.8

	72		20	2.5	1.3	54.29	41.76	62	47	1.7	5.2
	73		30	2.5	1.33	50.06	37.63	56	40	3.6	5.6
	74		40	2.5	1.36	48.1	35.37	51	35	4	5.6
	75		50	2.5	1.38	43.23	31.33	40	30	4.7	6.5

Table 6. Cont.

Code of the mixture	Disc no.	Firing temp. *°C*	Press pressure *MPa*	Average of three samples for each ceramic filter							
				Change in dimensions of disc due to firing, *%*	Bulk density *gm/cm³*	Porosity *%*	Absorption *%*	Hydraulic conductivity *mm/day*		Compressive strength *MPa*	Bending strength *MPa*
								Observed	Standard at 20 *°C*		
M6	76	1000	10	2	1.16	67.33	58.82	B	B	0.1	2.4
	77		20	2	1.2	60.64	50.57	112	87	0.6	3.2
	78		30	2	1.23	56.98	46.33	85	63	1.3	3.6
	79		40	2	1.25	54.3	43.45	75	55	1.3	4
	80		50	2	1.28	52.47	41	58	43	1.3	4.2
	81	1070	10	2.17	1.2	65.35	54.89	B	B	0.2	3.8
	82		20	2.17	1.23	58.24	47.45	149	118	1.3	4.6
	83		30	2.17	1.26	56.81	45.12	124	96	1.3	5.2
	84		40	2.17	1.27	53.69	42.28	108	88	1.3	5.2
	85		50	2.17	1.3	51.78	39.84	64	50	1.7	5.6
	86	1100	10	2.67	1.23	62.92	51.68	B	B	0.3	4.6
	87		20	2.67	1.25	57.96	46.37	189	139	1.3	4.9
	88		30	2.67	1.28	55.35	43.24	149	107	2.1	5.6
	89		40	2.67	1.32	51.48	38.99	126	90	2.1	5.6
	90		50	2.67	1.33	48.25	36.28	97	70	2.5	6.5

B = broken during hydraulic conductivity test

Table 7. The range of the physical properties categorized according to the percentage of sawdust content.

physical properties	Range of variation					
	Sawdust content, *%*					
	0	5	7.5	10	12.5	15
Change in dimension, *%*	0.33-1.33	0.57-1.67	0.87-2.00	1.17-2.33	1.50-2.50	2.00-2.67
Bulk density, *g/cm*^{3}	1.57-1.91	1.38-1.60	1.35-1.58	1.30-1.56	1.19-1.38	1.16-1.33
Porosity, *%*	30.17-37.51	37.20-55.78	38.59-57.99	41.71-58.80	43.23-59.43	48.25-67.33
Absorption, *%*	15.75-23.89	23.25-40.43	24.42-42.96	26.75-45.22	31.33-50.11	36.28-58.82
Hydraulic conductivity, *m/day*	0-10	2-60	7-71	9-71	22-78	58-189
Compressive strength, *MPa*	52.60-71.30	5.10-27.60	4.20-20.00	0.60-11.47	0.30-4.70	0.10-2.50
Bending strength, *MPa*	12.50-14.95	4.60-14.40	4.50-11.10	4.10-10.80	4.00-6.50	2.40-6.50

Table 8. The range of the physical properties categorized according to the firing temperature.

physical properties	Range of variation		
	Temperature, *°C*		
	1000	1070	1100
Change in dimension, %.	0.33-2.00	1.00-2.17	1.33-2.67
Bulk density, g/cm^3	1.16-1.85	1.20-1.88	1.23-1.91
Porosity, *%*	32.39-67.33	30.82-65.35	30.17-62.92
Absorption, *%*	17.51-58.82	16.39-54.89	15.75-51.68
Hydraulic conductivity, *mm/day*	0-112	1-149	1-189
Compressive strength, *MPa*	0.1-64.9	0.2-60.7	0.3-71.3
Bending strength, *MPa*	2.4-12.7	3.8-13.3	4.6-14.95

Table 9. The range of the physical properties categorized according to the press pressure.

physical properties	Range of variation				
	Press pressure, *MPa*				
	10	20	30	40	50
Change in dimension, *%*	0.33-2.67	0.33-2.67	0.33-2.67	0.33-2.67	0.33-2.67
Bulk density, *g/cm*^{3}	1.16-1.66	1.20-1.77	1.23-1.81	1.25-1.85	1.28-1.91
Porosity, *%*	36.24-67.33	35.14-60.64	33.84-56.98	31.98-54.30	30.17-52.47
Absorption, *%*	21.83-58.82	19.83-50.57	18.70-46.33	17.30-43.45	15.75-41.00
Hydraulic conductivity, *mm/day*	-*	2-189	1-149	0-126	0-97
Compressive strength, *MPa*	0.10-61.1	0.6-65.8	1.3-66.2	1.3-68.7	1.3-71.3
Bending strength, *MPa*	2.40-12.82	3.20-12.82	3.60-12.82	4.00-13.20	4.20-14.95

* Incomplete set of the produced ceramic filters due to exclusion of filters made of M5 and M6 mixtures.

دراسة تأثير العامل المايكروبي على صفات وخصائص متراكبة النوفولاك المدعم بألياف الزجاج/ الاسبست

رولا عبد الخضرعباس
العلوم التطبيقية/ فرع علم المواد
الجامعة التكنولوجية

اسراء عطية عجيل
العلوم التطبيقية/ فرع الكيمياء التطبيقية
الجامعة التكنولوجية

صالح عبد الرضا الصالح
مركز بحوث البيئة
الجامعة التكنولوجية

الخلاصة:

تم دراسة انعكاس تأثير الاستخدام المسهب لمواد متراكبة بوليمرية مكونة من مادة النوفولاك المقواة بألياف الزجاج مرة وألياف الاسبست مرة أخرى وبكسر وزني مقداره (60%) وبنسبة (10%) من المادة المصلدة (الهيكاسامثيلين تترا أمين Hexamethylene- tetraamine) (HMTA)على خواصها الفيزيائية والتي شملت (الصلادة Hardness مقاومة التشوه ألانضغاطي، Compressive deformation معامل المرونة ألانضغاطي modulus of elasticity Compressive معامل المرونة ألانعطافيFlexural modulus of elasticity، مقاومة الثني القصوى strength Flexural، معامل الرجوعية ألانعطافي Flexural resilience modulus، طاقة انفعال الثنيstrain energy Flexural ومقاومة قص الطبقات الداخلية تحت حمل ثلاثي الركيزه)، باعتبار ثبوت أهمية الأوساط البكتيرية كأحد مصادر التلوث التي تسهم بطريقة مباشرة أو غير مباشرة في عملية تقادم هذه المواد المتراكبة. علما بأن متراكبات النوفولاك المدعمة بألياف الزجاج حضرت بنسبتين مختلفتين من المادة المصلدة (HMTA) والمتمثلة بنسبة (14%) وزنا مرة و(10%) وزنا مرة أخرى.

لقد أظهرت نتائج المقارنة بأن تعرض المتراكبات المحضرة للوسط البكتيري يؤثر بشكل سلبي على الصلادة ومقاومة الانضغاط ومقاومة الثني وطاقة انفعال الثني المخزونة.كما خلص البحث أيضا إلى نتائج واضحة وجليه وهو انه يمكن تأخير عملية التقادم بسبب الأوساط البكتيرية باستعمال ألياف الزجاج في مادة النوفولاك أكثر مما هو عليه عند استبدال ألياف الزجاج بألياف الاسبست وخصوصاً مع زيادة نسبة المادة المصلدة من (10%) إلى (14%) حيث تبين أن معامل الرجوعية الانعطافي لهذه المتراكبة يكون اقل مما هو عليه في بقية النماذج المحضرة مما يؤدي إلى رفع الشغل المبذول فيها عند حد التناسب.

Study the effect of microbial factor on the qualities and characteristics of Novolak composite material, reinforced glass fibers / Asbestos fibers.

Rola Abdul Khader Abbas
Applied Sciences / Materials Science Branch
Technology University

Asirae atiya Agil
Applied Sciences / Applied Chemistry Branch
Technology University

Saleh Abdol Reza ALSaleh
Environmental Research Center
Technology University

ABSTRACT

The study was reflection of the impact of the widespread use of polymer Novolak composite reinforced Glass fiber and Asbestos fiber once again with weight fraction 60% on the physical properties, which included (Hardness, Compressive deformation, compressive modulus of

elasticity, Flexural modulus of elasticity, Resilience modulus, the maximum of Flexural strength, Flexural strain energy and Shear strength inner layers); it is known how much important the media as a source of bacterial contamination, which contributes directly or indirectly in the process of aging of these materials. These Novolak composite reinforced, prepared by weight fraction of (10%) and (14%) of the Hexamethylene-tetraamine (HMTA) hardener material.
It showed the results of the comparison, the composite prepared to offer bacterial media, negatively effect on Hardness, Compressive strengths, Flexural strength and Flexural strain stored energy The research also concluded clear results, which is that there is the possibility to delay the aging process of the presence of bacterial circles, using glass fibers in the polymer Novolak composite reinforced, more than it is the use of asbestos fiber. And increase the weight fraction of hardener material to be 14%, coefficient of resilience reversal less than it is in the rest of the models, which leads to raise the value of the work done at the end of proportionality.

المقدمة :

تعرف المواد المتراكبة على أنها تلك الأنظمة الناتجة عن اشتراك مادتين أو أكثر مرتبطة مع بعضها بروابط ميكانيكية وكيميائية بحيث تمثل كل مادة طورا منفصلا في النظام ، بهدف الحصول على مواد جديدة ذات خواص وتراكيب مناسبة مابين خواص المواد الداخلة في تحضير هذه المواد المتراكبة وتتجاوز الصفات غير المرغوب فيها لتكون أكثر ملائمة للتطبيقات الصناعية [1]. وعادة ما يطلق على المادة والتي تقوم بربط مواد التقوية ونقل القوى والاجهادات بالطور المضيف الأساس(Matrix material) والذي غالبا ما يكون عبارة عن مواد بوليمرية او معدنية او سيراميكية [2] [3]، بينما يطلق على المواد التي تعمل على تقوية الطور المضيف بطور التقوية (Rein forcing phase)الذي غالبا ما يكون عبارة عن دقائق أو ألياف أو شعيرات أو صفائح [3].

فالعديد من التقنيات الحديثة تتطلب مجموعة مواد ذات خواص متميزة لا يمكن الحصول عليها عند استخدام سبائك تقليدية او سيراميكية او بوليمرية [4]، فعلى سبيل المثال يبحث مهندسو الطائرات عن مواد متراكبة تمتلك كثافة منخفضة وقوية ذات جساوة (Stiff)عالية ومقاومة التصادم والخدش والتآكل ومن النادر تألف هذه المواد معا في مادة واحدة كالمعادن أو السيراميك، لذا فالمواد المتراكبة تعتبر الحل الأمثل لتناقض هذه الصفات وقد تلتها بحوث تطويرية للإيفاء بمتطلبات التقدم التكنولوجي[5]. ومن اجل توسيع استخداماته التطبيقية أجريت عدة دراسات بتدعيم جسم البوليمر بالألياف أو باستخدام الأملاح الفلزية أو اللاعضوية وإنتاج متراكب مقاوم لظروف الاستخدام القاسية ،فعلى سبيل المثال تمكن كل من (L.Franke) و(H.J.Meyer) عام (1992) من إنتاج متراكبات مقاومة للرطوبة والتحلل المائي[6]. وبعده قام الباحث (Gardiner) عام (1997) بإثبات إن توافر تأثير الظروف الجوية مثل الأشعة فوق البنفسجية والأوكسجين والرطوبة مع بعضها يزيد من عملية تحلل البوليمر أكثر من فعل الأشعة فوق البنفسجية بمفردها [2].

إما الباحث (Mendil) فقد توصل عام (2008) إلى تدعيم مادة البولي استر الغير مشبع بألياف الجوت المحاكة على شكل حصيرة وألياف موجه طوليا هي الأفضل في الحصول على خواص ميكانيكية وفيزيائية وبايلوجية جيدة تتلائم مع البيئة العراقية (شمس قوية وفترة سطوع طويلة وجفاف وغبار) [7].

إما الدراسة الحالية فهي تهدف الى التقليل من الآثار السلبية الناتجة عن تراكم أوساط بكتيرية يوم بعد يوم في جسم متراكبة مكونة من النوفولاك المدعمة بـ(60%) من ألياف الاسبست الغير مستمرة الأشبه بالشعيرات المتقطعة (fiber -whiskers Discontinuous) المعروفه بـ (Chrysolite) مرة وبألياف الزجاج قصيرة مقطعة بأطوال تتراوح مابين (6-8mm) وقطر بحدود (10-14µm) مرة اخربوبنسة ثابتة من المادة المصلدة (HMTA) مقداره (10%)

وكما حضرت أيضا متراكبة النوفولاك المدعمة من ألياف الزجاج في حدود الكسر ألوزني السابق الذكر وفي الوقت نفسه تكون محتوية على قدر من (HMTA) أعلى من (10%) بحوالي (4%) لتوقع عمر المتراكب البوليمري التشغيل عندما يتطلب الأمر تخزين أثار الأوساط البكترية في أجسامها بمعرفة قدرتها على التقاط هذه الآثار عبر دراسة الانحراف الحاصل في بعض الخصائص الميكانيكية بفعل عملية التعتيق بالاستنبات البكتيري في تطبيقات العوازل الحرارية للبنايات التي تحتاج إلى أن تصمد أمام التغيرات السريعة والقاسية للظروف البيئية وهي متعرضة لاجهادات انضغاطية وانعطافية.

الجانب العملي:

المواد المستخدمة:-

تم استخدام راتنج النوفولاك المنتج محليا في شركة ذات الصواري كمادة أساس وهو عبارة عن كتل صلبة يتم طحنها وخلطها مع المادة المصلدة (HMTA) للحصول على خليط (HMTA -Novolak) مناسب للقولبة بالحرارة والضغط. إما مواد التقوية المستخدمة تتمثل بألياف صناعية قصيرة تعمل على تقوية المادة الأساس وهي ألياف الزجاج نوع (E) وهي بشكل ألياف قصيرة (Short fibers) متقطعة بأطوال معينة تتراوح بين (6-8 mm) وذات قطر بحدود(10-14µm) بحيث تكون هذه الألياف موزعه بصورة عشوائية في جسم مادة الأساس النوفلاكية الذي يسبب تناظر Isotropic خواص المواد المتراكبة المصنعة منه في جميع اتجاهات وإما ألياف الاسبست المعروفة Chrysolite فهي عبارة عن ألياف غير مستمرة أشبه ما تكون بالشعيرات المتقطعة (Discontinuous fibers- whiskers) ذات تراكيب نقية مغلقة علاوة على ذلك تم استخدام عوامل تحسين النوعية المتمثلة بالمواد التالية سترات الرصاص،(Aniline, PVA,Olic,MgO).

الأجهزة المستخدمة: (Instruments)

1- جهاز الانحناء(Bending) :لحساب معامل يونك (معامل المرونة ألانعطافي) المصنع من قبل شركة (Phywe) الألمانية والذي تثبت في العينة من طرفيها على مرتكزين وتعلق الكتل (Masses) بصورة تدريجية على الحامل المثبت عند منتصف العينة مما يسبب انحنائها تدريجيا ومن خلال مؤشر مقياس الانحراف يمكن قراءة مقدار الانحراف (Defection) الحاصل للعينة ذات الإبعاد المعلومة كما هو موضح بشكل رقم (1).

2- جهاز الصلادة السطحية (Durometer hardness) نوع (shore-A) والمصنع من قبل شركة (Time group Inc.). كما هو موضح بشكل رقم (2)

3- جهاز الانضغاطية : لحساب مقاومة الانضغاط (Compressive strength) باستعمال المكبس الهيدروليكي (Ley Bold Harris No.36110) والذي يمكننا من تسليط حمل داخل مدى قوة مسلطة تتراوح بين (100 N الى 7.5 KN). حيث توضع العينة في آلة الاختبار بين رؤوس الماكينة، ويطبق الحمل بالتدريج على العينة حتى نقطة انهيار المادة والتي تدل على متانة انضغاطها . كما يقرأ التغيير في طول المقطع الطولي لعينة الاختبار تحت تأثير حمل الانضغاط والذي يدل على تشوه الانضغاط (Compressive deformation). كما هو موضح بشكل رقم (3)

تحضير المحلول الميكروبي:-

حضرت أربع علب زجاجية معقمة سعه(1لتر) لإستحصال المياه العادمة- الحمأة أجريت عملية تنقيتها من الشوائب وجهزت لغمر متراكبة النوفولاك فيها.

طريقة تحضير وفحص النماذج:

تم تحضير عينات مقواة بألياف قصيرة بنسبة وزنيه تقدر ب (60%) و من هذا الكسر ألوزني المرتفع نوعا ما لمواد التدعيم بلا شك له صله مؤكدة بسيئات النوفولاك باعتبار من أكثر البوليمرات هشاشة ما لم يتم تقويته حيث نادراً ما يستخدم في القولبة دون تقوية، عموما تم تطبيق المعادلة التالية لتحديد الكسر الوزني السابق الذكر [8]:

$$\psi = \frac{W_f}{W_c} \times 100\% \ldots\ldots(1)$$

$$W_c = W_f + W_m \ldots\ldots(2)$$

إن(W_c, W_m, W_f) : كتلة الألياف والمادة الأساس والمواد المتراكبة على التوالي.
حيث كانت المواد المتراكبة مكونة من النوفولاك المقواة بألياف الزجاج والنوفولاك المقواة بألياف الاسبست. في الواقع تمت عملية التحضير الابتدائي للمزيج الداخل في تحضير النماذج المتراكبة بالاعتماد على طريقة التشرب(method Impregnation) والتي تعد أهم طرائق القولبة الفينولية. استنادا إلى ذلك تم إتباع الخطوات التالية في تحضير المتراكبات من راتنج النوفولاك وكما يلي:

* تحضير مزيج الراتنج الفينول وذلك بإذابة الخليط (Novolak –HMTA) في كحول الايثانول باستعمال خلاط ذو سرعة عالية ، بعد ذلك يتم إضافة (عوامل تحسين النوعية) بشكل تدريجي مع مراعاة استمرار الخلط.

* تغمر الألياف في مزيج الراتنجي الفينولي مع التحريك ومراقبة تشبع كافة الألياف بالراتنج وهكذا نعود إلى تكرار الخطوات السابقة الذكر مع خليط (Novolak –HMTA) ذو نسبة (14%) وزنا مع (HTMA).

* بعد التأكد من الغمر الجيد وتشبع الألياف بالمزيج الراتنجي ننتقل إلى مرحلة التجفيف بالهواء الساخن بدرجة تتراوح بين (80-70 C°)، حيث تترك المادة في جو الفرن عند هذه الدرجة الحرارية لمدة ثلاثة ساعات وبذلك يتم التخلص من كحول الايثانول المستخدم في المزيج عندئذ تصبح المادة المحضرة جاهزة للقولبة ومن ثم يتم كبس النماذج المستخدمة في الاختبارات التي تم إعدادها باستخدام المكابس نصف الإلية المصنفة من قبل شركة (Batten feld/Berge) ، حيث ان عملية القولبة بمكابس الضغط تتم باستعمال القوالب الفولاذية فأن ذلك يؤدي الى الحصول على عينات نظامية من هذه القوالب الشكل (4).

وعلية قطعت العينات المبينة في الشكل (2) حسب المواصفات القياسية العالمية:-

1- عينات اختبار الانحناء ومتانة الانحناء أعدت حسب النظام القياسي (ASTM-D790) بسـمك (6mm) وعرض (15.9 mm) وطول (120 mm).
2- عينات اختبار الصلادة (Shore –A) أعدت حسب النظام القياسي (ASTM-D2240)،
3- عينات اختبار الانضغاطة أعدت حسب النظام القياسي حسب نشرة (ASTMD-695) على شكل مكعبات بمقاسـات (12 ×6×6 mm^3).

ومن جهة ثانية استخدمت لكل اختبار نموذجين.

بعد تحضير المتراكبات أجريت عليها الفحوصات التالية:-
أولا: اختبار الانحناء الثلاثي الركيزة:-

تحسب قيمة معامل المرونة ألانعطافي (flexural modulus of elasticity) بتطبيق المعادلة التالية [9]:

$$E_b = \frac{mass}{Deflection} \times \frac{(gL^3)}{48I} \ldots\ldots(3)$$

حيث إن E_b : معامل المرونة ألانعطافي والذي يقاس بوحدات (N/m^2).

($\frac{mass}{Deflection}$) : تمثل الميل(Slope) المحسوب من منحني(mass- deflection).

(L): البعد بين نقطتي التحميل(m).

(I) : يمثل عزم الانحناء الهندسي (m^3) والذي يعطى بالمعادلة التالية [9]:

$$I = \frac{bd^3}{12} \quad .....(4)$$

حيث إن : (d): سمك العينة (m).
(b): عرض العينة (m) .

يحسب معامل الرجوعية الانظغاطي (Flexural resilience modulus) بتطبيق المعادلة التالية [10]:-

$$R = \frac{9PD}{2bdL} \quad .....(5)$$

R: معامل الرجوعية ألانعطافي (Flexural resilience modulus) . تقاس بوحدات (P_a)
D: الانحراف الحاصل في العينة مقاسا بـ(m).
P: الحمل المسلط في مركز العينة مقاسا بـ(N).

تحسب مقاومة الثني القصوى عند نقطة الثل (Flexural strength) بتطبيق المعادلة التالية [11]:-

$$\partial_{\max}{}^{b} = Flexural\ \ strength = \frac{3PL}{2bd} \quad .....(6)$$

تحسب طاقة انفعال الثني (Flexural strain energy, u) مقاسا بـ (KJ/m^2) بتطبيق المعادلة التالية [12]:

$$u = \frac{p^2 (L/2)^3}{E_b \times b \times d^3} \quad .....(7)$$

تحسب مقاومة قص الطبقات الداخلية عند نقطة الكسر بتطبيق المعادلة التالية [8]:

$$\tau_{\max} = \frac{3P}{4bd} (N/m^2) \quad .....(8)$$

حيث إن $\tau_{\max}$: مقاومة القص القصوى تحت حمل الثني المؤدي إلى فشل العينة الخاضعة له.

ثانيا: اختبار الصلادة بطريقة (shore –A):-

إن اختبار الصلادة يمكن اعتباره مقياسا للتشوه اللدن الذي تعاني منه المادة تحت تأثير الإجهاد الخارجي ثم إجراء اختبار الصلادة بطريقة (Shore –A) باستخدام أداة غرز نقطية وبتغلغل أداة الغرز النقطية داخل سطح المادة تحت حمل معين حيث تنتقل المقاومة رأسا إلى عداد القياس لتحديد قيمة الصلادة لتقرأ مباشرة من الجهاز.

ثالثا :اختبار مقاومة الانضغاط (Compressive strength):-

تحسب مقاومة الانضغاط عند نقطة الفشل بتطبيق المعادلة التالية [13]:

$$\partial_{\max}^{com} = \frac{\text{أقصى حمل ضغط أثناء الاختبار}}{\text{اقل مساحة مقطع قبل الاختبار}} \quad .....(9)$$

وتقاس مقاومة الانضغاط $\partial_{\max}$ بوحدة (N/m^2).

يحسب قيمة معامل المرونة ألانضغاطي (Compressive modulus of elasticity) بتطبيق المعادلة التالية [15]:-

$$E_{com} = \frac{\partial_{com}}{\in_{com}}$$

حيث إن ∂_{com} :- الإجهاد ألانضغاطي عند حد التناسب (N).

$\in_{com}$: الانفعال عند حد التناسب (m).

النتائج والمناقشة:

اختبار مقاومة الانحناء الاستاتيكي:-

إن الهدف الرئيسي من اختبار الانحناء هو التعرف على السلوك الخطي او ما يدعى أحيانا (Hoohean behavior) للمادة الواقفة تحت تأثير الحمل المسلط بالاتجاه العمودي على المستوى السطحي لها [16] . لقد تبين من الشكل (5) إن الانحراف يتناسب طرديا مع الحمل المحدث له ، فعند زوال تأثير الحمل المسلط سوف تسترجع المادة حالتها الأولى ، إي ضمن حد التشوه المرن حيث يتناسب الانفعال طرديا مع الإجهاد المحدث له ويستنتج من ذلك إن المادة تخضع لقانون هوك (Hook's) وان النسبة بين (Mass/Deflection) مقدارا ثابت [8] ،وهذا يمثل الميل (Slope) المحسوب من الشكل السابق الذكر وعليه من اختبار الانحناء تم حساب قيم معامل المرونة ألانعطافي (E_b) بأتباع المعادلتين (4,3).

إن الشكل (6) يوضح لنا عند تعريض النماذج المحضرة لوسط بكتيري فأن قيم معامل المرونة (E_b) ينخفض وبشكل ملحوظ تبعا لقيم معامل المرونة للنماذج قبل المعاملة البايولوجية (الجدول رقم1) وقد يعزى ذلك إلى حقيقة إن المعاملة البكتيرية تؤدي إلى تحلل الجسور الكيميائية الموجودة بين سطح الألياف والبوليمر ، وبالتالي سوف ينتج عن هذا حصول انفعال كبير مما يؤدي انخفاض هذه القيم.

إما الجدول (2) فقد بين ان أفضل قيمة لمعامل المرونة ألانعطافي تم الحصول عليه بعد المعاملة البكتيرية هي تلك لنموذج راتنج النوفولاك المدعم بألياف الزجاج وذلك لما تمتاز به ألياف الزجاج من خواص متانة عالية تجعل المادة المتراكبة الحاوية عليها ذات خواص أفضل.

علاوة على ما ذكر فقد تبين ان زيادة نسبة المادة المصلدة (HTMA) تؤدي الى زيادة الترابط التشابكي (link density Cross-) [17] مما يؤثر بصورة ملحوظة في مقاومة المادة المتراكبة الراتنجية للوسط البكتيري.

كما أوضحت هذه الدراسة من خلال الشكل (7) إن الانحلال والتدهور في مادة النوفولاك المدعمة بالألياف الصناعية ينشط شيئا فشيئا على حسب العمر الزمني والذي امتد في هذه الدراسة لأكثر من ثلاث أشهر ((لإبقائها معرضة للوسط البكتيري)) حيث تشاهد أثاره في حصول قصور كبير في مقدرة هذه المواد على إرجاع الطاقة المرنة الميكانيكية الممتصة بعد زوال حمل الثني المؤثر عليها تبعا لمقدار طاقة انفعال المتراكمة فيها من ناحية ومقدار معامل الرجوعية الانعطافي من ناحية أخرى (الجدول 3).

إما الشكل (8) بين إن قيمة مقاومة الثني القصوى ($\partial^b_{\max}$) لمتراكبة النوفولاك المدعمة بالألياف الزجاجية ذو نسبة (10%) من (HTMA) بعد المعاملة البايلوجية تقدر بحوالي (37.602 MPa) وهذا يعني إن الشقوق المتأصلة في المتراكبة النوفولاكية المدعمة بالألياف الاسبستية تنمو بصورة سريعة جدا عند تعرضه لهذا النوع من الاجهادات مما يقوده الى الفشل عند اجهادات واطئة تحت هكذا أوساط بكتيرية مقارنة بالمتراكبة المدعمة بألياف الزجاج للأسباب سابقة الذكر (الجدول رقم 4).فلقد أوضحت الدراسة الحالية إن طاقة انفعال الثني عند نقطة الكسر(Flexural strain energy at break point) بالنسبة للنماذج التي عانت في الوسط البكتيري تزداد عن مثيلاتها الغير متعرضة للوسط البكتيري (الشكل9) وكذلك الجدول(5).

وهذه المؤشرات دليل على ان مقاومة قص الطبقات الداخلية عند نقطة الكسر تنخفض بعد المعاملة البايلوجية الشكل (10) فهذه البكتيريا تحدث تحلل لجسم المتراكب في اتجاه تفكيك سلاسله البوليمرية (الجدول رقم6).

اختبار الصلادة بطريقة (Shore-A):-

لقد وجد إن قيم الصلادة السطحية المحسوبة بعد المعاملة البايلوجية قد انخفضت من (94.13No.) إلى (86.6No.) لمادة النوفولاك المدعمة بألياف الزجاج ذات نسبة 14% من (HTMA) ومن (92.58No.) إلى (86.466No.) لمادة النوفولاك المدعمة بألياف الزجاج ذات نسبة 10%من (HTMA) (الجدول رقم 7,1).

وهكذا تتباين قيم صلادة النماذج المحضرة وفقا لنوع ألياف التدعيم ونسبة المادة المصلدة (HTMA) عند تعرضها للأوساط البكتيرية بتفوق المادة المتراكبة المقواة بألياف الزجاج ذات نسبة 14% من (HTMA) في مقاومتها للغرز على بقية النماذج المدروسة رغم حقيقة وجود ألياف الاسبست ذات التركيب الليفي المغلق في المادة النوفولاكية في ظروف طبيعية (قبل المعاملة) يعمل على تحسين صلادة النوفولاك مقارنة بألياف الزجاج (الجدول رقم1) ويعزى سبب ذلك إلى حقيقة إن النمو البكتيري يؤدي إلى زيادة ليونة المادة الأساس (النوفولاك) بسبب تحللها وهذا بدوره سوف يعمل على تحطيم وفك الروابط البينية بين الألياف والمادة الأساس في المواد المتراكبة وعليه ستكون هذه المناطق مراكز تتغلغل من خلالها الوسط البكتيري داخل المادة وعليه فأن كفاءة الترابط الكيميائي بين سطح الألياف الزجاجية المعاملة بالمادة الرابطة (Coupling agent) وبين الراتنج يجعلها تتفوق على ألياف الاسبست في حالة التدعيم إثناء عملها في البيئة البكتيرية لان ألياف الاسبست غير معاملة بالمادة الرابطة(Coupling agent) [8] [18] [19].

يفهم من ذلك بأنه كلما كانت الألياف المستخدمة للتدعيم معاملة بالمادة الرابطة (Coupling agent) ازداد مقاومة المادة المتراكبة للأوساط البكتيرية لأنها تعمل على تكوين جسور كيميائية بين سطح الألياف البوليمر حيث تزيد هذه الجسور الكيمائية في مقاومة التحلل البكتيري (الشكل11).

اختبار الانضغاطية:-

لقد تم حساب معامل المرونة ألانضغاطي E_{com} لجميع النماذج المهيأة بأتباع العلاقة رقم (11) وبالاستعانة بمنحني (الإجهاد – الانفعال) (الشكل رقم 12) ، ومن خلال النتائج المستحصله المتمثلة بالشكل (13) والجدول (8) وجد إن عملية تعرض النماذج المحضرة لوسط بكتيري مع خضوعها لإجهاد انضغاطي يؤدي إلى انخفاض معاملات اختبار المقاومة الانضغاط والمتمثلة بمعامل المرونة الانضغاطي ومقاومة الانضغاط عند نقطة كسر تبعاً لقيم هذه المعاملات قبل التعريض وحسب البيانات المتوفرة في الجدول (1). أما الشكل (14) والجدول (9) فقد بين تدني قيمة مقاومة الانظغاط بعد المعاملة البكتيرية لنموذج متراكبة النوفولاك المدعمة بألياف الزجاج ذات نسبة (10%) من (HMTA) بمقدار 58.705% ويعود السبب في ذلك إلى أن المواد المقواة بالألياف الزجاجية تكون موزعة فيها هذه الألياف بصورة عشوائية وبذلك تكون قناظرة الخواص (Isotropic) كما هو مذكور سابقاً. فإذا كانت جميع الألياف مرصوفة بأتجاه قوى الانضغاط فأن الانهيار سيحدث في المادة عند اجهادات أقل بكثير من اجهادات الفشل الشدي [21]، ومما يزيد الطين بله أن الوسط البكتيري يتسبب بالتسريع بهذا الانهيار بينما يبدي متراكبة النوفولاك المدعمة بالاسبست مقاومة عالية اتجاه الحمل الانضغاطي المحوري مقارنة مع بقية النماذج بسبب تراكيبها الليفية المغلقة والتي سبقا الإشارة إليها ولكن من المؤكد أن التعرض المستمر للوسط البكتيري لابد من أن يؤثر في ضعف مقاومة الانضغاط اتجاه الحمل الانضغاطي عند هذا النوع من المتراكبات المحضرة والتي تقدر بحوالي 15.252%. وهذا هو الحال مع انخفاض نسبة المادة المصلدة (HMTA) بمقدار 4% حيث ارتفع مقدار الفقد في مقاومة الانضغاط اتجاه الحمل الانضغاطي من 33.456% إلى 58.705%.

الاستنتاجات:-

أن هذه الدراسة أظهرت بأن هناك العديد من العوامل تعمل على التعجيل بعملية تعتيق المتراكبات البوليمرية منها الأوساط البكتيرية. ويمكن تمييز خمس صور تشير إلى حصول عملية التعتيق لمتراكبات النوفولاك المحضرة:-

* ففي الطليعة تعد طبيعة الوسط ألزرعي من أهم العوامل التي تؤثر في خواص هذه المواد ويعني ذلك ان الوسط البكتيري ذو تأثير سلبي على المتراكبات المحضرة نظرا لانخفاض معامل المرونة ألانعطافي مع زيادة معامل الرجوعية بشكل كبير مقارنة مع قيم هذه الكميات الفيزيائية قبل تعرضها لهذا الوسط .

* لقد بلغ مقدار ما تفقده المادة المتراكبة المدعمة بألياف الزجاج ذات نسبة 14% من (HMTA) من إجمالي مقاومتها القصوى (∂^{b}_{max}) بسبب تعرضها للوسط البكتيري بما يقدر (35.17Mpa) بينما يقدر ما تفقده المادة المتراكبة المدعمة بألياف الزجاج ذات نسبة 10%من (HMTA) تحت نفس الظروف من اجمالي (∂^{b}_{max}) بما يقدر ب (53.851 Mpa) و (42.338 Mpa) بالنسبة لمتراكب ة النوفولاك المدعمة بالاسبست ذات نسبة 10% من (HMTA).

* لقد زادت طاقة انفعال الثني عند نقطة الكسر في متراكبة النوفولاك المدعمة بألياف الزجاج ذات نسبة 14% حوالي (18.188 kJ/m^2) و(14.226k J/m^2) في متراكبة النوفولاك المدعمة بألياف الزجاج ذات نسبة من (HMTA) 10% و (2.125 kJ/m^2) في متراكبة النوفولاك المدعمة بألياف الاسبست ذات نسبة 10% من (HMTA).

* لقد نقص نصيب المادة المتراكبة المدعمة بألياف الزجاج ذو نسبة 14% من (HMTA) من قيمة مقاومة قص الطبقات الداخلية عند نقطة الكسر تحت حمل الثني الى حوالي 38.246% و 59.30% من إجمالي مقاومة قص الطبقات الداخلية لمتراكبة النوفولاك المدعمة بألياف الزجاج ذات 10%من (HMTA) و (62.248%)من إجمالي مقاومة الطبقات الداخلية لمتراكبة النوفولاك المدعمة بألياف الاسبست ذات 10% من (HMTA) وسبب ذلك التعرض لأوساط بكتيرية.

* نجمت خسائر في قيم الصلادة ومقاومة الانضغاط القصوى ومعامل المرونة ألانضغاطي والتي تبدو أثارها في زيادة تشوه الانضغاط عند غمرها في المحلول البكتيري.

المصادر:

1- M.Grayson.,"Encyclopedia of composite materials and components", John Wiley and Sons,NewYork, (1983).

2- Burry ,"New Material and Their Applications",Proceedings of the Institute of physics conference, sep.(1987).

3- ا. د. قحطان الخزرجي و د.علي هوبي حليم و ا.د.عبد الواحد كاظم راجح و د.حسن شاكر مجدي. ،" تأثير عمق الشق على مقاومة الصدمة للدائن المقواة بالألياف"، مجلة اتحاد الجامعات العربية،العدد2، المجلد 14 و(2007)، ص (1-15).

4- P.Popper and D.G.S.Davice ,"The preemption and properties of self bonded silicon carbide",Power Metallurgy ,No.8,(1961),pp.(113-127).

5- W.D.Calloster etal.,"Material science and energeering ",An International 5th edition (USA)(2000),PP.(521-523),(527-543).

6- Frank,L.and Meyer,H.J.:Predieting the tensil strength and creep rapture behavior of product glass-rain forced polymer.J.mater,sci.27,1992, pp.(980-987).

7- طارق عبد الجليل مندل.،" استخدام الدولومايت العراقي لتحسين بعض الخواص الميكانيكية والفيزيائية لمتراكب راتنج البولي استر مع ألياف الجوت"،المجلة العراقية للهندسة المدنية ،العدد الثاني عشر – أيلول ، (2008) ، ص (10-26).

8- رولا عبد الخضر عباس. ،"دراسة بعض الخواص الفيزيائية لمتراكبات بوليمرية المستخدمة في بيئة كيميائية سلبية "، مجلة النهرين –العلوم ، المجلد الثالث – أيلول ،الصفحة (2010) ، ص (1-20).

9- رغد حسين محمد. ،"دراسة ظروف التجوبة (الإشعاع والمحاليل الكيميائية) على بعض خصائص متراكبات الايبوكسي "، رسالة ماجستير ،الجامعة التكنولوجية-قسم العلوم التطبيقية،(2004).

10- صاحب عبد المهدي الصفار.،"هندسة المعادن والسبائك "،الطبعة الأولى، دار الإيمان للطباعة والنشر والترجمة والتوزيع دمشق-سوريا،(2010).

11- M.D.Baijal. ,"Plastic polymer science and technology", John Wiley and Sons,NewYork, (1982).

12- رولا عبد الخضر عباس. ،"دراسة ارتباط الامطار الحمضية بتطور طاقة انفعال الثني المتراكمة في متراكبات النوفولاك وانعكاسه على ارتدادها المرن"، المجلة العراقية للعلوم والتكنولوجيا ،المجلد(3) العدد(3)،(2012)، ص (152-139).

13- محمد الجودة إسماعيل. ،" الجودة واختبارات مواد البلاستيك "، الدار العربية للنشر والتوزيع ،القاهرة – جمهورية مصر العربية ،(2001).

14- سليمان خليفة وجمال عمران.،"البلاستيك تصميم وإنتاج"، دار دمشق للطباعة والنشر والتوزيع،(1991).

15- د.محمود رشاد الدين مصطفى. ،"خواص مواد البناء واختباراتها "، منشورات الراتب للأبحاث الجامعية-بيروت ،(1983).

16- S.S.You, T.W.Chou and F.K.Ko,"Composites",Vol.17,No.3,July, (1986),pp.(227-232).

17- W.Y.Chiang and S.Y.Yang, "Journal of Applied Polymer Science", Vol.37,(1989),pp.(499-512).

18- آنا.أ.تاكر،ترجمة دز اكرم محمد عزيز.،"الكيماء الفيزيائية للبوليمرات "، جامعة الموصل،(1984).

19- د.كوركيس عبدال ادم و د. حسين علي كاشف الغطاء.،"تكنولوجيا وكيمياء البوليمرات"،كلية العلوم –جامعة البصرة،(1983).

20- L.Kacir and M.Narkis.,"Composites",Vol.10,No.1 ,Jan,(1979),pp.(31-36).

21-M.O.W.Richarson.,"Polymer Engineering Composites", (1977) Applied Scieuce pub.LTD, London.

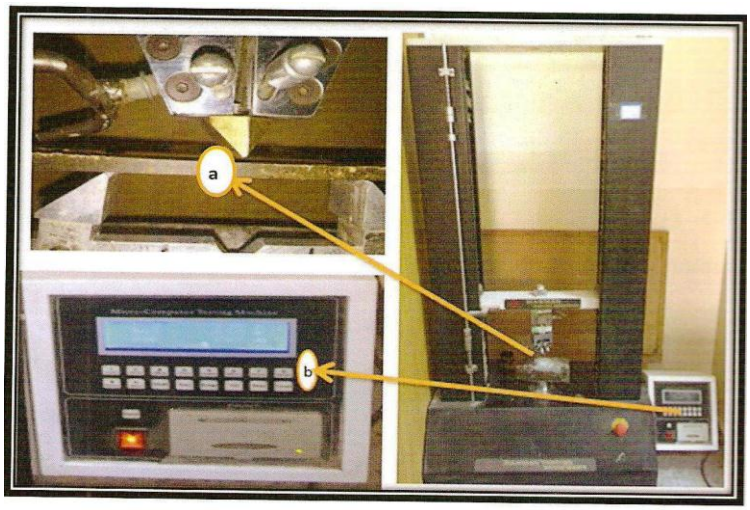

الشكل (1) جهاز اختبار متانة ثلاثي الركيزة. a- تثبيت العينة. b- اخذ القراءة.

الشكل (2) جهاز اختبار الصلادة (Shore D).

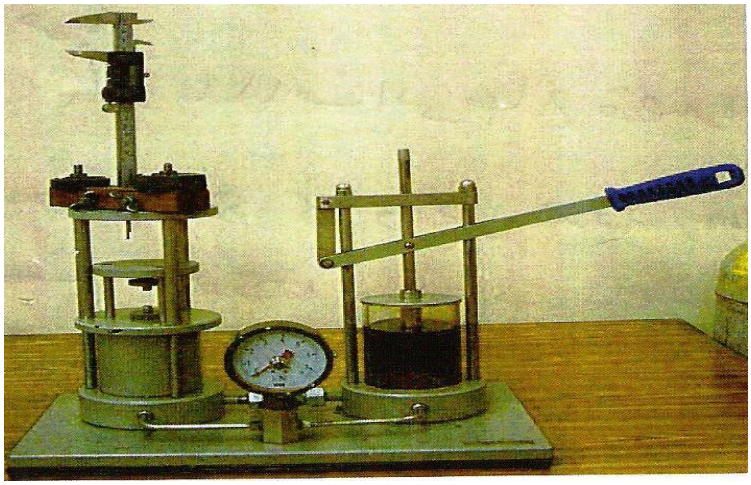

الشكل (3) جهاز اختبار الانضغاطية

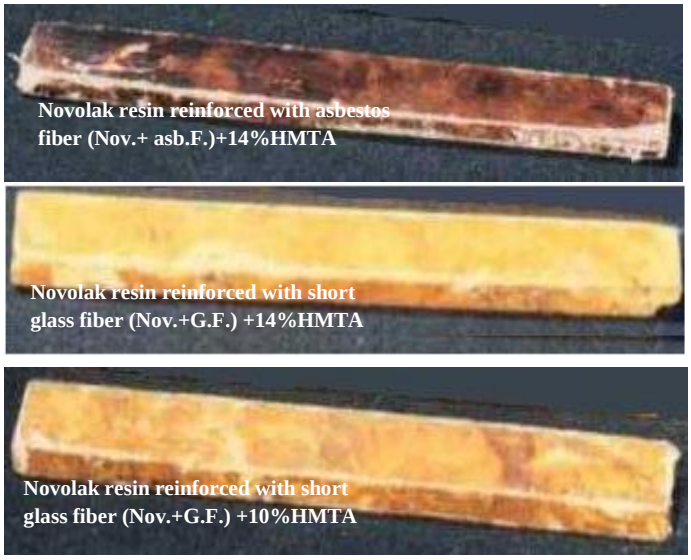

الشكل (4) صور فوتوغرافية للعينات المستخدمة في الدراسة الحالية.

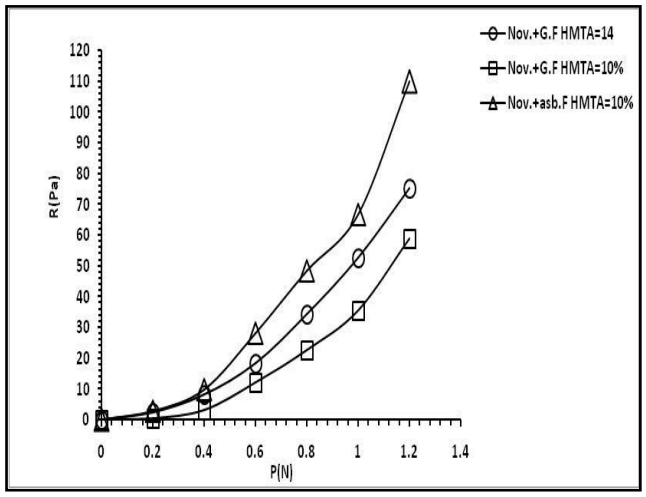

الشكل(7) العلاقة بين معامل الرجوعية وحمل الثني المسلط على مادة النوفولاك المدعمة بالألياف الصناعية وبنسب مختلفة من (HMTA) المتعرضة في الوسط الزرعي.

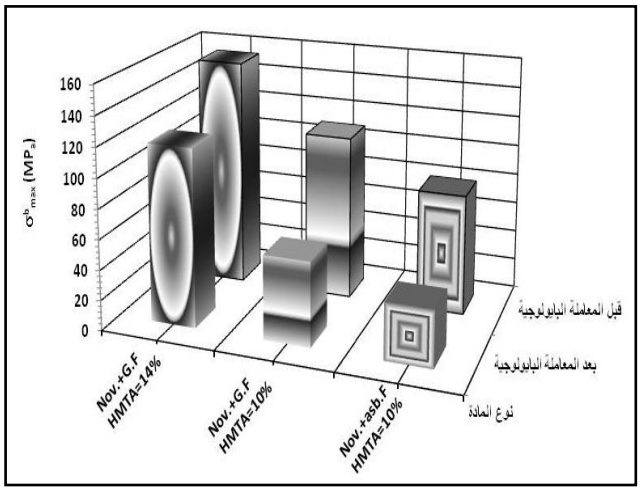

الشكل (8) تغيير مقاومة الثني القصوى عند نقطة الكسر الحاصلة في متراكبات النوفولاك المعاملة بايولوجيا مقارنة مع النماذج الغير معاملة بايولوجيا.

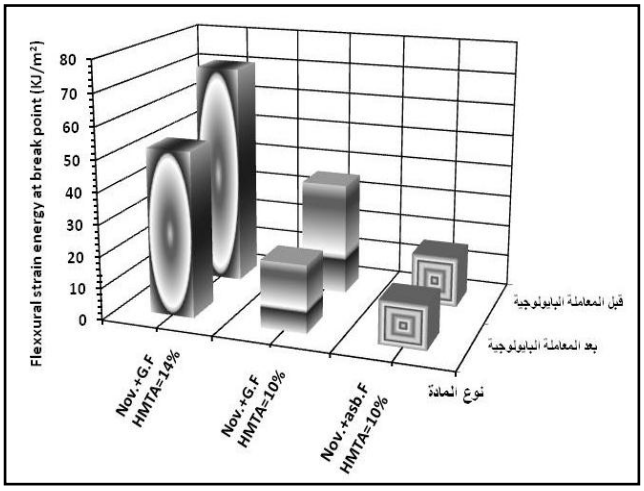

الشكل (9) تأثير المعاملة البايولوجية في اختلاف قيم طاقة انفعال الثني عند نقطة الكسر لمادة النوفولاك المدعمة بالألياف المختلفة.

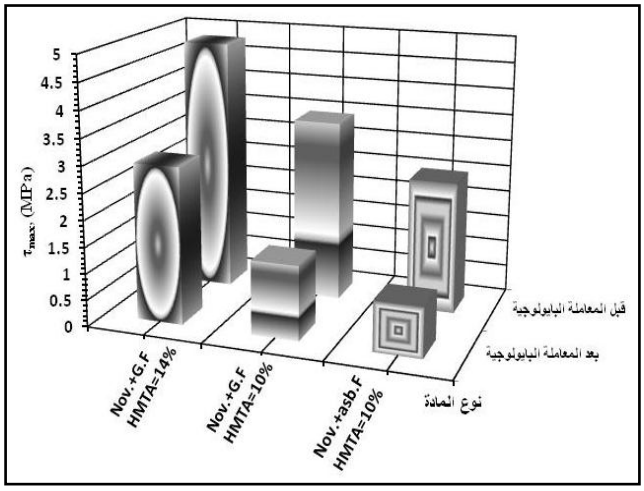

الشكل (10) تأثير المعاملة البايولوجية على مقاومة قص الطبقات الداخلية الحاصلة في متراكبات النوفولاك المحضرة والواقعة تحت حمل الثني.

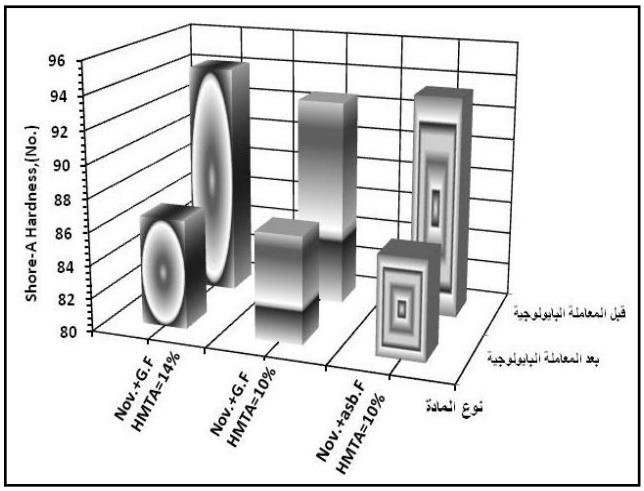

الشكل (11) تأثير المعاملة البايولوجية على الصلادة السطحية لمتراكبات النوفولاك المحضرة.

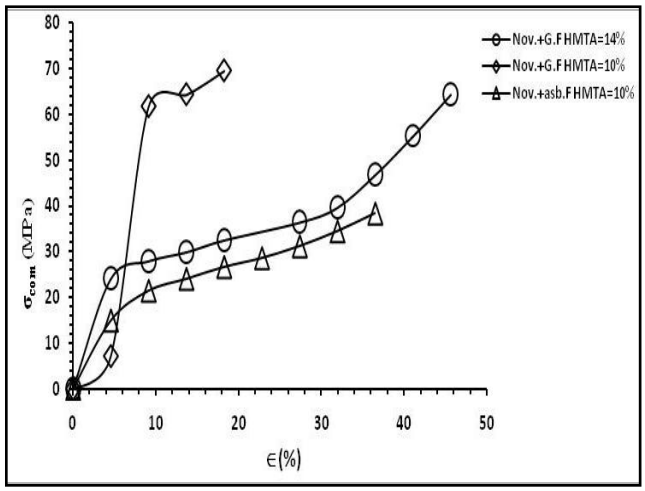

الشكل (12) العلاقة بين الإجهاد الانضغاطي وانفعال الانضغاط لمتراكبات من النوفولاك عند فترة نمو بكتيري.

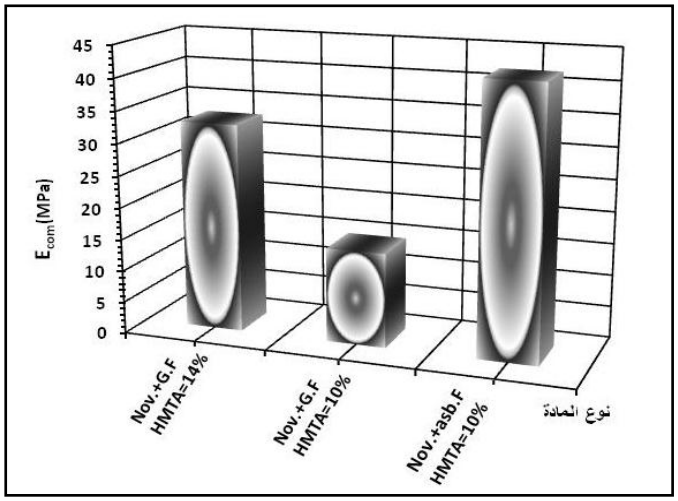

الشكل (13) معامل المرونة الانضغاطية لمتراكبات النوفولاك المحضرة بنسب مختلفة من HMTA والمدعمة بالألياف المختلفة في إطار المعاملة البايولوجية.

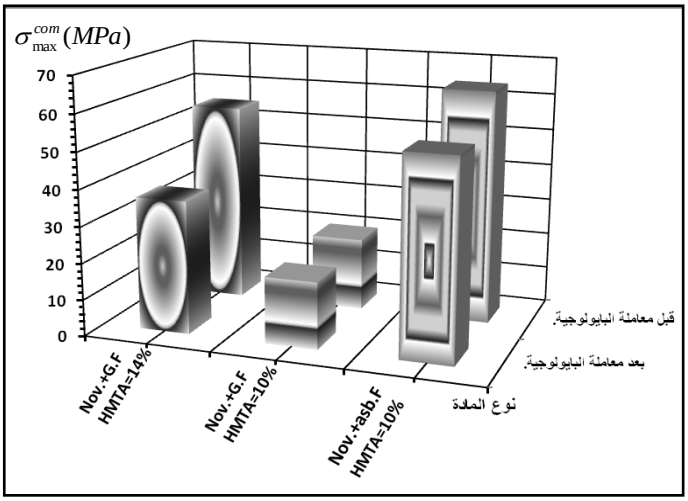

الشكل (14) تغير مقاومة الانضغاط القصوى عند نقطة الكسر الحاصلة في متراكبات النوفولاك المعاملة بايولوجياً مقارنة مع النماذج الغير معاملة بايولوجياً.

الجدول (1) يستعرض بعض الخواص المدروسة قبل المعاملة البكتيرية[8].

نوع المادة	E_b(Gpa)	σ_{max}^{b} (GPa)	τ_{max} (MPa)	σ_{max}^{b} (MPa)	Shore-A Hardness (No.)
Nov.+G.F. HTMA14%	3.01	153.5	4.79	54.88	94.13
Nov.+G.F. HTMA10%	2.26	109.7	3.43	20	92.58
Nov.+asb.F. HTMA10%	2.68	79.94	2.49	63.97	93.4

الجدول (2) يستعرض قيم معامل المرونة الانعطافي (E_b) لجميع النماذج بعد المعاملة البكتيرية.

نوع المادة	E_b(Gpa)
Nov.+G.F. HTMA14%	1.327
Nov.+G.F. HTMA10%	0.978
Nov.+asb.F. HTMA10%	0.648

الجدول(3) يستعرض قيم معامل الرجوعية الانضغاطي (R) لمادة النوفولاك المدعمة بالألياف الصناعية عند حد التناسب في إطار المعاملة البايلوجية.

نوع المادة	R(Pa)
Nov.+G.F. HTMA14%	58.962
Nov.+G.F. HTMA10%	75.471
Nov.+asb.F. HTMA10%	109.905

الجدول(4) يوضح قيم متانة الثني القصوى(σ_{max}^{b}) للنماذج المحضرة بعد المعاملة البايلوجية .

نوع المادة	σ_{max}^{b} (MPa)
Nov.+G.F. HTMA14%	118.33
Nov.+G.F. HTMA10%	55.849
Nov.+asb.F. HTMA10%	37.602

الجدول(5) يوضح قيم طاقة انفعال الثني عند نقطة الكسر للنماذج المحضرة في إطار المعاملة البايلوجية.

نوع المادة	Flexural strain energy (KJ/m^2)
Nov.+G.F. HTMA14%	70.342
Nov.+G.F. HTMA10%	35.486
Nov.+asb.F. HTMA10%	15.894

الجدول(6) يوضح قيم مقاومة قص الطبقات الداخلية عند نقطة الكسر $\tau^{b}_{\max}$ للنماذج المحضرة في إطار المعاملة البايلوجية.

نوع المادة	$\tau^{b}_{\max}$ (MPa)
Nov.+G.F. HTMA14%	2.958
Nov.+G.F. HTMA10%	1.396
Nov.+asb.F. HTMA10%	0.940

الجدول(7) يوضح قيم الصلادة للنماذج (Shore-h) المحضرة بعد المعاملة البايلوجية.

نوع المادة	(Shore-A) Hardness No.
Nov.+G.F. HTMA14%	86.6
Nov.+G.F. HTMA10%	86.466
Nov.+asb.F. HTMA10%	85.966

الجدول(8) يوضح قيم معامل المرونة الانضغاطي(E_{com}) للنماذج المحضرة بعد المعاملة البايلوجية.

نوع المادة	E_{com} (MPa)
Nov.+G.F. HTMA14%	32.69
Nov.+G.F. HTMA10%	14.789
Nov.+asb.F. HTMA10%	42.014

الجدول(9) قيم مقاومة الانضغاط ($\sigma^{com}_{\max}$)عند نقطة الكسر للنماذج المجهز في إطار المعاملة البايلوجية.

نوع المادة	$\sigma^{com}_{\max}$ (MPa)
Nov.+G.F. HTMA14%	36.519
Nov.+G.F. HTMA10%	8.259
Nov.+asb.F. HTMA10%	54.213

https://www.researchgate.net/journal/17264073_University_of_Baghdad_Engineering_Journal

Journal ID: 3631

E-ISSN 2520-3339

P-ISSN 1726-4073

Journal of Engineering

A Scientific Refereed Journal
Published by
College of Engineering
University of Baghdad

May
2017

Number 5

Volume 23

E-ISSN 2520-3339

P-ISSN 1726-4073

مجلة الهندسة

مجلة علمية محكمة تصدرها
كلية الهندسة ـ جامعة بغداد

أيار
2017

العدد 5
المجلد 23

رقم الايداع في دار الكتب والوثائق ببغداد
2231 لسنة 2017